University of Colorado, Boulder
CU Scholar

Aerospace Engineering Sciences Graduate Theses & Dissertations

Aerospace Engineering Sciences

Spring 1-1-2016

A Framework for Precise Orbit Determination of Small Body Orbiting Spacecraft

Siamak Ghanizadeh Hesar
University of Colorado at Boulder, siamak.hesar@colorado.edu

Follow this and additional works at: https://scholar.colorado.edu/asen_gradetds

 Part of the Aerospace Engineering Commons

Recommended Citation
Hesar, Siamak Ghanizadeh, "A Framework for Precise Orbit Determination of Small Body Orbiting Spacecraft" (2016). *Aerospace Engineering Sciences Graduate Theses & Dissertations*. 141.
https://scholar.colorado.edu/asen_gradetds/141

This Dissertation is brought to you for free and open access by Aerospace Engineering Sciences at CU Scholar. It has been accepted for inclusion in Aerospace Engineering Sciences Graduate Theses & Dissertations by an authorized administrator of CU Scholar. For more information, please contact cuscholaradmin@colorado.edu.

www.manaraa.com

A Framework for Precise Orbit Determination of Small Body Orbiting Spacecraft

by

Siamak G. Hesar

B.S., Industrial Engineering,

Sharif University of Technology, Tehran, Iran, 2004

M.S., Manufacturing Engineering,

University of Rhode Island, Kingston RI, 2006

M.S., Astronautical Engineering,

University of Southern California, Los Angeles CA, 2012

A thesis submitted to the

Faculty of the Graduate School of the

University of Colorado in partial fulfillment

of the requirements for the degree of

Doctor of Philosophy

Department of Aerospace Engineering Sciences

2016

www.manaraa.com

This thesis entitled:
A Framework for Precise Orbit Determination of Small Body Orbiting Spacecraft
written by Siamak G. Hesar
has been approved for the Department of Aerospace Engineering Sciences

Daniel J. Scheeres

Jeffrey S. Parker

Jay W. McMahon

Webster Cash

Shyam Bhaskaran

Date

The final copy of this thesis has been examined by the signatories, and we find that both the content and the form meet acceptable presentation standards of scholarly work in the above mentioned discipline.

www.manaraa.com

Hesar, Siamak G. (Ph.D., Aerospace Engineering Sciences)

A Framework for Precise Orbit Determination of Small Body Orbiting Spacecraft

Thesis directed by Prof. Daniel J. Scheeres

Spacecraft flying in close proximity of small bodies face a very complex dynamical environment with numerous types of perturbing forces acting on them. Development of new techniques are needed for precise navigation of spacecraft in such environments. This study focuses on furthering our understanding of precise orbit determination of spacecraft in close proximity of small bodies via implementation of new methods for precise representation of strong and weak perturbing forces acting on spacecraft, such as the irregular gravitational field, strong solar radiation pressure effects, and thermal radiation pressure effects from the surface of small bodies.

Solar radiation pressure is a strong perturbing force acting on spacecraft in the orbital environment of small bodies that constantly pushes the spacecraft in a general direction away from the Sun. The existence of strong solar radiation pressure effects creates a complex dynamical environment around asteroids and comets that results in a particular set of orbital regimes, such as the family of the terminator or close to terminator orbits, whose dynamical evolution may not be intuitive. Small perturbations caused by maneuver errors and other sources may lead to large deviations in a spacecraft trajectory from its nominal orbit. Understanding the evolution of errors and uncertainties in the orbital elements of spacecraft is a crucial piece of mission planning and spacecraft navigation. In this thesis, we derive analytical expressions that govern the secular motion of the perturbed orbital elements in an environment that is strongly perturbed by the solar radiation pressure effects. Furthermore, we study a framework based on a Fourier series expansion for precise representation of the solar radiation pressure and small body surface thermal radiation pressure effects on spacecraft. This method is utilized in generating precise orbit determination solutions for simulated spacecraft in orbit about small bodies in the presence of dynamical and modeling errors.

www.manaraa.com

Gravitational perturbations are other major disturbing forces in the proximity of a small body. This is especially true for spacecraft that come close to the surface of asteroids or comets in a landing or touch-and-go (TAG) scenario. Due to the irregular shape of these objects, a significant portion of the landing or TAG trajectory may lie inside a circumscribing sphere, where the conventional spherical harmonics expansion of the gravitational field is not convergent. Recent studies developed a so-called *interior* gravity field spherical harmonics expansion that extends down to the surface of the object without divergence issues. The interior gravity field, however, is not studied in the context of orbit determination and spacecraft navigation. This study investigates the feasibility of the utilization of such model to navigate spacecraft in a trajectory that is close to the surface of an irregularly shaped body of mass. The study will further examine the capability of estimating the spherical harmonics coefficients for an interior gravity field via orbit determination solutions.

www.manaraa.com

Dedication

To my wife, Carmen, for her unwavering support and for keeping me focused and on track; to my soon-to-be-born baby boy, who with his upcoming arrival made sure that I finish my thesis on time; and to my parents, Manijeh and Firouz, for their unconditional love and encouragement every day of my life.

www.manaraa.com

Acknowledgements

There are so many people that have helped and supported me throughout my graduate studies at CU. First and foremost, I would like to sincerely thank my advisor, Dan Scheeres, whose advice and guidance was instrumental in the completion of this work; the best advisor one could ask for. I will always be grateful for his support and for giving me the confidence that I needed to complete this degree. I am also grateful to Dan for offering me the opportunity to continue working on the OSIRIS-REx mission, which is the coolest mission ever! I am also deeply indebted to Jeff Parker who advised me during the first two years of my graduate studies at CU. Jeff's guidance and support was key in learning the fundamental concepts and tools that I have used through out my research. I would also like to thank the other members of my committee, Jay McMahon, Shyam Bhaskaran, and Webster Cash. I am thankful to Jay whom I have had the privilege to work with during the past year. With his amazing intuition of mathematical and engineering concepts he is always able to break down complex problems into simpler pieces easier to understand. I also look forward to working more closely with Jay on the OSIRIS-REx mission after my graduation. I am also grateful to Shyam Bhaskaran for his advice and expert insight into my research and for kindly hosting me at JPL and teaching me the JPL Small Body Toolkit. Furthermore, I am thankful to Webster Cash for his insightful advice and suggestions for my research. I would also like to remember and honor the late George Born. During a short while that I had the honor of working on a research project with him, I learned so much from him and I will always be indebted to him for his advice and remarkable insight in the field of astrodynamics. This work was also supported by NASA contract NNM10AA11C (D. S. Lauretta, PI) and related

www.manaraa.com

subcontracts from the University of Arizona.

I would also like to thank many of my fellow graduate students some of whom have graduated already. In particular, I would like to thank Jason Leonard and Yu Takahashi who helped me in a significant in the development of some of the tools that I have used in this work. I would also like to sincerely thank Nicola Baresi, Matthieu Talpe, David Surovik, Antonella Albuja, Inkwan Park, Hyun Chul Ko, Ryan Mcgranaghan for their help and advice. Also, to all of the members of the Celestial and Spaceflight Mechanics Laboratory, thank you all for creating a fun and intellectually stimulating environment every day. Aside from the academic challenges, graduate school can have its own administrative complexities and challenges. But, thanks to the amazingly capable Ann Brookover and Sarah Melssen it all seemed very easy.

Finally, I would like to extend my gratitude to my family. To my amazing wife, Carmen, who has always believed in me and supported me in whatever I set my mind in achieving. There were times that research seemed so daunting and formidable. It was always Carmen's unconditional love and support that kept me going through those hard times. We are also very excited for the upcoming arrival of our first child. To my parents, Manijeh and Firouz, who did everything in their power to make sure that I receive a great education and who always supported me in achieving my goals, even when it meant that I would travel to the U.S. for the graduate school and that they may not see their son for many years in between visits. Words cannot describe how grateful I am to the best parents in the world. And last but not the least, many thanks to my sister, Laleh, and my brother, Goudarz, who always encouraged their little brother to dream big.

www.manaraa.com

Contents

Chapter

www.manaraa.com

www.manaraa.com

www.manaraa.com

www.manaraa.com

www.manaraa.com

Tables

Table

www.manaraa.com

www.manaraa.com

Figures

Figure

www.manaraa.com

www.manaraa.com

www.manaraa.com

www.manaraa.com

www.manaraa.com

www.manaraa.com

www.manaraa.com

www.manaraa.com

Chapter 1

Introduction

For thousands of years, humans have gazed at the night sky wondering about the secrets that lie behind the flickering lights of the stars. Yet, only in the past few decades have we been able to travel far distances away from the Earth and expand our reach out into the solar system, thanks to the incredible advances in the science and technology of space exploration. We are able to place cameras and other scientific instruments on probes that travel to distant objects within our solar system and beam back dazzling images and a wealth of information from these alien worlds. Numerous such missions have been flown to the other planets and their moons. These missions have profoundly changed our understanding of the solar system and our place within it. Also, in the past decades the scientific interest in exploring the small bodies within the solar system has grown significantly with several previous and currently ongoing missions as well as planned future ones under consideration. Asteroids and comets are primitive objects that remain from the formation of the solar system. Scientists of various fields are interested in studying the physical parameters and the composition of these objects since they are believed to contain pristine material from the early history of the solar system [28] and even primitive organic compounds that might have led to life on Earth [1] .

Aside from the scientific appeal of exploring small bodies, they are also the subject of interest for several other reasons. Exploration of deep space may be a stepping stone in technological advancement for future manned space flight to Mars and outer solar system targets. Advanced

[1] http://neo.jpl.nasa.gov/neo/life.html

www.manaraa.com

space robotics techniques may enable the *In-Situ* Resource Utilization (ISRU) and volatile extraction from asteroids for prolonged space missions [13] [2] or economic ventures of mining Near Earth Objects (NEO) for rare precious metals. Studying and surveying the NEO's is also necessary in identifying potentially hazardous objects and the development of techniques and strategies to mitigate the risk of a catastrophic collision with Earth [3] .

A mission to a small body is mainly tasked with a close encounter with the target object with the purpose of determining the shape and the rotational dynamics of the object, resolving the gravitational field, inferring its density distribution and the internal structure, determination of its composition, and performing close proximity operations where the spacecraft may come in contact with the surface of the object. A key component for the successful implementation of these tasks is the performance of precise navigation and orbit determination (OD) of the spacecraft in the close proximity of the body. This is, however, hindered by the challenging and complex dynamical environment that exists in close proximity to the object. Spacecraft in the proximity of a small body experience numerous types of perturbing forces acting on them. These include, but are not limited to, perturbations from non-uniform gravitational field, strong perturbing effects of the solar radiation pressure (SRP), thermal radiation pressure (TRP) effects from the surface of the object, outgassing of the surface volatiles around a comet, and other forces such as errors in the maneuver executions or heat radiation pressure from the spacecraft components. Due to relatively weak gravitational attraction of small bodies, each one of these forces may impart considerable perturbation on the spacecraft orbit, some of which are not fully understood. This naturally leads to the following thesis statement:

Thesis Statement

The complex and strongly perturbed dynamical environments about small bodies require the development of new methods for precise orbit determination of spacecraft in orbit about these objects. A general Fourier series representation of the solar radiation pressure and the small body surface thermal radiation pressure

[2] http://www.nasa.gov/exploration/analogs/isru/
[3] http://neo.jpl.nasa.gov/neo/

www.manaraa.com

acting on a spacecraft provides means for the accurate representation of these perturbing forces and the generation of precise orbit determination solutions. Derivation of the secular dynamics of the spacecraft orbit using the general Fourier representation of the perturbing forces sheds light on the long term evolution of the spacecraft orbit and the propagation of errors and uncertainties of the orbit. Furthermore, the use of the interior gravitational field expansion allows for precise spacecraft navigation in the surface proximity of irregularly shaped bodies, where the conventional gravitational field expansion fails to converge.

1.1 Secular Effects due to Strong SRP Perturbation

SRP is the force imparted on spacecraft due to the momentum transfer from sunlight photons that impinge and interact with the illuminated surfaces of the spacecraft. This force is generated due to the absorbtion of all the incident photons on a surface, a portion of which is then reflected from the surface or emitted off of that surface in the form of thermal radiation. SRP is a significant perturbing force for spacecraft in the orbital environment of small bodies that constantly pushes the spacecraft in a general direction away from the Sun. The existence of a strong SRP effect creates a highly complex and non-Keplerian dynamical environment about asteroids and comets [77]. The orbital dynamics of spacecraft under strong SRP perturbation has been studied before [58] and a closed form solution is derived [76] that approximates the motion of the secular orbital elements of a spacecraft orbit bound to a small body. Under the assumption of a fixed SRP perturbation direction, this relationship leads to the realization of set of periodic solutions for the secular motion of the orbit elements [73, 74]. Yet, due to the highly non-Keplerian dynamical environment, small errors may lead to large deviations from the nominal trajectory of the spacecraft. As a results we are interested in understanding the ways in which the spacecraft state errors and uncertainties propagate and evolve over time in an environment that is strongly perturbed by SRP. We dedicate a portion of this thesis for exploring this subject.

www.manaraa.com

1.2 Precise Representation of the SRP and TRP

The study of secular dynamics reveals an overall understanding of the SRP effects on the long term evolution of orbital elements of the spacecraft. This approach, however, does not treat the high fidelity representation of the perturbing forces imparted on spacecraft. To do so, one needs to take into account the interaction of the SRP, TRP, and other small perturbations with the actual shape and the surface properties of the spacecraft. There has been a substantial amount of work on the precise representation of the SRP effects on spacecraft. In general, they may be divided into two main approaches. One is an empirical approach that relies on fitting satellite observations to their orbit dynamics and inferring the effect of small forces from the orbit determination solutions [4, 83]. Such a method is useful for the precise representation of small perturbing forces on spacecraft that fly in a well characterized orbital environment. Another approach is to utilize the detailed shape and the surface properties of a spacecraft to numerically compute the interaction of the sunlight with every surface element and facet [49, 52, 72]. While this method may be able to accurately represent the perturbing effects of the SRP on spacecraft, it is computationally expensive and, in general, not suitable for the purpose of orbit determination.

In this work, we explore the use a relatively new method [79] for the precise representation of the perturbing forces imparted on the spacecraft in orbit about small bodies. This method reduces the shape and the surface properties of a spacecraft down to list of coefficients that form an infinite Fourier series expansion. While the values that are computed for such coefficients are specific for a given shape and surface properties of a spacecraft, their treatment within the Fourier expansion is general. This method is akin to representing the gravitational field of an object via a spherical harmonics expansion with its corresponding spherical harmonics coefficients. This method was first used in the context of the dynamical evolution of asteroids' motion [79] due to the Yarkovsky–O'Keefe-Raszievskii–Paddack or "YORP" effect [11, 67]. It was later expanded to represent the SRP effects on spacecraft [55], with a study on its use for generating precise orbit determination solution of spacecraft [56] or the evaluation of the evolution of the rotational state

www.manaraa.com

of space debris and defunct satellites due to the YORP effect [2, 1, 3].

There are several advantages for using a Fourier series to model the SRP effect on spacecraft. This model has a low computation cost compared to many other numerical methods. In addition, the periodic nature of the Fourier series representation allows for the derivation of analytical solutions for the secular effects of SRP on spacecraft orbits. Finally, this model is suitable for use in an orbit determination process and its coefficients may be estimated during the time that spacecraft is in orbit to improve the orbit determination solutions. In this work, we utilize this model in the derivation of a set of analytical solutions that govern the secular dynamics of the orbital elements of spacecraft in orbit about small bodies due to the SRP perturbation. Furthermore, we implement numerical simulations that demonstrate the use of this method in generating precise orbit determination solutions. Finally, the Fourier series representation is expanded to derive a new and precise model of the TRP effect on a spacecraft orbiting at a close distance from a small body.

1.3 Surface Proximity Gravitational Field of Small Bodies

Gravitational perturbations are another major perturbing force that can cause a spacecraft to diverge from its nominal trajectory. Spacecraft in the close proximity of a small body are significantly perturbed by the irregular and complex gravitational field that exists around the object. This is particularly important for spacecraft that plan to descend down to the surface of the object in a landing or a touch-and-go (TAG) trajectory. It is crucial to properly model the gravitational field of a small body for any point in space around it in order to perform successful landing or TAG operation. The well-known and extensively studied spherical harmonics expansion [31, 32, 39, 47] is often used to model the gravitational field the orbital environment around a object. However, this expansion is valid only outside a spherical region that encompasses the entire body of mass and diverges anywhere inside such a sphere. Due to this fundamental limitation [92], this method is not suitable for accurate representation of the gravitational field in the surface proximity of highly irregularly shaped objects such as asteroids and comets.

www.manaraa.com

A constant density polyhedron model of an object may be used for the accurate representation of the gravitational field anywhere on or around an irregularly shaped object [90, 91, 93]. While this method may serve as an *a priori* constraint on the surface proximity gravitational field of a small body, its constant density assumption and the high computational cost makes it unattractive for spacecraft navigation work. Ellipsoidal harmonic expansion (detailed in Reference [31] Ch-XI and Reference [47] Ch-VIII) may also be used to mitigate the divergence issue of the spherical harmonic expansion [21]. The convergence region of an ellipsoidal harmonics expansion lies closer to the surface of an elongated body of mass. Nonetheless, it also suffers from the same divergence issues at any point outside of its convergence region.

Recent studies [85, 92] have developed the *interior* gravity field spherical harmonics expansion that extent down to the surface of the object without divergence issues. Reference [85] showes that the interior gravity fields can accurately describe the surface gravitational potential and attraction of an arbitrary object. Despite this attractive property, the interior gravity field model has not been considered in the context of orbit determination and spacecraft navigation. Also, the direct estimation of its coefficients via orbit determination solutions has not been studied before. In this work we first examine the feasibility of estimating the interior gravity field coefficients via an orbit determination solution. Second, we evaluate the performance of the interior gravity field in tracking a simulated landing trajectory on the surface of a highly irregularly shaped object.

1.4 Dissertation Overview

This dissertation presents a framework for precise treatment of the perturbing forces acting on spacecraft in the close proximity of small bodies and utilizes these models in the generation of precise orbit determination solutions. First, we present an overview of the frequently used mathematical concepts in this work. This information is presented in Chapter 2 along with the definition of the coordinate frames and a brief discussion on the concept of the orbit determination process. This is followed by Chapter 3 with a discussion on the significant force models in the context of a small body orbiter. There are numerous types of forces acting on spacecraft in the close

www.manaraa.com

proximity of small bodies. We introduce several of the force models and delve further into the formulation of three force fields, namely the small body gravitation field, solar radiation pressure, and small body surface thermal radiation pressure. The material presented in these two chapters lays out the fundamental concepts and the mathematical models that are used in the rest of the dissertation.

Overall this dissertation is organized such that Chapters 4, 5, and 6 focus an the treatment of the SRP and the TRP perturbing forces on spacecraft, while Chapters 7 and 8 study the gravitational environment in close proximity to a small body.

Chapter 4 discusses the complex dynamical environment around small bodies due to the existence of strong SRP perturbation. A set of closed form solutions are presented in this chapter that govern the secular evolution of the orbital elements of spacecraft around small bodies. Following this, we derive a set of equations for the propagations of the errors and uncertainties of spacecraft orbit in such an environment. These equations are derived under the assumption of simplified cannonball type model [46] for the SRP perturbation effect. The derived expressions are utilized to analyze the sensitivity of the OSIRIS-REx [20] sun-terminator orbits to small maneuver errors and their uncertainties.

Chapter 5 discusses the development of a precise model for the representation of the SRP perturbation. This model leverages an infinite series expansion of the Fourier coefficients that takes into account the shape and the surface properties of the spacecraft. We utilize this model to derive the averaged equations for the secular dynamics of the orbit elements directly in the true anomaly space. Deriving these equations in the true anomaly space is particularly useful for a small body orbiter whose orbit eccentricity may increase significantly in the long term. An error analysis is then implemented to evaluate the sensitivity of the spacecraft orbital element to errors in the coefficients of the Fourier representation of SRP. Furthermore, we expand the Fourier series expansion to model the TRP effects on spacecraft in orbit around small bodies. This expansion is derived and its performance is tested against a numerical model that considers the exact shape of the spacecraft.

www.manaraa.com

Chapter 6 presents a comprehensive study of the numerical estimation of spacecraft orbit utilizing the precise SRP and TRP Fourier expansion models. After a detailed discussion on the derivation of the partial derivatives of the Fourier series model, results from a comprehensive covariance study is presented. The covariance study results show the expected level of estimation precision that one may achieve from an orbit determination solution on the Fourier series coefficients. Lastly, in Chapter 6, a set of full simulation studies tests the performance of the SRP and TRP Fourier expansion models in generating precise orbit determination solutions.

Chapter 7 moves the discussion to the concept of gravitational potential theory and the derivation of the gravitational force field. In particular it focuses on the limitations of the conventional spherical harmonics model in modeling the surface proximity gravitational field of irregularly shaped objects. The so-called *interior* field expansion is then presented and its benefits are discussed. Finally, Chapter 8 discusses the implementation of the interior gravity field in navigating spacecraft in the close proximity of highly irregularly shaped objects. A case study is implemented to characterize the gravitational field of Asteroid (433) Eros at a space close to the landing site of the NEAR spacecraft [14].

1.4.1 Contributions

The contributions of this dissertation are summarized as the followings:

- Derived a set of conditions on orbital elements that result in the generation of secularly non-precessing – *frozen-node* – orbits over the sun terminator plane around a small body.
- Derived analytical closed form expressions that govern the secular evolution of small errors in an orbit under a strong SRP perturbation.
- Performed a comprehensive sensitivity analysis of the OSIRIS-REx terminator orbits to small maneuver errors.
- Applied averaging theory to the effects of SRP using a Fourier series expansion model that

www.manaraa.com

is valid for an arbitrary shape of a spacecraft. These equations derive the secular dynamics of a spacecraft orbit directly in the true anomaly space that is suitable for eccentric orbits.

- Developed a precise model for the treatment of TRP effects on spacecraft with arbitrary shapes.
- Performed a sensitivity analysis of an orbit to errors in the SRP Fourier coefficients and implemented a covariance study to measure the expected level of estimation precision on the SRP Fourier coefficients and their potential couplings with the gravitational spherical harmonics coefficients.
- Implemented the SRP and TRP Fourier expansion models to generate precise orbit determination solutions.
- Performed surface proximity gravitational field characterization of Asteroid (433) Eros via orbit determination solutions.
- Implemented the interior gravity field expansion in precise navigation of a simulated spacecraft landing on the surface of Asteroid (433) Eros.

1.4.2 Publications

The relevant journal and conference papers are listed below:

Journal Papers

- D.J. Scheeres, S.G. Hesar, S. Tardivel, et al., "The Geophysical Environment of Bennu," Icarus, Vol. 276, 116-140, 2016, DOI:10.1016/j.icarus.2016.04.013.
- S.G. Hesar, D.J. Scheeres, and J.W. McMahon, "Precise Solar Radiation Pressure Models for Small Body Orbiters: Applications to OSIRIS-REx," to be submitted to the Journal of Guidance, Control, and Dynamics.

www.manaraa.com

- S.G. Hesar, D.J. Scheeres, J.W. McMahon, and Y. Takahashi, "Surface Proximity Gravitational Field Estimation of Asteroid (433) Eros," to be submitted to the Journal of Guidance, Control, and Dynamics.

- S.G. Hesar, D.J. Scheeres, and J.W. McMahon, "Sensitivity Analysis of the OSIRIS-REx Terminator Orbits to Maneuver Errors," Submitted to the Journal of Guidance, Control, and Dynamics, Under Review.

- S.G. Hesar, J.S. Parker, J.M. Leonard, R.M. McGranaghan, and G.H. Born, "Lunar Far Side Surface Navigation Using Linked Autonomous Interplanetary Satellite Orbit Navigation (LiAISON)," Acta Astronautica, Vol. 117, 116–129, 2015, DOI:10.1016/j.actaastro.2015.07.027.

Conference Papers

- S.G. Hesar, D.J. Scheeres, and J. McMahon, "Analysis of Solar Radiation Pressure Effects on the OSIRIS-REx Spacecraft in Orbit Around Bennu," 26th AAS/AIAA Space Flight Mechanics Meeting, Napa, CA, 2016.

- S.G. Hesar, D.J. Scheeres, J. McMahon, and Y. Takahashi, "Surface Proximity Gravitational Field Analysis of Asteroid (433) Eros," 39th AAS Guidance and Control Conference, Breckenridge, CO, 2016.

- S.G. Hesar, D.J. Scheeres, and J.W. McMahon, "Sensitivity Analysis of the OSIRIS-REx Terminator Orbits to Random De-sat Maneuvers," 2015 AAS/AIAA Astrodynamics Specialist Conference, Vail, CO, August 9–13, 2015.

- S.G. Hesar, J.S. Parker, J.W. McMahon, and G.H. Born, "Small Body Gravity Field Estimation Using LiAISON Supplemented Optical Navigation," 2015 AAS Guidance, Navigation, and Control Conference, No. AAS 15-024, Breckenridge, CO, Jan. 30 – Feb. 4, 2015.

- S.G. Hesar, J.S. Parker, R.M. McGranaghan, J.M. Leonard, K. Fujimoto, and G.H. Born, "Application of LiAISON Orbit Determination Architecture in Navigating a Rover on the

www.manaraa.com

Lunar Surface," Proceedings of the AAS/AIAA Astrodynamics Specialist Conference, No. AAS 13-738, AAS/AIAA, Hilton Head, South Carolina, 11–15 August 2013.

www.manaraa.com

Chapter 2

Mathematical Background

In this chapter, we present a review of frequently used mathematical concepts throughout this thesis. First, we review some of the basic vectoral, dyadic, and higher order tensor operations and their related identities, followed by the concept of averaging as it is utilized in celestial mechanics. Then, we present the definition of the coordinate frames that are used in this work. Finally, the process of orbit determination is described with an introduction on the square root information filter that the utilized in this work.

2.1 A Review of Vectors, Dyads, and Tensors

The material presented here are mainly extracted from References [26] and [77].

In a basic form, a vector is defined as a quantity that possesses a *magnitude* as well as a *direction* [26]. The magnitude of a vector is a scalar quantity with no direction, and in this work, we use an un-bolded typeface, e.g. "a", to specify a scalar quantity. Bolded typeface, e.g. "$\mathbf{a}$", is used to specify a vector quantity. The magnitude of an arbitrary vector $\mathbf{a}$ is also represented by $|\mathbf{a}|$. A *unit vector* is defined as a vector with the magnitude equal to unity and we use the overhead *hat* notation, i.e. "$\hat{}$", to represent a unit vector. A non-zero vector divided by its magnitude results in a unit vector that has the same direction as the original vector, i.e. $\hat{\mathbf{a}} = \mathbf{a}/|\mathbf{a}|$. A *direct* product, a.k.a a dot product, of two arbitrary vectors $\mathbf{a}$ and $\mathbf{b}$ is a scalar quantity that is denoted by $\mathbf{a} \cdot \mathbf{b}$. The magnitude of a vector is closely related to the dot product via $a = |\mathbf{a}| = \sqrt{\mathbf{a} \cdot \mathbf{a}}$. If the dot product of two non-zero vectors is equal to zero, then they are said to be orthogonal with respect to each

www.manaraa.com

other. A set of n mutually orthogonal unit vectors define an n-dimensional vector space ($\mathbb{R}^n$). In this thesis we only encounter vectors with 3 dimensions. Hence, in what follows, we refer to all of the 3-dimensional vectors simply as a vector without specifying the number of their dimensions. Let $\hat{\mathbf{i}}$, $\hat{\mathbf{j}}$, and $\hat{\mathbf{k}}$ be a set of three orthogonal unit vectors that define $\mathbb{R}^3$. Then, any vector, say $\mathbf{a}$, can be expressed as the linear combination of these vectors, i.e. $\mathbf{a} = a_1\hat{\mathbf{i}} + a_2\hat{\mathbf{j}} + a_3\hat{\mathbf{k}}$, such that $a_1 = \mathbf{a}\cdot\hat{\mathbf{i}}$, and so on. With an implied coordinate system we denote a vector as a column of its components, i.e.

$$\mathbf{a} = \begin{bmatrix} a_1 \\ a_2 \\ a_3 \end{bmatrix}, \tag{2.1}$$

with its transpose denoted by $\mathbf{a}^{\mathrm{T}} = [a_1 \;\; a_2 \;\; a_3]$ being a row vector.

A *dyad* is defined by "$\mathbf{ab}$" formed by the juxtaposition of two vectors $\mathbf{a}$ and $\mathbf{b}$ without the dot or cross symbol in between [26](Ch. V). In the context of the row and column vectors, a dyad is equivalent to the outer product of two vectors. A *dyadic* is defined as a linear combination of dyads, e.g. $\mathcal{A} = a_1b_1\hat{\mathbf{i}}\hat{\mathbf{i}} + a_1b_2\hat{\mathbf{i}}\hat{\mathbf{j}} + a_1b_3\hat{\mathbf{i}}\hat{\mathbf{k}} + \ldots + a_3b_3\hat{\mathbf{k}}\hat{\mathbf{k}}$. Given a coordinate system, dyadic $\mathcal{A}$ may be written in a following matrix form

$$\mathcal{A} = \begin{bmatrix} a_1b_1 & a_1b_2 & a_1b_3 \\ a_2b_1 & a_2b_2 & a_2b_3 \\ a_3b_1 & a_3b_2 & a_3b_3 \end{bmatrix}. \tag{2.2}$$

The first vector in a dyad is called the *antecedent* and the second vector is called the *consequent* of the dyad. The conjugate of a dyadic is given by switching the order of the antecedent and consequent in each term. This is equivalent to taking the transpose of a the matrix form of that dyadic. The *unity* dyadic is given by $\bar{\bar{U}} = \hat{\mathbf{i}}\hat{\mathbf{i}} + \hat{\mathbf{j}}\hat{\mathbf{j}} + \hat{\mathbf{k}}\hat{\mathbf{k}}$. The unity dyadic plays the same role as the identity matrix, such that $\mathbf{a}\cdot\bar{\bar{U}} = \bar{\bar{U}}\cdot\mathbf{a} = \mathbf{a}$. One of the major benefits of using the dyadic notation is the simplification of the vector operations. For instance the dyadic $\tilde{\mathbf{a}}$ is defined as the cross product operation and it may be used to reduce the cross product of two vectors to a simple

www.manaraa.com

dot product between this dyadic and another vector, i.e.

$$\mathbf{a} \times \mathbf{b} = \tilde{\mathbf{a}} \cdot \mathbf{b} = \mathbf{a} \cdot \tilde{\mathbf{b}} = -\tilde{\mathbf{b}} \cdot \mathbf{a}. \tag{2.3}$$

In the matrix notation the cross product dyadic or the cross product matrix is given by

$$\tilde{\mathbf{a}} = \begin{bmatrix} 0 & -a_3 & a_2 \\ a_3 & 0 & -a_1 \\ -a_2 & a_1 & 0 \end{bmatrix}. \tag{2.4}$$

There are two useful identities associated with the cross product operation given by

$$\begin{aligned} \widetilde{\mathbf{a} \cdot \mathbf{b}} &= \mathbf{ba} - \mathbf{ab}, \\ \tilde{\mathbf{a}} \cdot \tilde{\mathbf{b}} &= \mathbf{ba} - (\mathbf{a} \cdot \mathbf{b})\bar{\bar{U}}. \end{aligned} \tag{2.5}$$

A *tensor* is the generalization of the scalars, vectors, and dyadics. It is a mathematical object that is identified by its dimension and rank. A tensor with a rank 1 defines a vector and one with a rank 2 is a dyadic. The script capital latin letters are used to denote a tensor. In this work we only encounter tensors of dimension 3 and we use the subscript indexes to identify the rank and of the tensor. Therefore a tensor of dimension 3 and rank m is denoted by $\mathcal{A}_{i_1 i_2 \ldots i_m} \in \mathbb{R}^{3 \times m}$, where $i_j = 1, 2,$ and 3. Tensors of like dimension and rank can be added and subtracted term by term. The only multiplication operation that we use in this work is a generalization of the dot product, which lets two tensors with the same dimension to be multiplied together. The well-known Einstein summation convention[1] is used to show this multiplication, which basically sums the terms with similar indices. For instance let $\mathcal{A}_{ijk}$ and $\mathcal{B}_{kl}$ be tensors of dimension 3. The multiplication of these tensors is given by

$$\mathcal{C}_{ijl} = \mathcal{A}_{ijk}\mathcal{B}_{kl} = \sum_{k=1}^{3} a_{ijk} b_{kl}, \tag{2.6}$$

where a and b are the entries of the tensor $\mathcal{A}$ and $\mathcal{B}$, respectively. In this work we encounter tensors when taking the partial derivatives of dyadics with respect to vectors or the vectors with respect to dyadics. Let $\mathcal{A}_{ij}$ be a rank-2 tensor (a dyadic) and $\mathbf{a}$ be a rank-1 tensor (a vector). Then a tensor of rank-3 is generated by $\mathcal{A}_{ij,k} = \partial \mathcal{A}_{ij} / \partial a_k$ or $\mathcal{A}_{k,ij} = \partial a_k / \partial \mathcal{A}_{ij}$.

[1] Cubitt, T. "Einstein Summation Convention and δ-Functions." http://www.dr-qubit.org/teaching/summation_delta.pdf.

www.manaraa.com

2.2 Useful Partial Derivative Identities

Through out this work we derive the partial derivative of various vectorial and dyadic quantities with respect to one another. Here we present couple of expressions that will be used in the derivation of such partial derivatives in the future chapters. Let quantities $\mathbf{a}$ and $\mathbf{b}$ be vectors realized in the same coordinate reference frame with their magnitudes denoted by a and b, respectively. The following set of expressions are derived for the partial derivative of a vector with respect to another one.

$$\frac{\partial \hat{\mathbf{a}}}{\partial \mathbf{a}} = \frac{1}{a}\bar{\bar{U}} - \frac{1}{a^3}\mathbf{a}\mathbf{a}, \tag{2.7}$$

$$\frac{\partial \hat{\mathbf{b}}}{\partial \mathbf{a}} = \frac{1}{b}\frac{\partial \mathbf{b}}{\partial \mathbf{a}} + \mathbf{b}\frac{\partial}{\partial \mathbf{a}}\left(\frac{1}{b}\right), \text{ and} \tag{2.8}$$

$$\frac{\partial}{\partial \mathbf{a}}\left\{\arctan\left(\frac{b(2)}{b(1)}\right)\right\} = \left(b(1)\frac{\partial b(2)}{\partial \mathbf{a}} - b(2)\frac{\partial b(1)}{\partial \mathbf{a}}\right) \times \frac{1}{b(1)^2 + b(2)^2}, \tag{2.9}$$

where $b(1)$ and $b(2)$ are the first and second components of the vector $\mathbf{b}$, respectively.

2.3 Averaging Methods

Averaging of a dynamical system can be used to determine the long-term evolution of that system. For instance, for a perturbed orbital motion, the averaging method is used to filter out the secular evolution of a particular elements that normally occur in a long time scale from the short-term oscillations that exist within an orbital period time scale. Averaging may be done on different time scales for a given system. In this work, we consider the single averaged dynamics of orbit elements that are averaged over one orbital period. Therefore, the averaged value of an arbitrary orbit element "$\mathfrak{oe}$" over one orbit period is given by [77]

$$\overline{\mathfrak{oe}} = \frac{1}{2\pi}\int_0^{2\pi} \mathfrak{oe}(M)\mathrm{d}M, \tag{2.10}$$

where M is the mean anomaly. The resulting quantity $\overline{\mathfrak{oe}}$ is independent of the mean anomaly of the orbit while it is still a function other orbit elements defined by orbital dynamics. This equation

www.manaraa.com

defines the average of an orbit element with respect to the mean anomaly. However, there may be cases where computing the average of a parameter is more straightforward with respect to either the eccentric anomaly or the true anomaly. One may use the well-know relationships between these quantities [77] and the mean anomaly to derive the other forms of the averaging equation given as the following

$$\overline{\text{œ}} = \frac{1}{2\pi}\int_0^{2\pi} \text{œ}(E)(1 - e\cos E)\mathrm{d}E = \frac{1}{2\pi}\int_0^{2\pi} \text{œ}(f)\frac{(1-e^2)^{3/2}}{(1+e\cos f)^2}\mathrm{d}f, \tag{2.11}$$

where E is the eccentric anomaly, f is the true anomaly, and e is the eccentricity of an orbit.

2.4 Definition of the Relevant Coordinate Frames

The coordinate frames that are most relevant for this study are defined in the following sections.

2.4.1 Sun-asteroid Rotating Frame, $\widehat{\mathbf{dyz}}$

The sun-asteroid rotating coordinate frame is centered at the center of mass of an asteroid or comet. The first axis of the coordinate frame, $\hat{\mathbf{d}}$, is defined along the sunlight direction pointing away from the Sun. The third axis, $\hat{\mathbf{z}}$, is perpendicular to the asteroid's heliocentric orbit plane pointing towards the asteroids heliocentric angular momentum vector. Finally, the second axis, $\hat{\mathbf{y}} = \tilde{\hat{\mathbf{z}}} \cdot \hat{\mathbf{d}}$, is defined in the direction of the asteroid's heliocentric motion and completes the triad. Figure 2.1 illustrates this coordinate frame as well as the Sun-terminator plane defined in that frame.

2.4.2 Orbit Frame, $\widehat{\mathbf{ee}_\perp\mathbf{h}}$

This is the spacecraft orbit frame denoted by $\widehat{\mathbf{ee}_\perp\mathbf{h}}$. The first axis $\hat{\mathbf{e}}$ is the direction of the eccentricity vector. The third axis $\hat{\mathbf{h}}$ is aligned with the angular momentum vector of the orbit and finally the second axis $\hat{\mathbf{e}}_\perp = \tilde{\hat{\mathbf{h}}} \cdot \hat{\mathbf{e}}$ completes the triad. We use the orbit frame to derive the secular evolution of the orbit elements due to SRP perturbations.

www.manaraa.com

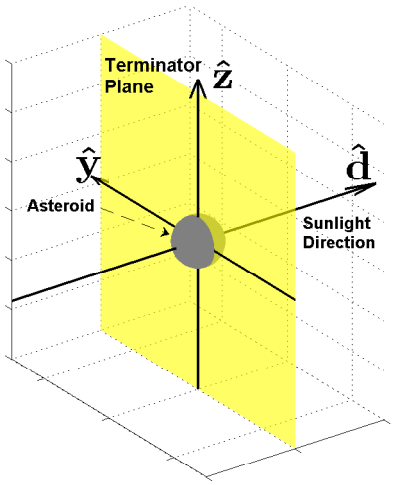

Figure 2.1: An illustration of the Sun-asteroid rotating frame.

2.4.3 Rotating Frame, $\widehat{\mathbf{pqh}}$

This is a rotating frame that is centered on the spacecraft and rotates along the orbit with the spacecraft. The axes of this frame are aligned with the radial, in-track, and cross-track directions along the orbit. The relationship between the orbit frame and the rotating frame is given by

$$\begin{aligned} \hat{\mathbf{p}} &= \cos(f)\hat{\mathbf{e}} + \sin(f)\hat{\mathbf{e}}_{\perp}, \\ \hat{\mathbf{q}} &= \cos(f)\hat{\mathbf{e}} + \sin(f)\hat{\mathbf{e}}_{\perp}, \text{ and} \\ \hat{\mathbf{h}} &= \hat{\mathbf{h}}. \end{aligned} \tag{2.12}$$

2.4.4 Spacecraft Body-fixed Frame, $\widehat{\mathbf{x}_b\mathbf{y}_b\mathbf{z}_b}$

This frame is fixed on the spacecraft body. The definition of this frame depends on the shape model of a spacecraft. In this study, we consider a generic box-wing model to represent the shape of the spacecraft. Figure 2.2 shows a schematic view of this model. As shown in the figure, the first axis of the spacecraft body fixed frame, $\hat{\mathbf{x}}_b$, points in the zenith direction of the spacecraft bus. The second axis, $\hat{\mathbf{y}}_b$ is aligned along the solar panels and the third axis $\hat{\mathbf{z}}_b = \tilde{\hat{\mathbf{x}}}_b \cdot \hat{\mathbf{y}}_b$ completes the triad. The latitude and longitude of the sunlight are also identified in this figure.

The spacecraft body-fixed frame is related to the other reference frames that are defined

www.manaraa.com

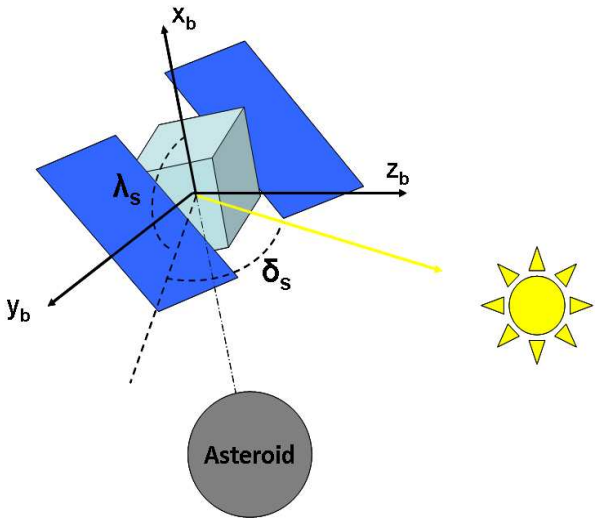

Figure 2.2: Spacecraft box-wing model and a view of the sunlight in the spacecraft body-fixed frame.

here based on the particular attitude profile that a spacecraft assumes. We explore three different attitude profiles that are most relevant for a small body orbiter, namely a nadir-pointing, a Sun-pointing, and an Earth-pointing attitude profile. During a nadir-pointing attitude, one side of the spacecraft bus (e.g. the science instrument deck) faces the astroid as the spacecraft moves along its orbit. Hence, the spacecraft $\hat{\mathbf{x}}_b$ axis is in the orbit radial direction while the $\hat{\mathbf{z}}_b$ axis is aligned with the orbit angular momentum vector $\mathbf{H}$. During a Sun-pointing and an Earth-pointing attitudes, the spacecraft $\hat{\mathbf{x}}_b$ axis is fixed in the inertial space. For the Sun-pointing case the spacecraft is oriented such that the $\hat{\mathbf{z}}_b$ axis points towards the general direction of the Sun as the Sun is placed in the $\hat{\mathbf{x}}_b\hat{\mathbf{z}}_b$ plane. For the Earth-pointing case the spacecraft orientation is such that Earth is placed in this plane.

2.5 The Orbit Determination Process

The following discussion details the orbit determination process using a linear estimation filter. The OD process starts from an initial state, $\mathbf{X}_0$, an *a priori* knowledge of the error, $\delta\bar{\mathbf{x}}_0$, and

www.manaraa.com

the uncertainty in the state elements. The *a priori* uncertainty of the state elements are arranged in a matrix denoted by $\bar{P}_0$ called the state estimate covariance matrix. After initializing the process, the state is propagated along a reference trajectory governed by the specified dynamics. In reality, the state follows a truth trajectory $\mathbf{X}$, which deviates from, but is close to, a reference trajectory $\mathbf{X}^*$. The dynamical and the measurement models are linearized about this reference trajectory. The difference between the truth and the reference trajectories, the *state deviation* vector $\delta\mathbf{x}$, is propagated in time by the linearized dynamics, while the measurements are processed to solve for the best estimate of the state deviation at each epoch [87] (Ch. 4).

2.5.1 Linearizing The Dynamics

The time evolution of the state vector may be represented by a set of ordinary first order differential equations given by

$$\dot{\mathbf{X}}(t) = f(\mathbf{X}, t). \tag{2.13}$$

The linearization of the dynamical equations is done by performing a Taylor series expansion on the dynamical model about the reference trajectory. This process is given by

$$\delta\dot{\mathbf{x}}(t) = \left.\frac{\partial f}{\partial \mathbf{X}}\right|_{\mathbf{X}^*} \delta\mathbf{x}(t) + \text{higher order terms}, \tag{2.14}$$

where

$$\delta\mathbf{x}(t) = \mathbf{X}(t) - \mathbf{X}^*(t). \tag{2.15}$$

We may re-write the expression (2.14) in the following form

$$\delta\dot{\mathbf{x}}(t) = A\delta\mathbf{x}(t), \tag{2.16}$$

where the Jacobian A is given by

$$A = \left.\frac{\partial f}{\partial \mathbf{X}}\right|_{\mathbf{X}^*}. \tag{2.17}$$

Note that we drop the higher order terms from Eq. (2.18) as this equation is valid to the first order. The effect of the mis-modeled dynamics or the *process noise* $\mathbf{u}$ may be added to this equation to get

www.manaraa.com

the linearized stochastic differential equation

$$\delta\dot{\mathbf{x}}(t) = A\delta\mathbf{x}(t) + B\mathbf{u}, \tag{2.18}$$

which has a solution in the form of [87] (§4.9)

$$\delta\mathbf{x}(t) = \Phi(t, t_0)\delta\mathbf{x}(t_0) + \int_{t_0}^{t} \Phi(t, \tau)B(\tau)\mathbf{u}(\tau)\mathrm{d}\tau, \tag{2.19}$$

with the initial condition $\Phi(t_0, t_0) = I$. The Jacobian B is the process noise mapping matrix. Matrix $\Phi(t, t_0)$ is referred to as the *state transition matrix* (STM), which maps the state deviation vector forward or backward in time. STM is solved by integrating its components along with the state vector via

$$\dot{\Phi}(t, t_0) = A\Phi(t, t_0). \tag{2.20}$$

The *process noise transition matrix* is denote by Γ and is defined by

$$\Gamma(t, t_0) = \int_{t_0}^{t} \Phi(t, \tau)B(\tau)\mathrm{d}\tau. \tag{2.21}$$

Linearizing the observation model is done by defining the measurement deviation vector $\delta\mathbf{y}$ given by

$$\delta\mathbf{y} = \mathbf{Y} - \mathbf{Y}^*, \tag{2.22}$$

such that

$$\delta\mathbf{y} = \tilde{H}\delta\mathbf{x} + \epsilon_y, \tag{2.23}$$

where $\mathbf{Y}$ is the observed measurement vector and $\mathbf{Y}^*$ is the computed measurement vector based on the reference trajectory. The variable ϵ_y is the error in the observation that is assumed to follow a zero mean Gaussian distribution with a variance-covariance matrix given by $E[\epsilon_y\epsilon_y^{\mathrm{T}}] = R$ ($E[\cdot]$ denotes the expected value of the enclosed parameter). The observation sensitivity Jacobian, $\tilde{H}$, is a mapping matrix from the state elements domain to the measurement domain. This is given by

$$\tilde{H} = \left.\frac{\partial Y}{\partial \mathbf{X}}\right|_{\mathbf{X}^*}. \tag{2.24}$$

www.manaraa.com

2.5.2 Linear Filter Solution

The OD process is inherently a discrete (even though the propagation of the state is continuous). The state of the system is propagated from one measurement epoch to the next epoch – the *time update* step – at which the best estimate update to the state is computed – the *measurement update* step. The linear, minimum variance, unbiased estimate of the state deviation vector at time t_k is given by [87] (§4.6)

$$\delta\hat{\hat{\mathbf{x}}}_k = P_k(\tilde{H}_k^{\mathrm{T}} R_k^{-1}\delta y_k + \bar{P}_k^{-1}\delta\bar{\mathbf{x}}_k), \tag{2.25}$$

where P_k is the state estimate covariance matrix at time t_k and is equal to

$$P_k = (\tilde{H}_k^{\mathrm{T}} R_k^{-1}\tilde{H}_k + \bar{P}_k^{-1})^{-1}. \tag{2.26}$$

The double-hat "$\hat{\ }$" notation in Eq. (2.27) is used to distinguish the best estimate solution from the single-hat notation used for a unit vector that is defined in Section 2.1. Quantities $\delta\bar{\mathbf{x}}_k$ and $\bar{P}_k^{-1}$ are the *a priori* values of the state deviation vector and state estimate covariance matrix,respectively. These quantities are given by

$$\begin{aligned}
\delta\bar{\mathbf{x}}_k &= \Phi(t_k, t_{k-1})\hat{\hat{\mathbf{x}}}_{k-1} + \Gamma(t_k, t_{k-1})\mathbf{u}_{k-1}, \\
\bar{P}_k &= \Phi(t_k, t_{k-1})P_{k-1}\Phi(t_k, t_{k-1})^{\mathrm{T}} + \Gamma(t_k, t_{k-1})Q_{k-1}\Gamma(t_k, t_{k-1})^{\mathrm{T}},
\end{aligned} \tag{2.27}$$

where Q is the process noise covariance matrix that, in the discrete format, is given by

$$E[\mathbf{u}_k\mathbf{u}_{k'}^{\mathrm{T}}] = Q_k\delta_{kk'}, \tag{2.28}$$

where $\delta_{kk'}$ is the Kroneker delta that is equal to unity if $k = k'$ and zero otherwise. The solution given in Eq. (2.27) is the result of what is called a sequential filter, which provides a best estimate solution of the state at every epoch. A well known sequential filter is called the conventional *Kalman* filter (CKF) [38] that provides the best estimate of the state along the reference trajectory without updating it at every epoch. The extended Kalman filter (EKF) is another variation of this algorithm with a difference that it updates the reference trajectory at every measurement epoch. If the best estimate solution is computed after collecting all the measurements and mapping those

www.manaraa.com

to a certain epoch, the algorithm is known as the linear *batch filter*. For more details on the formulation of the linear filters refer to [36] (Ch. 7), [61] (Ch. 8), or [87] (Ch. 4).

The process noise is often assumed to follow an uncorrelated Gaussian noise distribution with an expected value of zero. Under such assumption the algorithm for the treatment of the process noise is known as *State Noise Compensation* (SNC). The SNC algorithm simply inflates the covariance matrix commensurate to the assumed uncertainty on the mis-modeled dynamics. Other methods may assume a certain structure to the process noise that is not completely random. These methods in general are referred to *Dynamic Model Compensation* (DMC). The first-order Gauss-Markov process (GMP1) is one such method that is often used in an OD process. Under this model the process noise is assumed to follow a differential equation given by

$$\dot{\breve{\mathbf{u}}}(t) = -\beta\breve{\mathbf{u}}(t) + \mathbf{u}, \tag{2.29}$$

where $\mathbf{u}(t)$ is again a Gaussian white noise with zero mean. The quantity β in this formulation is called the correlation time. When using this method, the empirical acceleration $\breve{\mathbf{u}}$ is augmented to the state vector and is estimated along with the rest of the state parameters. Both the GMP1 and the SNC are utilized in this work. Other studies [45, 63] propose using a second-order Gauss-Markov process for precise orbit determination applications. A comprehensive discussion on the treatment of the process noise may also be found in Reference [36].

2.5.3 The Square Root Information Filter

Computation of the best estimate solution of the linear filter (see Eq. 2.27 and (2.26)) involves the computation of the inverse of the state estimate covariance matrix at each time step. Numerical issues may arise during this process that could adversely affect the performance of the filter. Several methods are developed to work around this issue. The well known Square Root Information Filter (SRIF) is one way for generating a numerically stable solution during an OD process. The SRIF is widely used in practice as it takes advantage of the information matrix ($\tilde{\Lambda} = P^{-1}$) to avoid the matrix inversions and its square root formulation allows for the simple and efficient *backward*

www.manaraa.com

substitution in solving the normal equations (Eq. (2.27)). We utilize the SRIF for generating all of the orbit determination solutions in this work.

The formulation of SRIF is detailed in References [87] (Ch. 5) and [10] (Ch. V). Here we briefly cover its basic equations. The time update for the SRIF at time step t_k starts with assembling the following matrix equation

$$\overline{T}\begin{bmatrix} R_u & \mathbf{0} & \bar{b}_{u_{k-1}} \\ -\tilde{R}_k\Gamma(t_k,t_{k-1}) & \tilde{R}_k & \hat{\tilde{b}}_{k-1} \end{bmatrix} = \begin{bmatrix} \bar{R}_{u_k} & \bar{R}_{ux_k} & \tilde{b}_{u_k} \\ \mathbf{0} & \bar{R}_k & \bar{\mathbf{b}}_k \end{bmatrix} \tag{2.30}$$

where R_u is defined such that $R_u^{-1}R_u^{-\mathrm{T}} = Q$ and the parameter $\bar{b}_{u_{k-1}}$ is given by

$$\bar{b}_{u_{k-1}} = R_u\bar{u}_{k-1}. \tag{2.31}$$

Matrix $\tilde{R}_k = \hat{\tilde{R}}_{k-1}\Phi^{-1}(t_k,t_{k-1})$ is the time propagation of square root of the information matrix $\tilde{\Lambda}_{k-1}$ from time t_{k-1} to t_k. Matrix $\hat{\tilde{R}}_{k-1}$ is defined such that

$$\tilde{\Lambda}_{k-1} = \hat{\tilde{R}}_{k-1}^{\mathrm{T}}\hat{\tilde{R}}_{k-1}. \tag{2.32}$$

Furthermore we have $\hat{\tilde{\mathbf{b}}}_{k-1} = \bar{R}_{k-1}\delta\hat{\tilde{\mathbf{x}}}_{k-1}$. The quantity $\overline{T}$ is an orthogonal operator, such as Householder transformation that acts on the left hand side of the equation to produce the form given in the right hand side. The matrix transformation shown in Eq. (2.30) performs the time update step of the filter that advances the state from time t_{k-1} to t_k in the presence of process noise $\mathbf{u}$. The measurement update step is accomplished by applying a second orthogonal transformation T such that,

$$T\begin{bmatrix} \bar{R}_k & \bar{\mathbf{b}}_k \\ \tilde{H}_k & \mathbf{y}_k \end{bmatrix} = \begin{bmatrix} \hat{\tilde{R}}_k & \hat{\tilde{\mathbf{b}}}_k \\ \mathbf{0} & e_k \end{bmatrix} \tag{2.33}$$

where e_k gives the sum of squares of observation residuals. The best estimated state deviation at time t_k and its corresponding covariance matrix are given by

$$\begin{aligned} \delta\hat{\tilde{\mathbf{x}}}_k &= \hat{\tilde{R}}_k^{-1}\hat{\tilde{\mathbf{b}}}_k, \\ P_k &= \hat{\tilde{R}}_k^{-1}\hat{\tilde{R}}_k^{-\mathrm{T}}. \end{aligned} \tag{2.34}$$

www.manaraa.com

Note that it is not necessary to compute the covariance matrix for this filter to work, however it may be computed at each time step to keep track of the uncertainty level of the estimated state parameters.

www.manaraa.com

Chapter 3

Force Models

In the context of Newtonian physics, the motion of a spacecraft orbiting a body of mass may be represented by the following differential equation

$$\ddot{\mathbf{r}} = \frac{1}{m_{sc}} \sum_{i}^{n} \mathbf{F}_i(t, \mathbf{r}, \mathbf{v}), \tag{3.1}$$

where $\ddot{\mathbf{r}}$ is the acceleration vector of the spacecraft and m_{sc} is the mass of the spacecraft. The vector $\mathbf{F}_i(t, \mathbf{r}, \mathbf{v})$ is the force imparted on the spacecraft from the source i, which may be a function of time t, the position vector of the spacecraft $\mathbf{r}$, and its velocity vector $\mathbf{v}$. The sources for the imparted force are central body gravitational attraction, the third body perturbation, solar radiation pressure, thermal radiation pressure, and etc. Here, we briefly describe some of these sources that have particular importance for a small body orbiter.

3.1 Small Body Gravitational Attraction

The main force imparted on spacecraft orbiting a small body is the gravitational attraction of the central body of mass. This force is derived from the gravitational potential function of the central body [39, 47] that is given by

$$U = G \int_{\mathscr{B}} \frac{\mathrm{d}m'}{\zeta}, \tag{3.2}$$

where G is the gravitational constant [60], ζ is the distance between the differential mass element $\mathrm{d}m'$ and the point in the gravitational field where the gravitational potential is evaluated. This

www.manaraa.com

point is called a *field point* hereafter. The integration is taken over the entire body of mass denoted by the subscript $\mathscr{B}$. Note that this is a general definition of the gravitational potential that applies for any body of mass with any shape. MacMillan [47](§ 24) shows that the derivatives of this function exist and in fact the components of the gravitational attraction, $\mathbf{a}_g$, are equivalent to the its first derivative taken in the direction of those components, i.e.

$$\mathbf{a}_g = \frac{\partial U(\mathbf{r})}{\partial \mathbf{r}}. \tag{3.3}$$

The accurate representation of the gravitational attraction of small bodies can be challenging. This is due to the fact that, in general, asteroids and comets have very irregular shapes for which a closed form solution of the integral expression given in Eq. (3.2) does not exist. Several methods have been developed to address this issue. Through a set of papers Werner [90, 91] and Werner and Scheeres [93] developed a method for the computation of the exact gravitational potential and attraction of an irregularly shaped body using a constant density polyhedron shape model of the object. For a polyhedron model formed with triangular facets f connected to each other with edges e and vertices v and with a constant density σ_g the gravitational potential and the acceleration are given by [93]

$$\begin{aligned} U(\mathbf{r}) &= \frac{1}{2} G\sigma_g \left[\sum_{e \in \text{edges}} \mathbf{r}_e \cdot \mathbf{E}_e \cdot \mathbf{r}_e \, L_e - \sum_{f \in \text{facets}} \mathbf{r}_f \cdot \mathbf{F}_f \cdot \mathbf{r}_f \, \omega_f \right], \text{ and} \\ \mathbf{a}_g &= -G\sigma_g \left[\sum_{e \in \text{edges}} \mathbf{E}_e \cdot \mathbf{r}_e \, L_e - \sum_{f \in \text{facets}} \mathbf{F}_f \cdot \mathbf{r}_f \, \omega_f \right], \end{aligned} \tag{3.4}$$

where $\mathbf{r}_e$ is a vector pointing from the field point to a point on the edge e of a facet and $\mathbf{r}_f$ is a vector pointing from the field point to a point on the facet f. The edge and face dyadics are defined by

$$\begin{aligned} \mathbf{E}_e &= \hat{\mathbf{n}}_{f_1} \hat{\mathbf{n}}_e^{f_1} + \hat{\mathbf{n}}_{f_2} \hat{\mathbf{n}}_e^{f_2}, \\ \mathbf{F}_f &= \hat{\mathbf{n}}_f \hat{\mathbf{n}}_f, \end{aligned} \tag{3.5}$$

where facets f_1 and f_2 are two facets connected to edge e with their corresponding surface normals $\hat{\mathbf{n}}_{f_1}$ and $\hat{\mathbf{n}}_{f_2}$. Vector $\hat{\mathbf{n}}_e^{f_i}$ is a edge normal unit vector perpendicular to edge e and facet normal $\hat{\mathbf{n}}_{f_i}$

www.manaraa.com

pointing away from the center of the facet i associated with that edge. Furthermore, we have the following definitions

$$L_e = \ln\left(\frac{r_1^e + r_2^e + |e|}{r_1^e + r_2^e - |e|}\right), \text{ and}$$
$$\omega_f = 2\arctan\left(\frac{\mathbf{r}_1^f \cdot \tilde{\mathbf{r}}_2^f \cdot \mathbf{r}_3^f}{r_1^f r_2^f r_3^f + r_1^f \mathbf{r}_2^f \cdot \mathbf{r}_3^f + r_2^f \mathbf{r}_3^f \cdot \mathbf{r}_1^f + r_3^f \mathbf{r}_1^f \cdot \mathbf{r}_2^f}\right). \tag{3.6}$$

where r_i^e is the distance of i^{th} end of edge e from the field point and $|e|$ is the length of the edge e. Vector $\mathbf{r}_i^f$ is the vector pointing from the field point to the i^{th} vertex of the facet f with its corresponding magnitude given by r_i^f.

The constant density polyhedron gravitational model is a powerful method for the computation of a baseline gravitational field for an arbitrarily shaped object. However, in general it is not suitable for spacecraft navigation due to high computation cost as well as the constant density assumption that may not hold in reality. Spherical harmonics expansion of the gravitational field [39] (§ 1.2) is more suitable for the spacecraft navigation purposes as it provides means for the estimation of the sensed gravitational field from the spacecraft orbital dynamics. Although, the spherical harmonics expansion is able to accurately represent the gravitation field at the orbital environment of an object, it has a fundamental limitation that may limit its use at surface proximity of an irregularly shaped object. Other methods are developed to address this issue [92]. In Chapter 7, we provide further details on this subject. The spherical harmonics expansion of the gravitational potential at a field point located at a latitude ϕ, longitude λ and a distance r from the center of the expansion is given by

$$U^e = \frac{\mu}{r}\sum_{n=0}^{\infty}\sum_{m=0}^{n}\left(\frac{R_\oplus}{r}\right)^n \bar{P}_{nm}(\sin\phi)\Big\{\bar{C}_{nm}^e\cos(m\lambda) + \bar{S}_{nm}^e\sin(m\lambda)\Big\}, \tag{3.7}$$

where n is the degree and m is the order of the expansion, $R_\oplus$ is the reference radius of the expansion, $\bar{C}_{nm}^e$ and $\bar{S}_{nm}^e$ are the normalized spherical harmonics coefficients, and $\bar{P}_{nm}$ is the normalized associated Legendre polynomial [89, 29]. The superscript e indicates that the expansion is performed for an *exterior* gravitational field of a body as supposed to an *interior* gravity field that we discuss in Chapter 7.

www.manaraa.com

The gravitational attraction of the body is computed by the first partial derivative of the potential function with respect to the field point position vector (see Eq. (3.3)). There exists an extensively body of literature on this subject and many researchers have explored various methods to compute the partial derivatives of the spherical harmonics expansion model. We refer the reader to References [7, 17, 18, 29, 92] and [89] (Ch. 6) among others. For this work, we derived the fully normalized version of the method given by Cunningham [17] to compute the first and the second partial derivatives of the gravitational potential as a function of the field point position. Details of the derivation are given in Appendix A.

3.2 Solar Radiation Pressure

Even though the name is a bit of misnomer, the solar radiation pressure is the force imparted on spacecraft due to the sunlight photons that impinge and interact with the irradiated surfaces. SRP is a major perturbing force for spacecraft in the proximity of small bodies. Usually, it accounts for a large percentage of the total perturbing forces acting on spacecraft even at distances close to the surface of small bodies. For instance, with the nominal area to mass ratio of the OSIRIS-REx spacecraft the force imparted on the spacecraft due to SRP exceeds the gravitational attraction of Asteroid (101955) Bennu at a distance larger than 6 km from the asteroid [78].

The force imparted on a surface due to the SRP may be represented by a total sum of three forces [53]: a force due to the absorbtion of all of the incident photons, a force due to the reflection of a percentage of the incident photons – either diffused or specular – that is characterized by the surface albedo ρ and its specular fraction s, and a force due to the emission of the energy from the absorbed photons in the form of thermal re-radiation. The thermal re-radiation of a surface is characterized by the front and back emissivity coefficients of that surface denoted by ϵ_f and ϵ_b, respectively. We denote the total sum of these forces as $\mathbf{f}_{SRP}$, which is formulated by McInnes [53]

www.manaraa.com

as the following

$$\mathbf{f}_{SRP} = -P(R)\left(\left[\rho s(2\hat{\mathbf{n}}\hat{\mathbf{n}} - \bar{\bar{U}}) + \bar{\bar{U}}\right] \cdot \hat{\mathbf{u}}\hat{\mathbf{u}} \cdot \hat{\mathbf{n}} + \left[B(1-s\rho) + (1-\rho)B\frac{\epsilon_f - \epsilon_b}{\epsilon_f + \epsilon_b}\right] \hat{\mathbf{n}}\hat{\mathbf{n}} \cdot \hat{\mathbf{u}}\right) H(\hat{\mathbf{u}})A, \tag{3.8}$$

where $\hat{\mathbf{n}}$ is a unit normal vector pointing outward from the surface, $\hat{\mathbf{u}}$ is the unit vector pointing from the surface to the Sun, and A is the lit surface area. Note that we have modified the equation above from its original form as it appears in Reference [53] using the formulation given by [79] that replaces trigonometric functions by dyadic representations of the surface normal and sunlight unit vectors. Following Reference [79], function $H(\hat{\mathbf{u}})$ is defined as a visibility function that is equal to 1 if the Sun is above the horizon of a particular surface and 0 otherwise. Variable B is the Lambertian scattering coefficient of the surface (ideally equal to 2/3) [79]. The function $P(R)$ is the pressure of the incident light at a distance R from the Sun. This is given by

$$P(R) = \frac{G_1}{R^2}, \tag{3.9}$$

where $G_1 \approx 1 \times 10^{14} kg\ km/s^2$ is the solar radiation constant. Eq. (3.8) defines the force imparted due to SRP on a single flat plate. One may easily expand this formulation for a spacecraft with a complex shape and many exposed surfaces. The force imparted on a spacecraft due to SRP with N surfaces is given by

$$\mathbf{F}_{SRP} = P(R)\sum_{i=1}^{N} \mathbf{f}_i. \tag{3.10}$$

The vector $\mathbf{f}_i$ is a geometry function of the exposed surface i with respect to the sunlight and is given by

$$\mathbf{f}_i = -\left(\left[\rho_i s_i(2\hat{\mathbf{n}}_i\hat{\mathbf{n}}_i - \bar{\bar{U}}) + \bar{\bar{U}}\right] \cdot \hat{\mathbf{u}}\hat{\mathbf{u}} \cdot \hat{\mathbf{n}}_i + \left[B(1-s_i\rho_i) + (1-\rho_i)B\frac{\epsilon_{f_i} - \epsilon_{b_i}}{\epsilon_{f_i} + \epsilon_{b_i}}\right] \hat{\mathbf{n}}_i\hat{\mathbf{n}}_i \cdot \hat{\mathbf{u}}\right) H_i(\hat{\mathbf{u}})A_i, \tag{3.11}$$

where the properties of a specific surface are identified by the subscript "i".

www.manaraa.com

3.3 Small Body Surface Radiation Pressure

Small body surface radiation pressure is due to the reflection and the emission of the sunlight energy intercepted by the asteroid or comet. The surface of small bodies interact with the incident sunlight and re-radiate a portion that light either in the form of diffused and specular reflection of the incident light, i.e. the albedo effect, or in the form of thermal radiation of the absorbed sunlight energy. The reflected and emitted radiation flux interacts with the spacecraft surface much like to the solar radiation flux and imparts a net force on the spacecraft. In general, the imparted force due to the thermal emission of the absorbed sunlight energy is much stronger than the albedo effect for asteroids and comets. Therefore, in this work, we refer to the small body surface radiation pressure – thermal emission and albedo effects combined – as small body thermal radiation pressure or TRP for short.

3.3.1 Small Body Surface Radiation Model

Knocke et al. [40] developed the formulation for treating the Earth radiation pressure on Earth orbiting satellites. This formulation divides the surface of a spherical Earth into smaller surface elements and then computes the radiation flux output of each surface element as a function of the incident sunlight angle and the surface temperature. The total albedo and thermal radiation flux from the surface is computed by aggregating the flux from each individual surface element. Figure 3.1 shows the geometry of this setup. As shown in this figure, $\mathbf{b}_j$ is the vector pointing from the center of coordinate system to the centroid of the j^{th} surface element. Vector $\mathbf{u}_j$ is the vector pointing from the spacecraft to the centroid of the j^{th} surface element. Angle θ_j is the angle between the incident sunlight and the j^{th} surface normal. Angle α_j is the angle between the incident sunlight and a vector pointing from the j^{th} surface element to the spacecraft, i.e. $-\mathbf{u}_j$. This model may be adapted to compute the radiation pressure imparted on spacecraft from the surface of small bodies. One thing to note is that the geometry given in Figure 3.1 is based on the assumption of an spherical central body. For small bodies with highly non-spherical shapes

www.manaraa.com

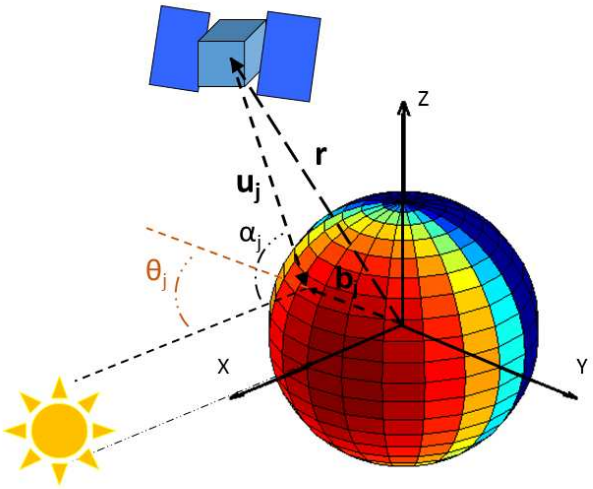

Figure 3.1: Geometry of the surface radiation pressure model.

this assumption does not hold. Nonetheless, this problem can be overcome rather easily by using a faceted shape model of a small body, such as the polyhedron shape model to apply the same formulation. In doing so, each facet (or a collection of facets) in the faceted shape model may be considered as a surface element in the TRP model.

In this work, we combine this model with the SRP formulation given by Scheeres [79] (see Section 3.2) to derive the equations that express TRP effects on spacecraft in close proximity to a small body, taking into account the shape of the spacecraft. We start the derivation by expressing the total force imparted on a spacecraft due to TRP as the following

$$\mathbf{F}_{TRP} = \sum_{j \in \mathcal{K}} P_j \sum_{i=1}^{N} \mathbf{f}_{ij}, \tag{3.12}$$

where the individual forces are summed across a total of N spacecraft irradiated surfaces and across all of the "effective" surface elements on the small body, which are in direct line of sight to the spacecraft. The set of effective surface elements are identified by the set $\mathcal{K}$. Variable P_j is the

www.manaraa.com

radiation pressure of the j^{th} surface element and $\mathbf{f}_{ij}$ is an area geometry function that describes the way the radiation from the surface element j is interacting with the spacecraft surface element i. Using the notation from Scheeres [79], this force may be given by

$$\mathbf{f}_{ij} = -\left[\left(\rho_i s_i (2\hat{\mathbf{n}}_i \hat{\mathbf{n}}_i - \bar{\bar{U}}) + \bar{\bar{U}}\right) \cdot \hat{\mathbf{u}}_\mathbf{j} \hat{\mathbf{u}}_\mathbf{j} \cdot \hat{\mathbf{n}}_i + B(1 - \rho_i s_i) \hat{\mathbf{n}}_i \hat{\mathbf{n}}_i \cdot \hat{\mathbf{u}}_j\right] H_i(\hat{\mathbf{u}}_j) A_i, \tag{3.13}$$

where $\hat{\mathbf{u}}_\mathbf{j}$ is the unit vector pointing from the spacecraft center to the centroid of that element. Note that in defining this vector we make the assumption that the size of the spacecraft is very small compared to the distance of the spacecraft from the small body. As a result, we are able to use the same unit vector pointing from different surfaces of a spacecraft to a particular small body surface element. While this assumption helps simplify the formulation, it is not necessary. The rest of the parameters shown in Eq. (3.13) are defined in Section 3.2.

Using Eq. (3.13) allows us to take into account the shape of a spacecraft when computing the TRP effect. This is one aspect where our derivation differs from the model provided by Knocke et al. [40], as they derive the equations of the TRP effect for a spherical object - i.e. a cannonball model. Therefore, the parameter P_j is given by

$$P_j = \left(\tau_j a_j G_R \cos(\theta_j) + f_\epsilon(T_j)\right) \frac{1}{c} \cos(\alpha_j) \frac{dA_j}{\pi u_j^2}, \tag{3.14}$$

where τ_j is the visibility function of the j^{th} surface element with respect to the sunlight, i.e. τ_j is equal to 1 if the surface element is lit by the sunlight and 0 otherwise. Variable a is the albedo of the body, which is defined as the fraction of the shortwave radiation reflected from the surface of the body to the incident shortwave solar radiation [61] (§ 3.7.1). Variable G_R is the solar flux at the distance R from the Sun and c is the speed of light. Variable dA_j is the surface area of the j^{th} surface element and u_j is the distance of the spacecraft from that surface element. Finally, the function $f_\epsilon(T_j)$ indicates the amount of thermal radiation flux emitted from the surface element j that has a surface temperature of T_j. The actual form of this function is another aspect that our derivation differs from the model given by Knocke et al. [40]. More details on this are provided in

www.manaraa.com

Section 3.3.2. Finally, the acceleration imparted on a spacecraft due to TRP is given by

$$\mathbf{a}_{TRP}^{b} = \frac{1}{m}\mathbf{F}_{TRP}. \tag{3.15}$$

The superscript b indicates that the acceleration is defined in the spacecraft body-fixed frame.

3.3.2 Asteroid Surface Temperature Distribution

Many of the previous models that are developed for the Earth radiation pressure assume an emissivity function $f_\epsilon(T_j)$ that is strictly latitude dependent [40, 42, 95]. Stephen et al. [84] shows that the terrestrial emissivity function may be modeled adequately by only using the zonal spherical harmonics up to degree 2. However, studying asteroids' surface temperature distribution using observational data supports the idea that there exists an strong temperature variation that has a strong latitudinal and longitudinal dependency [62]. Therefore, it is most appropriate to write the emissivity function $f_\epsilon(T_j)$ as the following

$$f_\epsilon(T_j) = \epsilon\sigma_B T_j^4, \tag{3.16}$$

where ϵ is the surface emissivity of the body and $\sigma_B = 5.670367 \times 10^{-8}\ W/m^2/K^4$ [60] is the Stefan Boltzmann constant. The popular Near-Earth Asteroid Thermal Model (NEATM) [30] and an earlier version of it called the standard thermal model (STM) [44] adopt the following expression to compute the temperature distribution on the surface of an asteroid:

$$T(\imath) = \begin{cases} T_{SS}\cos^{1/4}(\imath) & 0 \le \imath \le \pi/2 \\ 0 & \imath > \pi/2 \end{cases}, \tag{3.17}$$

where $\imath$ is the angular distance from the subsolar point and T_{SS} is the subsolar temperature that is given by

$$T_{SS} = \left(\frac{(1-a_b)G_R}{\epsilon\sigma_B}\right)^{1/4}. \tag{3.18}$$

Variable a_b in this expression is the bond albedo of the asteroid. In the literature [30, 37, 48] a so called *beaming parameter* (η) is included in the denominator of the Eq. (3.18). This is an empirical

www.manaraa.com

parameter that was devised to help the model better match the observed flux data and does not reflect the actual surface temperature on the asteroid [82]. In this work we choose to disregard this parameter as we are interested in the actual value of the temperature on the surface.

The NEATM assumes that the peak temperature occurs at the subsolar point on the surface of an asteroid and the temperature decreases with the increased angular distance away from this point. This is equivalent to an assumption of a zero thermal inertia for an asteroid, such that an instantaneous thermal equilibrium occurs on the surface of the object. The fast rotating model (FRM) [43] is another variation to the NEATM. This model assumes a very large value for the thermal inertia, such that the surface temperature is constant across different longitudes and is only a function of the latitude. However, in reality, for an asteroid with a finite thermal inertia, the surface temperature is not constant across different longitudes and the peak temperature occurs at an angular distance – *phase angle* – away from the subsolar point towards the evening side. A work by Spencer et al. [82] developed a so called *thermal parameter* (Θ) that combines the rotation rate, thermal inertia, and the possible peak surface temperature of an asteroid to characterize the temperature distribution on the surface. This parameter is given by [82]

$$\Theta = \frac{\Gamma\sqrt{\omega_r}}{\epsilon\sigma_B T_{SS}^3}, \tag{3.19}$$

where Γ is the thermal inertia and ω_r is the rotation rate of the asteroid. Note that the thermal parameter is a dimensionless quantity. A $\Theta = 0$ corresponds to the NEATM, while a $\Theta = \infty$ corresponds to the FRM. By solving a boundary value problem Spencer et al. [82] generated a set of reference curves for the maximum and minimum surface temperatures and the phase angle as a function of the thermal parameter Θ. These curves are depicted in Figure 3.2 [1] . Using Eq. (3.19) and (3.18) one may compute the thermal parameter for an arbitrary asteroid and then use Figure 3.2 to identify the corresponding maximum and minimum surface temperatures and the phase angle. We use this method to compute the surface temperature distribution for the TRP

[1] Reprinted from Icarus, Vol. 78, Issue 2, J. R. Spencer, L. A. Lebofsky, and M. V. Sykes, Systematic biases in radiometric diameter determinations, Pages 337-354, Copyright (1989), with permission from Elsevier, under the License No. 3843790713370.

www.manaraa.com

model.

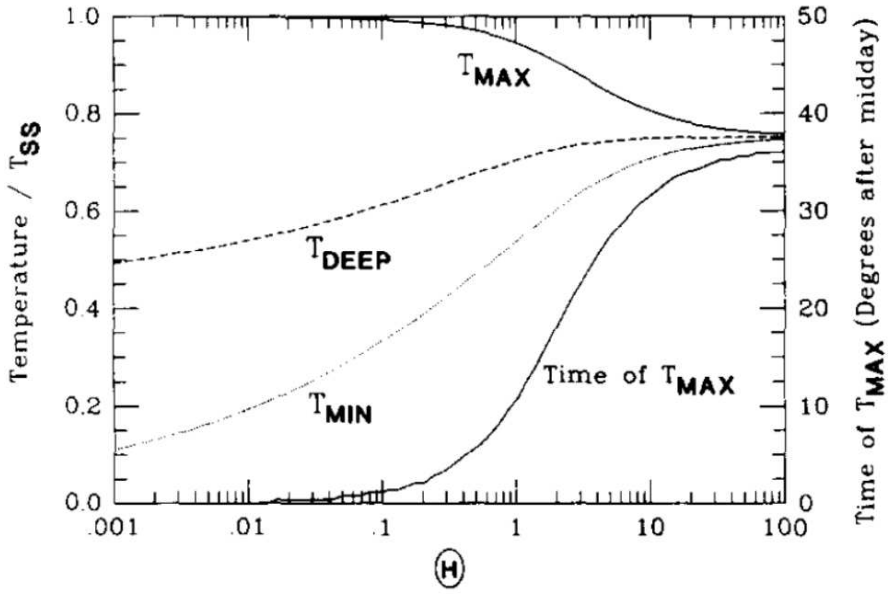

Figure 3.2: The maximum (T_{max}) and minimum (T_{min}) surface temperatures and the subsurface (T_{DEEP}) temperature of an asteroid as a function of the thermal parameter Θ. The figure also shows the time of maximum temperature as the number of degrees after midday.

3.4 Other Perturbing Forces

There are other perturbing forces that act on spacecraft orbiting about small bodies, such as the third body perturbations, outgassing effects from the surface of comets, and thermal radiation pressure due to the heat emission from the spacecraft structure. Third body perturbations are due to the direct and indirect gravitational pull from mainly the Sun and other major planetary bodies, e.g. Jupiter, on the spacecraft [87] (§ 2.3.5). The acceleration imparted on a spacecraft due to the third body effect is given by

$$\mathbf{a}_{3rd} = -\sum_{p=1}^{P} \mu_p \left[\frac{\mathbf{r}_{ps}}{r_{ps}^3} + \frac{\mathbf{r}_{\oplus p}}{r_{\oplus p}^3} \right], \tag{3.20}$$

where P is the total number of the perturbing bodies considered in the model, μ_p is the gravitational parameter of the perturbing body p, $\mathbf{r}_{ps}$ is the position vector of the spacecraft with respect

www.manaraa.com

to the Sun or a planetary body with a magnitude of r_{ps}. Finally, $\mathbf{r}_{\oplus p}$ is a vector pointing from the center of the mass of the central body to the perturbing body with a magnitude of $r_{\oplus p}$. We include the third body perturbation of the Sun in all of simulations and spacecraft state propagations that are done numerically, unless otherwise is mentioned.

An outgassing event is mainly a feature of comets that occurs as these objects come close to the Sun in their orbit. The surface volatiles are liberated due to the heat from the Sun elevating ice and dust particles are elevated into space. Some of the elevated ice and duct particles may form a cloud around the comet nucleus, while others may be ejected far into space in the form of powerful jets [12]. Such particles and jets, if intersected by a spacecraft, can have a significant perturbing effect on the orbit of the spacecraft. However, the intensity and the frequency of the jettisoned particles are highly dependent on the physical and orbital characteristics of a particular comet and one needs to study these effects on a case by case basis. The detailed analysis of the comet outgassing effects is out of the scope of this work and the interested reader is encouraged to refer to References [12, 16, 81] among others for an in-depth discussion on this subject.

Lastly, the spacecraft thermal radiation effect is the force due to the radiation of the thermal energy generated by the spacecraft. The heat generated from spacecraft subsystems, such as the Radioisotope Thermoelectric Generator (RTG), may radiate directly from the surface of these subsystems or be reflected off of other surfaces of the spacecraft, such as the solar panels or the high gain antenna [71]. The spacecraft thermal radiation may result in an small perturbation on the spacecraft trajectory that may be visible form the orbit determination solutions [69, 70]. Characterization of this force may be very important for precise orbit determination solution. However, this effect is dependent on the specifics of a spacecraft and should be studied in a case by case basis for difference spacecraft. We do not consider this perturbation as it does not fit in the scope of this work.

www.manaraa.com

Chapter 4

Sensitivity Analysis of Spacecraft Orbits Under Strong SRP Perturbation

There are different methods that are developed to model the force that is imparted by SRP on spacecraft. The simplest method is the cannonball model that assumes the SRP force is strictly pointing in a direction away from the Sun [46]. Although it is relatively simple, the cannonball model may be used to get an overall understanding of the secular effects of SRP on orbit elements.

Due to the weak gravitational attraction of small bodies, even in close proximities to these objects, SRP can be a significant perturbing force that constantly pushes the spacecraft in a general direction away from the Sun. The existence of a strong SRP effect creates a high level of complexity to the dynamical environment about asteroids and comets [77] (Ch. 12, 13, and 14). In such a highly non-Keplerian dynamical environment, small perturbations can lead to large deviations from the nominal trajectory of spacecraft. Such small perturbations may arise from errors in the spacecraft reaction wheel de-saturation (de-sat) maneuvers or orbit insertion and targeting maneuvers. In this chapter, we aim to systematically analyze the ways in which errors and uncertainties in spacecraft trajectory propagate over time in a highly perturbed environment by SRP and gain insight into such complex dynamical environments.

To move forward with this analysis and reduce the complexity of the system, we study the averaged evolution of an orbit under the strong SRP perturbation. Previous research has shown that there exists a simple closed form solution that approximates the motion of averaged orbital elements of a spacecraft orbit bound to a small body. The existence of such solution was contemplated before [58], however recent research [76] provided a complete and simple form of

www.manaraa.com

the solution accounting for the heliocentric motion of the asteroid. This subject is further discussed in several other studies [74, 73] and [77] (Ch. 13). Posing the problem in terms of a special set of orbital elements one can represent the solution to the secular motion of an orbit in a highly perturbed environment due to SRP by a simple linear relationship [76]. This simple formulation leads to the generation of a family of quasi-stable orbits, e.g. Sun-terminator orbits, that are of interest to missions to small bodies.

First, we review the formulation of the secular dynamics of the orbital elements in an environment that is highly perturbed by SRP and the existence of a set of special solutions to this formulation. We follow with the derivation of a set of equations that govern the secular dynamics of an orbit that is perturbed from its nominal state. We then utilize these expressions to analyze the sensitivity of the perturbed orbital elements to small errors and study the propagation of their uncertainties over time. Lastly, we verify the results of the secular analysis with numerical simulations.

4.1 Secular Dynamics due to a Cannonball Model

We study the perturbing effect of SRP on an orbit by analyzing the secular motion of a set of non-standard orbit elements, namely the eccentricity vector $\mathbf{e}$, the angular momentum vector $\mathbf{H}$, and the specific energy of the orbit $\mathscr{E}$. This set of elements is sufficient to provide detail information about the shape, size, and the orientation of an orbit about a central body. These elements of interest are defined by

$$\begin{aligned} \mathbf{e} &= \frac{1}{\mu}\,\tilde{\mathbf{v}}\cdot\tilde{\mathbf{r}}\cdot\mathbf{v} - \frac{\mathbf{r}}{r}, \\ \mathbf{H} &= \tilde{\mathbf{r}}\cdot\mathbf{v}, \text{ and} \\ \mathscr{E} &= \frac{v^2}{2} - \frac{\mu}{r}, \end{aligned} \tag{4.1}$$

where $\mathbf{r}$ and $\mathbf{v}$ are the position and velocity vectors of the spacecraft with their magnitudes denoted by r and v, respectively. Variable μ is the gravitational parameter of the small body. The

www.manaraa.com

position of velocity vectors are given by

$$\begin{aligned} \mathbf{r} &= r\left[\cos(f)\hat{\mathbf{e}} + \sin(f)\hat{\mathbf{e}}_{\perp}\right], \\ \mathbf{v} &= \sqrt{\frac{\mu}{a(1-e^2)}}\left[-\sin(f)\hat{\mathbf{e}} + (e+\cos f)\hat{\mathbf{e}}_{\perp}\right], \end{aligned} \tag{4.2}$$

where $r = a(1-e^2)/(1+e\cos f)$. For an unperturbed 2-Body orbital motion, the orbital elements that are given here are unchanged and constant over time. That is not the case, however, for a perturbed motion. To study the effect of a perturbing force on an orbit, one may analyze the rate of change of the orbit elements as a function of that perturbing force. The time rate of change for an arbitrary orbit element œ is related to a perturbing acceleration $\mathbf{a}_{prt}$ via the well known Gauss' variational equations given by Battin [5] (§ 10.5) in the following form

$$\dot{\text{œ}} = \frac{\partial \text{œ}}{\partial \mathbf{v}} \cdot \mathbf{a}_{prt}. \tag{4.3}$$

The perturbing acceleration $\mathbf{a}_{prt}$ is derived from a perturbing potential $\mathcal{R}_{prt}$ that is only a function of the position vector. The disturbing acceleration considered in the section is an acceleration due to the SRP force imparted on the spacecraft. Under the simple cannonball model assumption the SRP acceleration may be written as

$$\mathbf{a}_{SRP} = a_{SRP}\hat{\mathbf{d}}, \tag{4.4}$$

where $\hat{\mathbf{d}}$ is a unit vector pointing in the sunlight direction and a_{SRP} is the magnitude of the SRP acceleration at a distant d from the Sun and is given by [78]

$$a_{SRP} = P(R)\frac{(1+\rho)}{B}, \tag{4.5}$$

where $P(R)$ is the solar radiation pressure at a distance R from the Sun, which is defined in Section 3.2. The variable ρ is the albedo of the reflecting surface and B is the mass to area ratio of the spacecraft.

Taking the partial derivative of expressions in Eq. (4.1) with respect to the velocity vector and substituting Eq. (4.4) in as the perturbing force, results in the following set of expressions for

www.manaraa.com

the time derivative of the orbit elements [75]

$$\begin{aligned}\dot{\mathbf{e}} &= \frac{a_{srp}}{\mu}\left[2\mathbf{rv} - \mathbf{vr} - (\mathbf{r}\cdot\mathbf{v})\bar{\bar{U}}\right]\cdot\hat{\mathbf{d}},\\ \dot{\mathbf{H}} &= a_{srp}\,\tilde{\mathbf{r}}\cdot\hat{\mathbf{d}},\ \text{and}\\ \dot{\mathscr{E}} &= a_{srp}\,\mathbf{v}\cdot\hat{\mathbf{d}}.\end{aligned} \tag{4.6}$$

We use the dyadic identities given by Eq. 2.5 to derive the expression for the time derivative of the eccentricity vector. The secular dynamics of the orbit elements are derived by averaging the effect of SRP on the orbit elements over one orbit period. This procedure is described in Section 2.3. Averaging Eq. (4.6) results in the following set of expressions

$$\begin{aligned}\overline{\dot{\mathbf{e}}} &= -\frac{3a_{srp}}{2\mu}\,\tilde{\mathbf{H}}\cdot\hat{\mathbf{d}},\\ \overline{\dot{\mathbf{H}}} &= -\frac{3a_{srp}\,a}{2}\tilde{\mathbf{e}}\cdot\hat{\mathbf{d}},\ \text{and}\\ \overline{\dot{\mathscr{E}}} &= 0.\end{aligned} \tag{4.7}$$

Note that the energy of the orbit is conserved, on average, due to a cannonball model of SRP perturbation. This means that the semi-major axis of the orbit is also constant, on average. Therefore, there is no need to continue considering the orbit energy for derivation of the secular equations of motion. Furthermore, we may define a scaled angular momentum vector $\mathbf{h}$, which is given by

$$\mathbf{h} = \frac{\mathbf{H}}{\sqrt{\mu a}}. \tag{4.8}$$

Substituting the scaled angular momentum vector in Eq. (4.7) and rearranging terms results in the following set of symmetric secular equations of motions

$$\begin{aligned}\overline{\dot{\mathbf{e}}} &= \frac{3a_{srp}}{2}\sqrt{\frac{a}{\mu}}\tilde{\hat{\mathbf{d}}}\cdot\mathbf{h},\\ \overline{\dot{\mathbf{h}}} &= \frac{3a_{srp}}{2}\sqrt{\frac{a}{\mu}}\tilde{\hat{\mathbf{d}}}\cdot\mathbf{e}.\end{aligned} \tag{4.9}$$

This new pair of orbit elements, namely the eccentricity and the scaled angular momentum vectors, ($\mathbf{e}$ & $\mathbf{h}$) allows for the derivation of a compact and symmetric set of solutions to the secular dynamics of the orbit due to SRP perturbation under the cannonball model assumption [77] (Ch.

www.manaraa.com

13). Rosengren and Scheeres [74] provide a historical discussion of the origin and the use of this set of vectorial orbit elements and other Milankovitch type formulation for perturbed Keplerian motion.[1] The relationship between these elements and the more classical orbit elements Ω, i, and ω are given by

$$\Omega = \tan^{-1}\left(-\frac{\hat{\mathbf{d}}\cdot\mathbf{h}}{\hat{\mathbf{y}}\cdot\mathbf{h}}\right),$$

$$i = \cos^{-1}\left(\frac{\hat{\mathbf{z}}\cdot\mathbf{h}}{h}\right), \text{ and} \tag{4.10}$$

$$\omega = \tan^{-1}\left(\frac{(\hat{\mathbf{z}}\cdot\mathbf{e})h}{\mathbf{e}\cdot\tilde{\hat{\mathbf{z}}}\cdot\mathbf{h}}\right),$$

where $e = \sqrt{\mathbf{e}\cdot\mathbf{e}}$ and $h = \sqrt{1-e^2}$. Variable Ω is the longitude of the ascending node, i is the inclination, and ω is the argument of the periapsis. Note that these elements are defined with respect to the sun-asteroid rotating frame $\widehat{\mathbf{dyz}}$. It turns out that expressing the secular dynamics of the orbit elements in the rotating frame allows for the derivation of a simple closed form solution.

The set of secular equations of motion given by Eq. (4.9) may be expressed in the sun-asteroid rotating reference frame via[2]

$$\begin{aligned}\dot{\mathbf{e}}_r &= \frac{3a_{srp}}{2}\sqrt{\frac{a}{\mu}}\tilde{\hat{\mathbf{d}}}\cdot\mathbf{h} - \dot{\nu}\tilde{\hat{\mathbf{z}}}\cdot\mathbf{e},\\ \dot{\mathbf{h}}_r &= \frac{3a_{srp}}{2}\sqrt{\frac{a}{\mu}}\tilde{\hat{\mathbf{d}}}\cdot\mathbf{e} - \dot{\nu}\tilde{\hat{\mathbf{z}}}\cdot\mathbf{h},\end{aligned} \tag{4.11}$$

where $\dot{\nu}$ is the heliocentric rate of the asteroid in its orbit in its orbit. Note that the set of expressions in Eq. (4.11) are time variant since both the magnitude of the SRP acceleration and the heliocentric rate of the asteroid vary in time. However, also note that both of these quantities are inversely proportional to d^2, the square of the distance of the asteroid from the Sun. Reference [58]

[1] See if you should include some more reference in this footnote regarding the Milankovitch elements.

[2] Note that the bar ($^-$) operator is omitted in what follows for the sake of simplifying the expressions as the orbit elements $\mathbf{e}$, $\mathbf{h}$, Ω, inclination, and ω are averaged variables. We use the bar operator in the last section to distinguish between the averaged and osculating orbit elements.

www.manaraa.com

recognized this fact and defined the parameter Λ such that

$$\tan\Lambda = \frac{3(1+\rho)P_0}{2B}\sqrt{\frac{a}{\mu\mu_S A(1-E^2)}}. \tag{4.12}$$

where μ_S is the gravitational parameter of Sun and A and E are asteroid's heliocentric orbit semi-major axis and eccentricity, respectively. This quantity is basically the ratio of the SRP acceleration over the time rate of change of asteroid's heliocentric true anomaly. Using this definition for the parameter Λ and performing a change of variable from the time domain to asteroid's heliocentric true anomaly (ν) allow us to express the secular motion of the orbit elements by a set of linear, time-invariant, first order differential equations given by [76]

$$\begin{aligned} \mathbf{e}' &= \tan\Lambda\tilde{\hat{\mathbf{d}}}\cdot\mathbf{h} - \tilde{\hat{\mathbf{z}}}\cdot\mathbf{e}, \\ \mathbf{h}' &= \tan\Lambda\tilde{\hat{\mathbf{d}}}\cdot\mathbf{e} - \tilde{\hat{\mathbf{z}}}\cdot\mathbf{h}. \end{aligned} \tag{4.13}$$

The prime superscript indicates the rate of the change of the orbit elements with respect to this new independent variable, i.e. $\mathbf{e}' = \mathrm{d}\mathbf{e}/\mathrm{d}\nu$. The general solution for these set of equations is given by

$$\mathbf{X}(\nu) = \Phi(\nu-\nu_0)\mathbf{X}_0, \tag{4.14}$$

where the state vector is defined by

$$\mathbf{X} = \begin{bmatrix} \mathbf{e} \\ \\ \mathbf{h} \end{bmatrix} \tag{4.15}$$

and the state transition matrix Φ is given by

$$\begin{aligned} \Phi(\psi) = \cos(\psi)I_{6\times6} + (1-\cos(\psi)) \\ \times \begin{bmatrix} \cos^2\Lambda\hat{\mathbf{z}}\hat{\mathbf{z}} + \sin^2\Lambda\hat{\mathbf{d}}\hat{\mathbf{d}} & -\sin\Lambda\cos\Lambda(\hat{\mathbf{z}}\hat{\mathbf{d}} + \hat{\mathbf{d}}\hat{\mathbf{z}}) \\ -\sin\Lambda\cos\Lambda(\hat{\mathbf{z}}\hat{\mathbf{d}} + \hat{\mathbf{d}}\hat{\mathbf{z}}) & \cos^2\Lambda\hat{\mathbf{z}}\hat{\mathbf{z}} + \sin^2\Lambda\hat{\mathbf{d}}\hat{\mathbf{d}} \end{bmatrix} \\ + \sin(\psi)\begin{bmatrix} -\cos\Lambda\tilde{\hat{\mathbf{z}}} & \sin\Lambda\tilde{\hat{\mathbf{d}}} \\ \sin\Lambda\tilde{\hat{\mathbf{d}}} & -\cos\Lambda\tilde{\hat{\mathbf{z}}} \end{bmatrix}. \end{aligned} \tag{4.16}$$

Variable ψ is defined by $\psi = (\nu-\nu_0)/\cos\Lambda$ for convenience of the notations. Note that the solution to the Eq. (4.14) is periodic in ψ with a period of 2π. Details of the derivation of the state transition matrix are given in Reference [74].

www.manaraa.com

4.2 Special Solutions to the Secular Dynamics

Previous section detailed the derivation of the secular dynamics of an orbit under strong perturbing effect from due to SRP. There are several special solutions to the general solution given by Eq. (4.14) that are of interest for spacecraft orbiting around small bodies [76]. For this work we explore a family of these special solutions that are on or close to the Sun terminator plane in the sun-asteroid rotating frame (see Figure 2.1 for the illustration of the Sun terminator plane). These are the frozen-node orbits, frozen terminator orbits, and circular terminator orbits. The frozen-node orbits are derived in this work and the derivation is detailed in the next section. Frozen and circular terminator orbits are introduced in the following section and the detail of their derivations is given by Reference [77] (Ch. 13).

4.2.1 Frozen-Node Orbits

The frozen-node orbits refer to a set of solutions to the secular dynamics of the orbit elements under SRP perturbation for which the orbit plane does not precess over time, i.e.

$$\overline{\Omega}(\psi) = \pm 90^{\circ}, \text{ and } \dot{\overline{\Omega}}(\psi) = 0, \ \forall \psi. \tag{4.17}$$

For the derivation we start with the general solution given by Eq. (4.14). Carrying out the matrix multiplication and simplifying the expressions gives the general solution for the time progression of the averaged eccentricity and scaled angular momentum as the following

$$\begin{aligned}
\mathbf{e}(\psi) = &\Big[\big(\cos\psi - \sin^2\Lambda(\cos\psi - 1)\big)(\mathbf{e}_0 \cdot \hat{\mathbf{d}}) + \cos\Lambda\sin\psi(\mathbf{e}_0 \cdot \hat{\mathbf{y}}) \\
&\qquad + \cos\Lambda\sin\Lambda(\cos\psi - 1)(\mathbf{h}_0 \cdot \hat{\mathbf{z}})\Big]\hat{\mathbf{d}} \\
&+ \Big[\cos\psi(\mathbf{e}_0 \cdot \hat{\mathbf{y}}) - \cos\Lambda\sin\psi(\mathbf{e}_0 \cdot \hat{\mathbf{d}}) - \sin\Lambda\sin\psi(\mathbf{h}_0 \cdot \hat{\mathbf{z}})\Big]\hat{\mathbf{y}} \\
&+ \Big[\big(\cos\psi - \cos^2\Lambda(\cos\psi - 1)\big)(\mathbf{e}_0 \cdot \hat{\mathbf{z}}) + \sin\Lambda\sin\psi(\mathbf{h}_0 \cdot \hat{\mathbf{y}}) \\
&\qquad + \cos\Lambda\sin\Lambda(\cos\psi - 1)(\mathbf{h}_0 \cdot \hat{\mathbf{d}})\Big]\hat{\mathbf{z}},
\end{aligned} \tag{4.18}$$

www.manaraa.com

$$\begin{aligned}\mathbf{h}(\psi) = &\Big[(\mathbf{h}_0\cdot\hat{\mathbf{d}})(\cos\psi - \sin^2\Lambda(\cos\psi-1)) + (\mathbf{h}_0\cdot\hat{\mathbf{y}})\cos\Lambda\sin\psi \\ &\qquad +(\mathbf{e}_0\cdot\hat{\mathbf{z}})\cos\Lambda\sin\Lambda(\cos\psi-1)\Big]\hat{\mathbf{d}} \\ &+\Big[(\mathbf{h}_0\cdot\hat{\mathbf{y}})\cos\psi - (\mathbf{h}_0\cdot\hat{\mathbf{d}})\cos\Lambda\sin\psi - (\mathbf{e}_0\cdot\hat{\mathbf{z}})\sin\Lambda\sin\psi\Big]\hat{\mathbf{y}} \\ &+\Big[(\mathbf{h}_0\cdot\hat{\mathbf{z}})(\cos\psi - \cos^2\Lambda(\cos\psi-1)) + (\mathbf{e}_0\cdot\hat{\mathbf{y}})\sin\Lambda\sin\psi \\ &\qquad +(\mathbf{e}_0\cdot\hat{\mathbf{d}})\cos\Lambda\sin\Lambda(\cos\psi-1)\Big]\hat{\mathbf{z}}.\end{aligned} \tag{4.19}$$

The following identities are used to simplify the cross product matrices in the form of simple dyadic notations

$$\begin{aligned}\tilde{\hat{\mathbf{d}}}\cdot\mathbf{a} &= (\mathbf{a}\cdot\hat{\mathbf{y}})\hat{\mathbf{z}} - (\mathbf{a}\cdot\hat{\mathbf{z}})\hat{\mathbf{y}}, \\ \tilde{\hat{\mathbf{z}}}\cdot\mathbf{a} &= (\mathbf{a}\cdot\hat{\mathbf{d}})\hat{\mathbf{y}} - (\mathbf{a}\cdot\hat{\mathbf{y}})\hat{\mathbf{d}}.\end{aligned} \tag{4.20}$$

where $\mathbf{a}$ is an arbitrary vector expressed in the $\widehat{\mathbf{dyz}}$ coordinate system. For the condition given by Eq. (4.17) to be true, the component of the scaled angular momentum vector in the $\hat{\mathbf{y}}$ direction much be zero at all time, i.e.

$$\mathbf{h}(\psi)\cdot\hat{\mathbf{y}} = (\mathbf{h}_0\cdot\hat{\mathbf{y}})\cos\psi - (\mathbf{h}_0\cdot\hat{\mathbf{d}})\cos\Lambda\sin\psi - (\mathbf{e}_0\cdot\hat{\mathbf{z}})\sin\Lambda\sin\psi = 0 \quad \forall\ \psi. \tag{4.21}$$

For Eq. (4.21) to hold for all values of ψ, we must have

$$\begin{aligned}\mathbf{h}_0\cdot\hat{\mathbf{y}} &= 0 \\ \mathbf{e}_0\cdot\hat{\mathbf{z}} &= -(\mathbf{h}_0\cdot\hat{\mathbf{d}})\cot\Lambda.\end{aligned} \tag{4.22}$$

Equation 4.22 is the first set of equations that place constrain on the initial conditions that generate the frozen-node orbits. Next conditions arise from the orthogonality constraint ($\mathbf{e}\cdot\mathbf{h}=0$) and the magnitude constraint ($\mathbf{e}\cdot\mathbf{e}+\mathbf{h}\cdot\mathbf{h}=1$) on the eccentricity and scaled angular momentum vectors. By imposing the orthogonality condition we get the second constraint on the initial state as the following

$$\mathbf{e}_0\cdot\hat{\mathbf{d}} = \mathbf{h}_0\cdot\hat{\mathbf{z}}\cot\Lambda. \tag{4.23}$$

www.manaraa.com

Finally, using Eq. (4.23) together with Eq. (4.22) in the magnitude constraint gives the conditions on the initial state of the orbit elements to generate the frozen-node orbits, i.e.

$$|\mathbf{e}_0 \cdot \hat{\mathbf{y}}| = \sqrt{1 - \frac{(\mathbf{h}_0 \cdot \hat{\mathbf{d}})^2 + (\mathbf{h}_0 \cdot \hat{\mathbf{z}})^2}{\sin^2 \Lambda}},$$
$$(\mathbf{h}_0 \cdot \hat{\mathbf{d}})^2 + (\mathbf{h}_0 \cdot \hat{\mathbf{z}})^2 \leq \sin^2 \Lambda. \tag{4.24}$$

At this point, all the components of the initial state vector $[\,\mathbf{e}_0\ \mathbf{h}_0]^{\mathrm{T}}$ are constrained and specified by the $\hat{\mathbf{d}}$ and $\hat{\mathbf{z}}$ components of the initial scaled angular momentum vector $\mathbf{h}_0$. However, the magnitude of these components are free to choose within the specified constraint given by Eq. (4.24). Let us define

$$\begin{aligned} \mathbf{h}_0 \cdot \hat{\mathbf{d}} &= \eta \sin \Lambda \\ \mathbf{h}_0 \cdot \hat{\mathbf{z}} &= \zeta \sin \Lambda. \end{aligned} \tag{4.25}$$

Using this definition, we can re-write the constraints on the initial conditions as the following set of equations

$$\begin{aligned} &\mathbf{e}_0 \cdot \hat{\mathbf{d}} = \zeta \cos \Lambda \\ &\mathbf{e}_0 \cdot \hat{\mathbf{z}} = -\eta \cos \Lambda \\ &\mathbf{e}_0 \cdot \hat{\mathbf{y}} = \pm\sqrt{1 - (\eta^2 + \zeta^2)} \\ &\mathbf{h}_0 \cdot \hat{\mathbf{d}} = \eta \sin \Lambda \\ &\mathbf{h}_0 \cdot \hat{\mathbf{z}} = \zeta \sin \Lambda \\ &\mathbf{h}_0 \cdot \hat{\mathbf{y}} = 0 \\ &s.t.\ \ (\eta^2 + \zeta^2) \leq 1, \end{aligned} \tag{4.26}$$

which gives the general solution for the frozen-node orbits in the form of

$$\begin{aligned} \mathbf{e}(\psi) = \cos \Lambda(&\zeta \cos \psi \pm \sin \psi \sqrt{1 - (\eta^2 + \zeta^2)})\hat{\mathbf{d}} \\ &(\pm \cos \psi \sqrt{1 - (\eta^2 + \zeta^2)} - \zeta \sin \psi)\hat{\mathbf{y}} - \eta \cos \Lambda \hat{\mathbf{z}}, \\ \mathbf{h}(\psi) = \eta \sin \Lambda \hat{\mathbf{d}} + \sin \Lambda(&\zeta \cos \psi \pm \sin \psi \sqrt{1 - (\eta^2 + \zeta^2)})\hat{\mathbf{z}}. \end{aligned} \tag{4.27}$$

It is interesting to note that frozen orbit configuration is the specially subset of this general family of orbits. The terminator plane frozen orbits are recovered by setting $\eta = \pm 1$ and $\zeta = 0$. These or-

www.manaraa.com

bits are described further in Section 4.2.2. Values of $\eta = \zeta = 0$ result in a rectilinear orbit. Figure 4.1 shows the contour plot of the maximum eccentricity that is achieved with respect to the values the η and ζ for Frozen-node orbit about Bennu with a semi-major axis of 1 km and $\Lambda \approx 84.4°$. This value of the parameter Λ is computed from Eq. (4.12) assuming a spacecraft mass to area ratio of B = 62 kg/m^2 (nominal design mass to area ratio for the OSIRIS-REx spacecraft), a surface reflectivity of $\rho = 0.4$, and the Bennu's gravitational parameter of $\mu = 5.2e-9\ km^3/s^2$ [15]. Values for the orbital parameters of Bennu and other astronomical constants are detailed in Appendix B. As shown in this plot, the maximum eccentricity increases rapidly by reducing the value of η. Therefore, when designing such orbits, one has to keep the value of η close to unity in order to avoid generating highly eccentric orbits that may be unstable and impact the surface. Also note that based on what is shown in Figure 4.1 the maximum eccentricity achieved by a frozen-node orbit is only a function of η. This can also be shown by deriving the magnitude of $\mathbf{e}(\psi)$ from Eq. (4.27) and showing that the maximum magnitude of $\mathbf{e}(\psi)$ is not a function of ζ.

Let us look at one case of the Frozen-node about Bennu orbit with $\eta = 0.98$ and $\zeta = 0$ to see how such orbit evolves over time. The semi-major axis of again $1\ km$ and $\Lambda \approx 84.4°$. Figure 4.2 shows the evolution of the secular orbit elements for one secular revolution of $\psi = 0$ to 2π. The start and the end of the cycle are marked on the figure. As shown in this figure, the average Ω remains constant while the average inclination and eccentricity evolve in a periodic and bounded pattern. This figure further shows a frozen terminator orbit (shown with the asterisk) as a comparison. Note that the minimum value of the eccentricity of a frozen-node orbit is equal to that of a frozen terminator orbit of the same size and the same Λ parameter. We discuss the frozen terminator orbits in the following section. Finally, Figure 4.3 shows a 50 days long numerical propagation of a frozen-node orbit with $\eta = 0.98$, $\zeta = 0$, and semi-major axis of 1 km about Bennu. These plots are shown in the Sun-asteroid rotating frame. The plot on the XY plane clearly shows the frozen node of the orbit.

www.manaraa.com

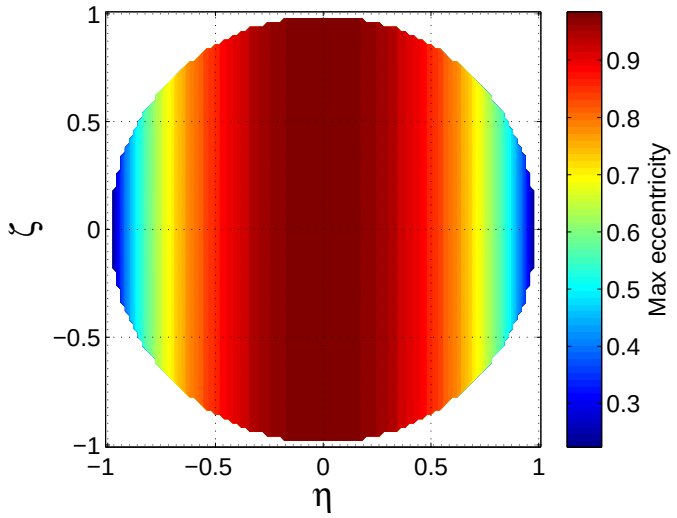

Figure 4.1: Contour of the maximum eccentricity achieved with respect to the values of η and ζ.

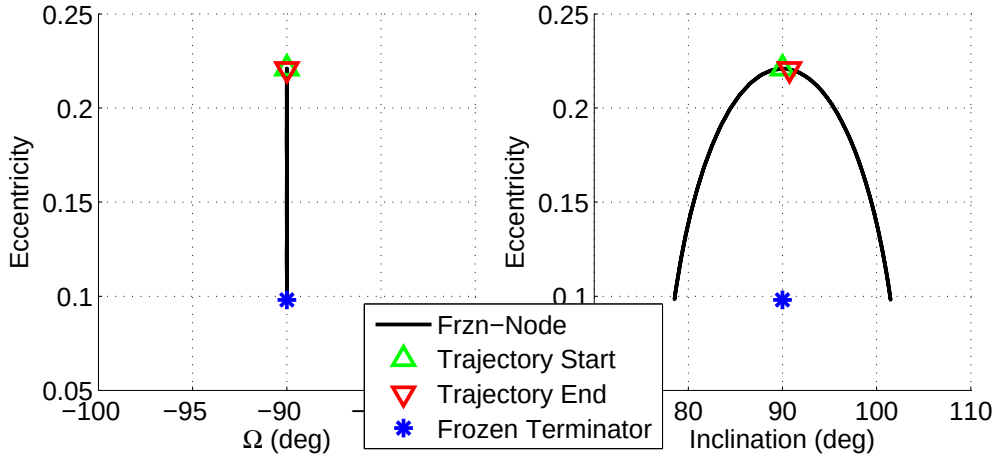

Figure 4.2: Secular evolution of the orbit elements of a frozen-node orbit with $\eta = 0.98$ and $\zeta = 0$.

4.2.2 Terminator Frozen Orbits

Another special solution to the secular dynamics of the orbit elements is the frozen terminator orbit solution. A frozen terminator orbit is an orbit on the Sun terminator plane, for which the secular rate of change of the state parameters vanish at all times, i.e. $\dot{\bar{\mathbf{e}}} = 0$ and $\dot{\bar{\mathbf{h}}} = 0$ [76]. Other family of the frozen orbits also exists that are not on the terminator orbit. Reference [77] (Ch. 13) provides further details on these type. Terminator frozen orbits remain unchanged overtime with

www.manaraa.com

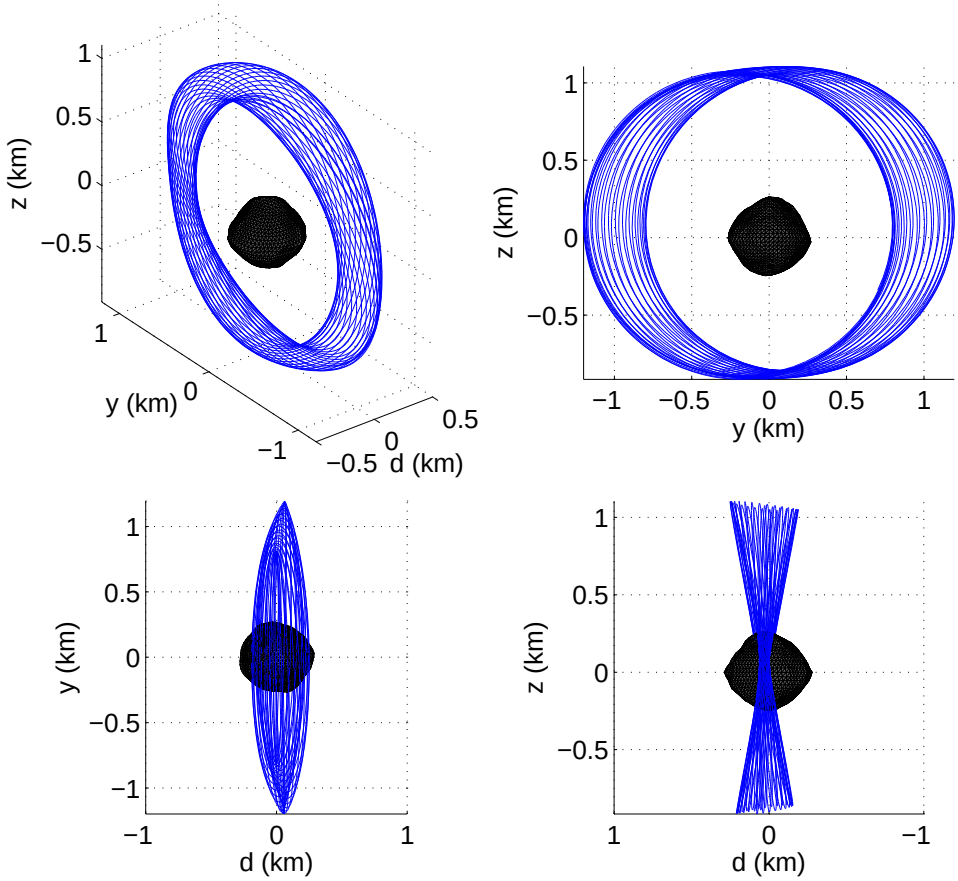

Figure 4.3: Numerical propagation of a frozen-node orbit with $\eta = 0.98$ and $\zeta = 0$ about Bennu.

respect to the sun-asteroid rotating frame. The angular momentum vector for these orbits is in the sun light direction pointing either towards the Sun (orbit facing the Sun) or away from the Sun (orbit facing away from the Sun). The eccentricity vector of a terminator frozen orbit that is facing the Sun points in the $-\hat{\mathbf{z}}$ direction and an orbit facing away from the Sun points in the $+\hat{\mathbf{z}}$ direction. More specifically the initial orbital elements for a terminator frozen orbit are given by

$$\begin{aligned}
\mathbf{h}_0 &= \pm\sqrt{1-e^2}\,\hat{\mathbf{d}}, \\
\mathbf{e}_0 &= \mp\cos(\Lambda)\,\hat{\mathbf{z}}, \\
\Omega_0 &= \pm 90^\circ, \\
i_0 &= 90^\circ, \text{ and} \\
\omega_0 &= \mp 90^\circ.
\end{aligned} \tag{4.28}$$

www.manaraa.com

This set of initial condition is derived by enforcing that the secular time rate of change of orbit elements vanish at all times. As it was mentioned, this family of orbits may also be derived from the formulation detailed in Section 4.2.1. This is simply accomplished by setting $\eta = \pm 1$ and $\zeta = 0$ in Eq. (4.26) to get the same initial condition given above. Figure 4.4(a) shows two terminator frozen orbits in the sun-asteroid rotating frame propagated for 20 days about Asteroid (101955) Bennu with a semi-major axis of 1 km. As shown in this figure, the frozen orbits are fixed on average in the sun-asteroid rotating frame.

4.2.3 Initially Circular, Terminator Orbits

Initially circular terminator orbits are also of great interest for small body mission such as NASA's OSIRIS-REx mission. The nominal orbit configuration in the radio science phase of this mission (Orbital Phase A and B) is a circular terminator orbit with $\Omega_0 = \pm 90^\circ$ ($\mathbf{h}_0 = \pm\hat{\mathbf{d}}$), $i_0 = 90^\circ$, and $e_0 = 0$[3] . Substituting these initial conditions in Eq. (4.14) and simplifying the matrix multiplication results in a set of explicit expressions that describe the secular motion of the orbit eccentricity and scaled angular momentum vectors as a function of ψ, which is given by

$$\begin{aligned} \mathbf{e}(\psi) &= \mp(1 - \cos\psi)\sin\Lambda\cos\Lambda\,\hat{\mathbf{z}}, \\ \mathbf{h}(\psi) &= \pm\left(1 - \cos^2\Lambda(1 - \cos\psi)\right)\,\hat{\mathbf{d}} \mp \sin\psi\cos\Lambda\,\hat{\mathbf{y}}. \end{aligned} \tag{4.29}$$

These expressions are periodic in ψ with a period of 2π. Note that the secular motion of the eccentricity vector exists only on the $\hat{\mathbf{z}}$ axis with a sign that is opposite of that for the initial scaled angular momentum vector, $\hat{\mathbf{h}}_0$. Therefore, for an initially circular terminator orbit facing away from the Sun, i.e. $\mathbf{h}_0 = +\hat{\mathbf{d}}$, the averaged eccentricity vector appears in the negative $\hat{\mathbf{z}}$ direction as its magnitude increases from 0 (at $\psi = 0$) to a maximum value of $\sin(2\Lambda)$ at $\psi = \pi$ and decreases back to 0 at $\psi = 2\pi$. The opposite of this is true for an initially circular terminator orbit that is facing the Sun, i.e. $\mathbf{h}_0 = -\hat{\mathbf{d}}$. Also, note that the secular motion of the angular momentum vector of an initially circular terminator orbit exists on the $\hat{\mathbf{d}}\hat{\mathbf{y}}$ plane as it oscillates back and forth about the $\hat{\mathbf{z}}$ axis. In other words, the orbit plane starts at the terminator plane (at $\psi = 0$) and rotates away

[3] OSIRIS-REx Design Reference Mission (DRM) - http://gsfcir.gsfc.nasa.gov/colloquia/4942

www.manaraa.com

from the terminator plane (about the $\hat{\mathbf{z}}$ axis) by a maximum angle of α_{max} that occurs at $\psi = \pi/2$ and $3\pi/2$. The magnitude of the angle α_{max} is given by

$$\alpha_{max} = \tan^{-1}\left(\frac{\cos\Lambda}{\sin^2\Lambda}\right). \tag{4.30}$$

Figure 4.4(b) shows an initially circular terminator orbit shown in the sun-asteroid rotating frame propagated for 20 days about Bennu with a semi-major axis of 1 km. From this figure it is clear that the orbit does not remain circular and its eccentricity changes over time in the $+\hat{\mathbf{z}}$ or $-\hat{\mathbf{z}}$ direction depending on the direction that the orbit is facing. To see the changes in the orientation of the orbit plane we plot the averaged eccentricity against the averaged Ω over time. Figure 4.5 shows this plot for both a frozen terminator orbit and an initially circular terminator orbit with a semi-major axis of $1\ km$ and $\Lambda \approx 84.4°$. Figure 4.5 shows that a frozen orbit does not have a secular motion in the sun-asteroid rotating frame as it remains a single point over time on the plot. An initially circular terminator orbit, however, rotates in and out of the terminator plane as its eccentricity value changes overtime. As a result it traces an elliptical contour in the e & Ω phase space as shown in Figure 4.5. However, the inclination of this orbit is constant and equals to $90°$ on average. For a choice of $\Lambda = 84.4°$ an initially circular terminator orbit repeats the cycle, on average, about once every 42 days with a $\Delta e = 0.19$ and $\Delta\Omega = 11.3°$. However, as it will be discussed in further detail in section 4.5, the period of the secular dynamics of the orbit elements in the time domain is highly dependent on the rate of the heliocentric true anomaly of the asteroid, i.e. the location of the asteroid in its orbit.

It is also interesting to note that the motion of the orbit in the e & Ω phase space is in the clock-wise direction regardless of which direction the orbit is facing. Further details about the dynamical properties of the frozen and circular terminator orbits are given in References [77] and [78].

www.manaraa.com

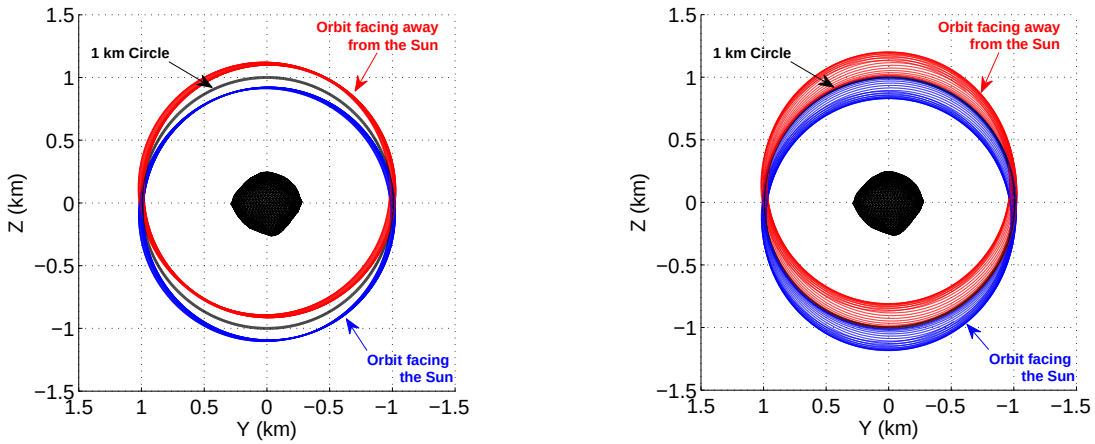

(a) Terminator Frozen Orbit

(b) Initially Circular Terminator Orbit

Figure 4.4: Plots of two terminator frozen and two initially terminator circular orbits around Bennu propagated for 20 days. Both orbit types have a semi-major axis of 1 km.

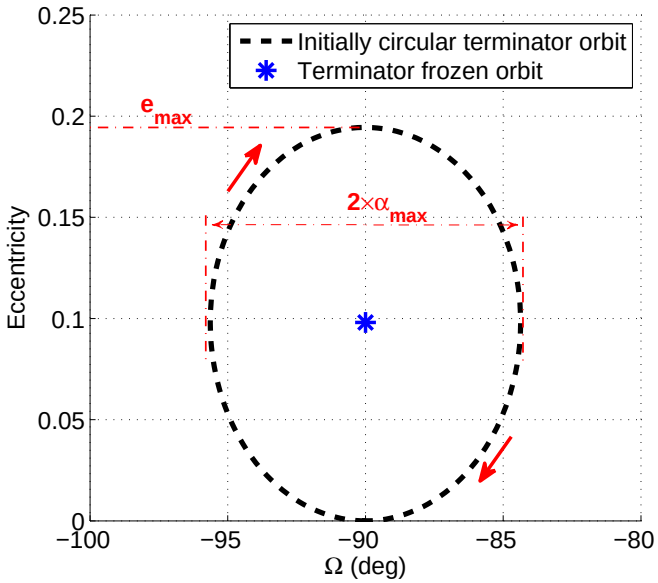

Figure 4.5: Plots of a terminator frozen and an initially terminator circular orbits around Bennu in the e & Ω phase space. Both orbit types have a semi-major axis of 1 km and $\Lambda \approx 84.4°$.

4.3 Sensitivity of Terminator Orbits to Maneuver Errors – Formulation

Previous sections introduced a set of special solutions to the secular dynamics of the orbit elements under strong SRP perturbation. Terminator orbits are an important group of this family

www.manaraa.com

and they are the most likely candidate to be selected for spacecraft orbiting small bodies. This is the case for the OSIRIS-REx mission, for which an initially circular terminator orbit is selected as the nominal orbit of the radio science phase of the mission. Terminator orbits are quasi-stable orbits that exist around small bodies. The delicate balance between the central body gravitational attraction and the strong SRP perturbation coupled by the motion of the small body in its orbit allows for the construction of such orbits. However, due to highly non-Keplerian dynamics that exist in such an environment, small perturbations can lead to large deviations from the nominal trajectory. Such perturbations arise from errors in the spacecraft reaction wheel de-saturation maneuvers, orbit insertion maneuvers, and targeting maneuvers. Hence, it is important to be able to quantify the sensitivity of such orbits to small maneuver errors. In this section we formulate a set of equations that may be used for such analysis.

4.3.1 Formulation of Orbit Response to Small Maneuver Errors

The key assumption in this derivation is that the magnitude of the velocity error is much smaller than the magnitude of the orbit velocity, i.e. $\delta v_0 \ll v_0$, where v_0 represents the velocity magnitude of the nominal trajectory. Recall the state vector and the state transition matrix given by Equations (4.15) and (4.16), respectively. Based on these equations the linearized averaged solution for the state deviation vector $\delta\mathbf{X}$ is given by

$$\delta\mathbf{X}(\psi) = \Phi(\psi)\delta\mathbf{X}_0. \tag{4.31}$$

The error in the initial state vector $\delta\mathbf{X}_0$ due to an error in the velocity vector $\delta\mathbf{v}_0$ may be approximated (to the first order) by Gauss's variational equation as the following:

$$\delta\mathbf{X}_0 = \left.\frac{\partial\mathbf{X}}{\partial\mathbf{v}}\right|_0 \cdot \delta\mathbf{v}_0, \tag{4.32}$$

where the Jacobian $\partial\mathbf{X}/\partial\mathbf{v}$ is evaluated at the initial epoch when the maneuver takes place. In this analysis, we use the eccentricity vector (see Eq. (4.1)) and the scaled angular momentum vectors (see Eq. (4.8)) as the set of orbital elements to be analyzed. Changes in the energy of the orbit are

www.manaraa.com

taken into account by formulating the effect of $\delta\mathbf{v}_0$ on the semi-major axis on a case by case basis. Further details on this are provided in the following paragraphs. Taking the partial derivative of these orbit elements with respect to the velocity vector gives

$$\Upsilon = \frac{\partial \mathbf{X}}{\partial \mathbf{v}} = \begin{bmatrix} \dfrac{\partial \mathbf{e}}{\partial \mathbf{v}} \\ \\ \dfrac{\partial \mathbf{h}}{\partial \mathbf{v}} \end{bmatrix} = \frac{1}{\mu} \begin{bmatrix} 2\mathbf{rv} - \mathbf{vr} - (\mathbf{r}\cdot\mathbf{v})\bar{\bar{U}} \\ \\ \sqrt{\dfrac{\mu}{a_0}}\tilde{\mathbf{r}} \end{bmatrix}, \tag{4.33}$$

where a_0 is the semi-major axis of the orbit at the maneuver epoch. Substituting Equations (4.32) & (4.33) into Eq. (4.31) results in the expression that maps the velocity error at an initial epoch to the state deviation vector at a different epoch. The expression is given in a simple form of

$$\delta\mathbf{X}(\psi) = \Phi(\psi)\ \Upsilon|_0 \cdot \delta\mathbf{v}_0. \tag{4.34}$$

There are, however, several caveats to this expression. First, note that altering the velocity magnitude of the nominal orbit may change the specific energy and therefore the value of the semi-major axis of the nominal orbit. The change in the semi-major axis may be represented by

$$a = a_0 + \delta a_0, \tag{4.35}$$

where a represent the value of the semi-major axis of the orbit after the implementation of the maneuver and δa_0 is amount of change in the semi-major axis due to the maneuver. The expression for δa_0 is given by Gauss's variational equations as

$$\delta a_0 = \frac{2}{h}\sqrt{\frac{a_0^3}{\mu}}\left(e_0 \sin(f)\delta v_{0_r} + \frac{a_0(1-e^2)}{r}\delta v_{0_\theta}\right), \tag{4.36}$$

where δv_{0_r} and δv_{0_θ} are the magnitude of the velocity change due a maneuver in the radial and in-track directions. Changes in the semi-major axis result in changes in the parameter Λ, which subsequently alters the value of the parameter ψ. Therefore, one must update values of these parameters by substituting the new value of the semi-major axis in Eq. (4.12) and the expression that defines the variable ψ before using them in Eq. (4.34).

Second, note that the Jacobian Υ is a function of the position and velocity vectors of the spacecraft. Therefore, its value depends on the initial orbit configuration as well as the point along

www.manaraa.com

the orbit at which it is evaluated. To take this fact into account, we break the problem into several subsections with each subsection exploring a specific scenario and the initial orbit configuration. The overall solution to the problem may be reconstructed by combining the solutions derived for each specific scenario.

4.3.2 Sensitivity of a Terminator Frozen Orbit to Maneuver Errors

This section considers a terminator frozen orbit as the reference orbit. As mentioned in the previous section, this type of orbit remains fixed – on average – with respect to the sun-asteroid rotating reference frame, $\widehat{\mathbf{dyz}}$. For a frozen orbit (with the initial condition given in Eq. (4.28)), the position and velocity vectors of the orbiter for a true anomaly f are given by

$$\begin{aligned} \mathbf{r}_0 &= r_0(\mp\cos f\hat{\mathbf{z}} + \sin f\hat{\mathbf{y}}), \\ \mathbf{v}_0 &= \sqrt{\frac{\mu}{a_0(1-e_0^2)}}(\pm\sin f\hat{\mathbf{z}} + (e_0+\cos f)\hat{\mathbf{y}}), \end{aligned} \tag{4.37}$$

where r_0 is given by

$$r_0 = \frac{a_0(1-e_0^2)}{1+e_0\cos f}. \tag{4.38}$$

We substitute the expressions above into Eq. (4.33) to compute the Jacobian Υ. The final expression for the $\Upsilon|_0$ is given by

$$\Upsilon|_0 = \beta_0 \begin{bmatrix} (\frac{\sin(2f)}{2} + \cos\Lambda_0\sin f)\hat{\mathbf{y}}\hat{\mathbf{y}} \pm (\cos^2 f - \cos\Lambda_0\cos f - 2)\hat{\mathbf{y}}\hat{\mathbf{z}} \\ \mp(\cos^2 f + 2\cos\Lambda_0\cos f + 1)\hat{\mathbf{z}}\hat{\mathbf{y}} - \frac{\sin(2f)}{2}\hat{\mathbf{z}}\hat{\mathbf{z}} - \cos\Lambda_0\sin f\,\bar{\bar{U}} \\ \\ \sin\Lambda_0(\mp\cos f\tilde{\hat{\mathbf{z}}} + \sin f\tilde{\hat{\mathbf{y}}}) \end{bmatrix}. \tag{4.39}$$

where

$$\beta_0 = \sqrt{\frac{a_0}{\mu}}\frac{\sin\Lambda_0}{1+\cos\Lambda_0\cos f} \tag{4.40}$$

and the variable Λ_0 refers to the reference value of the parameter Λ before the application of the maneuver. The expression above is effectively the sensitivity matrix of a terminator frozen orbit to a small change in the velocity vector. In addition to the nominal orbit configuration the final

www.manaraa.com

expression that defines the time progression of the state deviation vector also depends on the direction at which the velocity change is applied. To this end, we consider three basic impulsive velocity perturbations that occur in the radial, in-track, and cross-track directions. The governing expression for the time progression of the state deviation vector is derived for each scenario.

4.3.2.1 Let $\delta\mathbf{v}_0 = \pm\delta v_0\hat{\mathbf{d}}$

This is a case where the perturbing velocity error vector is parallel or anti-parallel to the angular momentum vector of the orbit. Since the velocity error is perpendicular to the orbit plane, it does not affect the semi-major axis of the orbit. In other words, $\delta a_0 = 0$ which is the direct result from Eq. (4.36). Substituting the velocity error vector in Eq. (4.31) and simplifying the expressions, results in the following state deviation solution over time.

$$\begin{aligned}\delta\mathbf{e}_c(\psi) = \operatorname{sgn}(\delta\mathbf{v}_0)\delta v_0\beta_0\Big(&-\cos\Lambda_0\cos(\psi)\sin f\hat{\mathbf{d}} + \sin f\sin(\psi)\hat{\mathbf{y}} \\ &\mp\sin^2\Lambda_0\cos f\sin(\psi)\hat{\mathbf{z}}\Big)\end{aligned} \tag{4.41}$$

$$\begin{aligned}\delta\mathbf{h}_c(\psi) = \operatorname{sgn}(\delta\mathbf{v}_0)\delta v_0\beta_0\Big(&\mp\sin\Lambda_0\cos\Lambda_0\cos f\sin(\psi)\hat{\mathbf{d}} \\ &\mp\sin\Lambda_0\cos f\cos(\psi)\hat{\mathbf{y}} - \sin\Lambda_0\cos(\psi)\sin f\hat{\mathbf{z}}\Big),\end{aligned} \tag{4.42}$$

where the subscript c indicates the perturbation of the state parameters due to a cross-track velocity perturbation. The expression $\operatorname{sgn}(\delta\mathbf{v}_0)$ indicates the sign of the velocity error vector.

4.3.2.2 Let $\delta\mathbf{v}_0 = \pm\delta v_0\hat{\theta}$

This case considers a scenario in which the velocity error vector is parallel or anti-parallel to the in-track direction of the orbit. For this case, the velocity error vector may be written as

$$\delta\mathbf{v}_0 = \operatorname{sgn}(\delta\mathbf{v}_0)\delta v_0(\pm\sin f\hat{\mathbf{z}} + \cos f\hat{\mathbf{y}}). \tag{4.43}$$

In-track changes in the velocity of the orbiter result in a change in the value of the semi-major axis. Substituting $\delta\mathbf{v}_0$ in Eq. (4.36) results in the following equation:

$$\delta a_0 = 2\delta v_0\sqrt{\frac{a_0^3}{\mu}}(1+\cos\Lambda_0\cos f)\csc\Lambda_0. \tag{4.44}$$

www.manaraa.com

The value of δa_0 is then added to the nominal semi-major axis value, a_0, to get the new value for the semi-major axis of the orbit after the application of the in-track maneuver. Substituting the velocity error vector for this scenario into Eq. (4.31) and performing the matrix multiplications results in the following expressions for the time progression of the components of the state deviation vector due an in-track maneuver.

$$\begin{aligned}\delta\mathbf{e}_\theta(\psi) = \operatorname{sgn}(\delta\mathbf{v}_0)\delta v_0\beta_0\Bigg\{ &\cos\Lambda\sin f\sin\psi(2+\cos\Lambda_0\cos f)\hat{\mathbf{d}} + \cos\psi\sin f(2+\cos\Lambda_0\cos f)\hat{\mathbf{y}} \\ &\mp\Bigg[\cos f\Big(\big(\cos\psi-\cos^2\Lambda(\cos\psi-1)\big)\big(1+\cos^2 f+2\cos\Lambda_0\cos f\big) \\ &-\cos\Lambda\sin\Lambda\sin\Lambda_0\cos f(\cos\psi-1)\Big)+\sin f\Big(\big(\cos f\sin f+\cos\Lambda_0\sin f\big) \\ &\times\big(\cos\psi-\cos^2\Lambda(\cos\psi-1)\big)-\cos\Lambda\sin\Lambda\sin\Lambda_0\sin f(\cos\psi-1)\Big)\Bigg]\hat{\mathbf{z}}\Bigg\}\end{aligned} \tag{4.45}$$

$$\begin{aligned}\delta\mathbf{h}_\theta(\psi) = \operatorname{sgn}(\delta\mathbf{v}_0)\delta v_0\beta_0\Bigg\{ &\pm\Bigg[\cos f\Big(\cos f\sin\Lambda_0\big(\cos\Lambda^2\cos\psi-\cos\Lambda^2+1\big)-\cos\Lambda\sin\Lambda \\ &\times(\cos\psi-1)\big(\cos f^2+2\cos\Lambda_0\cos f+1\big)\Big)+\sin f\Big(\sin f\sin\Lambda_0\big(\cos\Lambda^2\cos\psi-\cos\Lambda^2+1\big) \\ &-\cos\Lambda\sin\Lambda\sin f(\cos\psi-1)\big(\cos\Lambda_0+\cos f\big)\Big)\Bigg]\hat{\mathbf{d}} \\ &\pm\sin\psi\Big(\cos\Lambda_0\sin\Lambda-\cos\Lambda\sin\Lambda_0+2\sin\Lambda\cos f+\cos\Lambda_0\sin\Lambda\cos f^2\Big)\hat{\mathbf{y}} \\ &-\sin\Lambda\sin f\sin\psi\big(\cos\Lambda_0\cos f+2\big)\hat{\mathbf{z}}\Bigg\},\end{aligned} \tag{4.46}$$

where the subscript θ indicates the state parameter perturbations due to an in-track velocity error. Note that these expressions contain two values for the parameter Λ. The one with the subscript 0 is the nominal value of the parameter, while the one without this subscript is the updated value of the parameter due to a change in the semi-major axis.

4.3.2.3 Let $\delta\mathbf{v}_0 = \pm\delta v_0\hat{\mathbf{r}}$

Finally, we consider the case where the velocity error is applied parallel or anti-parallel to the radial direction. The velocity error vector for this case may be written as

$$\delta\mathbf{v}_0 = \operatorname{sgn}(\delta\mathbf{v}_0)\delta v_0(\mp\cos f\hat{\mathbf{z}}+\sin f\hat{\mathbf{y}}). \tag{4.47}$$

www.manaraa.com

Velocity changes in the radial direction also result in a change in the value of the semi-major axis. For this case, the change in the semi-major axis value is given by

$$\delta a_0 = 2\delta v_0 \sqrt{\frac{a_0^3}{\mu}} \cot \Lambda_0 \sin f. \tag{4.48}$$

Once again, the expression for the velocity error vector is substituted in Eq. (4.31) to result in the expressions that define the time progression of the components of the state deviation vector due to a small maneuver error in the radial direction. These expressions are given by

$$\begin{aligned} \delta \mathbf{e}_r(\psi) = \operatorname{sgn}(\delta \mathbf{v}_0)\delta v_0 \beta_0 \Big(& -\cos\Lambda \cos f \sin\psi(\cos\Lambda_0 \cos f + 1)\hat{\mathbf{d}} \\ & -\cos f \cos\psi(\cos\Lambda_0 \cos f + 1)\hat{\mathbf{y}} \\ & \mp \sin f(\cos\Lambda_0 \cos f + 1)(\cos\psi + \cos\Lambda^2 - \cos\Lambda^2 \cos\psi)\hat{\mathbf{z}} \Big) \end{aligned} \tag{4.49}$$

$$\begin{aligned} \delta \mathbf{h}_r(\psi) = \operatorname{sgn}(\delta \mathbf{v}_0)\delta v_0 \beta_0 \Big(& \mp \cos\Lambda \sin\Lambda \sin f(\cos\psi - 1)(\cos\Lambda_0 \cos f + 1)\hat{\mathbf{d}} \\ & \pm \sin\Lambda \sin f \sin\psi(\cos\Lambda_0 \cos f + 1)\hat{\mathbf{y}} \\ & -\sin\Lambda \cos f \sin\psi(\cos\Lambda_0 \cos f + 1)\hat{\mathbf{z}} \Big), \end{aligned} \tag{4.50}$$

where the subscript r indicates the perturbations of the state parameters due to a radial velocity error. The total variation for each of the state parameters is given by

$$\begin{aligned} \delta \mathbf{e}(\psi) &= \delta \mathbf{e}_c(\psi) + \delta \mathbf{e}_\theta(\psi) + \delta \mathbf{e}_r(\psi) \\ \delta \mathbf{h}(\psi) &= \delta \mathbf{h}_c(\psi) + \delta \mathbf{h}_\theta(\psi) + \delta \mathbf{h}_r(\psi). \end{aligned} \tag{4.51}$$

Consequently, the time progression of the state parameters is given by

$$\begin{aligned} \mathbf{e}(\psi) &= \Phi(\psi)\mathbf{e_0} + \delta \mathbf{e}(\psi) \\ \mathbf{h}(\psi) &= \sqrt{\frac{a_0}{a}}(\Phi(\psi)\mathbf{h_0} + \delta \mathbf{h}(\psi)), \end{aligned} \tag{4.52}$$

where the multiplier $\sqrt{a_0/a}$ in the second expression is used to re-scale the updated angular momentum vector due to the changes in the semi-major axis value. Figures 4.6 and 4.7 show the results of applying one small impulsive δv with equal amounts in all of the three radial, in-track,

www.manaraa.com

and cross-track directions and at the true anomalies of 45° & 90° along the orbit.[4] The nominal orbit is a frozen terminator orbit with a $1\ km$ semi-major axis around Bennu. The results show that the orbit eccentricity changes in complex patterns with respect to different orbit parameters. However, it is also important to note that despite these complex patterns, they are periodic and repeat themselves over the period of ψ. Furthermore, the figures show that the magnitude of the state deviation is directly related to the magnitude of the impulsive $\delta\mathbf{v}_0$. The sign of the velocity error vector shows a small effect on the shape of the generated patterns which starts to be discernable on the Ω and the inclination for a $3\ mm/s$ velocity error magnitude. A $3\ mm/s$ velocity error accounts for about 4% error in the orbit velocity, which is on the order of $7-8\ cm/s$ for a $1\ km$ orbit about Bennu. The red arrows on the plots show the direction of the motion of the orbit elements over time.

4.3.3 Sensitivity of an Initially Circular Terminator Orbit to Maneuver Errors

In this section we consider the effects of an instantaneous velocity perturbation on an initially circular terminator orbit. The eccentricity vector is not defined at time zero for this type of orbit. However, Eq. (4.29) shows that the averaged eccentricity vector evolves along the z axis. Therefore, at time $t=0$, we define the angle f to be the angle between the position vector and the z axis with the direction given by the averaged eccentricity vector. Furthermore, ω is defined as the angle between the ascending node of the orbit (this is along the $\hat{\mathbf{y}}$ axis for a terminator orbit) and the z axis at time $t=0$. Hence, the initial position and velocity vectors are given by

$$\begin{aligned}\mathbf{r}_0 &= a_0(\mp\cos f\hat{\mathbf{z}} + \sin f\hat{\mathbf{y}})\\ \mathbf{v}_0 &= \sqrt{\frac{\mu}{a_0}}(\pm\sin f\hat{\mathbf{z}} + \cos f\hat{\mathbf{y}}).\end{aligned} \tag{4.53}$$

Furthermore, for an initially circular terminator orbit Eq. (4.36) simplifies to

$$\delta a_0 = \sqrt{\frac{a_0^3}{\mu}}\frac{2}{h_0}\delta v_{0_\theta}. \tag{4.54}$$

[4] The sensitivity of the orbit elements to the individual directions of the applied δv depends on the value of the true anomaly (f) at which the δv is applied. For instance, orbit elements are most sensitive to an in-track δv when it is applied at $f=0^\circ$, while they are most sensitive to a radial δv when it is applied at $f=90^\circ$.

www.manaraa.com

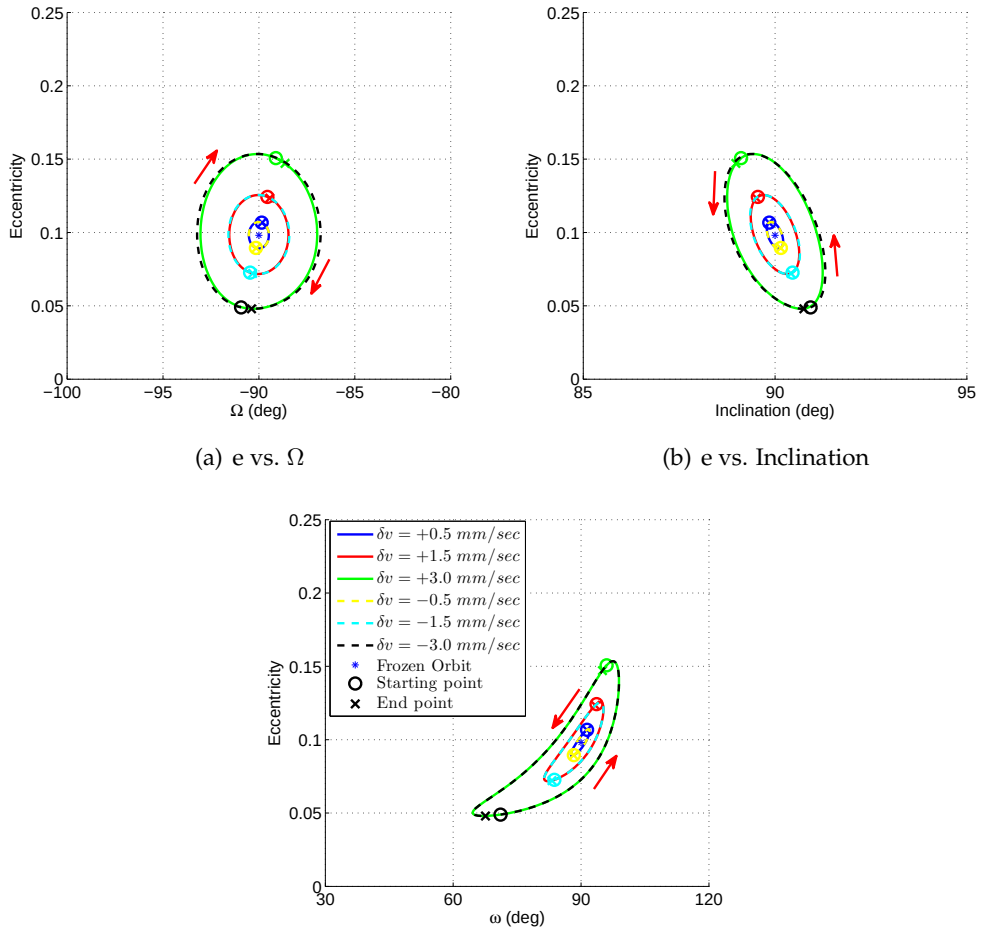

(a) e vs. Ω

(b) e vs. Inclination

(c) e vs. ω

Figure 4.6: Progression of the averaged orbit elements due to an instantaneous velocity perturbation applied at $f = 45°$. The initial orbit is a terminator frozen orbit with $a_0 = 1$ km about Bennu, $\Lambda \approx 84.4°$, and $\hat{\mathbf{h}}_0 = -\hat{\mathbf{d}}$.

In other words, δa_0 is only a function of the velocity error component in the in-track direction. We substitute Eq. (4.53) in Eq. (4.33) to get the following Jacobian:

$$\Upsilon|_0 = \sqrt{\frac{a_0}{\mu}} \begin{bmatrix} \mp(\cos^2 f - 2)\hat{\mathbf{y}}\hat{\mathbf{z}} + \dfrac{\sin(2f)}{2}\hat{\mathbf{y}}\hat{\mathbf{y}} \mp (2 - \sin^2 f)\hat{\mathbf{z}}\hat{\mathbf{y}} - \dfrac{\sin(2f)}{2}\hat{\mathbf{z}}\hat{\mathbf{z}} \\ \\ \mp\cos f\tilde{\hat{\mathbf{z}}} + \sin f\tilde{\hat{\mathbf{y}}} \end{bmatrix}. \tag{4.55}$$

Similar to the analysis carried out for the frozen orbit case, we consider three basic velocity perturbations that are applied in the radial, in-track, and cross-track directions.

www.manaraa.com

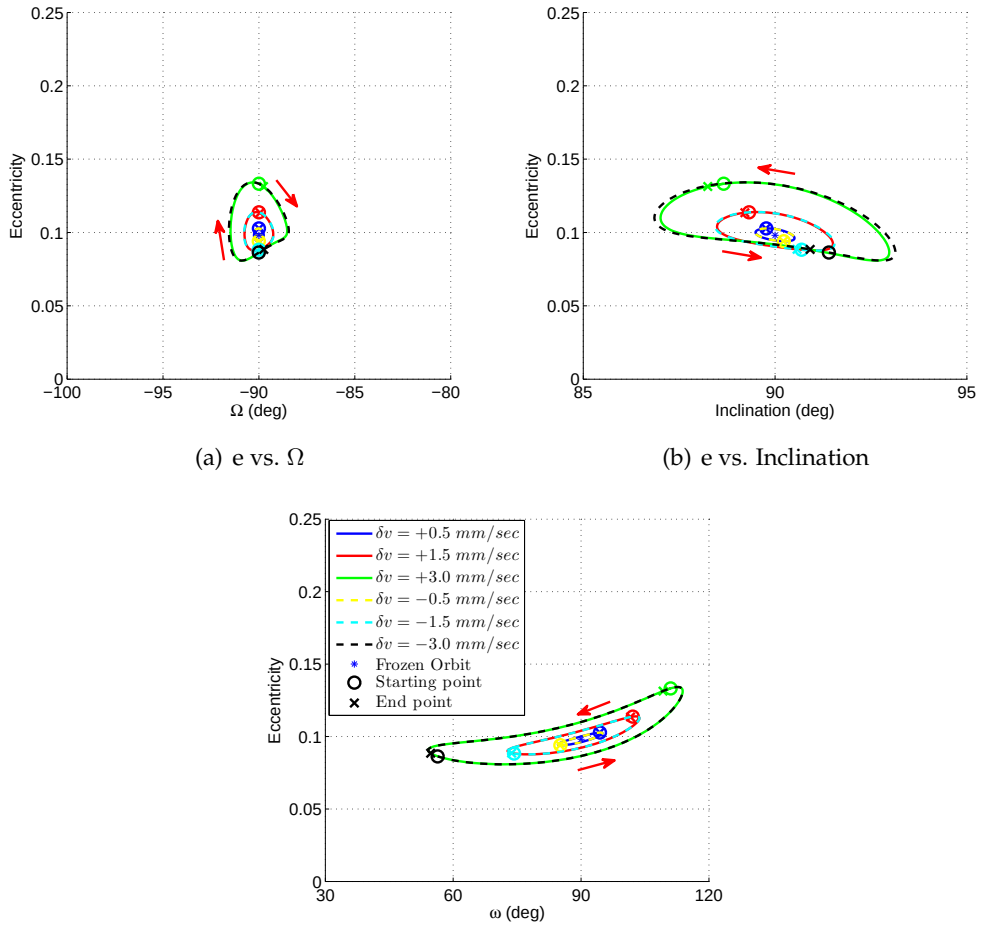

(a) e vs. Ω

(b) e vs. Inclination

(c) e vs. ω

Figure 4.7: Progression of the averaged orbit elements due to an instantaneous velocity perturbation applied at $f = 90°$. The initial orbit is a terminator frozen orbit with $a_0 = 1$ km about Bennu, $\Lambda \approx 84.4°$, and $\hat{\mathbf{h}}_0 = -\hat{\mathbf{d}}$.

4.3.3.1 Let $\delta\mathbf{v}_0 = \pm\delta v_0\hat{\mathbf{d}}$

For a velocity perturbation perpendicular to the orbit plane, the components of the state deviation vector are given by

$$\delta\mathbf{e}_c(\psi) = \mathrm{sgn}(\delta\mathbf{v}_0)\delta v_0\sqrt{\frac{a_0}{\mu}}\Big(\cos\Lambda_0\sin\Lambda_0\sin f(1-\cos\psi)\hat{\mathbf{d}} + \sin\Lambda_0\sin f\sin\psi\hat{\mathbf{y}} \mp \sin\Lambda_0\cos f\sin(\psi)\hat{\mathbf{z}}\Big), \tag{4.56}$$

www.manaraa.com

$$\delta\mathbf{h}_c(\psi) = \text{sgn}(\delta\mathbf{v}_0)\delta v_0\sqrt{\frac{a_0}{\mu}}\Big(\mp\cos\Lambda_0\cos f\sin\psi\hat{\mathbf{d}} \mp \cos f\cos\psi\hat{\mathbf{y}} \\ -\sin f(\cos\psi + \cos^2\Lambda_0(1-\cos\psi))\hat{\mathbf{z}}\Big). \tag{4.57}$$

Note that the value of the semi-major axis is preserved for this scenario, i.e. $\delta a_0 = 0$.

4.3.3.2 Let $\delta\mathbf{v}_0 = \pm\delta v_0\hat{\theta}$

For a velocity perturbation parallel or antiparallel to the in-track direction the changes in the semi-major axis is given by Eq. (4.54). Going through a similar process as before, we compute the expressions for the components of the state deviation vector. These expressions are given by

$$\delta\mathbf{e}_\theta(\psi) = \text{sgn}(\delta\mathbf{v}_0)\delta v_0\sqrt{\frac{a_0}{\mu}}\Big(2\cos\Lambda\sin f\sin\psi\hat{\mathbf{d}} + 2\cos\psi\sin f\hat{\mathbf{y}} \\ \mp\left((1-\cos\psi)(2\cos^2\Lambda\cos f + \cos\Lambda\sin\Lambda) + 2\cos f\cos\psi\right)\hat{\mathbf{z}}\Big), \tag{4.58}$$

$$\delta\mathbf{h}_\theta(\psi) = \text{sgn}(\delta\mathbf{v}_0)\delta v_0\sqrt{\frac{a_0}{\mu}}\Big(\pm\left((1-\cos\psi)(2\cos\Lambda\sin\Lambda\cos f - \cos^2\Lambda) + 1\right)\hat{\mathbf{d}} \\ \pm\sin\psi(2\sin\Lambda\cos f - \cos\Lambda)\hat{\mathbf{y}} + 2\sin\Lambda\sin f\sin\psi\hat{\mathbf{z}}\Big). \tag{4.59}$$

4.3.3.3 Let $\delta\mathbf{v}_0 = \pm\delta v_0\hat{\mathbf{r}}$

Applying the velocity perturbation parallel or antiparallel to the radial direction results in the following expressions of the state deviation vector components:

$$\delta\mathbf{e}_r(\psi) = \text{sgn}(\delta\mathbf{v}_0)\delta v_0\sqrt{\frac{a_0}{\mu}}\Big(-\cos\Lambda_0\cos f\sin\psi\hat{\mathbf{d}} - \cos f\cos\psi\hat{\mathbf{y}} \\ \mp\left(\sin f(\cos\psi + \cos^2\Lambda_0(1-\cos\psi))\right)\hat{\mathbf{z}}\Big), \tag{4.60}$$

$$\delta\mathbf{h}_r(\psi) = \text{sgn}(\delta\mathbf{v}_0)\delta v_0\sqrt{\frac{a_0}{\mu}}\Big(\pm\cos\Lambda_0\sin\Lambda_0\sin f(1-\cos\psi)\hat{\mathbf{d}} \\ \pm\sin\Lambda_0\sin f\sin\psi\hat{\mathbf{y}} - \sin\Lambda_0\cos f\sin\psi\hat{\mathbf{z}}\Big). \tag{4.61}$$

Note that $\delta a_0 = 0$ since the orbit is circular at the epoch when the velocity perturbation is applied, i.e. $e_0 = 0$.

For a velocity perturbation in an arbitrary direction, the total variation of the state deviation vector and the time progression of the state parameters may be calculated by Eq. (4.51) and (4.52), respectively. Figures 4.8 and 4.9 show the results of applying one small impulsive δv with equal

www.manaraa.com

amounts in all of the three radial, in-track, and cross-track directions and at $f = 45^\circ$ & 90° along the orbit. The nominal orbit is a circular terminator orbit about Bennu with $1\ km$ semi-major axis. The results show that similar to the frozen orbit case the orbit eccentricity changes in complex patterns with respect to different orbit parameters. However, comparing Figures 4.8 and 4.9 with Figures 4.6 and 4.7, it is clear that the range of changes of the orbit elements for an initially circular terminator orbit are larger than those for a frozen orbit. In other words, an initially circular terminator orbit is more sensitive to a velocity change than a frozen orbit of the same size. Large deviations in Ω (see Figure 4.8(a) and 4.9(a)) show that the perturbed circular orbit may oscillate out of the terminator plane by a large amount. Furthermore, the sign of the velocity error vector has a much more pronounced effect on an initially circular terminator orbit as compared to a frozen orbit. This may be attributed to the notion that an initially circular terminator orbit is far from the frozen equilibrium point for this system for which the response to small velocity errors is linear. Another important point to note here is that according to Figures 4.8(c) and 4.9(c), a velocity errors in the opposite direction of the orbit velocity results in large oscillations in the eccentricity vector. These figures show that for a negative velocity error the eccentricity vector may flip to the opposite pole without changing the direction of the angular momentum of the orbit. This may be useful for the asteroid surface observations and the radio science campaign as the point of the closes approach of the orbit changes poles. The magnitude of the eccentricity, however, is very small when this happens. A frozen orbit is more robust against this effect, such that the eccentricity vector of a perturbed frozen orbit remains above the same pole as that for the nominal orbit (see Figures 4.6(c) and 4.7(c)).

4.4 Offset Correction due to Short Periodic Terms

In order to improve the agreement between solutions given by the secular dynamics (Eq. (4.7)) and those generated by numerical integration of the osculating elements, one needs to take into account a correction to the initial condition of the secular dynamics. Without such a correction, solutions given by the two methods may diverge away from each other after multiple orbit periods.

www.manaraa.com

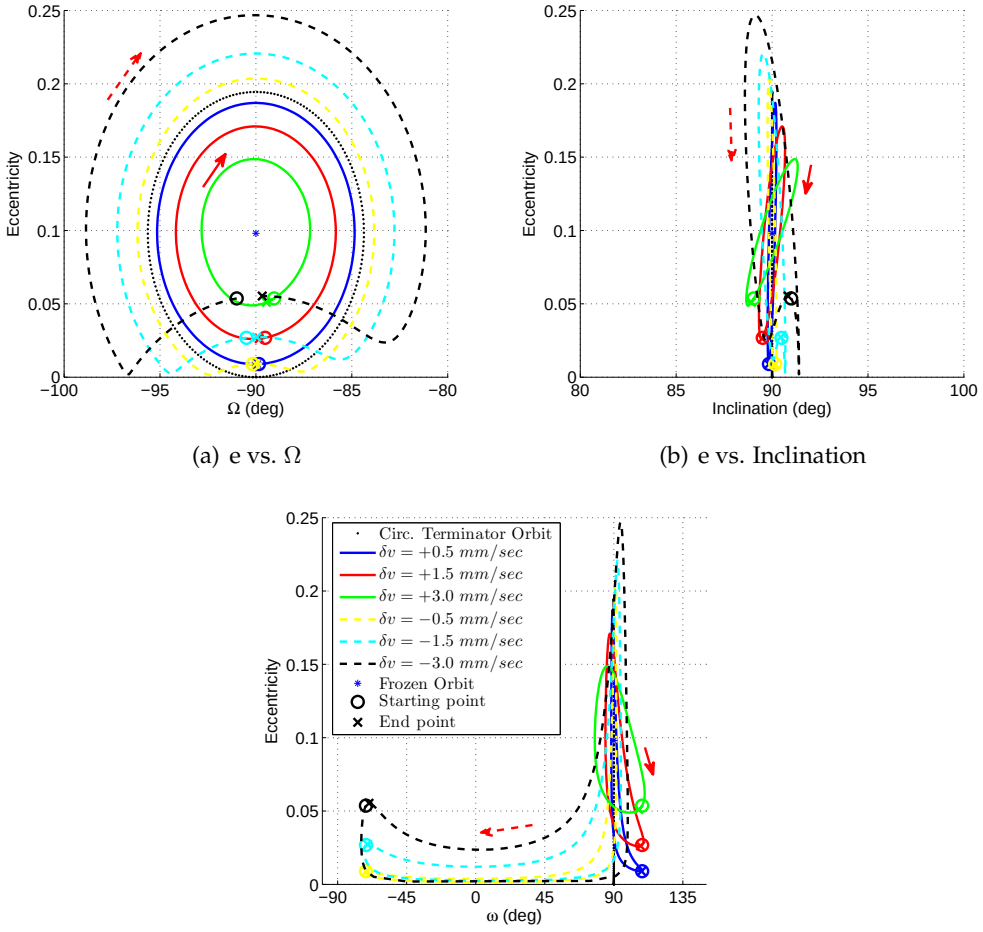

(a) e vs. Ω

(b) e vs. Inclination

(c) e vs. ω

Figure 4.8: Progression of the averaged orbit elements due to an instantaneous velocity perturbation applied at $f = 45°$. The initial orbit is a circular terminator orbit with $a_0 = 1$ km about Bennu, $\Lambda \approx 84.4°$, and $\hat{\mathbf{h}}_0 = -\hat{\mathbf{d}}$.

This is mainly attributed to an inconsistent choice of the initial condition that does not account for the short-period variations within one orbit period [77] (Ch. 6). The actual solution for osculating orbit elements $\mathbf{X}(t)$ starting from an initial condition $\mathbf{X}_0$ is given by

$$\mathbf{X}(t) = \mathbf{X}_0 + \dot{\overline{\mathbf{X}}}\, t + \mathbf{X}_p(t), \tag{4.62}$$

where $\mathbf{X}_p(t)$ it the value of the short periodic terms at time t. The secular dynamics of the orbit element $\dot{\overline{\mathbf{X}}}$ is assumed to be constant within one orbit period. Hence, the real average value of the

www.manaraa.com

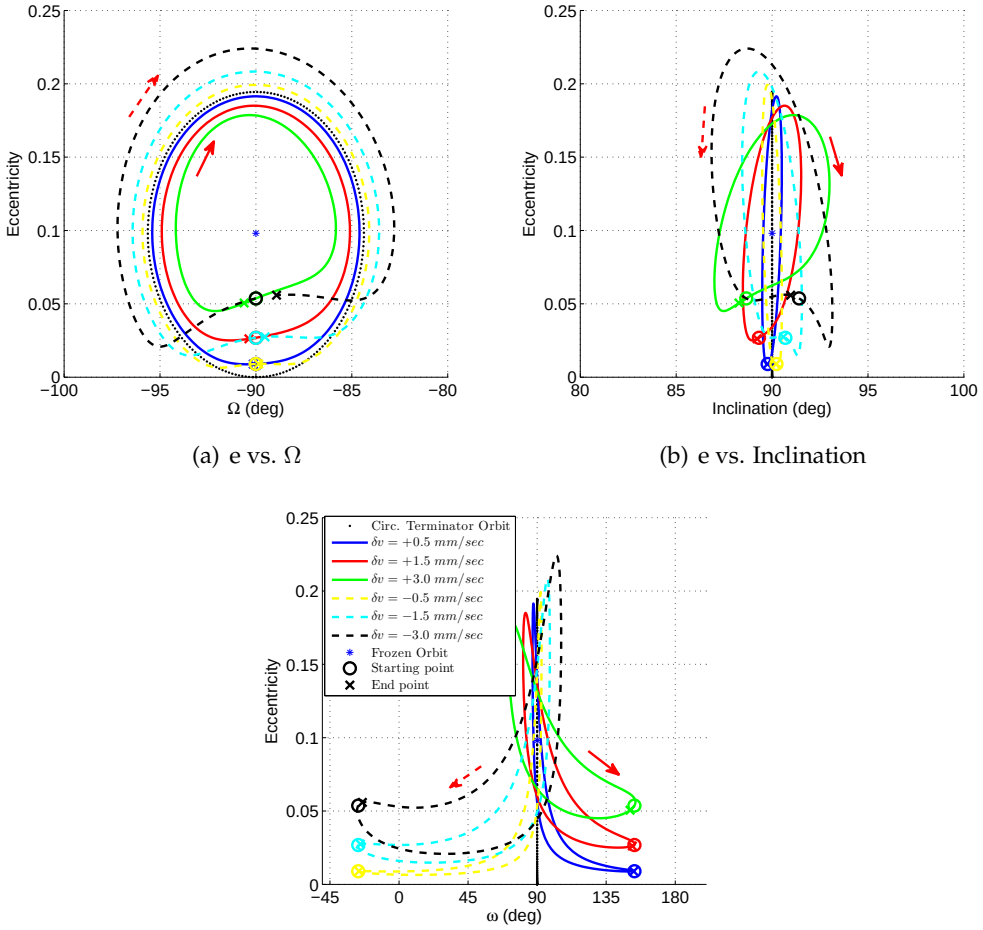

(a) e vs. Ω

(b) e vs. Inclination

(c) e vs. ω

Figure 4.9: Progression of the averaged orbit elements due to an instantaneous velocity perturbation applied at $f = 90°$. The initial orbit is a circular terminator orbit with $a_0 = 1$ km about Bennu, $\Lambda \approx 84.4°$, and $\hat{\mathbf{h}}_0 = -\hat{\mathbf{d}}$.

orbit elements over one orbit period T is given by

$$\overline{\mathbf{X}} = \mathbf{X}_0 + \frac{1}{2}\dot{\overline{\mathbf{X}}}\,T + \overline{\mathbf{X}}_p. \tag{4.63}$$

This equation shows that the real value of the osculating orbit element are offset from the secular terms and the initial condition by the amount of the averaged short-period terms. One may write the actual rate of orbit element by taking the time derivative of Eq. (4.62) to get

$$\dot{\mathbf{X}}(\mathbf{x}, t) = \dot{\overline{\mathbf{X}}}(\mathbf{x}) + \dot{\mathbf{X}}_p(t). \tag{4.64}$$

www.manaraa.com

Rearranging and solving the last equation for the short periodic term given an initial condition $\mathbf{x}_0$ results at

$$\mathbf{X}_p(t) = \int_0^t \dot{\mathbf{X}}(\mathbf{x}_0, \tau)\, \mathrm{d}\tau - \overline{\dot{\mathbf{X}}}(\mathbf{x}_0)\, t, \tag{4.65}$$

Taking the average of Eq. (4.65) and substituting it in Eq. (4.63) results in the following expression that shows the average value of the orbit elements over one orbit period.

$$\overline{\mathbf{X}} = \mathbf{X}_0 + \frac{1}{T} \int_0^T \left[\int_0^\tau \dot{\mathbf{X}}(\mathbf{x}_0, \tau')\, \mathrm{d}\tau' \right] \mathrm{d}\tau. \tag{4.66}$$

Initiating the secular dynamics with this value helps minimize the divergence issue that may exist between the secular solution of the orbit elements and the numerical propagation of the osculating elements. One may solve for the amount of the offset correction analytically by substituting the secular and osculating dynamics in Eq. (4.66) and taking the integral for one orbital period. However, here we computed this offset numerically by taking the difference between the osculating and secular solutions over one orbit period. These two methods are essentially equivalent.

Figures 4.10 and 4.11 show the evolution of the components of the orbit elements over a 20-day integration period for a frozen orbit and a circular terminator orbit about Bennu with a 1 km semi-major axis and different initial conditions. The initial heliocentric true anomaly is assumed to be $\nu_0 = 0^\circ$ as this is important to account for when comparing the secular dynamics with the numerical propagation results. More on this is discussed in the Sections 4.5 and 4.6. Note that, for these propagations, we only include a point mass asteroid gravity and a cannonball model of the SRP effect. The plots show that the solution of the secular orbit elements that are corrected for the initial offset follow the numerical integration much closer than those that start at the same initial condition as the numerical propagation. For a frozen orbit, the improvement is very clear for the first and second components of the eccentricity vector and for the first and third components of the scaled angular momentum vector. For a circular terminator orbit, the improvement is pronounced for the first and second components of the eccentricity vector and for the third component of the scaled angular momentum vector. However, also note that the amount of the correction of the

www.manaraa.com

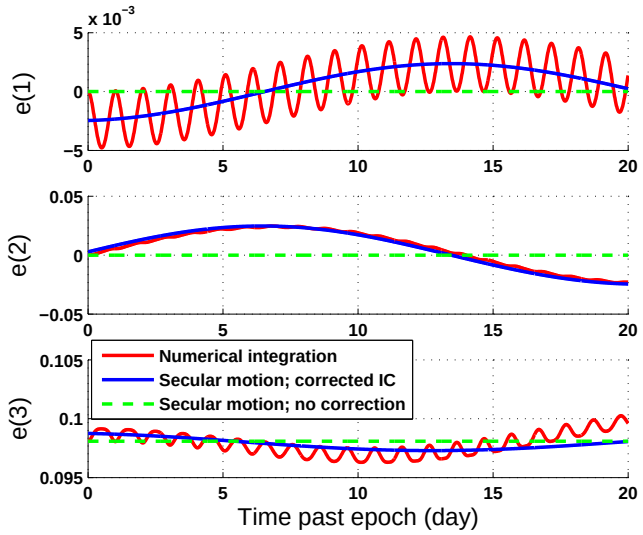

(a) Components of $\mathbf{e}$

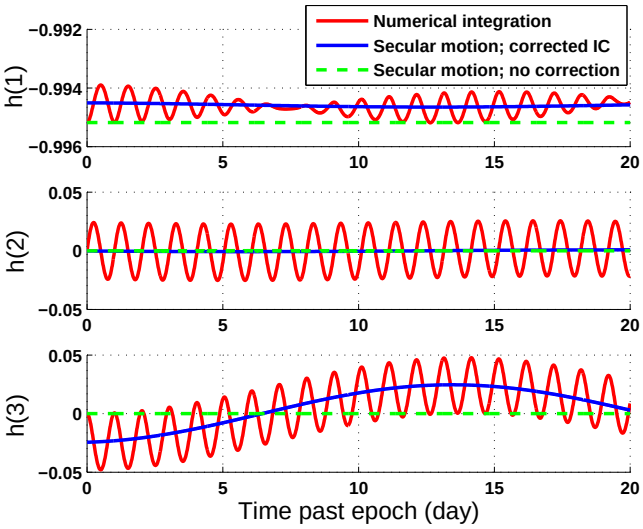

(b) Components of $\mathbf{h}$

Figure 4.10: Comparison of the numerical integration with the averaged dynamics with different initial conditions. The nominal orbit is a frozen orbit with semi-major axis of 1 km about Bennu, $\Lambda \approx 84.4°$, and $\hat{\mathbf{h}}_0 = -\hat{\mathbf{d}}$.

initial condition is fairly small in all of the orbit element components. Additionally, Figure 4.12 shows the initially circular terminator orbit in the e vs. Ω phase space. This plot shows a good agreement between the numerical integration and propagation of the secular dynamics using the same force model of point mass gravity and cannonball SRP perturbation.

www.manaraa.com

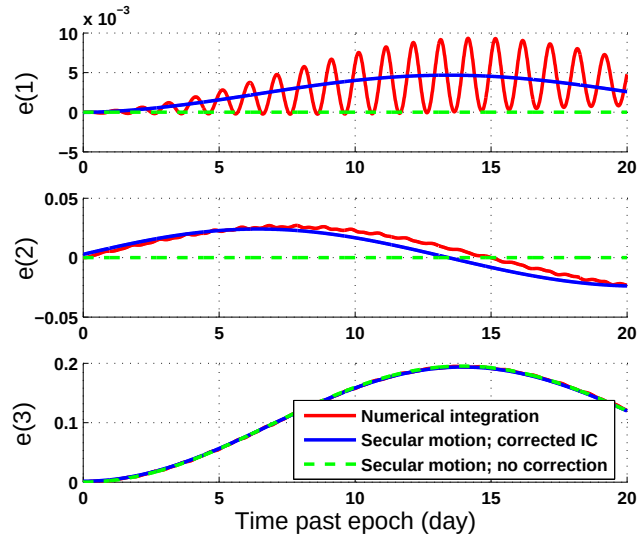

(a) Components of $\mathbf{e}$

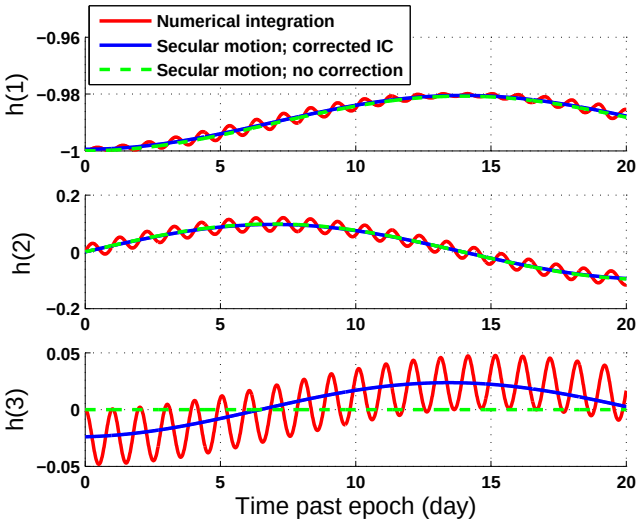

(b) Components of $\mathbf{h}$

Figure 4.11: Comparison of the numerical integration with the averaged dynamics with different initial conditions. The nominal orbit is an initially circular terminator orbit with a semi-major axis of 1 km about Bennu, $\Lambda \approx 84.4°$, and $\hat{\mathbf{h}}_0 = -\hat{\mathbf{d}}$.

4.5 Sensitivity of Terminator Orbits to De-sat Maneuver Errors

Section 4.3 discussed the formulation for the response of a sun-terminator plane orbit to a single impulsive velocity perturbation. This section evaluates the effect of several repeated velocity perturbations on a terminator orbit. This is akin to the effect that frequent maneuver errors

www.manaraa.com

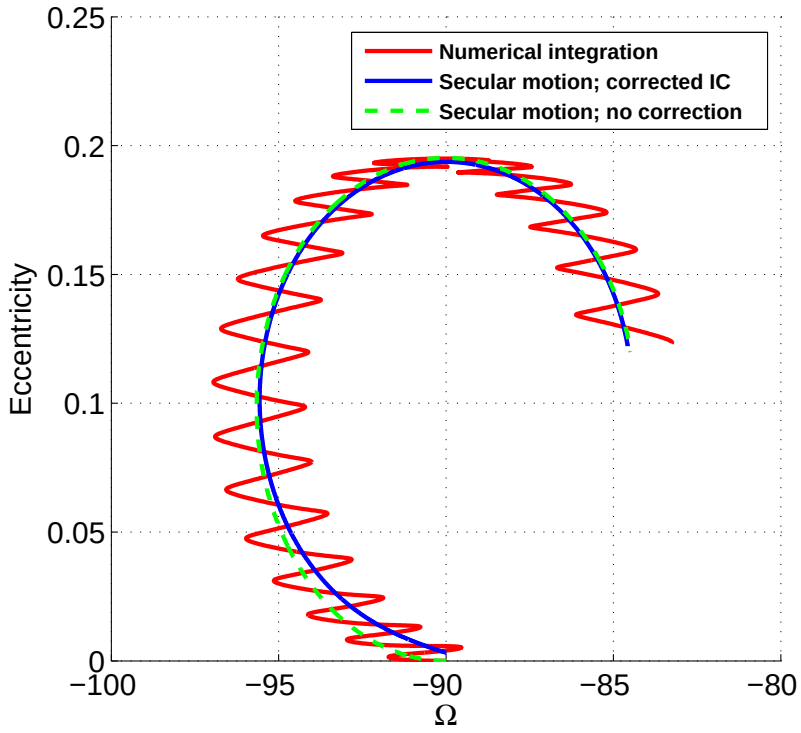

Figure 4.12: Comparison of the numerical integration with the averaged dynamics with different initial conditions. Initially circular terminator orbit about Bennu in the e vs. Ω phase space.

have on the orbit elements. Such frequent maneuver error may arise due to de-saturation (de-sat) maneuvers to dump the built-up momentum in the spacecraft reaction wheels. In the case of the OSIRIS-REx spacecraft, for instance, the spacecraft needs to perform a de-sat maneuver about once every 3 days during its science phase sun-terminator orbit. Errors in the de-sat maneuver execution impart small momentum on the spacecraft that could perturb it from its nominal orbit. This section discusses the effect that frequent de-sat maneuver errors have on the orbit elements of spacecraft around small bodies under the strong perturbation due to SRP.

4.5.1 Heliocentric True Anomaly Effects on Secular Dynamics

Before discussing the sensitivity analysis of the orbit element to de-sat maneuver errors, we should point out a nuance that differentiates the result of this section from those presented in

www.manaraa.com

Section 4.3. Eq. (4.13) defines the secular rate of orbit elements in the asteroid's heliocentric true anomaly (ν) domain. As a results, that formulation is independent of the location of the asteroid along it's orbit. However, when considering the sensitivity analysis of the orbit parameters to de-sat maneuvers that occur once every 3 days, one needs to express the solution in the time domain. Therefore, one must take into account the effect of asteroid's heliocentric rate on the orbit dynamics. The secular rate of an arbitrary orbit element "œ" in the time domain is given by $\dot{\text{œ}} = \text{œ}'\dot{\nu}$, where $\text{œ}' = \mathrm{d}\text{œ}/\mathrm{d}\nu$, i.e. the time rate of secular motion of an orbit element is directly proportional to the heliocentric rate of the asteroid in its orbit, $\dot{\nu}$.

In many cases, asteroids and comets have highly elliptical heliocentric orbits. Consequently, the heliocentric true anomaly rate of these objects varies significantly from the perihelion to the aphelion of their orbits, which in turn affects the secular rate of the orbit elements. For instance, for a 1 km sum-terminator orbit around Bennu the difference in the secular period of the orbit element from its perihelion to its aphelion could be as large as 35 days. This value is computed for an assumed spacecraft with a mass to area ratio of $62\ kg/m^2$, a surface albedo of $\rho = 0.4$, and the orbital parameters of Bennu given by Reference [15]. Using these parameters one can compute the value of the Λ parameter from Eq. (4.12) and the corresponding secular rate of the orbit elements at different epochs.

This has an important implication in analyzing effects of maneuvers on spacecraft orbit elements, since the asteroid heliocentric true anomaly dictates the rate of the orbit elements over time. We will provide further discussion on this in the following sections. At this point we provide an example that is more specific for the OSIRIS-REx mission, which helps put these findings into context. Figure 4.13 shows this example. It shows the secular period of the orbit elements at different segments of the mission timeline that are most relevant to this analyses and as a function of the heliocentric true anomaly of asteroid. The dates for the mission timeline are extracted from Reference [20]. Table 4.1 gives a brief description of each of the mission phases.

This figure shows that changes in the heliocentric rate of the asteroid has a significant effect on the secular period of orbit elements. To address this effect, we perform Monte Carlo analy-

www.manaraa.com

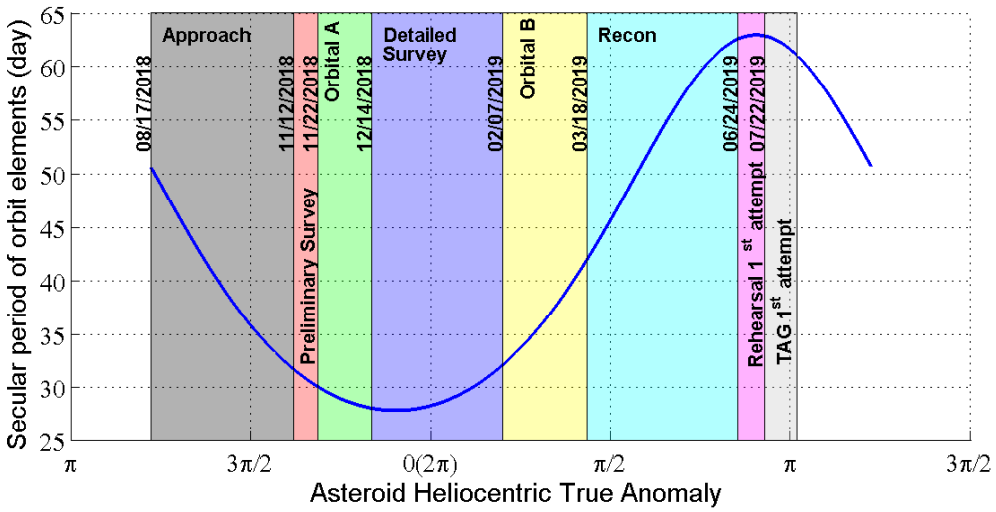

Figure 4.13: Secular period of the orbit elements at different mission phases as a function of asteroid's heliocentric true anomaly

Table 4.1: A brief description of some of the OSIRIS-REx asteroid operations phases. Adapted from "OSIRIS-REx Touch-and-go (TAG) Mission Design for Asteroid Sample Collection" by May et al., 2014, 65th International Astronautical Congress, Toronto, Canada. Copyright ©2014 by the International Astronautical Federation. IAC-14-A3.4.8

Phase	**Description**
Approach	Perform braking maneuvers; survey the Bennu orbital environment for natural satellites; collect the first resolved images
Preliminary Survey	Estimate the mass of Bennu; refine shape and spin state models
Orbital A	Demonstrate orbital flight; transition to landmark-based optical navigation
Detailed Survey	Spectrally map the entire Bennu surface; collect images and lidar data for global shape and spin state models; search for dust plumes
Orbital B	Collect lidar and radiometric data for high resolution topographic map and gravity model; observe candidate sampling sites and down–select for reconnaissance
Reconnaissance	Conduct sorties for closer look at up to 4 candidate sampling sites and select one
TAG Rehearsal	Systematically and deliberately practice steps of sample collection sequence
TAG and Sample Collection	Collect >60g of pristine bulk regolith and 26 cm^2 of surface material and stow it in the Sample Return Capsule

ses starting from the asteroid's perihelion and then compare their results with analyses that are performed at various locations on the orbit of the asteroid.

www.manaraa.com

4.5.2 Averaged Results

A set of Monte Carlo analyses are conducted to evaluate the effect of frequent de-sat maneuver errors on the evolution of terminator orbits and the growth of spacecraft state uncertainty overtime. We study this effect for both a frozen orbit as well as an initially circular terminator orbit. Errors due to the de-sat maneuvers are simulated with small impulsive velocity changes, δv, that are imparted on the spacecraft once every 3 days. The magnitudes of these δv's are sampled from a Gaussian distribution with a zero mean and a $0.5\ mm/sec$ standard deviation. The direction of the impulsive maneuvers are also generated randomly from a uniform distribution on the surface of a unit sphere. Table 4.2 summarizes the Monte Carlo study setup.

Table 4.2: Setup of the Monte Carlo analysis

Sample size:	1,000
De-sat maneuver frequency:	Once every 3 days
δv magnitude:	$\sim N(0, 0.5^2)\ mm/sec$
δv direction:	Randomized
Initial true anomaly:	0°
Central body:	Bennu
Nominal orbit semi-major axis:	$1\ km$
Nominal orbit angular momentum direction:	Pointing towards the Sun, i.e. $\hat{\mathbf{h}}_0 = -\hat{\mathbf{d}}$

For each of the Monte Carlo analysis, we use the equations derived in Section 4.3 to map the effect of an impulsive maneuvers to the averaged orbit elements. After each maneuver, Eq. (4.52) is used to map the averaged state parameters forward in time. A set of 1,000 sample points is considered for each Monte Carlo simulation. Tables 4.3 and 4.4 show a summary of the first Monte Carlo simulation results for different orbital elements and at different epochs into the simulation. Bennu is assumed to be at the perihelion of its orbit when the first de-sat maneuver is applied. Results of the first set of simulations show that the uncertainty of the orbit elements grow over time with a similar rate for both types of reference orbits. However, we also notice that the mean value of the orbit eccentricity and Ω for a frozen orbit remain unchanged, while they change significantly for an initially circular terminator orbit. These results are further confirmed by Figures 4.14

www.manaraa.com

and 4.15. These figures show the scatter plot of the averaged orbit parameters (e vs. Ω and e vs. i) at different epochs for a frozen orbit and an initially circular terminator orbit. Eq. (4.10) is used to computed the desired orbital elements at different epochs of the simulation. These figures also show the $3-\sigma$ uncertainty ellipse of the orbital elements at various epochs. One thing to note regarding Figures 4.14 and 4.15 and the other similar ones that follow is that from the perspective shown in these plots the uncertainty ellipse does not capture the dispersion of the points at $e = 0$. This is not due to any non-linearity in the dynamics at this point and is merely due to the fact that the eccentricity vector is not well defined at points close to $e = 0$. Since the eccentricity is always a non-negative value, the points simply fold back from the $e = 0$ line while the uncertainty ellipse does not capture this. Comparing the simulation results between the two types of orbits, it is

Table 4.3: Orbit element statistics for a frozen orbit at asteroid's perihelion; mean $\pm$ standard deviation

$\sigma_{\delta \mathbf{v}} = 0.5$ (mm/sec)	e	Ω (deg)	i (deg)	
Days after epoch	0.098	-90.00	90.00	$\Leftarrow$ Nominal
3	0.098 ± 0.007	-89.99 ± 0.34	90.01 ± 0.15	
7	0.098 ± 0.010	-90.01 ± 0.68	90.02 ± 0.30	
10	0.098 ± 0.012	-90.02 ± 0.79	90.03 ± 0.35	
28	0.099 ± 0.019	-89.95 ± 1.18	89.98 ± 0.58	

Table 4.4: Orbit element statistics for an initially circular terminator orbit at asteroid's perihelion; mean $\pm$ standard deviation

$\sigma_{\delta \mathbf{v}} = 0.5$ (mm/sec)	e	Ω (deg)	i (deg)	
Days after epoch	$0.00 - 0.20$	-90.00 ± 5.60	90.00	$\Leftarrow$ Nominal
3	0.022 ± 0.006	-93.52 ± 0.34	89.99 ± 0.14	
7	0.099 ± 0.011	-95.62 ± 0.67	90.00 ± 0.29	
10	0.159 ± 0.012	-94.36 ± 0.82	89.99 ± 0.34	
28	0.019 ± 0.012	-89.62 ± 1.20	89.98 ± 0.57	

clear that the uncertainty of the orbital elements (size of the uncertainty ellipses) grows over time with a similar rate for both the circular terminator and the frozen orbits. Furthermore, the results show that the orbit elements of a frozen orbit remain fixed about their nominal value. For a circular terminator orbit, however, the averaged orbit eccentricity and the longitude of ascending node,

www.manaraa.com

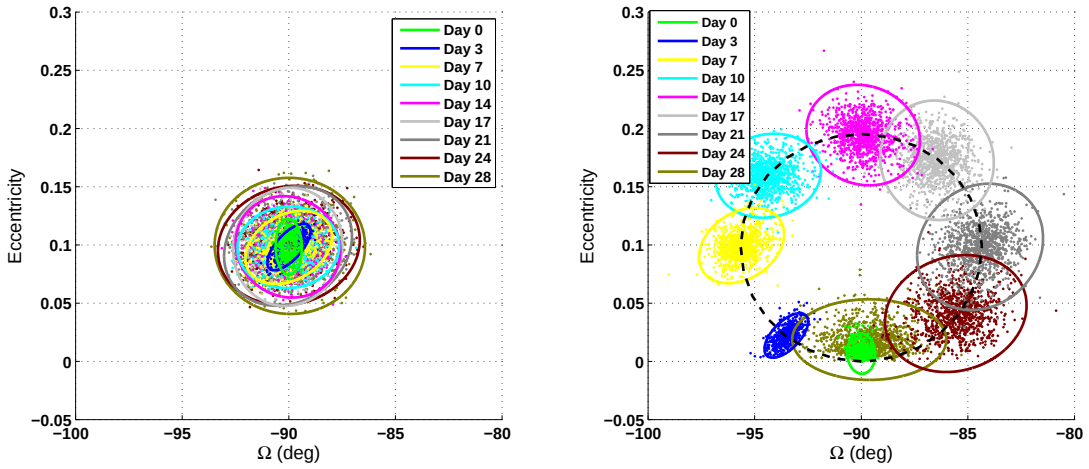

(a) Frozen Terminator Orbit

(b) Initially Circular Terminator Orbit

Figure 4.14: Monte Carlo analysis results for the distribution of the averaged orbit eccentricity vs. the longitude of the accenting node over time. The initial orbit has a semi-major axis of 1 km, $\Lambda \approx 84.4°$, and $\hat{\mathbf{h}}_0 = -\hat{\mathbf{d}}$. Bennu is assumed to be at its perihelion at t = 0.

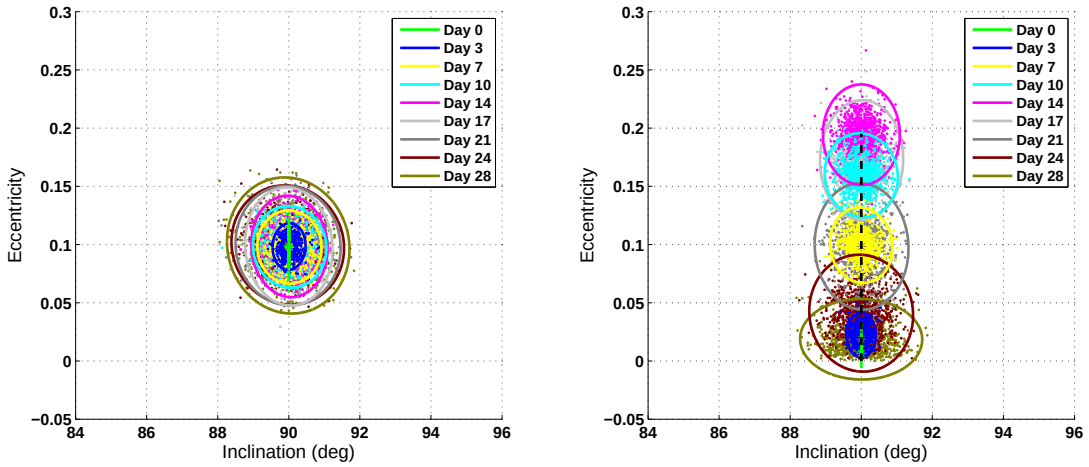

(a) Frozen Terminator Orbit

(b) Initially Circular Terminator Orbit

Figure 4.15: Monte Carlo analysis results for the distribution of the averaged orbit eccentricity vs. inclination over time. The initial orbit has a semi-major axis of 1 km, $\Lambda \approx 84.4°$, and $\hat{\mathbf{h}}_0 = -\hat{\mathbf{d}}$. Bennu is assumed to be at its perihelion at t = 0.

Ω, change by a large amount as the orbit migrates from its initial condition. The averaged inclination value of the circular terminator orbit remains about the nominal value without large changes in its mean value. Changes in the mean value of the orbit eccentricity and Ω for an initially circu-

www.manaraa.com

lar terminator orbit is further shown in Figure 4.17. This figure shows the histogram of the orbit elements generated from the Monte Carlo simulation results. This figure shows that the change in the mean value of the orbit eccentricity ranges from 0 to 0.2, the mean value of the Ω varies up to 12° over time. The mean value of these parameters are fixed about their nominal values for the case of a frozen orbit as shown by Figure 4.16. The results from the first simulation show that

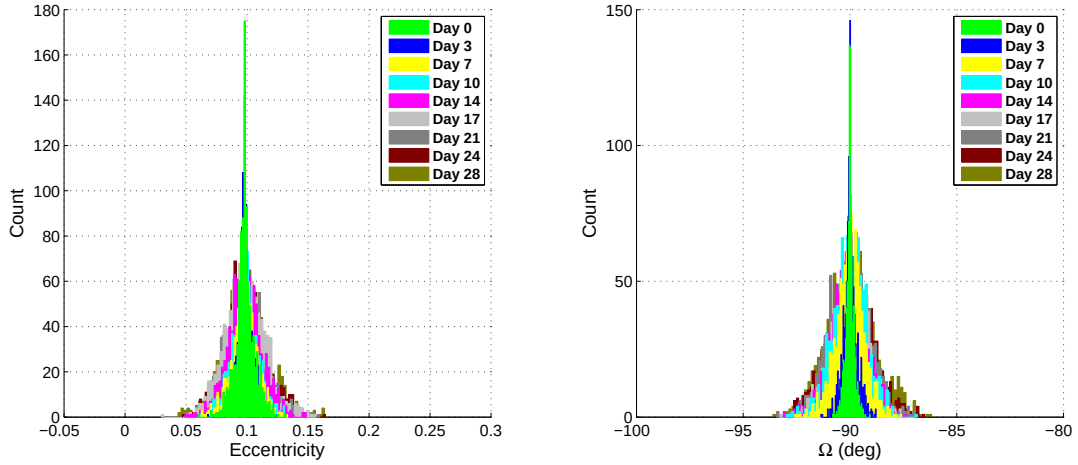

(a) Histogram of the averaged eccentricity

(b) Histogram of the averaged Ω

Figure 4.16: Histogram of the averaged orbit eccentricity and longitude of the ascending node, Ω for a frozen terminator orbit. The initial orbit has a semi-major axis of 1 km, $\Lambda \approx 84.4^\circ$, and $\hat{\mathbf{h}}_0 = -\hat{\mathbf{d}}$. Bennu is assumed to be at its perihelion at t = 0.

a frozen terminator orbit is more robust against the maneuver execution errors compared to an initially circular terminator orbit of the same size. This has an important mission design and planning implication. The significant motion of a circular terminator orbit in the eccentricity and Ω phase space results in added complications to the mission planning and maneuver execution. For instance, if the execution of a planned maneuver is delayed by a day or two, the current maneuver plan will not be valid anymore and the maneuver parameters have to be redesigned to take into account the changes in the orbit parameters that take place over the time that the plan it delayed. This task is simpler to perform around a frozen orbit by comparison since the orbit parameters of a frozen terminator orbit, on average, remain very close to their nominal values over time.

The first Monte Carlo simulation looks at the case where the asteroid is assumed to be at its

www.manaraa.com

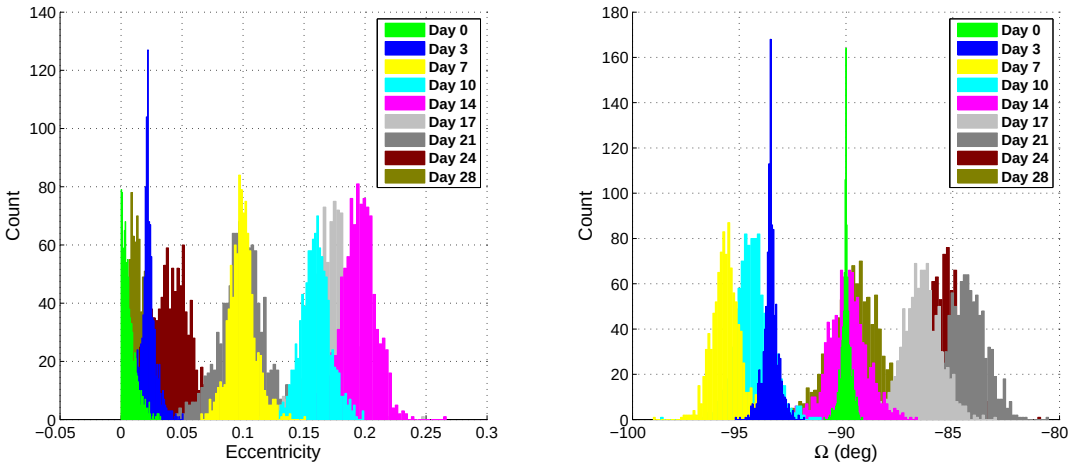

(a) Histogram of the averaged eccentricity

(b) Histogram of the averaged Ω

Figure 4.17: Histogram of the averaged orbit eccentricity and longitude of the ascending node, Ω for an initially circular terminator orbit. The initial orbit has a semi-major axis of 1 km, $\Lambda \approx 84.4°$, and $\hat{\mathbf{h}}_0 = -\hat{\mathbf{d}}$. Bennu is assumed to be at its perihelion at t = 0.

perihelion at the simulation epoch. As mentioned earlier, the secular period of the orbit elements, in the time domain, is a function of the asteroid's heliocentric true anomaly rate. This does not have much impact on the results for a frozen orbit, since all of the sample cases in the simulation tend to remain fixed about the nominal values of the orbit elements. However, the difference will be more clear for an initially circular terminator orbit since orbit elements migrate between a wide range of extreme values. To see how this effects our results, we repeat the Monte Carlo simulation for the cases when the heliocentric true anomaly of the asteroid is equal to $90°$ and $180°$ at the time the simulation epoch. All of the other simulation settings are kept unchanged. Figure 4.18 show the orbit eccentricity vs. Ω scatter plot snapshots for two simulation cases. The secular period of the orbit elements is longer when the asteroid is at a true anomaly of $90°$ and more so when it is at its aphelion compared to the case when the asteroid is at its perihelion. As a result, a 28-day period is too short for the secular motion of the orbit elements to make a full cycle. This is clear from the plots in Figure 4.18. After 28 days the orbit elements end up at very different spots in the eccentricity vs. Ω phase space that is dictated by the heliocentric true anomaly of the asteroid. Table 4.5 further summarizes the statistics of the orbit elements after 28 days of simulation with

www.manaraa.com

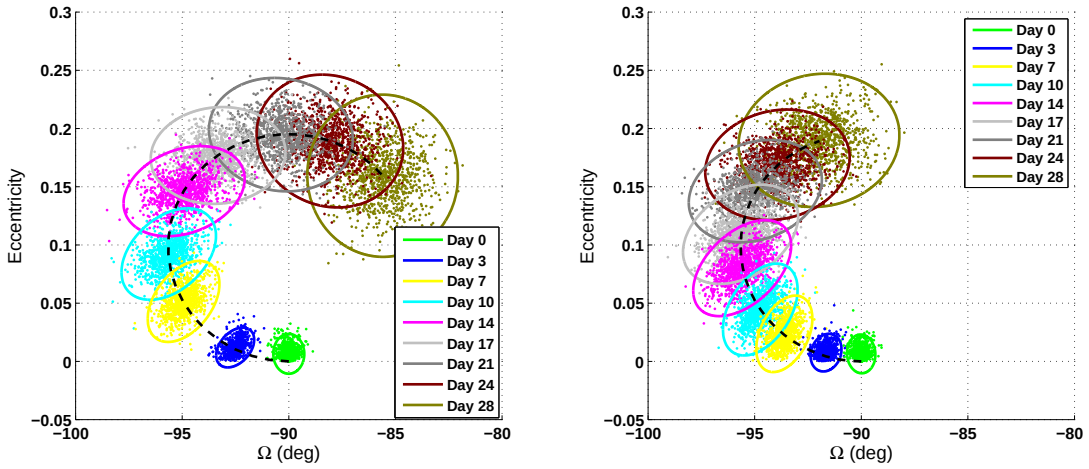

(a) Heliocentric $\nu = 90°$ (b) Heliocentric $\nu = 180°$

Figure 4.18: Monte Carlo analysis results for the distribution of the averaged orbit eccentricity vs. the longitude of the accenting node over time. Initial orbit is an initially circular terminator orbit with a semi-major axis of 1 km, $\Lambda \approx 84.4°$, and $\hat{\mathbf{h}}_0 = -\hat{\mathbf{d}}$. Bennu is assumed to be at a heliocentric true anomaly of $90°$ and $180°$.

respect to the asteroid's heliocentric true anomaly. As shown in this table, after the same amount of the time past the simulation epoch, the mean value and the uncertainty of the orbit eccentricity vary significantly as a function of the asteroid heliocentric true anomaly. The mean value of Ω also varies. However, the mean value of the orbit inclination and the uncertainty of the orbit Ω and inclination are not affected as a result of changes in the heliocentric true anomaly of the asteroid.

Table 4.5: Orbit element statistics vs. heliocentric true anomaly after 28 days; mean $\pm$ standard deviation

Heliocentric true anomaly	e	Ω (deg)	i (deg)
$0°$	0.019 ± 0.012	-89.62 ± 1.20	89.99 ± 0.57
$90°$	0.159 ± 0.023	-85.59 ± 1.18	89.97 ± 0.51
$180°$	0.190 ± 0.019	-91.98 ± 1.26	90.01 ± 0.57

www.manaraa.com

4.5.3 Numerical Results

Simulations discussed in Section 4.5.2 looked at the effect of the maneuver execution errors on the averaged orbit elements. Note that we have a simple point-mass gravity field for propagating the secular dynamics. As a final analysis, we look at the effect of random de-sat maneuvers on the osculating orbit elements by including a high fidelity force model. The Monte Carlo simulation uses the same setup given in Table 4.2. The force model used in the numerical propagation includes the point mass gravitational attraction of Bennu, a 16×16 spherical harmonic gravitational model of the asteroid generated from a constant density polyhedron model [64], solar radiation pressure based on a cannonball model, and the gravitational attraction of the Sun. The simulation epoch is chosen to be Jan. 9, 2019 14:37:8.488 TDB when Bennu is at its perihelion[5] . Hence, the results may be compared directly to the those given in the first Monte Carlo simulation run in Section 4.5.2. The force model setup is summarized in Table 4.6. Figures 4.19 and 4.20 show the results of the Monte Carlo study based on the numerical propagation of the orbits. There is, in general, a good agreement between the results given by the analytical secular equations of motion and the results given by the numerical propagations of the orbit. The most pronounced difference between the secular and numerical results is seen in the scatter plots of the orbit eccentricity vs. inclination. Numerical results in Figure 4.20 show that the orbit inclination changes by up to 5° (on average) over the course of the simulation for both types of the nominal orbit configurations. However, this is not the case for the results given by the analytical simulations, where the inclination is constant on average. (see Figure 4.15). This difference comes from the perturbing effect of the non-spherical gravitation (the J_2 effect) of the asteroid as it couples with the SRP effect to change the inclination of the orbit over time. References [77] (Ch. 14) and [73] study this effect in further details.

[5] Queried from the JPL Solar System Dynamics web interface @ http://ssd.jpl.nasa.gov/horizons.cgi

www.manaraa.com

Table 4.6: Force model summary for the numerical Monte Carlo simulation

Planetary Ephemeris:	DE431
Simulation Epoch:	2019-Jan-9 14:37:8.488 TDB
Force Model	
Central Body:	Bennu ($\mu = 5.2\ m^3/s^2$) [15]
Gravitational Perturbations:	16×16 spherical harmonic model (*Generated from a polyhedron model with a bulk density of* $1,260\ kg/m^3$.) [64]
Third body:	Sun (point mass)
Solar Radiation Pressure:	Cannonball model

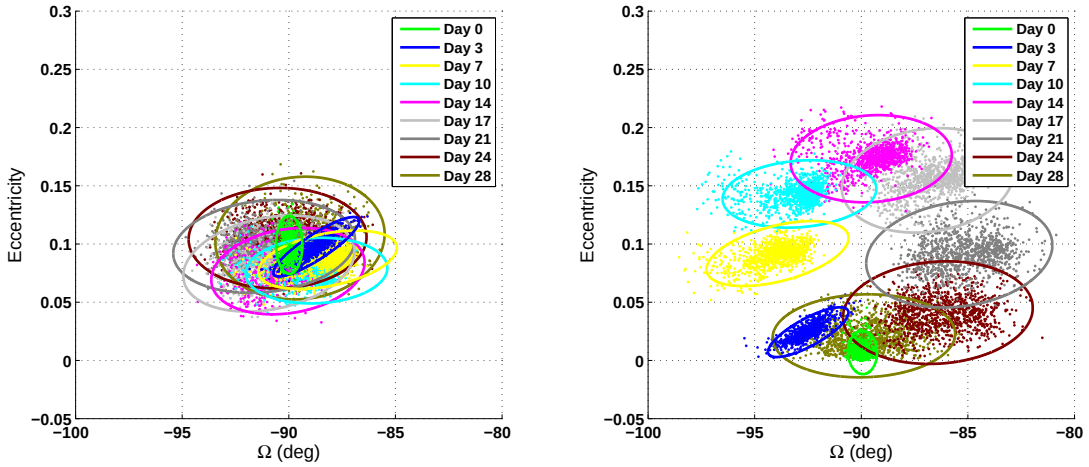

(a) Frozen Terminator Orbit

(b) Initially Circular Terminator Orbit

Figure 4.19: Orbit eccentricity vs. Ω scatter plots from the Monte Carlo simulation results based on the numerical analysis. The initial orbit has a semi-major axis of 1 km, $\Lambda \approx 84.4°$, and $\hat{\mathbf{h}}_0 = -\hat{\mathbf{d}}$.

4.6 Sensitivity of Terminator Orbits to Targeting Maneuver Errors

Section 4.5 provides a comprehensive analysis on the sensitivity of sun-terminator orbit elements to de-sat maneuver uncertainties. However, we are also interested in analyzing the sensitivity of sun-terminator orbits to targeting maneuver errors. Unlike the de-sat maneuvers, targeting maneuvers are not frequent and are performed to insert the spacecraft into an specific orbit configurations or to correct an existing orbit. For instance, during the OSIRIS-REx science phase, the mission team will target a circular terminator orbit before performing many of the critical maneuvers such as the TAG departure or TAG rehearsal maneuvers. To do this, the mission team will

www.manaraa.com

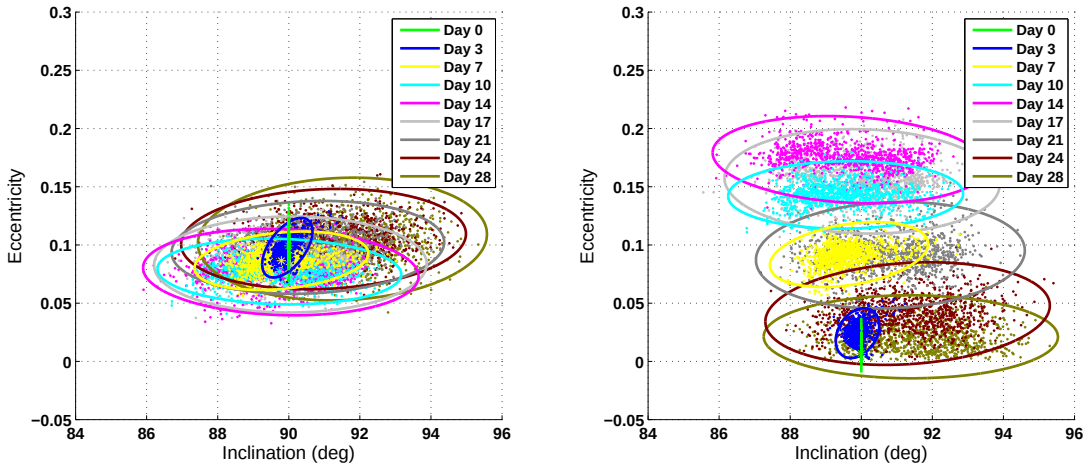

(a) Frozen Terminator Orbit

(b) Initially Circular Terminator Orbit

Figure 4.20: Orbit eccentricity vs. inclination scatter plots from the Monte Carlo simulation results based on the numerical analysis. The initial orbit has a semi-major axis of 1 km, $\Lambda \approx 84.4°$, and $\hat{\mathbf{h}}_0 = -\hat{\mathbf{d}}$.

perform a targeting maneuver several days (about two weeks) prior to the actual maneuver epoch in order to target a circular terminator orbit configuration. However, errors in the execution of the targeting maneuvers increase the uncertainty of the final target state and degrade the accuracy of achieving the desired target state. In this section we aim to quantify the uncertainty of the targeted state due to errors in the targeting maneuver execution and analyze the sensitivity of the targeted orbit parameters to such errors.

4.6.1 Formulation of the Targeting Problem

The target maneuver is assumed to be an impulsive burn. There are two strategies to target a circular orbit that lies on the terminator orbit, at a desired epoch. First, the target maneuver may insert the spacecraft into a trajectory that naturally evolves into a circular terminator configuration within the desired time span. Another strategy may target the final target state (after a desired time span) to be in the circular terminator orbit configuration without following the natural evolution of an initially circular terminator orbit. In this study we focus on the first strategy where the spacecraft is injected into a trajectory that naturally evolves into a circular terminator

www.manaraa.com

configuration within the desired time span. The desired final state $\mathbf{X}_f$ may be written as

$$\mathbf{X}_f = \begin{bmatrix} [0]_{3\times 1} \\ \pm\hat{\mathbf{d}} \end{bmatrix}. \tag{4.67}$$

One can compute the initial state $\mathbf{X}_{t_m}^+$ (post targeting maneuver) that leads to the desired final state, by propagating the evolution of a circular terminator orbit backwards in time. In this work we study the secular dynamics of the orbits elements. Hence, once may use the state transition matrix (see Eq. (4.16)) to map the state backwards in time. This is done using the following equation

$$\mathbf{X}_{t_m}^+ = \Phi^{-1}(\Delta\psi)\,\mathbf{X}_f, \tag{4.68}$$

where $\Delta\psi = \psi_f - \psi_{t_m}$ is the amount of time between the targeting maneuver and the target epoch. To study the sensitivity of the target state to maneuver errors, we expand the solution about the reference circular terminator orbit and analyze the perturbed trajectories due to small errors in the targeting maneuver. This process is shown pictorially in Figure 4.21 where the blue curve represents the reference trajectory that follows the natural evolution of an initially circular terminator orbit that arrives at a circular terminator configuration at a desired epoch. The targeting maneuver aims to place the spacecraft onto this trajectory. Due to the execution errors, however, the spacecraft is placed on a perturbed trajectory that is represented by the red trajectory in Figure 4.21, which does not hit the desired state.

With the assumption that the error in the targeting maneuver is small compared to the magnitude of the actual maneuver (e.g. errors on the order of 10% $3-\sigma$ are expected from the OSIRIS-REx spacecraft), the induced error in the initial state may be approximated to the first order by the following equation

$$\delta\mathbf{X}_{t_m} = \left.\frac{\partial\mathbf{X}}{\partial\mathbf{v}}\right|_{t_m} \cdot\ \delta\mathbf{v}_{t_m}. \tag{4.69}$$

Note that the Jacobian $\partial\mathbf{X}/\partial\mathbf{v}$ is evaluated at the time of the maneuver. The error in the state parameters at the time of the maneuver is mapped to the final epoch using the state transition

www.manaraa.com

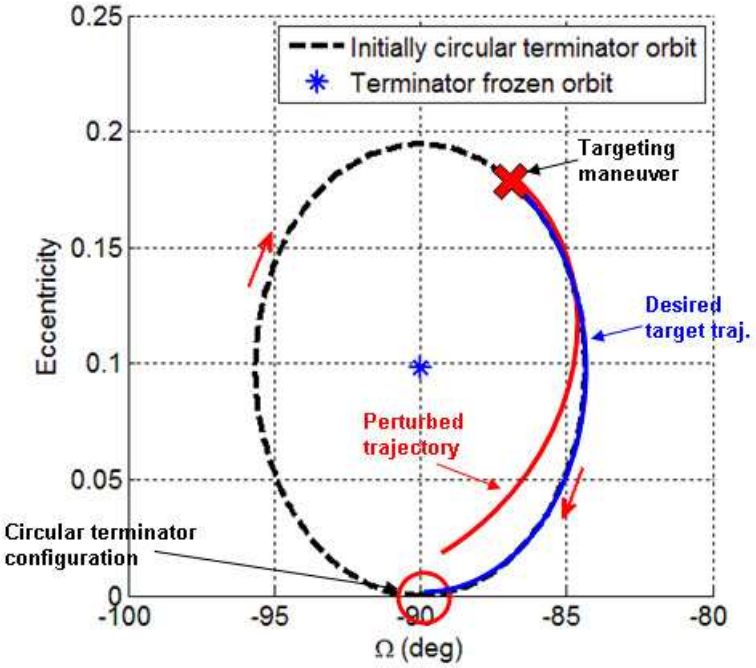

Figure 4.21: Schematic representation of targeting a circular terminator orbit.

matrix Φ following the equation below

$$\delta\mathbf{X}(\psi_f) = \Phi(\Delta\psi)\,\delta\mathbf{X}_{t_m}. \tag{4.70}$$

Hence, the final perturbed state is given by

$$\mathbf{X}(\psi_f) = \mathbf{X}_f + \Psi\,\delta\mathbf{X}(\psi_f). \tag{4.71}$$

where Ψ is used to re-normalize the state parameters after changes in the semi-major axis of the orbit due to the target maneuver error. This parameter is given by

$$\Psi = \begin{bmatrix} 1 & 0 \\ 0 & \sqrt{\dfrac{a^-}{a^+}} \end{bmatrix}. \tag{4.72}$$

Parameters a^- and a^+ are the semi-major axes of the orbit for the nominal trajectory and the perturbed trajectory, respectively. The semi-major axis of the perturbed trajectory is given by

$$a^+ = a^- + \delta a_{tm}, \tag{4.73}$$

www.manaraa.com

where δa_{tm} is the change in the semi-major axis as a result of the target maneuver error. This value is computed by substituting the radial and in-track components of the targeting maneuver error in Eq. (4.36).

4.6.2 Derivation of the Perturbed Trajectories

The targeted state is a circular terminator orbit configuration with $\mathbf{h}_f = \pm\hat{\mathbf{d}}$ ($\Omega_f = \pm 90^\circ$ & $i_f = 90^\circ$) and $e_f = 0$. This condition occurs periodically along the natural evolution of an initially circular terminator orbit at $\psi = 2k\pi$, where k is an integer. Using Eq. (4.68) to propagate the final state backward in time to the maneuver epoch results at the state elements at the time of the maneuver that is given by

$$\begin{aligned} \mathbf{e}_{tm} &= \mp(1-\cos\psi_{tm})\sin\Lambda\cos\Lambda\,\hat{\mathbf{z}}, \\ \mathbf{h}_{tm} &= \pm\left(1-\cos^2\Lambda(1-\cos\psi_{tm})\right)\,\hat{\mathbf{d}} \mp \sin\psi_{tm}\cos\Lambda\,\hat{\mathbf{y}}. \end{aligned} \tag{4.74}$$

Note that the expression above is equivalent to evaluating Eq. (4.29) at $\psi = \psi_{tm}$. This is trivial to show noting that the general solution of the nominal circular terminator orbit is periodic in ψ with a period of 2π and that $\Delta\psi = 2\pi - \psi_{tm}$. We can now expand the Eq. (4.69) by evaluating the partial derivative of the state elements with respect to the targeting maneuver error at the time of the maneuver. Details of the derivation of the partial derivatives are provided in Appendix C. Following this step, one can use Eq. (4.70) and (4.71) to derive the evolution of the perturbed trajectory due to an error in the targeting maneuver.

Let us now consider an example of targeting a circular terminator orbit with a semi-major of 1 km around Bennu. In this example we assume that a targeting maneuver is applied 14 days prior to the targeted epoch, when the desired state is reached. The error in the target maneuver is assumed to be 1 mm/sec in all three radial, in-track, and cross-track directions. Figure 4.22 shows the evolution of the averaged orbit parameters as a result of the targeting maneuver error. Asteroid is assumed to be located at its perihelion at the time of the maneuver for this figure. Figure 4.23 shows the same for a case where the asteroid is located at its aphelion at the time of the maneuver. Both figures show a locus of the starting and ending points of the perturbed trajectories

www.manaraa.com

as a function of the targeting maneuver true anomaly as well as the direction of maneuver error. These plots show that the true anomaly at which the target maneuver is applied has a significant effect on the error in the longitude of the ascending node and the inclination of the targeted orbit. The magnitude of the eccentricity error, however, is not affected by changes in the true anomaly of the targeting maneuver.

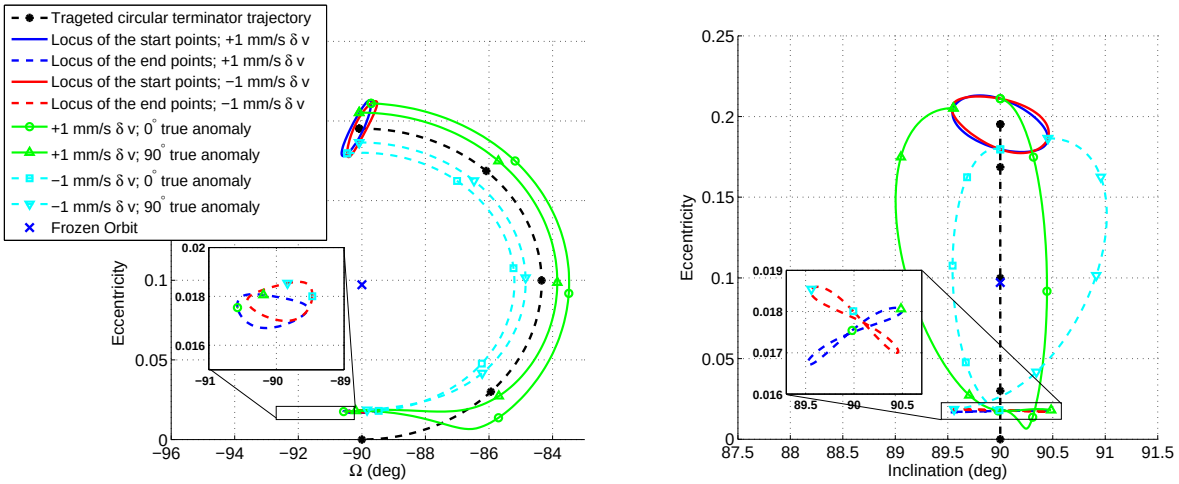

(a) e vs. Ω

(b) e vs. Inclination

Figure 4.22: Progression of the perturbed trajectories as a result of a targeting maneuver error. Target orbit is a circular terminator orbit about Bennu with a 1 km semi-major axis and angular momentum facing the sun. Asteroid is assumed to be at its perihelion.

As it was detailed in section 4.5.1, the secular rate of the orbit elements is directly proportional to the rate of the asteroid's heliocentric true anomaly. As a result, for a time span of 14 days, the amount of the motion of the averaged orbit elements is much larger when the asteroid is at its perihelion vs. when it is at its aphelion. Hence, the range of motion of the orbit parameters in Figure 4.22 is larger than that in Figure 4.23. In addition, these figures show that the heliocentric true anomaly of the asteroid at the time of the maneuver has a significant effect on the magnitude of the error in the targeted orbit elements. An important implication of this finding is that for a same amount of target maneuver error, one should expect different levels of target state accuracy as a function of the date and time that the target maneuver is applied.

www.manaraa.com

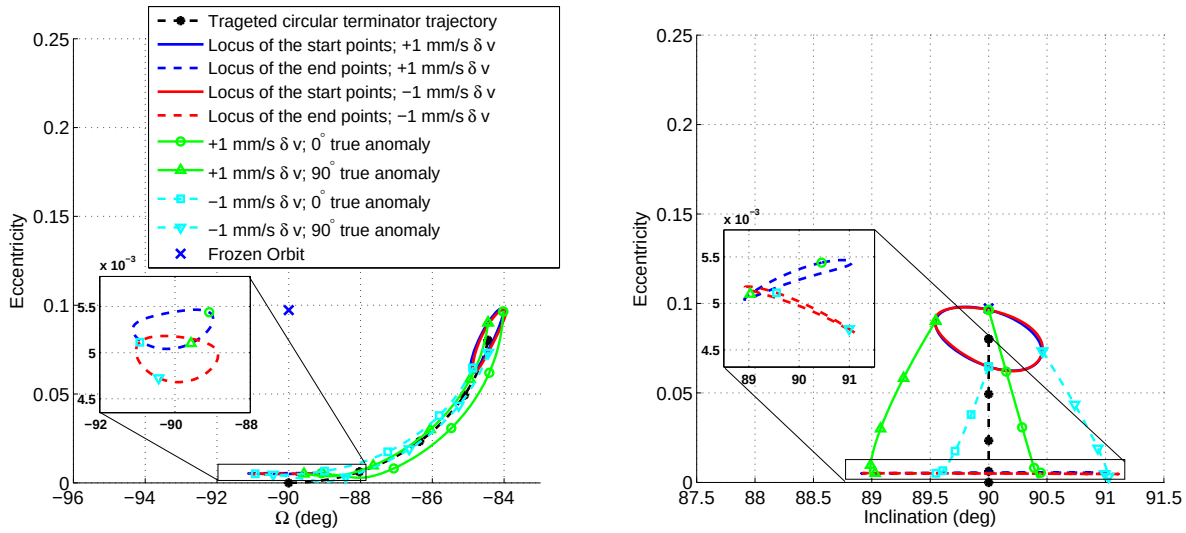

(a) e vs. Ω

(b) e vs. Inclination

Figure 4.23: Progression of the perturbed trajectories as a result of a targeting maneuver error. Target orbit is a circular terminator orbit about Bennu with a 1 km semi-major axis and angular momentum facing the sun. Asteroid is assumed to be at its aphelion.

4.6.3 Monte Carlo Analysis for Targeting a Circular Terminator Orbit

Previous section discussed the effects of targeting maneuver errors in a deterministic sense. This section evaluates the uncertainty of the targeted orbit parameters as a result of the uncertainty in the target maneuvers, via a Monte Carlo analysis. Once again, we consider targeting a circular terminator orbit configuration about Bennu. A set of 1,000 simulations is considered. In each case, a target maneuver error is applied to a nominal trajectory 14 days prior to the desired target epoch, when the target state is reached. The nominal trajectory is a trajectory of an initially circular terminator orbit with a semi-major axis of 1 km and an angular momentum vector that faces towards the Sun. For each simulation case the magnitude of the target maneuver error was generated randomly from a Gaussian distribution with a zero mean and 1 mm/sec standard deviation. The direction of the maneuver error is also generated randomly following a uniform distribution on the surface of a unit sphere. First, the Monte Carlo analysis was performed without the presence of de-sat maneuver errors in order to strictly evaluate the effect of the uncertainty of a target maneuver error on the precision of the targeted orbit parameters. Next, we repeat the same set of the

www.manaraa.com

Monte Carlo runs with including de-sat maneuver errors. For the second set of the Monte Carlo simulations the de-sat maneuver errors are injected into the perturbed trajectories once every 3 days. The de-sat maneuver errors are generated with a magnitude drawn from a Gaussian distribution with 0 mean and 0.5 mm/sec standard deviation and a randomized direction. Table 4.7 summarizes the setup of the Monte Carlo simulations.

Table 4.7: Setup of the Monte Carlo analysis

Sample size:	1,000
Target maneuver error magnitude:	$\sim N(0,1)\ mm/sec$
Target maneuver error direction:	Randomized
Initial true anomaly:	0° & 90°
Nominal orbit semi-major axis:	$1\ km$
Nominal orbit angular momentum direction:	Pointing towards the Sun, i.e. $\hat{\mathbf{h}}_0 = -\hat{\mathbf{d}}$
De-sat maneuver frequency (when included):	Once every 3 days
De-sat maneuver error magnitude:	$\sim N(0, 0.5^2)\ mm/sec$
De-sat maneuver error direction:	Randomized

Figures 4.24 and 4.25 show scatter plots of the orbit elements as a results of a target maneuver error applied at the heliocentric true anomaly of $\nu_0 = 0^\circ$ (asteroid's perihelion) and an initial spacecraft orbit true anomaly of $f_0 = 0^\circ$ and $f_0 = 90^\circ$, respectively. Figures 4.26 and 4.27 show the similar results for the cases that we include randomized de-sat maneuver errors once every 3 days as well. The secular period of the orbit elements at the perihelion is in the order of 28 days (refer to Figure 4.13). As a result, for these simulations, a 14 day period between applying the target maneuver and the targeted state epoch accounts for almost half of the secular period of the orbit parameters. Comparing the results from the simulations with and without the de-sat maneuvers show that including the de-sat maneuver errors simply increases the uncertainty of the targeted orbit parameters. This is also shown in Table 4.8. The results further show that target maneuver's true anomaly has a significant effect on the uncertainty of the targeted Ω and inclination without affecting the accuracy of these target parameters. There is a non-zero error on the targeted mean eccentricity with or without including the de-sat maneuvers. Furthermore, target maneuver's true anomaly does not show a significant effect on the accuracy and the uncertainty

www.manaraa.com

of the targeted eccentricity.

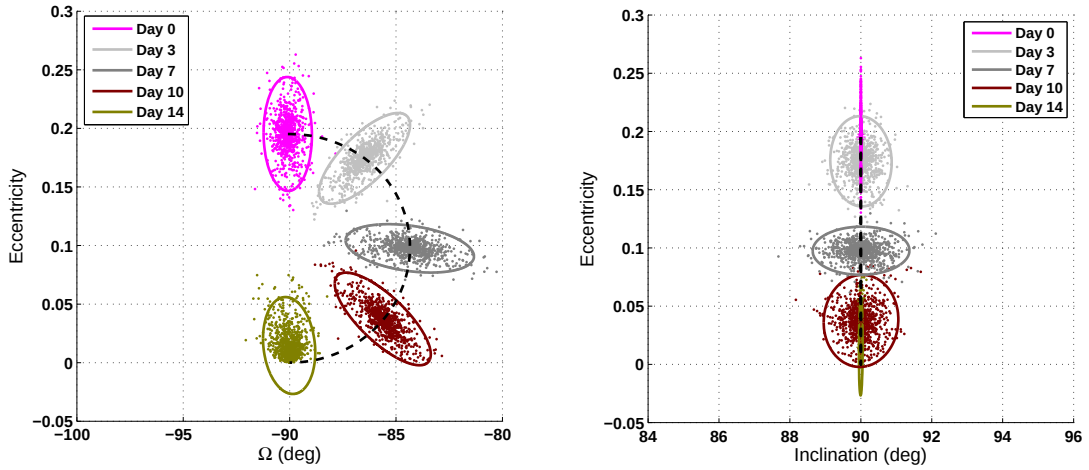

(a) e vs. Ω (b) e vs. Inclination

Figure 4.24: Monte Carlo analysis results for the distribution of the targeted orbit elements over time. Targeted orbit is a circular terminator orbit with a semi-major axis of 1 km, $\Lambda \approx 84.4°$, and $\hat{\mathbf{h}}_0 = -\hat{\mathbf{d}}$. Target maneuver is applied at the orbit true anomaly of $0°$. De-sat maneuver errors are not included. Bennu is assumed to be at its perihelion at t = 0.

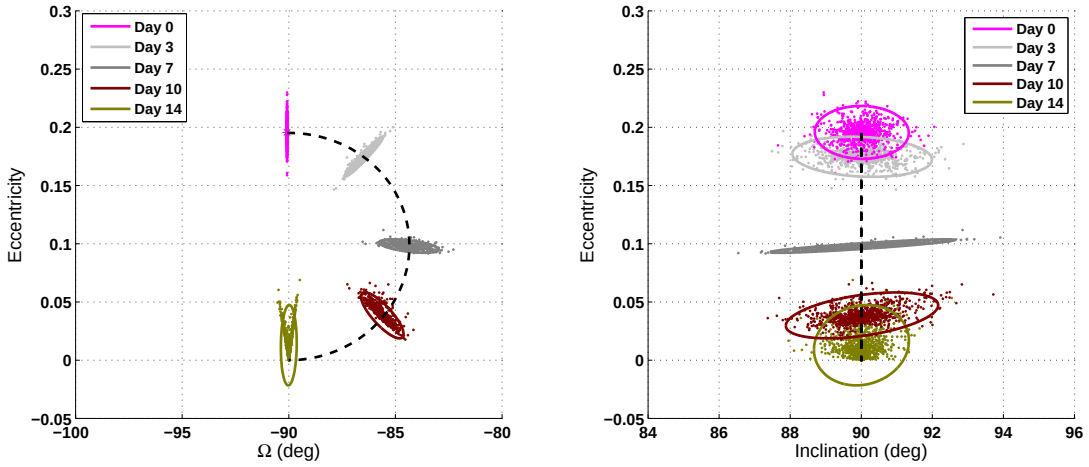

(a) e vs. Ω (b) e vs. Inclination

Figure 4.25: Monte Carlo results for the distribution of the targeted orbit elements over time. Targeted orbit is a circular terminator orbit about Bennu with a semi-major axis of 1 km, $\Lambda \approx 84.4°$, and $\hat{\mathbf{h}}_0 = -\hat{\mathbf{d}}$. Target maneuver is applied at the orbit true anomaly of $90°$. De-sat maneuver errors are not included. Bennu is assumed to be at its perihelion at t = 0.

www.manaraa.com

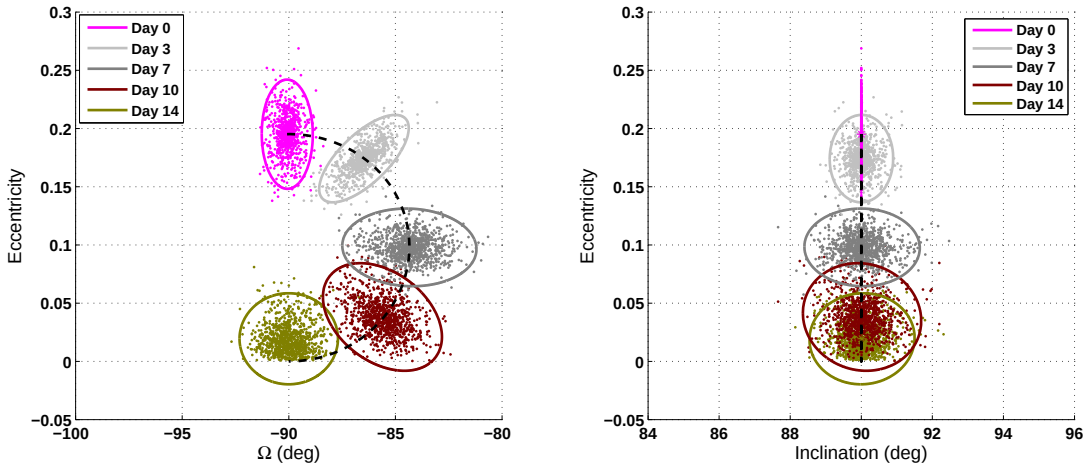

(a) e vs. Ω (b) e vs. Inclination

Figure 4.26: Monte Carlo results for the distribution of the targeted orbit elements over time. Targeted orbit is a circular terminator orbit about Bennu with a semi-major axis of 1 km, $\Lambda \approx 84.4°$, and $\hat{\mathbf{h}}_0 = -\hat{\mathbf{d}}$. Target maneuver is applied at the orbit true anomaly of $0°$. De-sat maneuver errors are applied once every 3 days. Bennu is assumed to be at its perihelion at t = 0.

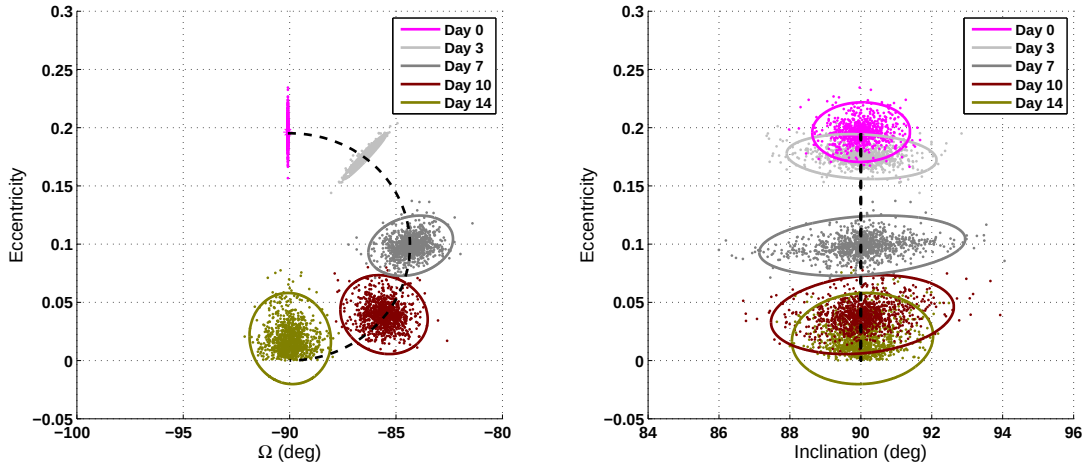

(a) e vs. Ω (b) e vs. Inclination

Figure 4.27: Monte Carlo results for the distribution of the targeted orbit elements over time. Targeted orbit is a circular terminator orbit about Bennu with a semi-major axis of 1 km, $\Lambda \approx 84.4°$, and $\hat{\mathbf{h}}_0 = -\hat{\mathbf{d}}$. Target maneuver is applied at the orbit true anomaly of $90°$. De-sat maneuver errors are applied once every 3 days. Bennu is assumed to be at its perihelion at t = 0.

Further Monte Carlo simulations are performed to evaluate the effect of asteroid's true anomaly on the errors of the targeted orbit parameters. Table 4.9 summarizes the results of two

www.manaraa.com

Table 4.8: Target orbit element statistics after 14 days; mean $\pm$ standard deviation

Targeting Maneuver true anomaly	e	Ω (deg)	i (deg)	
	0	-90.00	90.00	$\Leftarrow$ Target values
0°	0.015 ± 0.014	-90.02 ± 0.41	90.00 ± 0.02	Without De-sat
90°	0.013 ± 0.012	-90.00 ± 0.13	90.01 ± 0.45	
0°	0.019 ± 0.013	-90.00 ± 0.77	90.02 ± 0.49	With De-sat
90°	0.019 ± 0.013	-89.97 ± 0.69	90.05 ± 0.66	

sets of simulations where the target maneuver is applied in the asteroid's perihelion and aphelion. These results show the asteroid's heliocentric true anomaly, in general, has a significant effect on the accuracy and the uncertainty of the averaged targeted orbit elements. The difference is further clear when we compare the results shown in Figure 4.24 to those shown in Figure 4.28. Once again, the very important implication of the these results is that keeping all of the target maneuver parameters fixed, one might expect to see different targeting performances by changing the actual date (corresponding to different heliocentric true anomalies of the asteroid) of applying the target maneuver.

Table 4.9: Target orbit element statistics vs. heliocentric true anomaly

Heliocentric true anomaly	e	Ω (deg)	i (deg)	
	0	-90.00	90.00	$\Leftarrow$ Target values
0°	0.015 ± 0.014	-90.02 ± 0.41	90.00 ± 0.02	Without De-sat
180°	0.005 ± 0.005	-89.97 ± 0.86	89.99 ± 0.45	

4.7 Chapter Summary

This chapter presents a comprehensive sensitivity analysis of the sun-terminator orbits around small bodies to maneuver execution errors and uncertainties. Understanding the complex dynamical environment around a small body under a strong SRP perturbation is key to accurate modeling of spacecraft orbit and the precise propagation of the orbit uncertainties over time.

The chapter presents a background on the formulation of the secular dynamics of orbit ele-

www.manaraa.com

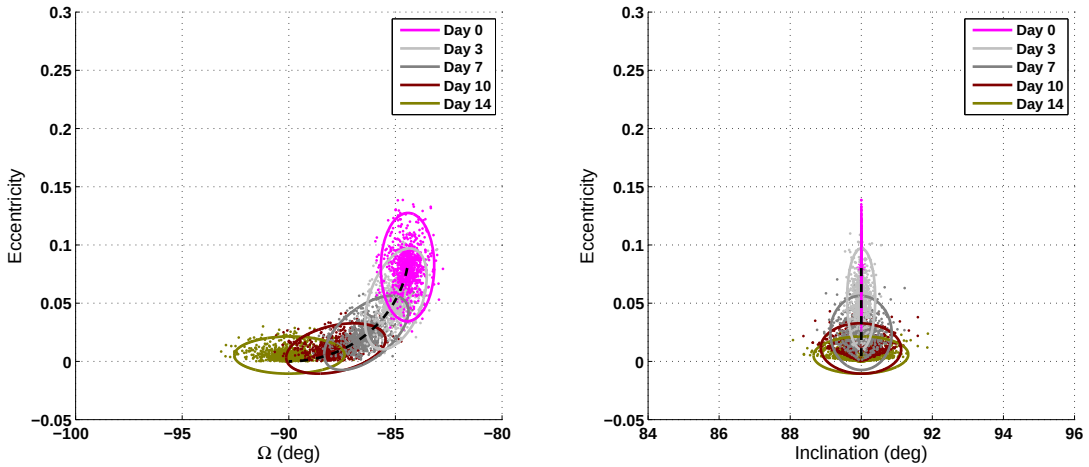

(a) e vs. Ω (b) e vs. Inclination

Figure 4.28: Monte Carlo analysis results for the distribution of the targeted orbit elements over time. Targeted orbit is a circular terminator orbit about Bennu with a semi-major axis of 1 km, $\Lambda \approx 84.4°$, and $\hat{\mathbf{h}}_0 = -\hat{\mathbf{d}}$. Target maneuver is applied at the orbit true anomaly of $0°$. De-sat maneuver errors are not included. Bennu is assumed to be at its aphelion at t = 0.

ments in an environment with a strong SRP perturbation. Based on this formulation, we present a set of special orbit configurations that exist in such strongly perturbed environment about a small body. Sun-terminator orbits are a family of these special solutions that are of particular interest to small body orbiting missions, such as the OSIRIS-REx mission. After a short discussion on some of the characteristics of these orbits, the chapter proceeds to study the response of an initially circular terminator orbit as well as a frozen terminator orbit to small maneuver execution errors. First, we derive a set of analytical equations that describe the secular motion of orbital elements due to a single maneuver error. The formulation shows that the secular motion of orbital elements of a perturbed terminator orbit may be represented by simple closed form solutions, to the first order. The motion of a perturbed terminator orbit is shown to follow complex, yet periodic, patterns with the amplitude of the deviation directly related to the magnitude of maneuver errors. The study also shows that, in general, a frozen terminator orbit is less sensitive to a small maneuver error compared to a circular terminator orbit of the same size.

After studying the effect of a single maneuver error, we evaluate the sensitivity of the frozen

www.manaraa.com

and circular terminator orbits to multiple frequent maneuver errors. Such frequent errors may represent errors due to the reaction wheel de-sat maneuvers. De-sat maneuvers occur frequently during time that a spacecraft is in orbit and they impart a small random velocity change on the spacecraft. A Monte Carlo analysis is implemented to simulate the effect of frequent de-sat maneuver errors on terminator orbits. The results of the Monte Carlo study shows that the uncertainty of orbital elements for both a circular terminator orbit as well as a frozen terminator orbit grows over time with a similar rate in both cases. However, a frozen terminator orbit is found to be more robust against small maneuver errors. The eccentricity and the longitude of the ascending node, Ω, for a circular terminator orbit are found to be affected the most. The change in the average value of the eccentricity of a circular terminator orbit ranges from $0 - 0.2$ due to a de-sat maneuver uncertainty of $0.5\ mm/sec$ that happens once every 3 days. The value of Ω for a circular terminator orbit changes by up to 12° over time. Such significant changes in the orbital parameters of a circular terminator orbit may impose added level of complexity to the planning and execution of mission events such as surface imaging or TAG maneuvers.

It is further shown that the asteroid's heliocentric true anomaly has a significant effect on the Monte Carlo simulation results. This is due to the fact that the secular rate of orbit elements is directly proportional to the heliocentric rate of the true anomaly of the asteroid. This is particularly important when studying the uncertainty of the targeted orbit elements due to errors in targeting maneuvers. Monte Carlo simulations show that with the same amount of error in a targeting maneuver, one should expect different levels of achieved uncertainty of the targeted orbit elements solely due to the changes in asteroid's heliocentric true anomaly. These simulations also show that the true anomaly of a spacecraft, at which the targeting maneuver is applied, has a significant effect on the amount of error on the targeted orbit Ω and inclination. The error in the targeted orbit eccentricity is mainly affected by the direction and the magnitude of the targeting maneuver error rather than its location along the orbit.

Finally, the results of averaged Monte Carlo analyses are tested against results from numerical analyses and good agreements are found between the analytical and numerical results.

www.manaraa.com

Although, the Monte Carlo simulations in this chapter focus on terminator orbits around Bennu, the analytical derivations and the conclusions of this study may be extrapolated to terminator orbits about other small bodies.

www.manaraa.com

Chapter 5

A Precise Solar/Thermal Radiation Pressure Model

While the cannonball model is a good method to get an overall understanding of SRP effects on the orbit dynamics of LAGEOS-type satellites [46], it is generally not sufficient for high fidelity representation of the force imparted on spacecraft with complex shapes. Other methods are developed for accurate representation of SRP effects on spacecraft. For instance, an empirical method is used to precisely model SRP effects on satellites in the global positioning system (GPS) constellation by fitting GPS measurements to their orbits [4, 83]. One may extrapolate such empirical methods to other satellites with repeatable shapes and surface properties that fly in a relatively well characterized orbital environment around the Earth. However, these methods are not suitable for spacecraft with unique shapes and surface properties orbiting in less well understood dynamical environments, such as those around small bodies. Other models may use a numerical method that takes into account a detailed shape model of a spacecraft to compute the interaction of the sunlight with every surface element on the spacecraft [49, 52, 72]. While such complex methods may be able to accurately represent the perturbing effects of the SRP on spacecraft, they are computationally expensive and, in general, not suitable for the purpose of orbit determination.

A Fourier series expansion of the SRP force was introduced by Scheeres (2007) [79] to model the dynamical evolution of asteroids' motion subject to the YORP effect [67]. McMahon and Scheeres (2010) [55], further expanded the use of this model to represent SRP effects on spacecraft. They derived analytical expressions that govern the secular effects of the SRP on Earth orbiting satellites and also utilized a Fourier series expansion of the SRP force to perform navigation of

www.manaraa.com

GPS type satellites. They also used this model to perform precise orbit determination of a simulated geosynchronous transfer orbit and a spacecraft in an orbit about a near-Earth asteroid [56]. Others have used this model to perform orbit determination of interplanetary spacecraft[41, 50] or study the evolution of the rotational sate of space debris and defunct satellites due to the YORP effect [2, 1, 3].

In this chapter, we use a Fourier representation of the SRP to derive analytical solutions that govern the secular dynamics of orbital elements as a function of the Fourier coefficients. We then identify a set of Fourier coefficients that have the largest contribution in modeling the SRP effect and its uncertainty. Following that, we use the OSIRIS-REx spacecraft as an example application for the implementation of the model. A set of error analyses are carried out to evaluate the sensitivity of the Fourier coefficient on various errors, such as the spacecraft attitude errors or spacecraft surface optical properties errors. We further evaluate the amount of the expected level of orbit propagation error as a function of errors in each one the coefficients. Finally, this method is expanded to derive a precise model of the TRP effect on a spacecraft orbiting at a close distance from a small body.

5.1 Formulation of the SRP Fourier Series Model

In this section we discuss a Fourier series expansion that is used to represent the force that is imparted on spacecraft due to SRP. First, we review the formulation of the model in a more general sense before applying it to the OSIRIS-REx spacecraft example.

5.1.1 SRP Fourier Series Expansion

The force imparted on spacecraft by the solar radiation pressure may be expressed using a Fourier series expansion that is given by

$$\mathbf{F}^b_{SRP} = P(R) \sum_{n=0}^{\infty} \left[\mathbf{A}_n(\delta_s) \cos(n\lambda_s) + \mathbf{B}_n(\delta_s) \sin(n\lambda_s) \right], \tag{5.1}$$

www.manaraa.com

where δ_s is the latitude, and λ_s is the longitude of the sunlight in a specified reference frame [55]. In general, it is preferred to compute this force in the spacecraft body-fixed coordinate frame, as denoted by the b superscript on the SRP force vector. Hence, the Fourier coefficients $\mathbf{A}_n(\delta_s)$ and $\mathbf{B}_n(\delta_s)$ are vectors of 3 components expressed in this frame. We use the unbolded notation $A_n(i)$ to refer to the i^{th} component of the $\mathbf{A}_n$ coefficient. The Fourier coefficients defined in the spacecraft body-fixed frame are time invariant functions of the solar latitude. These coefficients may be computed from a given shape model of a spacecraft and its corresponding surface properties. They are given by

$$\mathbf{A}_0 = \frac{1}{2\pi}\int_0^{2\pi} \frac{\mathbf{F}^b_{SRP}}{P(R)}\, d\lambda_s,$$

$$\mathbf{A}_n = \frac{1}{\pi}\int_0^{2\pi} \frac{\mathbf{F}^b_{SRP}}{P(R)} \cos(n\lambda_s)\, d\lambda_s, \text{ and} \tag{5.2}$$

$$\mathbf{B}_n = \frac{1}{\pi}\int_0^{2\pi} \frac{\mathbf{F}^b_{SRP}}{P(R)} \sin(n\lambda_s)\, d\lambda_s,$$

where $\mathbf{F}^b_{SRP}$ may be computed by the sum effect of the individual forces acting on each surface element. Eq. (3.10) provides the expression for this. The SRP acceleration is simply given by

$$\mathbf{a}^b_{SRP} = \frac{P(R)}{m_{sc}} \sum_{n=0}^{\infty} \left[\mathbf{A}_n(\delta_s)\cos(n\lambda_s) + \mathbf{B}_n(\delta_s)\sin(n\lambda_s)\right], \tag{5.3}$$

where m_{sc} is the mass of the spacecraft.

While the spacecraft body-fixed frame is the preferred reference frame for this formulation, it is not a suitable reference frame for many of the analyses involving orbit elements of the spacecraft and spacecraft navigation. For instance, an inertial reference frame is normally used to perform spacecraft orbit determination. In general, one may use a mapping matrix Ψ to map the SRP acceleration from the spacecraft body-fixed frame to another reference frame. The mapping expression is given by

$$\mathbf{a}_{SRP} = \Psi \mathbf{a}^b_{SRP}, \tag{5.4}$$

www.manaraa.com

where the actual form of the matrix Ψ depends on the frame of choice that $\mathbf{a}_{SRP}$ is expressed in.

5.1.2 Generalized SRP Fourier Series Expansion

Previous section discussed a Fourier series expansion of the SRP force as a function of the solar latitude and longitude in the spacecraft body-fixed frame. However, to study SRP effects on the orbit of a spacecraft we need to related this expression to a set of orbit parameters. To make such a connection, we choose the rotating frame $\widehat{\mathbf{pqh}}$ that is defined in Section 2.4. Recall that this frame rotates with the spacecraft as the spacecraft moves along the orbit. In the nadir-pointing attitude profile the spacecraft also performs a rotation about its $\hat{\mathbf{z}}_b$ axis such that one side of the spacecraft (the science instruments side) is always pointing to the astroid. As a result, the sun-line rotates in a retrograde fashion about the 3^{rd} axis in the rotating frame at the same rate as the spacecraft true anomaly. In other words, the solar longitude measured in the rotating frame is given by

$$\lambda_s = \lambda_{s_0} - f, \tag{5.5}$$

where λ_{s_0} is an initial value for the solar longitude that depends on the alignment of the spacecraft body-fixed frame with respect to the rotating frame at time $t = 0$. We may rewrite Eq. 5.3 by substituting in Eq. (5.5) to get

$$\mathbf{a}^r_{SRP} = \frac{P(R)}{m} \sum_{n=0}^{\infty} \left[\mathbf{A}_n \cos(n\lambda_{s_0} - nf) + \mathbf{B}_n \sin(n\lambda_{s_0} - nf) \right]. \tag{5.6}$$

The *sine* and *cosine* functions in this expression may be expanded to derive a generalized Fourier expansion [79] as a function of f. That is

$$\mathbf{a}^r_{SRP} = \frac{P(R)}{m} \sum_{n=0}^{\infty} \left[\mathbf{A}'_n \cos(nf) + \mathbf{B}'_n \sin(nf) \right], \tag{5.7}$$

where the generalized SRP Fourier coefficients are given by

$$\begin{aligned} \mathbf{A}'_n &= \cos(n\lambda_{s_0})\mathbf{A}_n + \sin(n\lambda_{s_0})\mathbf{B}_n, \\ \mathbf{B}'_n &= \sin(n\lambda_{s_0})\mathbf{A}_n - \cos(n\lambda_{s_0})\mathbf{B}_n. \end{aligned} \tag{5.8}$$

www.manaraa.com

Note that the $\mathbf{B}'_n$ coefficient, as defined here, is equal to the negative of that given in Reference [79]. We choose to do this so that Eq. (5.7) is consistent with Eq. (5.3). One may also express the SRP acceleration and the corresponding Fourier coefficients in the orbit frame $\widehat{\mathbf{ee}_\perp \mathbf{h}}$. It turns out that the derivation of the secular effects of SRP on an orbit is simpler in this frame. A rotation matrix is used to map the rotating frame to the orbit frame, i.e.

$$\mathbf{a}_{SRP} = \frac{P(R)}{m} \sum_{n=0}^{\infty} \left[[ROT3(-f)]\, \mathbf{A}'_n \cos(nf) - [ROT3(-f)]\, \mathbf{B}'_n \sin(nf) \right]. \tag{5.9}$$

where $[ROT3(-f)]$ is a simple rotation about the third axis by the amount of $-f$ degrees. By distributing the rotation matrix inside the Fourier expansion we can define a new expansion for which the coefficients are expressed in the orbit frame. The resulting expansion is given by

$$\mathbf{a}_{SRP} = \frac{P(R)}{m} \sum_{n=0}^{\infty} \left[\mathbf{A}''_n \cos(nf) + \mathbf{B}''_n \sin(nf) \right]. \tag{5.10}$$

where $\mathbf{A}''_n$ and $\mathbf{B}''_n$ coefficients are expressed in the orbit frame. The relationship between the single primed and the double primed coefficients may be derived by carrying out the matrix multiplication in Eq. (5.9) and taking advantage of the half angle trigonometric identities to regroup the relevant terms. These relationships are detailed in Reference [55]. Here we present these expressions without the detail on the derivation of them. They are

$$\mathbf{A}''_0 = \frac{1}{2} \begin{bmatrix} A'_1(1) - B'_1(2) \\ A'_1(2) + B'_1(1) \\ 2A'_0(3) \end{bmatrix}, \tag{5.11}$$

$$\mathbf{A}''_1 = \frac{1}{2} \begin{bmatrix} 2A'_0(1) + A'_2(1) - B'_2(2) \\ 2A'_0(2) + A'_2(2) + B'_2(1) \\ 2A'_1(3) \end{bmatrix}, \tag{5.12}$$

$$\mathbf{B}''_1 = \frac{1}{2} \begin{bmatrix} -2A'_0(2) + A'_2(2) + B'_2(1) \\ 2A'_0(1) - A'_2(1) + B'_2(2) \\ 2B'_1(3) \end{bmatrix}, \tag{5.13}$$

www.manaraa.com

$$\mathbf{A}''_n = \frac{1}{2}\begin{bmatrix} A'_{n-1}(1) + A'_{n+1}(1) + B'_{n-1}(2) - B'_{n+1}(2) \\ A'_{n-1}(2) + A'_{n+1}(2) - B'_{n-1}(1) + B'_{n+1}(1) \\ 2A'_n(3) \end{bmatrix}, \text{ and} \tag{5.14}$$

$$\mathbf{B}''_1 = \frac{1}{2}\begin{bmatrix} -A'_{n-1}(2) + A'_{n+1}(2) + B'_{n-1}(1) + B'_{n+1}(1) \\ A'_{n-1}(1) - A'_{n+1}(1) + B'_{n-1}(2) + B'_{n+1}(2) \\ 2B'_n(3) \end{bmatrix}. \tag{5.15}$$

5.2 Secular Dynamics due to the SRP Fourier Series Model

We are interested in identifying a set of SRP Fourier coefficients that have the most impact on the secular dynamics of the orbit of a spacecraft. Due to their secular effects, small errors in such coefficients can lead to large deviations in a spacecraft trajectory. On the other hand, by precisely estimating the dominant coefficients one may be able to minimize the rate at which a spacecraft trajectory error grows over time. To do so, we average the dynamics of an orbit over one orbital period. The averaging procedure is detailed in section 2.3. This derivation is worked out for three attitude profiles of a spacecraft that are most relevant to an small body orbiter, namely the nadir-pointing, the Sun-pointing, and the Earth-pointing attitudes.

According to Eq. (2.10), one may derive the average of an orbit element at any of the mean anomaly, eccentric anomaly, or true anomaly domains. Depending on the nature of the problem on hand, one formulation may be preferred over the others. For instance, for a circular or close to a circular orbit one may use the mean anomaly domain to derive the secular dynamics [54]. There are other instances that using an eccentric anomaly domain may be more suitable for this derivation [33]. In this work, we use the true anomaly domain to perform the averaging derivations. We prefer to use the true anomaly domain, since it does not lose its physical connection with the spacecraft state for highly eccentric orbits. The other two domains, on the other hand, loose their physical meaning with respect to the spacecraft location along the orbit as the orbit becomes more eccentric. This is important, since spacecraft orbits around small bodies could evolve to highly eccentric ones as a result of the SRP perturbation (as discussed in section 4.1).

www.manaraa.com

5.2.1 Secular Dynamics for the Nadir-pointing Attitude Profile

Once again, consider the set of three orbital elements that were discussed in chapter 4, namely the eccentricity vector $\mathbf{e}$, the angular momentum vector $\mathbf{H}$, and the orbit specific energy $\mathscr{E}$. These elements are defined in Eq. (4.1). The time derivative of the orbit elements due to a perturbing force is expressed by Gauss' equations and are given by Eq. 4.6. We may rewrite these equations in the true anomaly domain as the followings

$$\dot{\mathbf{e}} = \sqrt{\frac{a(1-e^2)}{\mu}}\frac{1}{(1+e\cos f)}\Big[-\frac{1}{2}\sin(2f)\hat{\mathbf{e}}\hat{\mathbf{e}} + (\cos^2 f + 2e\cos f + 1)\hat{\mathbf{e}}\hat{\mathbf{e}}_\perp + (\cos^2 f - e\cos f - 2)\hat{\mathbf{e}}_\perp\hat{\mathbf{e}} + \sin f(e+\cos f)\hat{\mathbf{e}}_\perp\hat{\mathbf{e}}_\perp + e\sin f\bar{\bar{U}}\Big]\cdot\mathbf{a}_{SRP}, \tag{5.16}$$

$$\dot{\mathbf{H}} = \frac{a(1-e^2)}{(1+e\cos f)}\Big[\cos f\tilde{\hat{\mathbf{e}}} + \sin f\tilde{\hat{\mathbf{e}}}_\perp\Big]\cdot\mathbf{a}_{SRP}, \text{ and} \tag{5.17}$$

$$\dot{\mathscr{E}} = \sqrt{\frac{\mu}{a(1-e^2)}}\,[-\sin(f)\hat{\mathbf{e}} + (e+\cos f)\hat{\mathbf{e}}_\perp]\cdot\mathbf{a}_{SRP}. \tag{5.18}$$

Substituting $\mathbf{a}_{SRP}$ with the Fourier series expansion given by Eq. (5.10) and expanding it inside the brackets, we get the following full set of equations for the time derivative of the orbit elements

$$\begin{aligned}\dot{\mathbf{e}} = \sqrt{\frac{a(1-e^2)}{\mu}}\frac{P(R)}{(1+e\cos f)m}\sum_{n=0}^{\infty}\Big[&-\frac{1}{2}\sin(2f)\cos(nf)\hat{\mathbf{e}}\hat{\mathbf{e}}\cdot\mathbf{A}_n'' + (\cos^2 f + 2e\cos f + 1)\\ &\times\cos(nf)\hat{\mathbf{e}}\hat{\mathbf{e}}_\perp\cdot\mathbf{A}_n'' + (\cos^2 f - e\cos f - 2)\cos(nf)\hat{\mathbf{e}}_\perp\hat{\mathbf{e}}\cdot\mathbf{A}_n''\\ &+\sin f(e+\cos f)\cos(nf)\hat{\mathbf{e}}_\perp\hat{\mathbf{e}}_\perp\cdot\mathbf{A}_n'' + e\sin f\cos(nf)\mathbf{A}_n''\\ &-\frac{1}{2}\sin(2f)\sin(nf)\hat{\mathbf{e}}\hat{\mathbf{e}}\cdot\mathbf{B}_n'' + (\cos^2 f + 2e\cos f + 1)\sin(nf)\hat{\mathbf{e}}\hat{\mathbf{e}}_\perp\cdot\mathbf{B}_n''\\ &+(\cos^2 f - e\cos f - 2)\sin(nf)\hat{\mathbf{e}}_\perp\hat{\mathbf{e}}\cdot\mathbf{B}_n'' + \sin f(e+\cos f)\sin(nf)\hat{\mathbf{e}}_\perp\hat{\mathbf{e}}_\perp\cdot\mathbf{B}_n''\\ &+e\sin f\sin(nf)\mathbf{B}_n''\Big],\end{aligned} \tag{5.19}$$

$$\begin{aligned}\dot{\mathbf{H}} = \frac{a(1-e^2)P(R)}{(1+e\cos f)m}\sum_{n=0}^{\infty}\Big[&\cos f\cos(nf)\tilde{\hat{\mathbf{e}}}\cdot\mathbf{A}_n'' + \sin f\cos(nf)\tilde{\hat{\mathbf{e}}}_\perp\cdot\mathbf{A}_n''\\ &+\cos f\sin(nf)\tilde{\hat{\mathbf{e}}}\cdot\mathbf{B}_n'' + \sin f\sin(nf)\tilde{\hat{\mathbf{e}}}_\perp\cdot\mathbf{B}_n''\Big], \text{ and}\end{aligned} \tag{5.20}$$

www.manaraa.com

$$\dot{\mathscr{E}} = \sqrt{\frac{\mu}{a(1-e^2)}}\frac{P(R)}{m}\sum_{n=0}^{\infty}\Bigg[-\sin f\cos(nf)\hat{\mathbf{e}}\cdot\mathbf{A}_n'' + (e+\cos f)\cos(nf)\hat{\mathbf{e}}_\perp\cdot\mathbf{A}_n'' \\ -\sin f\sin(nf)\hat{\mathbf{e}}\cdot\mathbf{B}_n'' + (e+\cos f)\sin(nf)\hat{\mathbf{e}}_\perp\cdot\mathbf{B}_n''\Bigg]. \tag{5.21}$$

These expressions define the time derivative of the orbit elements as a function of the SRP Fourier coefficients in the nadir-pointing attitude profile. In the following sections we use these expressions to derive the secular dynamics of the orbit elements in this attitude profile.

5.2.1.1 Circular orbit case

Let us discuss a case where the orbit is either circular or very close to a circular orbit, i.e. the eccentricity is very close to zero. The eccentricity vector is not defined for such an orbit. To resolve this we define an arbitrary vector $\hat{\mathbf{a}}$ on the orbit plane. This vector may be chosen to be in the direction of the spacecraft position vector at time $t = 0$, for simplicity. Hence, for this case, the angle f is simply defined as the angle between the current spacecraft position vector and vector $\hat{\mathbf{a}}$. The third axis of this coordinate frame is chosen to be along the orbit angular momentum vector $\hat{\mathbf{h}}$. Finally, vector $\hat{\mathbf{b}} = \tilde{\hat{\mathbf{h}}}\cdot\hat{\mathbf{a}}$ completes the triad. Now, let $e = 0$ in Eq. (5.19) – (5.21) to get

$$\dot{\mathbf{e}} = \sqrt{\frac{a}{\mu}}\frac{P(R)}{m}\sum_{n=0}^{\infty}\Bigg[-\frac{1}{2}\sin(2f)\cos(nf)\hat{\mathbf{a}}\hat{\mathbf{a}}\cdot\mathbf{A}_n'' + (\cos^2 f+1)\cos(nf)\hat{\mathbf{a}}\hat{\mathbf{b}}\cdot\mathbf{A}_n'' \\ +(\cos^2 f-2)\cos(nf)\hat{\mathbf{b}}\hat{\mathbf{a}}\cdot\mathbf{A}_n'' + \frac{1}{2}\sin(2f)\cos(nf)\hat{\mathbf{b}}\hat{\mathbf{b}}\cdot\mathbf{A}_n'' \\ -\frac{1}{2}\sin(2f)\sin(nf)\hat{\mathbf{a}}\hat{\mathbf{a}}\cdot\mathbf{B}_n'' + (\cos^2 f+1)\sin(nf)\hat{\mathbf{a}}\hat{\mathbf{b}}\cdot\mathbf{B}_n'' \\ +(\cos^2 f-2)\sin(nf)\hat{\mathbf{b}}\hat{\mathbf{a}}\cdot\mathbf{B}_n'' + \frac{1}{2}\sin(2f)\sin(nf)\hat{\mathbf{b}}\hat{\mathbf{b}}\cdot\mathbf{B}_n''\Bigg], \tag{5.22}$$

$$\dot{\mathbf{H}} = \sqrt{\frac{a}{\mu}}\frac{P(R)}{m}\sum_{n=0}^{\infty}\Bigg[\cos f\cos(nf)\tilde{\hat{\mathbf{a}}}\cdot\mathbf{A}_n'' + \sin f\cos(nf)\tilde{\hat{\mathbf{b}}}\cdot\mathbf{A}_n'' \\ +\cos f\sin(nf)\tilde{\hat{\mathbf{a}}}\cdot\mathbf{B}_n'' + \sin f\sin(nf)\tilde{\hat{\mathbf{b}}}\cdot\mathbf{B}_n''\Bigg], \text{ and} \tag{5.23}$$

$$\dot{\mathscr{E}} = \sqrt{\frac{\mu}{a(1-e^2)}}\frac{P(R)}{m}\sum_{n=0}^{\infty}\Bigg[-\sin f\cos(nf)\hat{\mathbf{a}}\cdot\mathbf{A}_n'' + \cos f\cos(nf)\hat{\mathbf{b}}\cdot\mathbf{A}_n'' \\ -\sin f\sin(nf)\hat{\mathbf{a}}\cdot\mathbf{B}_n'' + \cos f\sin(nf)\hat{\mathbf{b}}\cdot\mathbf{B}_n''\Bigg]. \tag{5.24}$$

www.manaraa.com

Note that for a circular orbit we have $df = dM$. Taking the average we encounter quadratures of the form

$$\int_0^{2\pi} \cos f \cos(nf) df = \begin{cases} \pi & n = 1 \\ 0 & \text{otherwise} \end{cases}, \tag{5.25}$$

$$\int_0^{2\pi} \sin f \cos(nf) df = 0 \quad \forall\, n, \tag{5.26}$$

$$\int_0^{2\pi} \cos f \sin(nf) df = 0 \quad \forall\, n, \text{ and} \tag{5.27}$$

$$\int_0^{2\pi} \sin f \sin(nf) df = \begin{cases} \pi & n = 1 \\ 0 & \text{otherwise} \end{cases}. \tag{5.28}$$

After implementing these results and simplifying the expressions we get the following set of expressions for the secular dynamics of the orbit elements for a circular orbit in the nadir-pointing attitude profile.

$$\overline{\dot{\mathbf{e}}} = \sqrt{\frac{a}{\mu}} \frac{P(R)}{m} \left[\frac{3}{2} (\hat{\mathbf{a}}\hat{\mathbf{b}} - \hat{\mathbf{b}}\hat{\mathbf{a}}) \cdot \mathbf{A}_0'' + \frac{1}{4} (\hat{\mathbf{a}}\hat{\mathbf{b}} + \hat{\mathbf{b}}\hat{\mathbf{a}}) \cdot \mathbf{A}_2'' - \frac{1}{4} (\hat{\mathbf{a}}\hat{\mathbf{a}} - \hat{\mathbf{b}}\hat{\mathbf{b}}) \cdot \mathbf{B}_2'' \right], \tag{5.29}$$

$$\overline{\dot{\mathbf{H}}} = \sqrt{\frac{a}{\mu}} \frac{P(R)}{m} \left[\frac{1}{2} \tilde{\hat{\mathbf{a}}} \cdot \mathbf{A}_1'' + \frac{1}{2} \tilde{\hat{\mathbf{b}}} \cdot \mathbf{B}_1'' \right], \text{ and} \tag{5.30}$$

$$\overline{\dot{\mathscr{E}}} = \sqrt{\frac{\mu}{a(1-e^2)}} \frac{P(R)}{2m} \Big(A_1''(2) - B_1''(1) \Big). \tag{5.31}$$

For a circular orbit case we arrive at a set of simple expressions, where the secular dynamics of the orbit elements are described by only 10 Fourier coefficients, namely $A_0''(1)$, $A_0''(2)$, $A_1''(2)$, $A_1''(3)$, $A_2''(1)$, $A_2''(2)$, $B_1''(1)$, $B_1''(3)$, $B_2''(1)$, and $B_2''(2)$. These coefficients contribute to the secular dynamics of the different components of orbit elements through the dot product with the dyadic notations of the basis vectors as given in the expressions above.

www.manaraa.com

One may also derive the above expressions as a function of the single primed coefficients. Having such expressions is particularly useful when we compare the results of the secular derivations with the results of the covariance analysis shown in the later sections. To do so, we utilize Eq. (5.11) – (5.15) to substitute the single primed coefficients in place of the double primed ones. After carrying out the substitutions and regrouping the relevant terms we arrive at the following set of secular equations that are given as a function of the single primed coefficients, i.e.

$$\overline{\dot{\mathbf{e}}} = \sqrt{\frac{a}{\mu}}\frac{P(R)}{2m}\left[(2\hat{\mathbf{a}}\hat{\mathbf{q}} - \hat{\mathbf{b}}\hat{\mathbf{p}})\cdot\mathbf{A}_1' + (2\hat{\mathbf{b}}\hat{\mathbf{q}} + \hat{\mathbf{a}}\hat{\mathbf{p}})\cdot\mathbf{B}_1'\right], \tag{5.32}$$

$$\overline{\dot{\mathbf{H}}} = \sqrt{\frac{a}{\mu}}\frac{P(R)}{2m}\left[2\hat{\mathbf{h}}\hat{\mathbf{q}}\cdot\mathbf{A}_0' - \hat{\mathbf{b}}\hat{\mathbf{h}}\cdot\mathbf{A}_1' + \hat{\mathbf{a}}\hat{\mathbf{h}}\cdot\mathbf{B}_1'\right], \text{ and} \tag{5.33}$$

$$\overline{\dot{\mathscr{E}}} = \sqrt{\frac{\mu}{a(1-e^2)}}\,\frac{P(R)}{2m}A_0'(2). \tag{5.34}$$

For a circular orbit, the secular dynamics of an orbit is described by only 7 single primed SRP coefficients, namely $A_0'(2)$, $A_1'(1)$, $A_1'(2)$, $A_1'(3)$, $B_1'(1)$, $B_1'(2)$, and $B_1'(3)$. These expressions are also given by Reference [55].

5.2.1.2 Eccentric orbit case

Let us now consider the case where the orbit eccentricity is not negligible. It is particularly important to study an eccentric orbit dynamics for an orbiter about a small body. Previous research [73, 74, 77] showed that a circular terminator orbit about a small body evolves into an eccentric orbit with rather a large value of eccentricity. For instance, the eccentricity of an initially circular terminator orbit with a radius of 1 km about Bennu could reach to as large as about 0.2. For an eccentric orbit, the derivation of secular equations is a lot more complicated compared to that for a circular orbit scenario. This is immediately clear due to the radius function that appears in the averaged expression as a result of change of variable from the mean anomaly to the true anomaly (see Eq. (2.10)). Reference [55] uses a series expansion for approximating the true anomaly as a function of the mean anomaly and derives the secular equations in the mean anomaly

www.manaraa.com

domain. That method is suitable for cases where the orbit eccentricity is relatively small. However, in the case of an eccentric orbit with relatively large eccentricity it is suitable to derive the secular equations directly in the true anomaly domain.

To proceed with the derivation, we use a Fourier series expansion of the radius function that is detailed in Appendix D. This is used to expand the radius function of the true anomaly in Eq. (2.11) and carry out the average of Eq. (5.19)– (5.21) in the true anomaly domain. The derivation of these equations is rather lengthy. Here we present the final expressions that are given by

$$\begin{aligned}\overline{\dot{\mathbf{e}}} = \sqrt{\frac{a}{\mu}}\frac{(1-e^2)^2 P(R)}{8m}\Big[&2\,\mathcal{F}_0^1(\hat{\mathbf{e}}\hat{\mathbf{e}}_\perp - \hat{\mathbf{e}}_\perp\hat{\mathbf{e}})\cdot\mathbf{A}_0'' + (\mathcal{F}_1^1\hat{\mathbf{e}}\hat{\mathbf{e}}_\perp + \mathcal{F}_1^2\hat{\mathbf{e}}_\perp\hat{\mathbf{e}})\cdot\mathbf{A}_1'' \\ &+(\mathcal{F}_2^1\hat{\mathbf{e}}\hat{\mathbf{e}}_\perp + \mathcal{F}_2^2\hat{\mathbf{e}}_\perp\hat{\mathbf{e}})\cdot\mathbf{A}_2'' + \sum_{n=3}^{\infty}(\mathcal{G}_n^1\hat{\mathbf{e}}\hat{\mathbf{e}}_\perp + \mathcal{G}_n^2\hat{\mathbf{e}}_\perp\hat{\mathbf{e}})\cdot\mathbf{A}_n'' \\ &+(\mathcal{Z}_1^1\hat{\mathbf{e}}\hat{\mathbf{e}} + \mathcal{Z}_1^2\hat{\mathbf{e}}_\perp\hat{\mathbf{e}}_\perp + \mathcal{Z}_1^3\bar{\bar{U}})\cdot\mathbf{B}_1'' + (\mathcal{Z}_2^1\hat{\mathbf{e}}\hat{\mathbf{e}} + \mathcal{Z}_2^2\hat{\mathbf{e}}_\perp\hat{\mathbf{e}}_\perp + \mathcal{Z}_2^3\bar{\bar{U}})\cdot\mathbf{B}_2'' + \\ &\sum_{n=3}^{\infty}(\mathcal{Y}_n^1\hat{\mathbf{e}}\hat{\mathbf{e}} + \mathcal{Y}_n^2\hat{\mathbf{e}}_\perp\hat{\mathbf{e}}_\perp + \mathcal{Y}_n^3\bar{\bar{U}})\cdot\mathbf{B}_n''\Big],\end{aligned} \tag{5.35}$$

$$\begin{aligned}\overline{\dot{\mathbf{H}}} = \sqrt{\frac{a}{\mu}}\frac{(1-e^2)^2 P(R)}{4m}\Big[&2b_1^3\tilde{\hat{\mathbf{e}}}\cdot\mathbf{A}_0'' + 2b_0^3\tilde{\hat{\mathbf{e}}}\cdot\mathbf{A}_1'' + \sum_{n=2}^{\infty}c_n\tilde{\hat{\mathbf{e}}}\cdot\mathbf{A}_n'' + 2b_0^3\tilde{\hat{\mathbf{e}}}_\perp\cdot\mathbf{B}_1'' \\ &+\sum_{n=2}^{\infty}d_n\tilde{\hat{\mathbf{e}}}_\perp\cdot\mathbf{B}_n''\Big],\end{aligned} \tag{5.36}$$

$$\overline{\dot{\mathscr{E}}} = \sqrt{\frac{\mu}{a}}\,\frac{(1-e^2)P(R)}{4m}\Big[\epsilon_1 A_1''(2) + \sum_{n=2}^{\infty}\epsilon_n A_n''(2) + \zeta_1 B_1''(1) + \sum_{n=2}^{\infty}\zeta_n B_n''(1)\Big]. \tag{5.37}$$

The basis functions b, c, d, ϵ, ζ, $\mathcal{F}$, $\mathcal{G}$, $\mathcal{Z}$, and $\mathcal{Y}$ are detailed in Appendix E.

Note that the resulting secular equations for an eccentric orbit are not as simple as those derived for the circular case. As shown in these equations, more number of Fourier coefficients show up in the secular dynamics. In fact, these equations are in the form of an infinite series expansion. This is due to the fact that a handful of quadratures appear during the averaging process that are non-zero for any value of the expansion order n. However, we should also point out that the values of these quadratures diminish very rapidly as n increases leaving only a handful of the

www.manaraa.com

coefficients with a significant secular contribution. An other important result that is given from these expressions is that those Fourier coefficients that are dominant for the secular dynamics of a circular orbit are still present and dominant for an eccentric orbit. In fact, these results shows that the eccentric orbit case is a more generalized version of the circular case, where in addition to a handful of dominant coefficients it also includes coefficients of higher orders. Figure 5.1 shows the set of first few dominant coefficients for the secular equations based on the magnitude of their multipliers in these equations. The value of the eccentricity is chosen to be e = 0 (circular orbit), 0.05, 0.1, and 0.2 for these plots. These plots show that the coefficients that appear in the secular equations for a circular orbit case are the same first few coefficients that appear for other eccentric orbit cases.

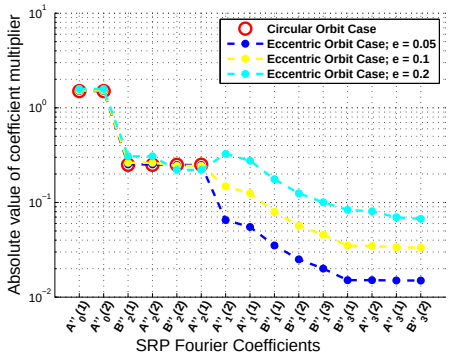

(a) Coefficients for $\overline{\dot{\mathbf{e}}}$

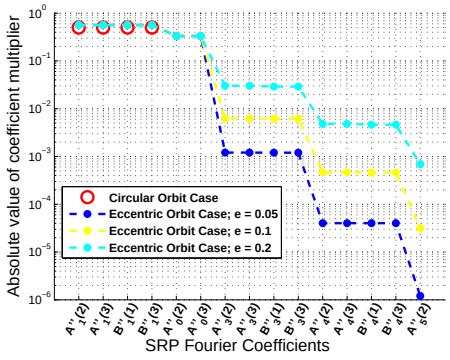

(b) Coefficients for $\overline{\dot{\mathbf{H}}}$

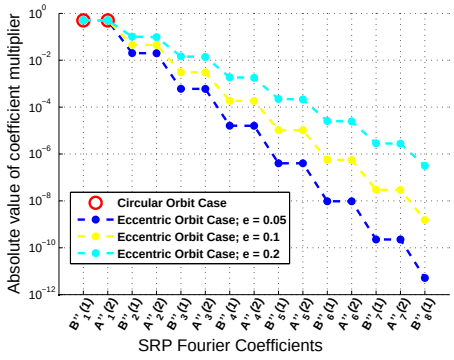

(c) Coefficients for $\overline{\dot{\mathscr{E}}}$

Figure 5.1: The set of first few coefficients for the secular dynamics based on the value of their multipliers in the secular equations.

www.manaraa.com

Similarly, one may use Eq. (5.11) – (5.15) to substitute the single primed coefficients in place of the double primed ones to express the secular equations as a function of the single primed coefficients. Performing these substitutions in Eq. (5.35) – (5.37) and regrouping the terms that involve the same SRP coefficients, we get the following set of expressions for the single primed coefficients.

$$\begin{aligned}\overline{\dot{\mathbf{e}}} = \sqrt{\frac{a}{\mu}}\frac{(1-e^2)^2P(R)}{8m}\Big[&(\mathcal{F}_0'^1\hat{\mathbf{e}}\hat{\mathbf{q}} - \mathcal{F}_0'^2\hat{\mathbf{e}}_\perp\hat{\mathbf{p}})\cdot\mathbf{A}_0' + (\mathcal{F}_1'^1\hat{\mathbf{e}}\hat{\mathbf{q}} + \mathcal{F}_1'^2\hat{\mathbf{e}}_\perp\hat{\mathbf{p}})\cdot\mathbf{A}_1' \\ &+(\mathcal{F}_2'^1\hat{\mathbf{e}}\hat{\mathbf{q}} + \mathcal{F}_2'^2\hat{\mathbf{e}}_\perp\hat{\mathbf{p}})\cdot\mathbf{A}_2' + \sum_{n=3}^{\infty}(\mathcal{G}_n'^1\hat{\mathbf{e}}\hat{\mathbf{q}} + \mathcal{G}_n'^2\hat{\mathbf{e}}_\perp\hat{\mathbf{p}})\cdot\mathbf{A}_n' \\ +(\mathcal{Z}_1'^1\hat{\mathbf{e}}\hat{\mathbf{p}} + \mathcal{Z}_1'^2\hat{\mathbf{e}}_\perp\hat{\mathbf{q}} + \mathcal{Z}_1'^3\hat{\mathbf{h}}\hat{\mathbf{h}})\cdot\mathbf{B}_1' &+ (\mathcal{Z}_2'^1\hat{\mathbf{e}}\hat{\mathbf{p}} + \mathcal{Z}_2'^2\hat{\mathbf{e}}_\perp\hat{\mathbf{q}} + \mathcal{Z}_2'^3\hat{\mathbf{h}}\hat{\mathbf{h}})\cdot\mathbf{B}_2' + \\ &\sum_{n=3}^{\infty}(\mathcal{Y}_n'^1\hat{\mathbf{e}}\hat{\mathbf{p}} + \mathcal{Y}_n'^2\hat{\mathbf{e}}_\perp\hat{\mathbf{q}} + \mathcal{Y}_n'^3\hat{\mathbf{h}}\hat{\mathbf{h}})\cdot\mathbf{B}_n'\Big],\end{aligned} \tag{5.38}$$

$$\begin{aligned}\overline{\dot{\mathbf{H}}} = \sqrt{\frac{a}{\mu}}\frac{(1-e^2)^2P(R)}{4m}\Big[&2(2b_0^3\hat{\mathbf{h}}\hat{\mathbf{q}} - b_1^3\hat{\mathbf{e}}_\perp\hat{\mathbf{h}})\cdot\mathbf{A}_0' + 2(b_1^3\hat{\mathbf{h}}\hat{\mathbf{q}} - b_0^3\hat{\mathbf{e}}_\perp\hat{\mathbf{h}})\cdot\mathbf{A}_1' \\ &+\sum_{n=2}^{\infty}(b_n^3\hat{\mathbf{h}}\hat{\mathbf{q}} - c_n\hat{\mathbf{e}}_\perp\hat{\mathbf{h}})\cdot\mathbf{A}_n' + 2b_0^3\hat{\mathbf{e}}\hat{\mathbf{h}}\cdot\mathbf{B}_1' - b_2^3\hat{\mathbf{h}}\hat{\mathbf{p}}\cdot\mathbf{B}_2' + \sum_{n=2}^{\infty}d_n\hat{\mathbf{e}}\hat{\mathbf{h}}\cdot\mathbf{B}_n'\Big], \text{ and}\end{aligned} \tag{5.39}$$

$$\begin{aligned}\overline{\dot{\mathscr{E}}} = \sqrt{\frac{\mu}{a}}\,\frac{(1-e^2)P(R)}{4m}\Big[&\epsilon_0'A_0'(2) + \epsilon_1'A_1'(2) + \epsilon_2'A_2'(2) + \sum_{n=2}^{\infty}\epsilon_n'A_n'(2) + \\ &\zeta_1'B_1'(1) + \zeta_2'B_2'(1) + \sum_{n=2}^{\infty}\zeta_n'B_n'(1)\Big].\end{aligned} \tag{5.40}$$

The basis functions $\mathcal{F}'$, $\mathcal{G}'$, $\mathcal{Z}'$, $\mathcal{Y}'$, ϵ', and ζ' are detailed in Appendix E.

5.2.2 Secular Dynamics for the Sun and Earth-pointing Attitudes

So far in this chapter we have presented a set of secular equations for the nadir-pointing attitude where the spacecraft rotates about its $\hat{\mathbf{z}}_b$ axis at the same rate as the orbital motion. In this section, we discuss the derivation of secular dynamics of an orbit during the Sun-pointing and the Earth-pointing attitudes.

www.manaraa.com

5.2.2.1 Sun-pointing attitude

During a Sun-pointing attitude profile, the spacecraft is aligned such that the Sun is placed in the $\hat{\mathbf{x}}_b\hat{\mathbf{z}}_b$ plane of the spacecraft body-fixed frame as the $\hat{\mathbf{z}}_b$ axis points towards the general direction of the Sun. Hence, we have

$$\lambda_s^{\odot} = 0. \tag{5.41}$$

Therefore the SRP acceleration given in Eq. (5.3) is simplified to

$$\mathbf{a}_{SRP}^{\odot} = \frac{P(R)}{m_{SC}} \sum_{n=0}^{\infty} \mathbf{A}_n. \tag{5.42}$$

Let $\mathbf{A}_0^{\odot} = \sum_{n=0}^{\infty} \mathbf{A}_n$. Hence, we may rewrite the above equation as

$$\mathbf{a}_{SRP}^{\odot} = \frac{P(R)}{m_{SC}} \mathbf{A}_0^{\odot}. \tag{5.43}$$

Therefore, the time derivatives of the orbit element set become

$$\begin{aligned}
\dot{\mathbf{e}} &= \frac{1}{\mu}\frac{P(R)}{m_{SC}}[2\mathbf{rv} - \mathbf{vr} - (\mathbf{r}\cdot\mathbf{v})\bar{\bar{U}}] \cdot \mathbf{A}_0^{\odot}, \\
\dot{\mathbf{H}} &= \frac{P(R)}{m_{SC}} \tilde{\mathbf{r}} \cdot \mathbf{A}_0^{\odot}, \text{ and} \\
\dot{\mathscr{E}} &= \frac{P(R)}{m_{SC}} \mathbf{v} \cdot \mathbf{A}_0^{\odot}.
\end{aligned} \tag{5.44}$$

Taking average of these equations we get the following set of expressions

$$\begin{aligned}
\overline{\dot{\mathbf{e}}} &= -\frac{3}{2\mu}\frac{P(R)}{m_{SC}} \tilde{\mathbf{H}} \cdot \mathbf{A}_0^{\odot}, \\
\overline{\dot{\mathbf{H}}} &= -\frac{3a}{2}\frac{P(R)}{m_{SC}} \tilde{\mathbf{e}} \cdot \mathbf{A}_0^{\odot}, \text{ and} \\
\overline{\dot{\mathscr{E}}} &= 0.
\end{aligned} \tag{5.45}$$

There are couple of points to note here. First, we see that according to the definition of $\mathbf{A}_0^{\odot}$ none of the $\mathbf{B}_n$ coefficients are involved in the secular equations during the Sun-pointing attitude. Furthermore, note that the secular rate of the orbit energy, $\overline{\dot{\mathscr{E}}}$, vanishes at all times. As a result, the

www.manaraa.com

energy of the orbit is conserved, on average. In fact this scenario is a more general case of the formulation that is discussed in Section 4.1. That section assumes a cannonball model for SRP where the perturbing force is assumed constantly pointing in the $\hat{\mathbf{d}}$ direction. In the scenario given here, the SRP is fixed in the Sun-asteroid rotating frame and is constantly pointing in the direction of the $\mathbf{A}_0^{\odot}$ vector. Rosengren and Scheeres [74] provide a closed form solution for such a general case.

5.2.2.2 Earth-pointing attitude

The Earth-pointing attitude is very similar to the Sun-pointing attitude with a small difference. In the Earth-pointing attitude, the spacecraft is aligned such that Earth is placed in the $\hat{\mathbf{x}}_b\hat{\mathbf{z}}_b$ plane as the $\hat{\mathbf{z}}_b$ axis points towards the Earth. The main assumption made here is that the for the period of one orbit the angle between the sunlight and the line of sight from the spacecraft to Earth is constant. This is a valid assumption, since the period of one orbit around a small body is very short compared to the time that it takes to change the geometry of the Sun and the Earth with respect to the central body. Therefore, we assume that the solar longitude has a non-zero, but constant value, i.e.

$$\lambda_s^{\oplus} = \text{const.} \neq 0. \tag{5.46}$$

The SRP acceleration give by Eq. (5.3) is simplified to

$$\mathbf{a}_{SRP}^{\oplus} = \frac{P(R)}{m} \sum_{n=0}^{\infty} \left[\mathbf{A}_n \cos(n\lambda_s^{\oplus}) + \mathbf{B}_n \sin(n\lambda_s^{\oplus}) \right]. \tag{5.47}$$

One may define

$$\mathbf{A}_0^{\oplus} = \sum_{n=0}^{\infty} \left[\mathbf{A}_n \cos(n\lambda_s^{\oplus}) + \mathbf{B}_n \sin(n\lambda_s^{\oplus}) \right]. \tag{5.48}$$

Hence, we may re-write the SRP acceleration as

$$\mathbf{a}_{SRP}^{\oplus} = \frac{P(R)}{m_{SC}} \mathbf{A}_0^{\oplus}. \tag{5.49}$$

www.manaraa.com

Similar to the Sun-pointing case one may derive the secular equations for the time derivative of the orbit element set as

$$\overline{\dot{\mathbf{e}}} = -\frac{3}{2\mu}\frac{P(R)}{m_{SC}}\tilde{\mathbf{H}}\cdot\mathbf{A}_0^{\oplus},$$

$$\overline{\dot{\mathbf{H}}} = -\frac{3a}{2}\frac{P(R)}{m_{SC}}\tilde{\mathbf{e}}\cdot\mathbf{A}_0^{\oplus}, \text{ and} \tag{5.50}$$

$$\overline{\dot{\mathscr{E}}} = 0.$$

Note that for the Earth-pointing attitude, the energy of the orbit is conserved on averaged. As was the case for the Sun-pointing attitude, the secular equations of the eccentricity vector and the angular momentum vector may be solved in a close form solution. One minor difference from the Sun-pointing case is that, based on the definition given by Eq. (5.48) both of the $\mathbf{A}_n$ and the $\mathbf{B}_n$ coefficients contribute to the secular dynamics of the element set.

5.3 Error Analysis of the Fourier Coefficients

So far, we have derived a series of expressions that govern the secular dynamics of an orbit due to SRP perturbations represented by a SRP Fourier series expansion. From these expressions we identified a handful of Fourier coefficients that have a prominent effect on the secular equations. Errors in the computation of such coefficients could result in large mis-modeling of SRP effects on spacecraft. Hence, we are interested to study the sensitivity of the Fourier coefficients to some of the main error sources that may affect the computation of these coefficients.

In this study, we use a simple 10-plate box-wing model of the OSIRIS-REx spacecraft as an example. The box-wing model is shown in Figure 2.2. Reflective properties of the spacecraft surface elements are summarized in Table 5.1. The coordinates in the table are aligned with the spacecraft body fixed frame given by Figure 2.2. These surface properties are used to compute the nominal values of the Fourier coefficients for our example. One can relate the surface properties given in Table 5.1, namely the C_s and C_d, to those introduced by Eq. (3.11) using the following

www.manaraa.com

Table 5.1: Surface properties for a 10-plate box-wing model of the OSIRIS-REx spacecraft.

	Normal vector			Surface properties		
	$\hat{\mathbf{x}}^b$	$\hat{\mathbf{y}}^b$	$\hat{\mathbf{z}}^b$	Specular Coeff. C_s	Diffused Coeff. C_d	Area (m^2)
+x bus	1	0	0	0.056	0.435	6.471
-x bus	-1	0	0	0.000	0.440	6.471
+y bus	0	1	0	0.076	0.411	5.175
-y bus	0	-1	0	0.076	0.411	5.175
+z bus	0	0	1	0.000	0.473	5.174
-z bus	0	0	-1	0.000	0.473	5.174
-y solar panel Front	0.707	0	0.707	0.080	0.000	4.903
+y solar panel Front	0.707	0	0.707	0.080	0.000	4.903
-y solar panel back	-0.707	0	-0.707	0.000	0.070	4.903
+y solar panel back	-0.707	0	-0.707	0.000	0.070	4.903

relationships

$$\begin{aligned} C_s &= \rho s, \\ C_d &= 1 - \rho s. \end{aligned} \tag{5.51}$$

Although we consider a simple shape model for this study, the remarkable fact about this formulation is that Fourier coefficients may be pre-computed in the same fashion for any level of complexity of a spacecraft shape model without affecting the amount of computation required during a numerical propagation or an orbit determination process. Figure 5.2 shows the nominal Fourier coefficients up to $n = 25$ computed for the 10-plate model using the surface properties given in Table 5.1. These coefficients are shown as a function of the solar latitude, δ_s, in the spacecraft body-fixed frame. The legend on each plot identifies the first four coefficients. Note that for this particular shape model of the spacecraft, all of the $A_n(2)$, $B_n(1)$, and $B_n(3)$ coefficients are equal to zero. Also, note that in this work we do not consider the self-shadowing and self-illumination effects of the different surfaces of the spacecraft when computing the coefficients. Although, it may be desired to include these effects in generating the Fourier coefficients for spacecraft in real-world applications, the inclusion or lack of inclusion on these effects will not have any effect on the overall findings of this study.

A Monte Carlo analysis is implemented to analyze the sensitivity of the Fourier coefficients

www.manaraa.com

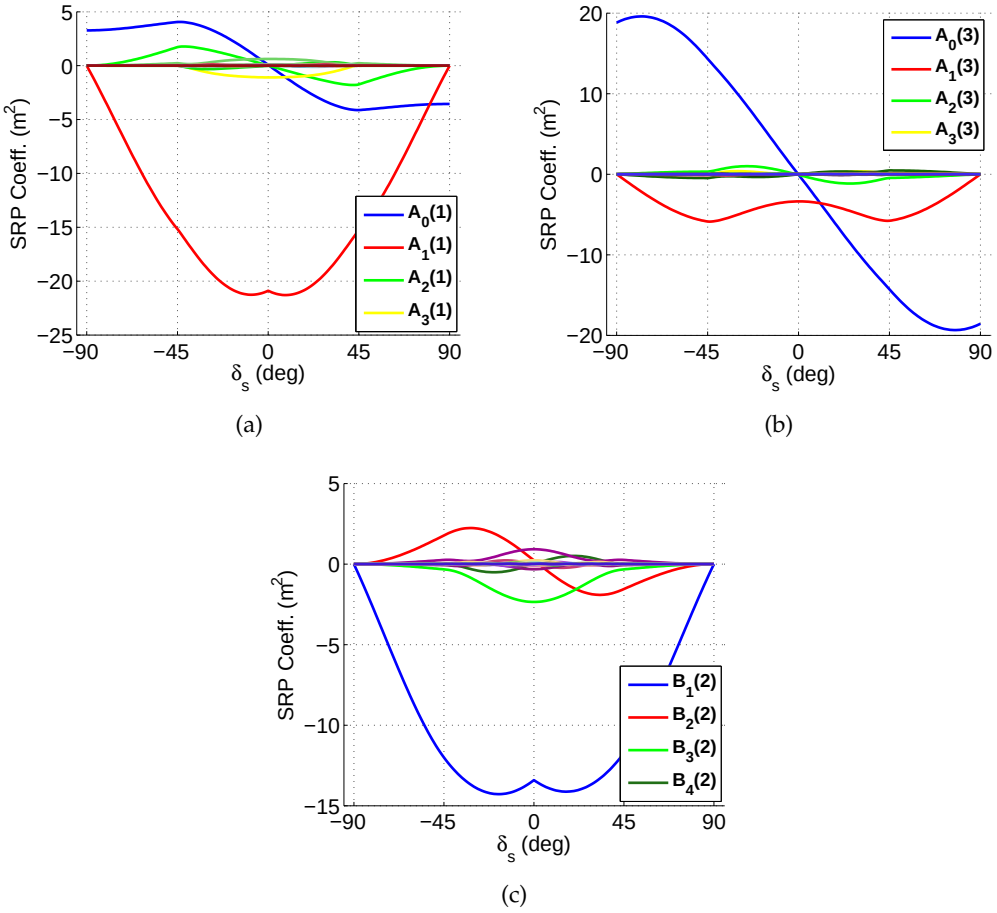

Figure 5.2: Fourier coefficients for the 10-plate shape model of the OSIRIS-REx spacecraft. The coefficients are given in the spacecraft body-fixed frame.

to the main error sources. This analysis evaluates the effect of four error sources, namely the uncertainty in a spacecraft surface properties, errors in a spacecraft nominal attitude, errors in a spacecraft shape model, and finally errors in the solar panel orientation relative to a spacecraft bus. In regards to the uncertainty in the optical properties of the surface elements a Gaussian error of zero mean and 10% standard deviation is introduced to the nominal values of ρ and s derived from Table 5.1. Spacecraft attitude errors are generated by a Gaussian noise of zero mean and 3° standard deviation in all three pitch, yaw, and roll directions relative to a nominal attitude profile. For generating errors in the spacecraft shape model, we start with a 10 cm resolution triangular vertex and facet model of the bus and distort the shape model by moving the vertices in the 3D

www.manaraa.com

space with a Gaussian noise of zero mean and 2 cm standard deviation. Finally, the solar panel pointing error is generated by rotating the solar panels about the $\hat{\mathbf{y}}_b$ axis with a Gaussian noise of zero mean and 3° standard deviation.

A set of 1,000 perturbed spacecraft shape models are generated for each one of the error sources, which are then used to compute a set of Fourier coefficients for each case. The resulting Fourier coefficients are aggregated to compute the maximum and minimum values of the coefficients for each solar latitude. The range between the maximum and minimum limits may be used as the range of uncertainty in each of the Fourier coefficients. Figure 5.3 shows these limits for the three components of the $\mathbf{A}_0$ coefficient as an example. Note that even though $A_0(2)$ is nominally zero across all solar latitude values, errors in a spacecraft shape model, surface properties, and attitude result in a non-zero coefficient. This is important since according to the analysis presented in the previous section the $A_0(2)$ coefficient has a prominent secular effect on the dynamics of orbit elements.

A subsequent Monte Carlo analysis is performed to evaluate effects of the uncertainty in the Fourier coefficients on spacecraft trajectory errors. Bennu is considered to be the central body and a spacecraft is assumed to in a circular terminator orbit with a radius of 1 km. We examine the nadir-pointing and the Sun-pointing attitudes as well as an attitude profile that is akin to the Earth-pointing attitude with a difference that we control the fixed angle between the Sun and the spacecraft $\hat{\mathbf{z}}_b$ axis. We call this the *beta* (β) angle. By controlling the value of the beta angle, we can expose different surfaces of the spacecraft to the sunlight as would be the case for the Earth-pointing attitude profile at different epochs. A full range of $-\pi$ to $+\pi$ is considered for the beta angle in this Monte Carlo simulation. However, we acknowledge that in reality, for a specific asteroid the range of possible values for the beta angle is dictated by the geometry of Earth's orbit and the orbit of that asteroid. Also, note that $\beta = 0^\circ$ is equivalent to the Sun-pointing attitude. The nominal trajectory is generated using the nominal values of the Fourier coefficients up to an expansion order of 25. The force model for the trajectory propagation include the central body point mass attraction, SRP, non-spherical gravitational perturbation of Bennu, and Sun's third

www.manaraa.com

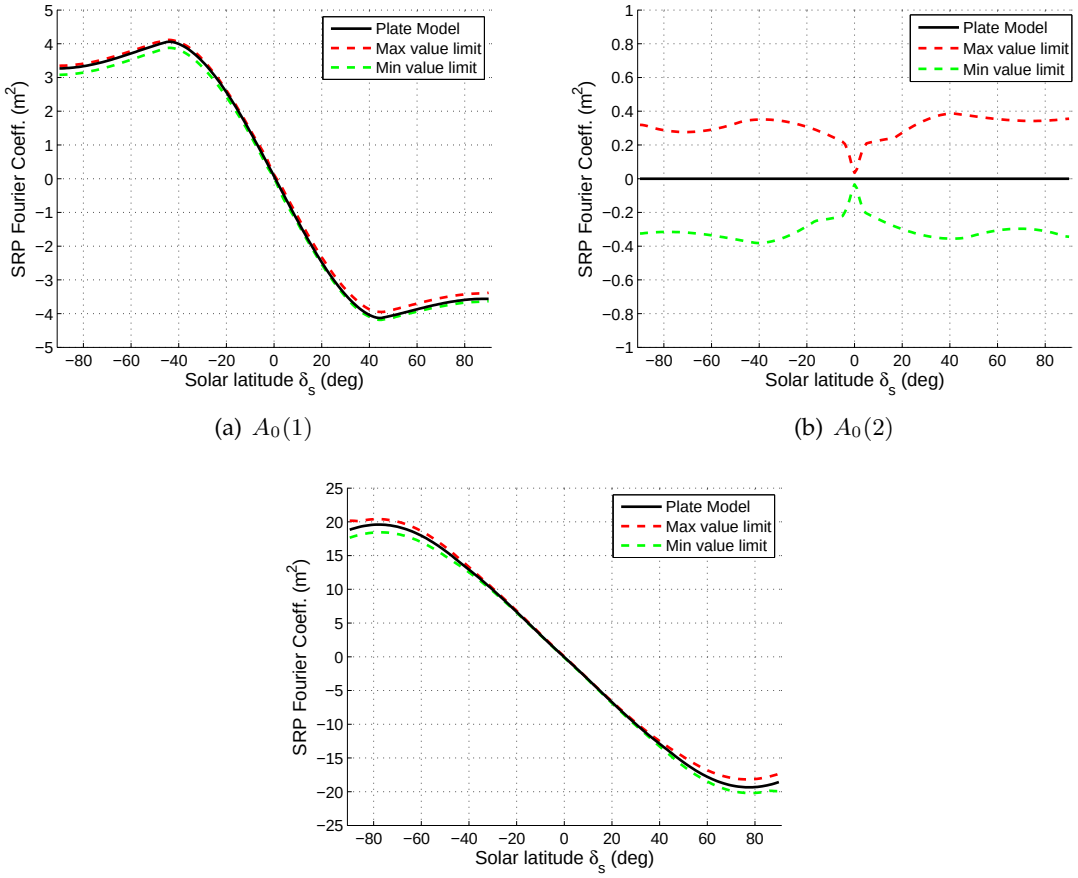

(a) $A_0(1)$ (b) $A_0(2)$

(c) $A_0(3)$

Figure 5.3: Maximum and minimum error envelopes for the $\mathbf{A}_0$ coefficients.

body perturbation. The TRP effect is not considered for this simulation. A set of 500 trajectories are propagated for each one of the Fourier coefficients by perturbing the value of one coefficient while keeping the rest unchanged. The perturbed values of the coefficients are generated randomly between the maximum and minimum limits established earlier. Each trajectory is propagated for a 5-day arc.

Figure 5.4 shows the simulation results for the nadir-pointing attitude profile. It shows the maximum magnitude of the position error of the perturbed trajectories compared to the nominal trajectory with respect to each of Fourier coefficients for the nadir-pointing attitude. A number of the coefficients that result in the highest level of error are shown here. This figure shows that errors in $A_0(2)$ coefficient result in the largest magnitude of the trajectory error. Many of the

www.manaraa.com

prominent secular coefficients (shown in red) also contribute to large error values in the spacecraft trajectory. The $A_0(1)$ and $A_0(3)$ coefficients are also among those that result in relatively large errors. These coefficients do not contribute to the secular dynamics, however, their large values at a solar latitude of $\approx 90^\circ$ (see Figure 5.2) suggests a large periodic effect due to errors in these coefficients. Note that at the nadir-pointing attitude, the solar latitude is about 90°. Furthermore, the figure shows that the error magnitude decays rapidly as we move towards the higher order coefficients.

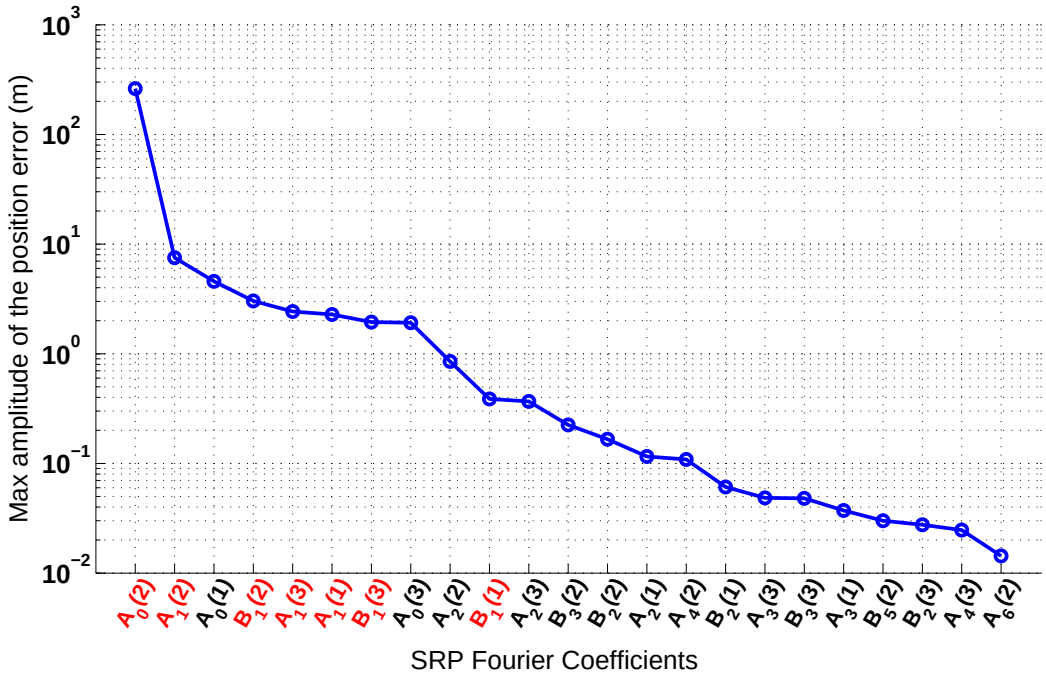

Figure 5.4: Spacecraft position error after 5 days due to errors in Fourier coefficients for the nadir-pointing attitude.

Results for the Sun-pointing attitude profile is shown in Figure 5.5. A similar trend is apparent in this plot as the one shown for the nadir-pointing attitude, where couple of the lower order coefficients contribute to the largest value of errors in the trajectory and the error magnitude diminishes rapidly for the higher order coefficients. However, note that none of the $\mathbf{B}_n$ coefficients contribute to the error in the trajectory, since for this attitude the solar longitude is equal to zero

www.manaraa.com

resulting in all the $\sin(\lambda_s)$ terms to vanish. Finally, Figure 5.6 shows the Monte Carlo simulation results as a function of the beta angle. The vertical axis of the mosaic plot labels the Fourier coefficients arranged such that the top three are the three components of the $\mathbf{A}_0$ followed by the three components of the $\mathbf{A}_1$ up to $\mathbf{A}_{10}$ and $\mathbf{B}_1$ up to $\mathbf{B}_{10}$. This figure shows that a symmetric pattern emerges across different beta angle values centered at $\beta = 0°$. The largest position error occurs at $\beta = 90°$, due to errors in $\mathbf{B}_1(1)$ coefficient. Furthermore, note that in general, only the even order $\mathbf{A}$ coefficients and the odd order $\mathbf{B}$ coefficients contribute to large errors in the trajectory with the magnitude of the error diminishing as the coefficient order increases. The case where $\beta = 0°$ is equivalent to the Sun-pointing attitude.

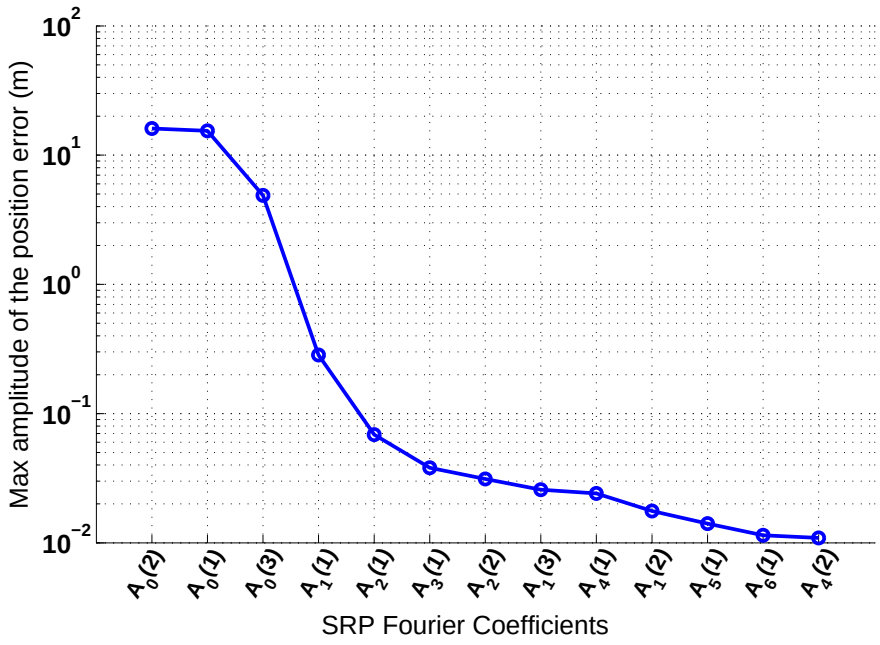

Figure 5.5: Spacecraft position error after 5 days due to errors in Fourier coefficients for the Sun-pointing attitude.

5.4 Small Body Radiation Pressure Fourier Series Model

In Section 3.3 we presented a model for an asteroid's surface radiation pressure imparted on spacecraft orbiting it. That formulation considered a plate model of a spacecraft to compute

www.manaraa.com

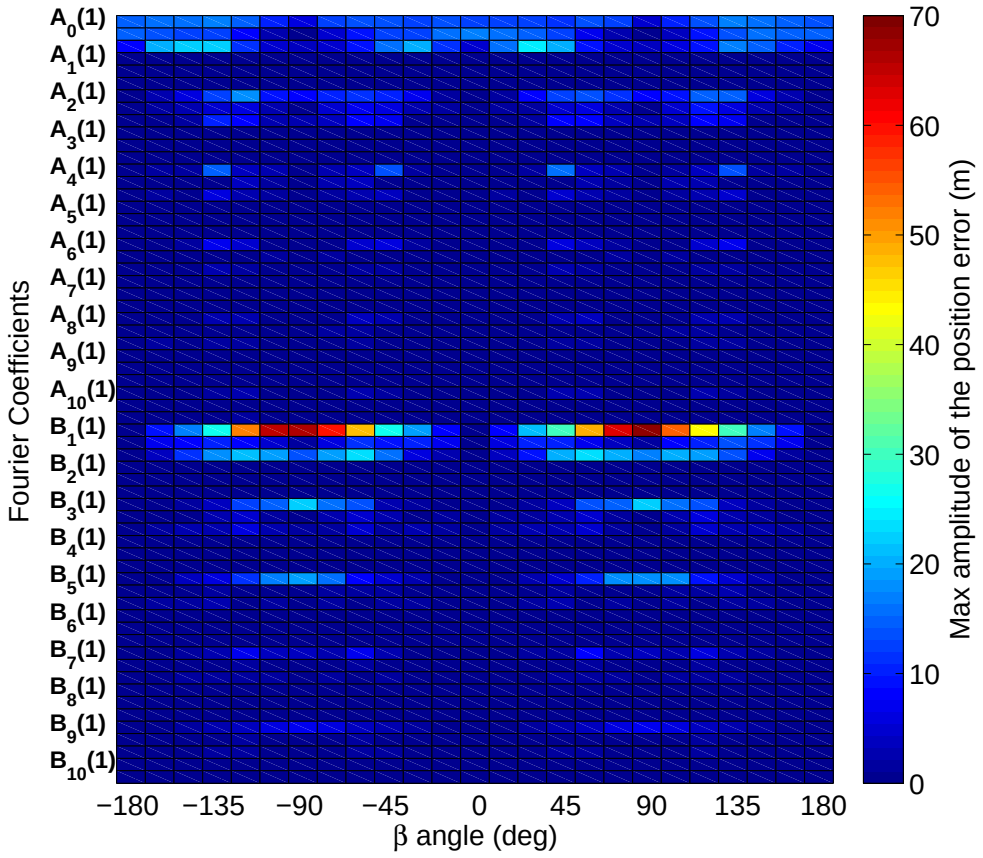

Figure 5.6: Spacecraft position error after 5 days due to errors in Fourier coefficients as a function of the beta angle.

the interaction of TRP with the orbiter (see Eq. (3.13)). However, as discussed in the previous sections, one may use a Fourier series expansion to compute an accurate representation of the SRP perturbation on a spacecraft. In this section we expand the Fourier series expansion to represent the TRP effect. Through this method, one can utilize the same Fourier series coefficients that were derived earlier in the computation of TRP perturbations, in addition to being able to formulate it easily in the estimation process. The Fourier series representation of the TRP force is given by

$$\mathbf{F}^b_{TRP} = \sum_{j\in\mathcal{K}} P_j \sum_{n=0}^{\infty} \left[\mathbf{A}_n(\delta_j)\cos(n\lambda_j) + \mathbf{B}_n(\delta_j)\sin(n\lambda_j)\right], \tag{5.52}$$

where δ_j and λ_j are the latitude and the longitude of an asteroid surface element j with respect to the spacecraft body fixed reference frame. Coefficients $\mathbf{A}_n(\delta_j)$ and $\mathbf{B}_n(\delta_j)$ are evaluated at the

www.manaraa.com

latitude δ_j. The produced acceleration due to this force is easily given by

$$\mathbf{a}^b_{TRP} = \frac{1}{m_{SC}} \sum_{j \in \mathcal{K}} P_j \sum_{n=0}^{\infty} \left[\mathbf{A}_n(\delta_j) \cos(n\lambda_j) + \mathbf{B}_n(\delta_j) \sin(n\lambda_j) \right]. \tag{5.53}$$

Figure 5.7 shows a comparison of the TRP acceleration computed using different methods, namely the plate model and the Fourier series representation of various expansion orders. The 10-plate model of the spacecraft detailed in Table 5.1 is used for the plate model computation of TRP effects. The simulated spacecraft is assumed to be in a circular terminator orbit about Bennu with an orbit radius of 1 km following a nadir-pointing attitude profile. The TRP force is generated from 32 surface elements on the asteroid. The surface temperature distribution is computed by the method described in Section 3.3.2. Using Eq. (3.19) we compute a thermal parameter of $\Theta = 1.6$ for Bennu. The assumed surface properties and the rotation rate of Bennu are given in Appendix B. A phase angle of $\approx 17^\circ$ towards the evening side from the sub-solar point is chosen for Bennu as it corresponds to the thermal parameter of $\Theta = 1.6$ according to Figure 3.2. The maximum and the minimum surface temperatures are also located from this figure. Figure 5.8 shows the temperature distribution that is simulated on the surface of Bennu.

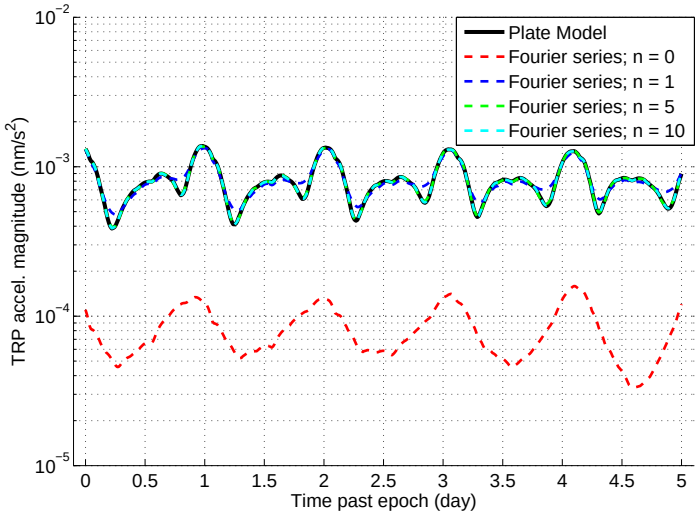

Figure 5.7: A comparison of the plate model vs. the Fourier series expansion for the computation of the TRP acceleration.

First thing that stands out from Figure 5.7 is the distinct difference between the zeroth order

www.manaraa.com

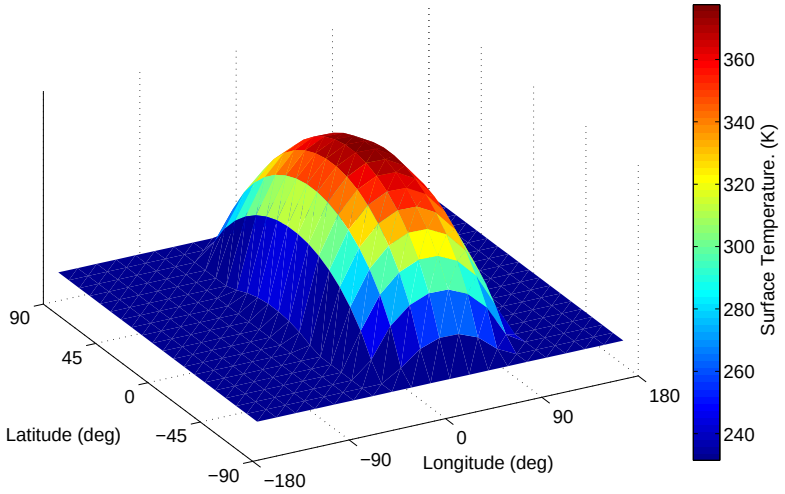

Figure 5.8: Simulated temperature distribution on the surface of Bennu.

expansion and the rest of the models. To understand this difference we need to consider the geometry of the setup. For the nadir-pointing attitude the spacecraft body fixed frame is oriented such that the $\hat{\mathbf{z}}_b$ axis is aligned with the orbit angular momentum vector. As a result, the asteroid surface as seen from the spacecraft body fixed frame occupies a latitudinal region of about $\pm 14^\circ$ (assuming asteroid radius of 250 meters and the orbit radius of 1 km). Furthermore, note that for this model we are using the same Fourier coefficients that are shown in Figure 5.2. As shown in that figure the zeroth order coefficients are very small and tend to zero at small latitude values, while the degree one coefficients capture the majority of the geometry magnitude. Increasing the expansion degree from 1 to higher will only fine tune the way the true TRP effect is captured. This is clear from Figures 5.7 as one can not easily distinguish the difference between the TRP acceleration magnitude given by an order 5 expansion and that given by an order 10 expansion.

Figure 5.9 shows a comparison of the SRP and TRP accelerations for the 1 km terminator orbit. At a distance of about 750 meters (1 km orbit radius) from the surface the magnitude of the TRP acceleration is about 2 orders of magnitude smaller than that for the SRP acceleration. The orbit being on the terminator plane contributes to the weak TRP effect, since the spacecraft

www.manaraa.com

is not directly exposed to the hotter sunlit side of the asteroid surface. To put this effect in a context, Figure 5.10 shows the average TRP acceleration magnitude along a circular terminator orbit with different radii. This figure shows that by decreasing the orbit radius by a half, the average TRP magnitude increases by a factor of 4, from 1% to about 4% of the magnitude of the SRP acceleration. This is an intuitive results as the intensity of the TRP acceleration is inversely related to the square of distance of spacecraft from the asteroid surface.

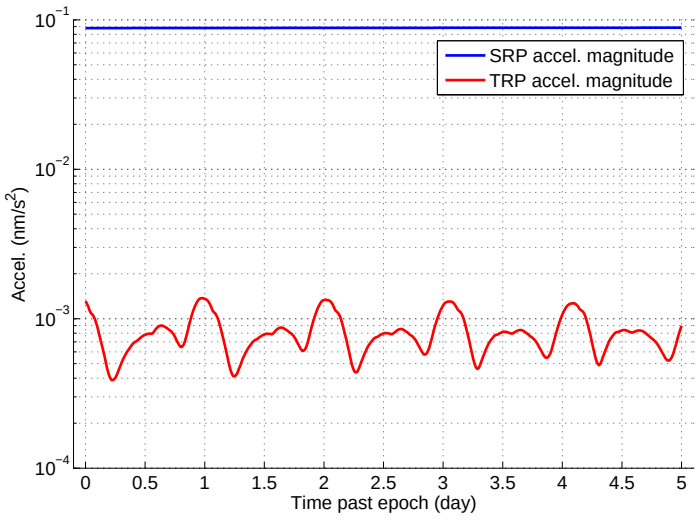

Figure 5.9: TRP and SRP acceleration magnitudes imparted on a spacecraft in a 1 km circular terminator orbit about Bennu.

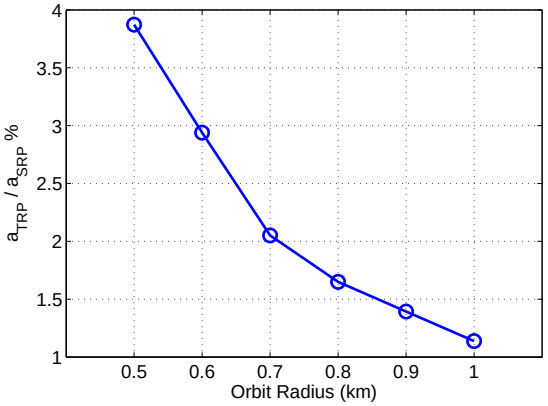

Figure 5.10: average TRP acceleration vs. different terminator orbit radii about Bennu.

www.manaraa.com

A TRP acceleration magnitude of 1–4% of the SRP acceleration is a small amount that may not be of much importance. However, for other trajectories that come close to the surface of the asteroid on the sunlit side the TRP effect may have more pronounced effects. For instance, this is the case for the TAG rehearsal and TAG departure trajectories of the OSIRIS-REx mission where the spacecraft is planned to fly over the designated TAG site from a distance of about 125 meters above the asteroid surface on the sunlit side [6]. Figure 5.11 shows a simulated TAG rehearsal trajectory of the spacecraft that starts from a 1 km circular terminator orbit and passes through a check point that is 125 meters above the planned TAG point at the -45° latitude. Figure 5.12 shows the TRP and the SRP acceleration magnitudes along this trajectory. As shown on this plot at the maximum point the intensity of the TRP acceleration may increase up to about 20% of the SRP acceleration magnitude. This is a potentially strong perturbation that may have a notable effect on orbit determination solutions and a spacecraft uncertainty propagation if it is not modeled properly.

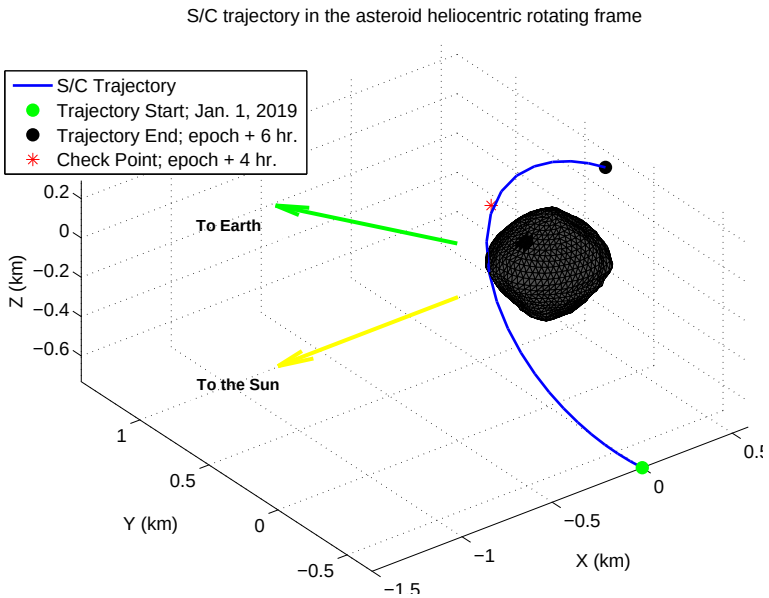

Figure 5.11: A simulated TAG rehearsal trajectory for the OSRIRIS-REx spacecraft about Bennu.

www.manaraa.com

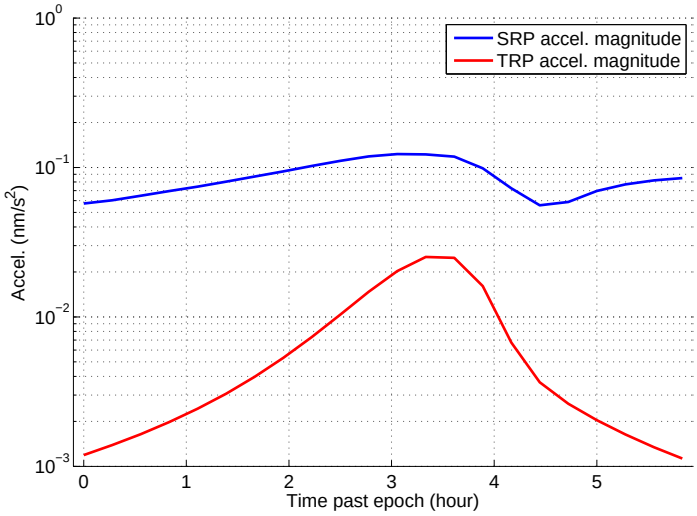

Figure 5.12: The TRP and the SRP acceleration magnitudes along the simulated TAG rehearsal trajectory.

5.5 Chapter Summary

This chapter presents a framework for precise modeling of SRP and TRP effects on spacecraft orbiting around small bodies with an example application for the OSIRIS-REx spacecraft. It uses a Fourier series expansion to model these perturbations. The Fourier series expansion is an efficient method for the computation of SRP and TRP effects. It also allows for the derivation of analytical solutions to the secular dynamics of an orbit due to the SRP perturbation. The derived analytical solutions show that there is a set of prominent Fourier coefficients that contribute the most to the secular evolution of an orbit. These expressions are derived for three different attitude profiles, namely the nadir-pointing, the Sun-pointing, and the Earth-pointing attitudes, which are defined before. Expressions given for the Sun-pointing and the Earth-pointing attitude profiles show that the orbit energy is conserved, on average. This results in the derivation of a simple closed form solution for the secular dynamics of an orbit under strong SRP perturbation.

Following the analytical derivations, we show the results from an error analysis. This study evaluates the sensitivity of the Fourier coefficients to some of the error sources that may occur in the computation of these coefficients. These are errors in the nominal attitude of a spacecraft,

www.manaraa.com

solar panel pointing errors, distortions in the nominal shape model of a spacecraft, and errors in the reflective properties of a spacecraft surfaces. The results show that such errors do change the nominal values of SRP coefficients, however the amount of the change is not significant. Nonetheless, this exercise establishes an error envelope around the nominal values for each SRP coefficient that is later utilized in the estimation studies. A subsequent Monte Carlo simulation analyzed the effects of errors in the Fourier coefficients on errors in the spacecraft trajectory. Results from this error analysis show that a handful of the lower order coefficients, mainly those that result in the secular dynamics, result in the largest amount of the error in the trajectory and the error magnitude diminishes rapidly for the higher order coefficients. Same trend is found for different attitude profiles.

Finally, we extend the Fourier series representation to model surface radiation pressure effects on spacecraft orbiting in a close proximity to a small body. We show that the Fourier series expansion is able to accurately represent TRP effects by utilizing the same Fourier coefficients that are derived in the spacecraft body-fixed frame for modeling SRP perturbations. A comparison of the TRP magnitude with the SRP effect showed that one might be able to ignore its effect for orbits that are relatively far from the surface of the asteroid, however its effects become more pronounced as a spacecraft passes close to the surface of an asteroid over its sunlit side.

www.manaraa.com

Chapter 6

Numerical Estimation and Covariance Analysis

In Chapter 5, we presented a Fourier series model for the precise representation of SRP and TRP perturbations on spacecraft orbiting around small bodies. We identified a set of prominent Fourier coefficients and studied their impact on the secular dynamics of an orbit. It was further shown that errors in modeling such prominent coefficient may potentially lead to considerable errors in modeling SRP effects on spacecraft. Errors in representing TRP effects may also result in small errors that could accumulate overtime to increase errors in the trajectory propagation of spacecraft about a small body. In this chapter, we continue with the study of this model and evaluating its performance in providing precise orbit determination solutions in the presence of errors and mis-modeling of the perturbing forces.

Section 6.1 presents a framework that utilizes a Fourier series model to perform the orbit determination of spacecraft around small bodies. Section 6.2 implements the laid out estimation framework to perform a comprehensive covariance analysis of the expected level of estimation precision on the spacecraft state and the Fourier coefficients. Finally, Section 6.3 uses this model to perform a precise orbit determination of a simulated spacecraft in orbit about Asteroid (101955) Bennu.

6.1 Estimation Framework

In this section we present an estimation framework that may be used to perform precise orbit determination of spacecraft orbiting in environments that are highly perturbed by solar radi-

www.manaraa.com

ation pressure and other perturbing forces, such as small body surface thermal radiation pressure effects.

6.1.1 Performance Metrics

Several performance metrics are considered to draw comparisons between different estimation results. We introduce three of the main ones here. The first performance metric that we consider is the weighted RMS of the post-fit residuals [87] (§ 4.6). We simply refer to this as the RMS of the residuals. A weighted RMS that is close to unity means that the estimation process is performing well and is able to extract all of the signals out of the measurement residuals. An RMS value larger than unity means that there exits a signal within the measurement residuals that is not accounted for by the estimation process. The second metric that we consider is the 3D-RMS of accuracy for the spacecraft position and velocity. In the cases that the truth model is available, one may difference the best estimate state from the truth model to compute the error (accuracy) of the estimated state. The 3D-RMS is basically the RMS of the magnitudes of the estimated state error vector. The smaller this number is, the better the fit is with the truth model. Finally, a correlation coefficient between two estimated state parameters is a measure of coupling between the two parameters. The correlation coefficient between estimated parameters i and j is given by

$$\rho_{ij} = \frac{\sigma_{ij}}{\sigma_i \sigma_j}, \tag{6.1}$$

where σ_{ij} is the covariance of the parameters i and j (ij^{th} element in the state estimate covariance matrix P) with the uncertainties of σ_i and σ_j. The value of the correlation coefficient ranges from -1 to $+1$. A $\rho_{ij} = \pm 1$ means that the two parameters are perfectly correlated, while $\rho_{ij} = 0$ means that there is no correlation between those parameters. Ideally, for a well-posed estimation problem, the correlation coefficient between different estimated parameters should be as small as possible. Large correlations between two parameters could indicate an ill-conditioned problem that could adversely affect the estimation results.

www.manaraa.com

6.1.2 Cramér-Rao Lower Bound

The results from a covariance study, e.g. studies shown in Section 6.2, show the best possible precision level of the estimated elements that is feasible for a given estimation problem and a set of measurements. This best possible level of precision is measured by the Cramér-Rao Lower Bound (CRLB) [88]. This limit is a useful threshold for analyzing the capability of an estimation problem without the need to produce a full solution. The CRLB is given by

$$\mathrm{P}_k \geq \mathrm{J}_k^{-1}, \tag{6.2}$$

where P_k is the state estimate covariance matrix and J_k is the Fisher Information Matrix (FIM) at time t_k. For a sequential Kalman filter, FIM may be computed using the following recursive formula [88]

$$\mathrm{J}_k = (\Phi(t_k, t_{k-1})\mathrm{J}_{k-1}^{-1}\Phi^{\mathrm{T}}(t_k, t_{k-1}))^{-1} + \tilde{H}_k^{\mathrm{T}} R_k^{-1} \tilde{H}_k, \tag{6.3}$$

where the dynamical model and the measurement model are linearized about the truth trajectory. The quantity R_k is the measurement error covariance matrix at time t_k. The recursion process starts by setting $J_0 = \bar{P}_0^{-1}$. This method is fairly simple and has been used extensively in performing covariance analyses of different kinds.

6.1.3 Partial Derivatives of the Force Models

In order to use a force model in a linear estimation filter or covariance analysis, one needs to compute the partial derivatives of that force model with respect to the estimated state elements. These partial derivatives are used to form a Jacobian for the dynamical model with respect to the state elements (see Eq. (2.17)), which is then used to derive the linearized dynamics and the STM of the estimated state elements. This process is detailed in Section 2.5. In this section, we present the derivation of the partial derivatives of the force models that are used in our numerical estimation studies.

www.manaraa.com

6.1.3.1 Partial derivative of the central body gravitational attraction

First, we discuss the partial derivative of the gravitational attraction of the central body. This chapter utilizes a spherical harmonics expansion of the gravitational potential and the derived acceleration from that expansion to model the gravitational attraction of the central body. The spherical harmonics expansion of the gravitational potential is presented in Section 3.1 and we will discuss this model in further detail in Chapter 7.

The Jacobian of the gravitational attraction is given by the second partial derivative of the gravitational potential function with respect to the spacecraft position vector. As mentioned in Section 3.1 we use Cunningham's method [17] to derive the fully normalized second partial of the spherical harmonics expansion with respect to the spacecraft position vector. The derivation of these partial derivative is very involved. The final set of the expressions for the second partial of the spherical harmonics expansion is given in Appendix A. This appendix also shows the partial derivatives of the gravitational acceleration with respect to the spherical harmonics coefficients.

6.1.3.2 Partial derivative of the third body acceleration

The gravitational acceleration of the third body perturbation is given by Eq. 3.20. The partial derivative of this force model with respect to the spacecraft position vector is simply given by

$$\frac{\partial \mathbf{a}_{3rd}}{\partial \mathbf{r}} = -\sum_{p=1}^{P} \frac{\mu_p}{r_{ps}^3} \left[\bar{\bar{U}} - 3\frac{\mathbf{r}_{ps}\mathbf{r}_{ps}}{r_{ps}^2} \right]. \tag{6.4}$$

6.1.3.3 Partial Derivatives for the SRP Fourier Series Model

The partial derivative of the Fourier series force model are required to perform the covariance studies (Section 6.2) and the simulations (Section 6.3). First we look at the partial derivatives of the SRP Fourier series expansion. To do so, we start the derivation by rewriting the Fourier series expansion of the SRP acceleration expressed in a reference frame suitable for performing numerical propagations. Such a frame is often chosen to be an inertial reference frame centered at

www.manaraa.com

the primary body. This is identified by the superscript I in the following expression

$$\mathbf{a}^I_{SRP} = \Psi \mathbf{a}^b_{SRP} = \Psi \frac{P(R)}{m_{SC}} \sum_{n=0}^{\infty} \left[\mathbf{A}_n \cos(n\lambda_s) + \mathbf{B}_n \sin(n\lambda_s) \right], \tag{6.5}$$

where a^b_{SRP} is the SRP acceleration expressed in the spacecraft body-fixed frame (see Eq.5.3). As a result, we define the rotation matrix Ψ to map the SRP acceleration from the spacecraft body-fixed frame to an inertial frame. The actual form of this mapping matrix depends on the attitude profile of the spacecraft. In this work, we look at three special attitude profiles that are most relevant to small body orbiting spacecraft missions. However, before focusing on the specifics of each attitude profile we first derive the general form of the partial derivative of the SRP acceleration with respect to the spacecraft state vector and the Fourier coefficients.

Partial derivative of the SRP acceleration with respect to a spacecraft position vector: The partial derivative of the SRP acceleration with respect to a spacecraft position vector $\mathbf{r}$ is given by

$$\frac{\partial \mathbf{a}^I_{SRP}}{\partial \mathbf{r}} = \frac{\partial \mathbf{a}^I_{SRP}}{\partial \Psi} \frac{\partial \Psi}{\partial \mathbf{r}} + \frac{\partial \mathbf{a}^I_{SRP}}{\partial P(R)} \frac{\partial P(R)}{\partial \mathbf{r}} + \frac{\partial \mathbf{a}^I_{SRP}}{\partial \lambda_s} \frac{\partial \lambda_s}{\partial \mathbf{r}}. \tag{6.6}$$

Note that in deriving the expression above we assume that the spacecraft mass m_{SC} and the SRP Fourier coefficients are constant values and are not a function of the spacecraft position vector. The first term in Eq. (6.6) is given by

$$\frac{\partial \mathbf{a}^I_{SRP}}{\partial \Psi} = \mathcal{A}_{a,\psi_1\psi_2}, \tag{6.7}$$

where $\mathcal{A}_{a,\psi_1\psi_2}$ is a rand 3 tensor. The subscript a indicates the component index of the vector $\mathbf{a}^I_{SRP}$, while the subscripts ψ_1 and ψ_2 identify the component index of the matrix Ψ. For a set value of the index $a = k$, the $\mathcal{A}^k_{\psi_1\psi_2}$ becomes a rank 2 tensor (a dyadic) that is given by

$$\mathcal{A}^k_{\psi_1\psi_2} = a_{SRP}(k)\bar{\bar{U}}, \ k = 1, \ 2, \text{ and } 3, \tag{6.8}$$

where $a_{SRP}(k)$ is the k^{th} component of the vector $\mathbf{a}_{SRP}$. Similarly we have

$$\frac{\partial \Psi}{\partial \mathbf{r}} = \mathcal{B}_{\psi_1\psi 2,r}, \tag{6.9}$$

where $\mathcal{B}_{\psi_1\psi 2,r}$ is a rank 3 tensor. The subscript r indicates the component index of the position vector $\mathbf{r}$, and should not be confused with the magnitude of the position vector that is used in

www.manaraa.com

other equations. The actual form of this tensor depends on the attitude profile of the spacecraft. In the case of the Sun-pointing or the Earth-pointing attitudes this partial derivative is equal to zero, i.e. $\partial\Psi/\partial\mathbf{r} = [0]_{\psi_1\psi 2,r}$. However, in the case of the nadir-pointing attitude profile the computation is more involved. For the nadir-pointing attitude profile Ψ is given by

$$\Psi = [\,\hat{\mathbf{r}}\;\hat{\mathbf{q}}\;\hat{\mathbf{h}}\,], \tag{6.10}$$

where $\hat{\mathbf{r}}$ is a unit vector in the radial direction, $\hat{\mathbf{q}}$ is a unit vector perpendicular to $\hat{\mathbf{r}}$ in the in-track direction, and $\hat{\mathbf{h}}$ is a unit vector in the cross-track direction parallel to the angular momentum vector of the spacecraft orbit. To proceed with the derivation of the partial derivatives, we derive the partial derivative of each column of matrix Ψ with respect to the position vector. In tensor notation this is $\mathcal{B}^k_{\psi_1,r}$ which is a dyadic and indicates the partial derivative of the k^{th} column of Ψ with respect to $\mathbf{r}$. Therefore we have

$$\mathcal{B}^1_{\psi_1,r} = \frac{\partial\hat{\mathbf{r}}}{\partial\mathbf{r}}. \tag{6.11}$$

Using the result from Eq. (2.7) we get

$$\mathcal{B}^1_{\psi_1,r} = \frac{\partial\hat{\mathbf{r}}}{\partial\mathbf{r}} = \frac{1}{r}\bar{\bar{U}} - \frac{1}{r^3}\mathbf{r}\mathbf{r}. \tag{6.12}$$

Next we discuss the partial derivative of the third column of the matrix Ψ with respect to $\mathbf{r}$, namely

$$\mathcal{B}^3_{\psi_1,r} = \frac{\partial\hat{\mathbf{h}}}{\partial\mathbf{r}}. \tag{6.13}$$

Using the result from Eq. (2.8) we have

$$\frac{\partial\hat{\mathbf{h}}}{\partial\mathbf{r}} = \frac{1}{h}\frac{\partial\mathbf{h}}{\partial\mathbf{r}} + \mathbf{h}\frac{\partial}{\partial\mathbf{r}}\left(\frac{1}{h}\right). \tag{6.14}$$

Note that $\mathbf{h} = \tilde{\mathbf{r}}\cdot\mathbf{v}$. Using this definition and the result from Eq. (2.8) one may rewrite Eq. (6.14) as

$$\mathcal{B}^3_{\psi_1,r} = \frac{\partial\hat{\mathbf{h}}}{\partial\mathbf{r}} = -\frac{1}{h}\left(\tilde{\mathbf{v}} - v^2\frac{\mathbf{h}\mathbf{r}}{h^2}\right). \tag{6.15}$$

The partial derivative of the second column of the matrix Ψ may be derived using the results from the other two columns and their partial derivatives, as $\hat{\mathbf{q}} = \tilde{\hat{\mathbf{h}}}\cdot\hat{\mathbf{r}}$. Therefore, we have

$$\mathcal{B}^2_{\psi_1,r} = \frac{\partial\hat{\mathbf{q}}}{\partial\mathbf{r}} = \tilde{\hat{\mathbf{h}}}\cdot\frac{\partial\hat{\mathbf{r}}}{\partial\mathbf{r}} - \tilde{\hat{\mathbf{r}}}\cdot\frac{\partial\hat{\mathbf{h}}}{\partial\mathbf{r}}, \tag{6.16}$$

www.manaraa.com

where the expressions for the first and the second partial derivatives are given by Eq. (6.12) and (6.15), respectively. Finally, collecting all the terms, the first component of Eq. (6.6) becomes

$$\frac{\partial \mathbf{a}_{SRP}^{I}}{\partial \Psi}\frac{\partial \Psi}{\partial \mathbf{r}} = \mathcal{A}_{a,\psi_1\psi_2}\mathcal{B}_{\psi_1\psi 2,r} = \mathcal{C}_{a,r}, \tag{6.17}$$

where we use Einstein's summation rule (see Eq. (2.6)) to sum over the common indices of tensors $\mathcal{A}$ and $\mathcal{B}$. As a results, $\mathcal{C}_{a,r}$ is a rank 2 tensor.

The second term in Eq. (6.6), i.e. the partial derivative of the SRP acceleration with respect to with respect to the solar radiation pressure function, is simply given by

$$\frac{\partial \mathbf{a}_{SRP}^{I}}{\partial P(R)} = \Psi\frac{1}{m}\sum_{n=0}^{\infty}\left[\mathbf{A}_n\cos(n\lambda_s) + \mathbf{B}_n\sin(n\lambda_s)\right]. \tag{6.18}$$

Eq. (3.9) expresses the radiation pressure function as a function of R which is the magnitude of the position vector of the spacecraft with respect to the Sun. This vector is given by

$$\mathbf{R} = \mathbf{r} + \mathbf{R}_{\oplus}, \tag{6.19}$$

where $\mathbf{R}_{\oplus}$ is the position vector of the central body with respect to the Sun. Therefore, we may write the following expression

$$\frac{\partial P(R)}{\partial \mathbf{r}} = \frac{\partial}{\partial \mathbf{r}}\left(\frac{G_1}{\mathbf{R}\cdot\mathbf{R}}\right) = -2\frac{G_1\mathbf{R}}{R^4}. \tag{6.20}$$

Combining this expression with Eq. (6.18) we have

$$\frac{\partial \mathbf{a}_{SRP}^{I}}{\partial P(R)}\frac{\partial P(R)}{\partial \mathbf{r}} = -\frac{2}{R^2}\mathbf{a}_{SRP}\mathbf{R}. \tag{6.21}$$

Lastly, we discuss the third term in Eq. (6.6). The partial derivative of the SRP acceleration with respect to the solar longitude is easily derived from Eq. (6.5), i.e.

$$\frac{\partial \mathbf{a}_{SRP}^{I}}{\partial \lambda_s} = \Psi\frac{P(R)}{m}\sum_{n=0}^{\infty} n\left[-\mathbf{A}_n\sin(n\lambda_s) + \mathbf{B}_n\cos(n\lambda_s)\right]. \tag{6.22}$$

To derive the partial derivative of the solar latitude with respect to the position vector we express the solar latitude as

$$\lambda_s = \arctan\left(\frac{u_b(2)}{u_b(1)}\right), \tag{6.23}$$

www.manaraa.com

where $u_b(1)$ and $u_b(2)$ are the first and the second components of the Sun vector $\mathbf{u}$ expressed in the spacecraft body-fixed frame. These are given by

$$u_b(1) = \hat{\mathbf{x}}_b \cdot \Psi^{\mathrm{T}} \mathbf{u} = \Psi^1 \cdot \mathbf{u},$$
$$u_b(2) = \hat{\mathbf{y}}_b \cdot \Psi^{\mathrm{T}} \mathbf{u} = \Psi^2 \cdot \mathbf{u}, \tag{6.24}$$

where Ψ^1 and Ψ^2 are simply the first and the second columns of the mapping matrix Ψ, respectively. Using the definition of λ_s given by Eq. 6.23 and the Eq. 2.9 we have

$$\frac{\partial \lambda_s}{\partial \mathbf{r}} = \left(u_b(1) \frac{\partial u_b(2)}{\partial \mathbf{r}} - u_b(2) \frac{\partial u_b(1)}{\partial \mathbf{r}} \right) \times \frac{1}{u_b(1)^2 + u_b(2)^2}. \tag{6.25}$$

Using Eq. (6.24), the partial derivatives of the Sun vector components with respect to the position vector are given by

$$\frac{\partial u_b(1)}{\partial \mathbf{r}} = \Psi^1 \cdot \frac{\partial \mathbf{u}}{\partial \mathbf{r}} + \mathbf{u} \cdot \frac{\partial \Psi^1}{\partial \mathbf{r}},$$
$$\frac{\partial u_b(2)}{\partial \mathbf{r}} = \Psi^2 \cdot \frac{\partial \mathbf{u}}{\partial \mathbf{r}} + \mathbf{u} \cdot \frac{\partial \Psi^2}{\partial \mathbf{r}}. \tag{6.26}$$

The Sun vector is defined as a vector pointing from the spacecraft to the Sun, i.e. $\mathbf{u} = -\mathbf{R}$. Hence, we simply derive

$$\frac{\partial \mathbf{u}}{\partial \mathbf{r}} = -\bar{\bar{U}}. \tag{6.27}$$

The partial derivatives of the columns of matrix Ψ with respect to the position vector in the Sun-pointing and the Earth-pointing attitudes are zeros. For the nadir-pointing attitude these quantities are given by Eq. (6.12) and (6.16).

Partial derivative of the SRP acceleration with respect to the spacecraft velocity vector: The partial derivative of SRP acceleration with respect to the spacecraft velocity vector may be derived using similar steps as those given in the previous section. This is given by

$$\frac{\partial \mathbf{a}^I_{SRP}}{\partial \mathbf{v}} = \frac{\partial \mathbf{a}^I_{SRP}}{\partial \Psi} \frac{\partial \Psi}{\partial \mathbf{v}} + \frac{\partial \mathbf{a}^I_{SRP}}{\partial \lambda_s} \frac{\partial \lambda_s}{\partial \mathbf{v}}. \tag{6.28}$$

The partial derivative of the mapping matrix Ψ with respect to the velocity vector is given by

$$\frac{\partial \Psi}{\partial \mathbf{v}} = \mathcal{B}_{\psi_1 \psi 2, v}, \tag{6.29}$$

www.manaraa.com

where $\mathcal{B}_{\psi_1\psi 2,v}$ is a rank 3 tensor. The subscript v indicates the component index of the velocity vector $\mathbf{v}$. This index notation should not be confused with the magnitude of the velocity vector. The value of this tensor, once again, depends on the attitude profile of a spacecraft. In the case of a Sun-pointing and an Earth-pointing attitude profiles for a spacecraft this partial derivative is equal to zero, i.e. $\partial\Psi/\partial\mathbf{v} = [0]_{\psi_1\psi 2,v}$. However, for the nadir-pointing attitude this partial is non-zero and the derivation of it is presented here. Recalling the notation introduced in the previous section we have

$$\mathcal{B}^1_{\psi_1\psi_2,v} = \frac{\partial\hat{\mathbf{r}}}{\partial\mathbf{v}} = \mathbf{0}. \tag{6.30}$$

Using the expression given by Eq. (2.8) and the definition of the angular momentum vector one may derive the following expression

$$\mathcal{B}^3_{\psi_1\psi_2,v} = \frac{\partial\hat{\mathbf{h}}}{\partial\mathbf{v}} = \frac{\tilde{\mathbf{r}}}{h}\cdot\left(\bar{\bar{U}} - \frac{r^2}{h^2}\mathbf{v}\mathbf{v}\right). \tag{6.31}$$

Finally, the partial derivative of the second column of the mapping matrix Ψ with respect to the velocity vector is given by

$$\mathcal{B}^2_{\psi_1,v} = \frac{\partial\hat{\mathbf{q}}}{\partial\mathbf{v}} = -\tilde{\hat{\mathbf{r}}}\cdot\frac{\partial\hat{\mathbf{h}}}{\partial\mathbf{v}}. \tag{6.32}$$

Collecting all of the terms for the first component of Eq. (6.28), results in

$$\frac{\partial\mathbf{a}^I_{SRP}}{\partial\Psi}\frac{\partial\Psi}{\partial\mathbf{v}} = \mathcal{A}_{a,\psi_1\psi_2}\mathcal{B}_{\psi_1\psi 2,v} = \mathcal{C}_{a,v}, \tag{6.33}$$

where $\mathcal{A}_{a,\psi_1\psi_2}$ is given by Eq. (6.7). Let us discuss the second term in Eq. (6.28). The partial derivative of the SRP acceleration with respect to the solar longitude is given by Eq. (6.22). Combining Eq. (6.23) with the result given by Eq. (2.9) the partial derivative of the solar longitude with respect to the velocity vector is simply given by

$$\frac{\partial\lambda_s}{\partial\mathbf{v}} = \left(u_b(1)\frac{\partial u_b(2)}{\partial\mathbf{v}} - u_b(2)\frac{\partial u_b(1)}{\partial\mathbf{v}}\right)\times\frac{1}{u_b(1)^2+u_b(2)^2}. \tag{6.34}$$

From Eq. (6.24) we may derive the following expressions

$$\begin{aligned}\frac{\partial u_b(1)}{\partial\mathbf{v}} &= \Psi^1\cdot\frac{\partial\mathbf{u}}{\partial\mathbf{v}} + \mathbf{u}\cdot\frac{\partial\Psi^1}{\partial\mathbf{v}},\\ \frac{\partial u_b(2)}{\partial\mathbf{v}} &= \Psi^2\cdot\frac{\partial\mathbf{u}}{\partial\mathbf{v}} + \mathbf{u}\cdot\frac{\partial\Psi^2}{\partial\mathbf{v}}.\end{aligned} \tag{6.35}$$

www.manaraa.com

Note that $\partial \mathbf{u}/\partial v = 0$. Therefore one only needs to compute the partial derivatives of the first and second columns of the Ψ matrix with respect to the velocity vector. But, for the Sun-pointing and the Earth-pointing attitude profiles these quantities are zeros. Therefore for these attitude profiles we have $\partial \lambda_s/\partial v = 0$. For the nadir-pointing attitude we have

$$\begin{aligned} \frac{\partial \Psi^1}{\partial \mathbf{v}} &= \frac{\partial \hat{\mathbf{r}}}{\partial \mathbf{v}} = 0, \text{ and} \\ \frac{\partial \Psi^2}{\partial \mathbf{v}} &= \frac{\partial \hat{\mathbf{q}}}{\partial \mathbf{v}} = -\tilde{\hat{\mathbf{r}}} \cdot \frac{\partial \hat{\mathbf{h}}}{\partial \mathbf{v}}. \end{aligned} \tag{6.36}$$

The quantity $\partial \hat{\mathbf{h}}/\partial \mathbf{v}$ is given by Eq. (6.31). As a result, for a nadir-pointing attitude Eq. (6.37) simplifies to

$$\frac{\partial \lambda_s}{\partial \mathbf{v}} = \frac{-u_b(1)}{u_b(1)^2 + u_b(2)^2}\, \mathbf{u} \cdot \tilde{\hat{\mathbf{r}}} \cdot \frac{\partial \hat{\mathbf{h}}}{\partial \mathbf{v}}. \tag{6.37}$$

Partial derivative of SRP acceleration with respect to the Fourier coefficients: In order to perform estimation of the SRP Fourier coefficients via the orbit determination process, it is necessary to compute the partial derivative of the SRP acceleration with respect to each of the estimated SRP coefficients. Derivation of such partial derivatives is fairly simple using the expression given for the SRP acceleration by Eq. (6.5) and the constant value assumption for the SRP fourier coefficients. Partial derivatives of the SRP acceleration with respect to order ℓ Fourier coefficients are given by

$$\begin{aligned} \frac{\partial \mathbf{a}_{SRP}^I}{\partial \mathbf{A}_\ell} &= \Psi \frac{P(R)}{m} \cos(\ell \lambda_s), \text{ and} \\ \frac{\partial \mathbf{a}_{SRP}^I}{\partial \mathbf{B}_\ell} &= \Psi \frac{P(R)}{m} \sin(\ell \lambda_s). \end{aligned} \tag{6.38}$$

This concludes the derivation of the partial derivative of the SRP acceleration with respect to the spacecraft state and the Fourier coefficients.

6.1.3.4 Partial derivative of TRP Fourier series expansion

In this section we brief the partial derivative of the TRP Fourier model. Due to the similarity between the SRP and the TRP Fourier expansion models, many of the derivations shown in the

www.manaraa.com

previous section apply for both of the models. Here, we only point out what is different for the case of the TRP model. The Fourier series expansion of the TRP acceleration is given in the spacecraft body-fixed frame by Eq. (5.53). Similar to the SRP acceleration, this acceleration is mapped into a reference frame suitable for the estimation purposes, e.g. an inertial reference frame. Hence, we rewrite the TRP Fourier expansion as

$$\mathbf{a}^I_{TRP} = \Psi \mathbf{a}_{TRP} = \frac{\Psi}{m} \sum_{j \in \mathcal{K}} P_j \sum_{n=0}^{\infty} \Big[\mathbf{A}_n(\delta_j) \cos(n\lambda_j) + \mathbf{B}_n(\delta_j) \sin(n\lambda_j) \Big], \tag{6.39}$$

where $\mathbf{a}_{TRP}$ is the TRP acceleration expressed in the spacecraft body-fixed frame (see Eq.3.15). We use this equation to compute the partial derivatives of the TRP acceleration with respect to the state parameters.

Partial derivative of the TRP acceleration with respect to the spacecraft position vector: With the assumption that the spacecraft mass and the TRP Fourier coefficients are independent of the position vector, the partial derivative of the TRP acceleration with respect to spacecraft position vector is given by

$$\frac{\partial \mathbf{a}^I_{TRP}}{\partial \mathbf{r}} = \frac{\partial \mathbf{a}^I_{TRP}}{\partial \Psi} \frac{\partial \Psi}{\partial \mathbf{r}} + \sum_{j \in \mathcal{K}} \frac{\partial \mathbf{a}^I_{TRP}}{\partial P_j} \frac{\partial P_j}{\partial \mathbf{r}} + \sum_{j \in \mathcal{K}} \frac{\partial \mathbf{a}^I_{TRP}}{\partial \lambda_j} \frac{\partial \lambda_j}{\partial \mathbf{r}}. \tag{6.40}$$

This equation is composed of three main parts. For the first part we have

$$\frac{\partial \mathbf{a}^I_{SRP}}{\partial \Psi} = \mathcal{L}_{a,\psi_1\psi_2}, \tag{6.41}$$

where $\mathcal{L}_{a,\psi_1\psi_2}$ is a tensor of rank 3 and dimension 3. The subscript a indicates the components of the vector $\mathbf{a}^I_{TRP}$, while the subscripts ψ_1 and ψ_2 identify the components of the matrix Ψ. For a set value of the index $a = k$, the $\mathcal{L}^k_{\psi_1\psi_2}$ becomes a dyadic that is given by

$$\mathcal{L}^k_{\psi_1\psi_2} = a_{TRP}(k)\bar{\bar{U}}, \ k = 1, \ 2, \text{ and } 3, \tag{6.42}$$

where $a_{TRP}(k)$ is the k^{th} component of the TRP acceleration vector expressed in the spacecraft body-fixed frame. The quantity $\partial\Psi/\partial\mathbf{r}$ is given by Eq. (6.9). For the second part in Eq. (6.40) we have

$$\frac{\partial \mathbf{a}^I_{TRP}}{\partial P_j} = \frac{\Psi}{m} \sum_{n=0}^{\infty} \Big[\mathbf{A}_n(\delta_j) \cos(n\lambda_j) + \mathbf{B}_n(\delta_j) \sin(n\lambda_j) \Big]. \tag{6.43}$$

www.manaraa.com

In computing the quantity $\partial P_j/\partial \mathbf{r}$ we refer to Eq. (3.14) and note that

$$\cos(\alpha_j) = \frac{(\mathbf{r}-\mathbf{b}_j)\cdot\mathbf{b}_j}{b\,u_j}, \text{ and}$$
$$u_j = \sqrt{(\mathbf{r}-\mathbf{b}_j)\cdot(\mathbf{r}-\mathbf{b}_j)}. \tag{6.44}$$

Substituting these expressions in Eq. (3.14) and taking its partial derivative with respect to the position vector $\mathbf{r}$ we get

$$\frac{\partial P_j}{\partial \mathbf{r}} = \left(\tau_j a_j G_R \cos(\theta_j) + f_\epsilon(T_j)\right)\frac{dA_j}{c\,\pi\,u_j^3}\left[\hat{\mathbf{b}} - 3(\hat{\mathbf{u}}_j\cdot\hat{\mathbf{b}})\hat{\mathbf{u}}_j\right]. \tag{6.45}$$

Finally, the third part in Eq. (6.40), i.e. the partial derivative of the TRP acceleration with respect to the surface element longitude, is simply given by

$$\frac{\partial \mathbf{a}^I_{SRP}}{\partial \lambda_j} = \Psi\frac{P_j}{m}\sum_{n=0}^{\infty} n\left[-\mathbf{A}_n(\delta_j)\sin(n\lambda_j) + \mathbf{B}_n(\delta_j)\cos(n\lambda_j)\right]. \tag{6.46}$$

To derive the quantity $\partial\lambda_j/\partial\mathbf{r}$ we repeat the same process that we followed for deriving the partial derivative of the solar longitude λ_s with respect to the position vector, i.e. Eq. (6.25) and (6.26), by substituting $\mathbf{u}_j$ and its components in place of $\mathbf{u}$ and the components of vector $\mathbf{u}$. Further, note that

$$\frac{\partial \mathbf{u}_j}{\partial \mathbf{r}} = -\bar{\bar{U}}, \tag{6.47}$$

and that the rest of the expressions are computed the same way as before.

Partial derivative of the TRP acceleration with respect to the spacecraft velocity vector: The partial derivative of the TRP acceleration with respect to the velocity vector is given by

$$\frac{\partial \mathbf{a}^I_{TRP}}{\partial \mathbf{v}} = \frac{\partial \mathbf{a}^I_{TRP}}{\partial \Psi}\frac{\partial \Psi}{\partial \mathbf{v}} + \sum_{j\in\mathcal{K}}\frac{\partial \mathbf{a}^I_{TRP}}{\partial \lambda_j}\frac{\partial \lambda_j}{\partial \mathbf{v}}. \tag{6.48}$$

The only quantity that is not discussed in the earlier equations is $\partial\lambda_j/\partial\mathbf{v}$. This quantity can be computed by following the same steps given in Eq. (6.34) and (6.37) and replacing the vector $\mathbf{u}$ and its components with vector $\mathbf{u}_j$ and its components.

Partial derivative of TRP acceleration with respect to the Fourier coefficients: One needs to compute these partial derivatives in order to perform estimation of the TRP Fourier coefficients

www.manaraa.com

via an orbit determination process. This derivation is very similar to the one given in the previous section for the SRP coefficients, it that the partial derivatives of the TRP acceleration with respect to order ℓ Fourier coefficients are given by

$$\begin{aligned} \frac{\partial \mathbf{a}^I_{TRP}}{\partial \mathbf{A}_\ell(\delta_j)} &= \frac{\Psi}{m} P_j \cos(\ell\lambda_j), \text{ and} \\ \frac{\partial \mathbf{a}^I_{SRP}}{\partial \mathbf{B}_\ell(\delta_j)} &= \frac{\Psi}{m} P_j \sin(\ell\lambda_j). \end{aligned} \tag{6.49}$$

This concludes the derivation of the partial derivative of the TRP acceleration with respect to the spacecraft state and the Fourier coefficients.

6.1.4 Measurement Models

In this section we briefly describe the measurement types that are used in the subsequent estimation simulation studies. We describe the models that are used to generate the simulated measurements as well as the derivations of their partial derivative with respect to the relevant estimated state parameters.

6.1.4.1 Radiometric measurements

A measurement type that is used in the simulation studies presented in this work is a radiometric type measurement between the Earth-based antennas and the spacecraft. We simulate and process idealized range and range-rate measurements. These are given by

$$\begin{aligned} \rho_i(t) &= |\mathbf{r}_i(t) - \mathbf{r}(t)| + \epsilon_\rho, \\ \dot{\rho}_i(t) &= \frac{(\mathbf{r}_i(t) - \mathbf{r}(t)) \cdot (\mathbf{v}_i(t) - \mathbf{v}(t))}{|\mathbf{r}_i(t) - \mathbf{r}(t)|} + \epsilon_{\dot{\rho}}, \end{aligned} \tag{6.50}$$

where ρ_i and $\dot{\rho}_i(t)$ are the idealized range range-rate between the i^{th} Earth-based antenna and a spacecraft. Vectors $\mathbf{r}_i(t)$ and $\mathbf{v}_i(t)$ are the inertial position and velocity vectors of the i^{th} Earth-based antenna at time t and ϵ_ρ and $\epsilon_{\dot{\rho}}$ are the noises associated with the range and the range-rate measurements, respectively. This is a simplified way of simulating radiometric measurements between spacecraft and Earth-based antennas such as the DSN network. In reality there are several

www.manaraa.com

factors that should be considered in generating these measurements, such as the measurement bias, light travel time correction, corrections due to Earth's ionosphere effects, errors in spacecraft clock (if one-way ranging is done), and so on. However, none of these subjects are the focus of the simulations that we implement here and as a result we choose to simulate the simplified measurements instead. During the simulation we corrupt the simulated measurements with a certain amount of noise that is comparable with realistic measurement noise levels that exist due to some of the factors mentioned earlier. To process these measurements, the estimation filter requires their partial derivatives with respect to the estimated state elements (see Eq. (2.24)). These partial derivatives are given in Appendix F.

6.1.4.2 Optical landmark measurements

Optical navigation (OpNav) is a powerful tool that has been used in several previous deep space [8, 9, 27, 68] and currently ongoing [34, 35, 51, 66] missions. It uses imaging data from an onboard camera to aid spacecraft navigation by supplementing relative information between the spacecraft and the target body. In a general sense, the process of generating optical measurements that may be used by an orbit determination algorithm may be divided into two steps; resolving the location of a target object within an image and relating the image location of a target to the attitude and location of the spacecraft with respect to that target body. The former falls within the realm of image processing while the latter is related to geometry of optical navigation process.

Several methods are used to process the image of a target body and the features on it. Some of these methods, such as the target center finding or limb scanning algorithms [94] are mainly used during the approach phase of a spacecraft to a target when the entire or a considerable portion of the target body fits inside the image taken by the navigation camera. Another method that is used in generating optical observables is called stereo-photoclinometry (SPC) [25]. In this work, we focus on this method. The SPC is performed in conjunction with the characterization of the shape of the small body when the spacecraft is in a fairly close distance from the object when the surface features are discernable by the imagery.

www.manaraa.com

The SPC is a technique that has been developed over the last few decades [22, 23, 24]. The process involves taking multiple images of the surface features at different view angles, surface illuminations, and distances from the surface. These images are then correlated with each other to render a set of small digital maps of surface topography and albedo, each one called an L-map. The individual L-maps each overlapping with one or more other L-maps are assembled into a global topography solution (a basic shape model) of the small body. The main product of the SPC process that is used in the determination of the spacecraft orbit is a set of surface landmarks each defined as the center point of an L-map [25]. A landmark is basically a position vector that identifies the location of the center point of an L-map on the surface of the object. At the beginning, this is an iterative process in which the landmarks are used in improving the state estimate of the orbiting spacecraft which in turn is used in generation of more accurate landmark set and more precise shape model for the small body. After the solution is converged on a precise shape model of the object, the orbit determination of the spacecraft may use the generated landmark set only as the observable set input for the estimation filter. In this work we assume that the SPC is performed in advance an a landmark set is available to generate the OpNav observables.

The geometry of the landmark tracking process is described in detail by Owen [94]. Here, we present a brief review of this process. The line of sight (LOS) vector from the camera (assumed to be rigidly mounted on the spacecraft) to the ith landmark, ∇_i, is defined by

$$\nabla_i^I = \ell_i - \mathbf{r}, \tag{6.51}$$

where ℓ_i and $\mathbf{r}$ are the position vectors of the ith landmark and the spacecraft, respectively, both expressed in an inertial coordinate system. This vector is then projected onto the navigation camera focal plane to identify the *sample* and *line* observables, which are basically the horizontal and vertical location of the camera's charged-coupled device (CCD) for a give landmark image. These observables are defined in the camera-fixed frame $\widehat{\mathbf{MNL}}$, which is defined such that $\hat{\mathbf{L}}$ is in the direction of the camera's boresight, $\hat{\mathbf{M}}$ is to the right of the camera, and $\hat{\mathbf{N}}$ completes the triad. Note that the actual pointing directions of the $\hat{\mathbf{M}}$ and $\hat{\mathbf{N}}$ axes are not important. The LOS vector

www.manaraa.com

coordinates are expressed in the camera-fixed frame via the following transformation

$$\nabla^C = \begin{bmatrix} o_1 \\ o_2 \\ o_3 \end{bmatrix} = \Xi \nabla^I, \tag{6.52}$$

where

$$\Xi = \mathrm{Rot3}(\phi)\mathrm{Rot2}(90 - \delta)\mathrm{Rot3}(\alpha). \tag{6.53}$$

The matrices $\mathrm{Rot2}$ and $\mathrm{Rot3}$ are simple Euler angle rotations about the 2nd and 3rd axes, respectively. Angles α, δ, and ϕ are camera's inertial pointing direction expressed in the right ascension, declination, and a twist around the boresight. Using a gnomonic projection the LOS vector is projected onto camera focal plane. The projected coordinates are identified by $[\xi, \eta]$ such that,

$$\begin{bmatrix} \xi \\ \eta \end{bmatrix} = \frac{f}{o_3} \begin{bmatrix} o_1 \\ o_2 \end{bmatrix}. \tag{6.54}$$

The variable f is the focal length of the camera. Usually, these coordinates are specified in the units of mm. The projected coordinates are corrected due to the distortion effects and the misalignment (tip and tilt) of the detector with respect to a plane that is perfectly perpendicular to the boresight axis. The corrected coordinates are given by

$$\begin{bmatrix} \xi' \\ \eta' \end{bmatrix} = \begin{bmatrix} \xi \\ \eta \end{bmatrix} + \begin{bmatrix} \xi\gamma^2 & \xi\eta & \xi^2 \\ \eta\gamma^2 & \eta^2 & \xi\eta \end{bmatrix} \begin{bmatrix} \epsilon_1^c \\ \epsilon_2^c \\ \epsilon_3^c \end{bmatrix}, \tag{6.55}$$

where $\gamma^2 = \xi^2 + \eta^2$, ϵ_1^c is the distortion coefficient, and ϵ_2^c and ϵ_3^c are the error coefficients due to the detector misalignment specified for a given camera [66]. Finally, the sample and line (s, l) observables are given by

$$\begin{bmatrix} s \\ l \end{bmatrix} = \begin{bmatrix} s_0 \\ l_0 \end{bmatrix} + \begin{bmatrix} K_{11} & K_{12} \\ K_{21} & K_{22} \end{bmatrix} \begin{bmatrix} \xi' \\ \eta' \end{bmatrix}, \tag{6.56}$$

where the matrix K contains the information about the pixel dimensions of the CCD in the units of pixels/mm. For an ideal CCD with square pixels the diagonal terms are equal to each other and

www.manaraa.com

the off-diagonal terms are zeros. This is not the case for a rectangular pixel. The actual form of the matrix K is computed by calibrating the camera [94].

6.2 Covariance Analysis

In this section we implement a set of covariance studies to evaluate the expected level of estimation precision possible for an estimation framework that uses a Fourier series expansion to model the perturbing effects of SRP and TRP. In doing so, we are interested in finding the level of estimation precision possible for the Fourier coefficients, specially those that have the most dominant effect on the spacecraft state error propagation. The covariance study is performed separately for three main spacecraft attitude profiles that were described earlier, namely the nadir-pointing, the Sun-pointing, and the Earth-pointing attitudes. First we explain the setup of the covariance study and then present its results.

6.2.1 Covariance Study Setup

The estimated state $\mathbf{X}$ that is considered for the covariance analysis is given by

$$\mathbf{X} = \left[\mathbf{r}^{\mathrm{T}} \;\; \mathbf{v}^{\mathrm{T}} \;\; \mathbf{AB}_{SRP} \;\; \mathbf{AB}_{TRP}^{1} \;\; \mathbf{AB}_{TRP}^{2} \;\; \ldots \;\; \mathbf{AB}_{TRP}^{K} \;\; \mu \;\; \mathbf{CS}^{e}\right]^{\mathrm{T}}, \tag{6.57}$$

where $\mathbf{r}$ and $\mathbf{v}$ are the spacecraft position and velocity vectors, respectively. The vector $\mathbf{AB}_{SRP}$ is a vector of the realized Fourier coefficients for the SRP Fourier model and $\mathbf{AB}_{TRP}^{j}$ is a vector of the realized coefficients for the TRP model associated with the small body surface element j. Superscript K indicates the total number of the surface elements used in the TRP Fourier model. It is important to note that these coefficients are essentially the same physical coefficients that are included in both the SRP and TRP models. However, depending on the value of the radiation line latitude (i.e. the sunlight vector for the SRP model and the vector from the spacecraft to the surface element j, $\mathbf{u}_j$, for the TRP model) they assume different values. This is the reason that the two sets of the coefficients are considered separately. Finally, μ is the gravitational parameter and $\mathbf{CS}^{e}$ is a vector of the spherical harmonics coefficients for the gravitational attraction of the

www.manaraa.com

central body. See Chapter 7 for detailed information regarding these coefficients. Estimating these coefficients is not the focus of this particular study, however we include the spherical harmonics in the estimation process to identify the presence of any strong correlation that may exist between the gravity coefficients and the Fourier coefficients. Such strong correlations, if present, may adversely affect the performance of the estimation process.

The form of the $\mathbf{AB}_{SRP}$ vector depends on the attitude profile of the spacecraft. For the nadir-pointing attitude this vector takes the form

$$\mathbf{AB}_{SRP} = [\mathbf{A}^s_{0\ldots\ell} \;\; \mathbf{B}^s_{1\ldots\ell}], \tag{6.58}$$

where $\mathbf{A}^s_{0\ldots\ell}$ and $\mathbf{B}^s_{1\ldots\ell}$ stand for the vectors of the body-fixed $\mathbf{A}$ and $\mathbf{B}$ Fourier coefficients up the estimated order ℓ, that is

$$\begin{aligned}
\mathbf{A}^s_{0\ldots\ell} &= [A^s_0(1) \;\; A^s_0(2) \;\; A^s_0(3) \;\; A^s_1(1) \;\; A^s_1(2) \;\; \ldots \;\; A^s_\ell(3)], \\
\mathbf{B}^s_{1\ldots\ell} &= [B^s_1(1) \;\; B^s_1(2) \;\; B^s_1(3) \;\; B^s_2(1) \;\; B^s_2(2) \;\; \ldots \;\; B^s_\ell(3)].
\end{aligned} \tag{6.59}$$

The superscript s indicates that these coefficients are evaluated at the proper solar latitude for the SRP model. In the case of the Sun-pointing attitude, $\mathbf{AB}_{SRP}$ takes the form

$$\mathbf{AB}_{SRP} = \mathbf{A}^{\odot^{\mathrm{T}}}, \tag{6.60}$$

while for the Earth-pointing attitude profile this vector is given by

$$\mathbf{AB}_{SRP} = \mathbf{A}^{\oplus^{\mathrm{T}}}. \tag{6.61}$$

The $\mathbf{A}^{\odot}$ and $\mathbf{A}^{\oplus}$ coefficients are defined in Section 5.2.2. The $\mathbf{AB}^j_{TRP}$ is the set of the Fourier coefficients are associated with the small body surface element j. This is given by

$$\mathbf{AB}^j_{TRP} = [\mathbf{A}^j_{0\ldots\jmath} \;\; \mathbf{B}^j_{1\ldots\jmath}], \tag{6.62}$$

where $\mathbf{A}^j_{0\ldots\jmath}$ and $\mathbf{B}^j_{1\ldots\jmath}$ are the vectors of the body-fixed TRP coefficients associated with the surface element j and up the estimated order $\jmath$, i.e.

$$\begin{aligned}
\mathbf{A}^j_{0\ldots\jmath} &= [A^j_0(1) \;\; A^j_0(2) \;\; A^j_0(3) \;\; A^j_1(1) \;\; A^j_1(2) \;\; \ldots \;\; A^j_\jmath(3)], \\
\mathbf{B}^j_{1\ldots\jmath} &= [B^j_1(1) \;\; B^j_1(2) \;\; B^j_1(3) \;\; B^j_2(1) \;\; B^j_2(2) \;\; \ldots \;\; B^j_\jmath(3)].
\end{aligned} \tag{6.63}$$

www.manaraa.com

Finally, the vector $\mathbf{CS}^e$ is given by

$$\mathbf{CS}^e = [\bar{C}^e_{20}\ \bar{C}^e_{21}\ \bar{S}^e_{21}\ \ldots\ \bar{C}^e_{\imath\imath}\ \bar{S}^e_{\imath\imath}], \tag{6.64}$$

where the $\bar{C}^e$ and $\bar{S}^e$ are the well known fully normalized spherical harmonics coefficients of the gravitational attraction of the central body up to a degree and order $\imath$. Note that we assume the center of the spherical harmonics expansion is coincident with the center of mass (COM) of the central body such that the degree and order 1 coefficients vanish [77] (Ch. 2).

6.2.2 Dynamical Model

The time evolution of the estimated state is given by

$$\begin{aligned}
&\dot{\mathbf{r}} = \mathbf{v},\\
&\dot{\mathbf{v}} = \mathbf{a}_{\oplus} + \mathbf{a}^I_{SRP} + \mathbf{a}^I_{TRP} + \mathbf{a}_{3^{\mathrm{rd}}},\\
&\dot{\mathbf{AB}}_{SRP} = 0,\\
&\dot{\mathbf{AB}}^j_{TRP} = 0,\ j = 1, 2, \ldots K,\\
&\dot{\mu} = 0,\ \text{and}\\
&\dot{\mathbf{CS}}^e = 0,
\end{aligned} \tag{6.65}$$

where $\mathbf{a}_{\oplus}$ is the acceleration due to the central body, which in this case is the asteroid. This acceleration includes the asteroid point mass gravitational attraction as well as the non-spherical gravitational perturbations given by Eq. (3.7). The accelerations due to SRP and TRP are given by $\mathbf{a}_{SRP}$ and $\mathbf{a}_{TRP}$, respectively. The Sun's third-body perturbation is denoted by $\mathbf{a}_{3^{\mathrm{rd}}}$. The SRP and TRP accelerations are specified in an inertial frame.

The set of the expressions given by Eq. (6.65) are used to generate a set of truth trajectories for different attitude regimes of the spacecraft, namely the nadir-pointing, Sun-pointing, and Earth-pointing attitude profiles. We perform an example covariance analysis for an orbit about Bennu. The nominal trajectory is chosen to be an initially circular terminator orbit with a radius of 1 km. Table 6.1 summarizes the parameters that are used in generating the truth trajectories. The simulation epoch is chosen such that Bennu is at its perihelion at that epoch. We should also note

www.manaraa.com

that for the nadir-pointing attitude profile the spacecraft is oriented such that at the epoch of the simulation $\lambda_{s_0} = 0$. Therefore, according to Eq. (5.8) $\mathbf{A}'_n = \mathbf{A}_n$ and $\mathbf{B}'_n = -\mathbf{B}_n$. While this is not necessary for the estimation process, it allows us to directly related the covariance analysis results that are based on the body-fixed coefficients to the secular equations given by Eq. (5.38) and (5.40).

Table 6.1: Truth Model Parameters

Simulation Epoch:	2019 Jan 10 18:42:10.321 TDB
Force Model	
Central Body:	101955 Bennu ($\mu = 5.2\ m^3/s^2$) [15]
Gravitational Perturbations:	16×16 spherical harmonic model, Eq. (3.7) (*Generated from a polyhedron model with a bulk density of* $1,260\ kg/m^3$ [64].)
Solar Radiation Pressure:	Fourier series expansion up to degree 25, Eq. (5.3)
Asteroid Surface Radiation Pressure:	Fourier series expansion up to degree 10, Eq. (3.15) The expansion contains 32 surface elements, K = 32.
Third body:	Sun (point mass)

6.2.3 Measurement Model

We process a combination of simulated optical landmark measurements from the surface of the asteroid as well as simulated radiometric measurements between three simulated DNS antennas and a spacecraft. Optical landmark observations consist of a set of sample and line measurements from a total of 100 landmarks that are selected randomly on the surface of the asteroid. A fairly wide-angle camera is assumed to be mounted on the spacecraft with a focal length of about 12 mm and a 30° field of view (FOV) with a 512×512 pixels array. Landmarks go in and out of the camera FOV as the orbiter goes around the asteroid and as the asteroid rotates about its rotation axis. A 2° limit above the horizon determines when a landmark is in view of the camera, given that it falls within the FOV limit of the camera and that it is illuminated by the

www.manaraa.com

sunlight. Figures 6.1 and 6.2 show the number of the visible landmarks along the observation arc for the nadir-pointing and the Sun-pointing attitude profiles, respectively. Note that during the Sun-pointing attitude profile, landmarks are in view of the camera only a small portion of the orbit as the camera is pointing at a fixed direction in space. This is not the case for the nadir pointing attitude and as a results the average number of the visible landmarks is higher for this attitude profile.

For the radiometric measurements we simulate idealized range and range-rate between DSN antennas and a spacecraft. Three DSN antennas are chosen for simulating these measurements, namely DSS14 in Goldstone, CA, DSS43 in Canberra, Australia, and DSS63 in Madrid, Spain. A local antenna mask of 10° is applied to the DSN antennas when generating the measurements. The observations are generated when the line-of-sight between a DSN antenna and the spacecraft is not occulted. Further details on these measurement models are given in Section 6.1.4. The landmark sample and line observations are generated once every 5 minutes continuously

Table 6.2: Summary of the estimated state *a priori* uncertainties and measurement errors

Parameter	1-σ *a priori* Uncertainty
Spacecraft position	
X, Y, Z	10 m
Spacecraft velocity	
V_x,V_y,V_z	10 cm/sec
SRP Fourier Coefficients	*Derived from the established range of uncertainties given in Section 5.3.*
TRP Fourier Coefficients	*Derived from the established range of uncertainties given in Section 5.3.*
Gravitational Parameter μ	1E-2 for the 1st simulation
Spherical Harmonics Coefficients	1E-2
Measurements weighting	
Sample and Line	0.25 pixels
DSN Observations	
Range	3 meter
Range-rate	0.1 mm/sec

(whenever a landmark is in view of the camera and is lit) along the observation arc of 5 days. The DSN radiometric observations are collected once every 1 minute for the same period, but with

www.manaraa.com

an 8-hour gap in between two consecutive measurement arcs (16 hours of daily DSN observations). Table 6.2 summarizes the *a priori* uncertainties and measurement errors that are used in the covariance study.

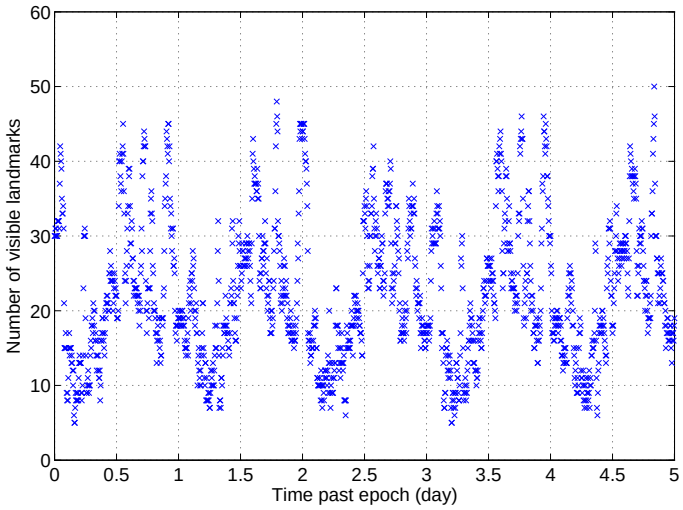

Figure 6.1: Number of visible landmarks from a 1 km circular orbit for the nadir-pointing attitude profile.

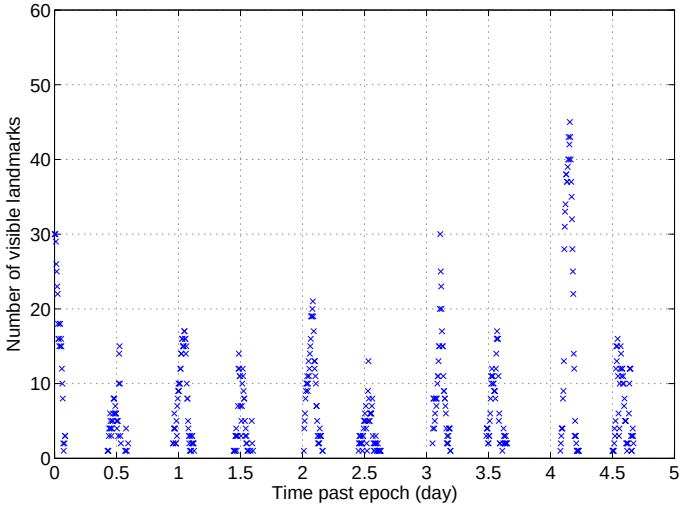

Figure 6.2: Number of visible landmarks from a 1 km circular orbit for the Sun-pointing attitude profile.

www.manaraa.com

6.2.4 Covariance Analysis Results

The results from two different sets of covariance studies are presented here. The two different studies aim to measure the effect of the coupling that might exist between the central body gravitational terms and the SRP coefficients on the estimation outcome. For the first covariance study, we include the gravitational parameter μ inside the estimated state. The second study does not estimate the gravitational parameter. The assumption for the second study is that the parameter μ is estimated to high level of precision through other sources prior to performing a precise estimation process. This is not an unrealistic assumption, since the gravitational parameter of an object may be estimated to a high degree of precision through alternate ways, e.g. flybys, prior to placing a spacecraft in an orbit about a small body. Furthermore, as is shown later in this covariance study the parameter μ may be estimated precisely by placing the spacecraft in the Sun or Earth-pointing attitude profile without suffering from correlation issues that may occur in the nadir-pointing attitude profile.

6.2.4.1 Results of the 1^{st} covariance study

Figure 6.3 shows correlation coefficients (see Eq. 6.1) between the estimated SRP coefficient, the gravitational parameter μ, and the gravitational spherical harmonics coefficients for a nadir-pointing attitude. This figure arranges the correlation coefficient values between different estimated parameters in a lower triangle matrix with their values corresponding to the color bar on the right side of the plot. Immediately, it is clear from this figure that there exists an almost perfect correlation between $A_0(1)$ SRP coefficient and the μ. This is supported by intuition as the $A_0(1)$ SRP coefficient is constantly aligned with the radial direction for a nadir-pointing attitude. As a result for this attitude profile these parameters are closely coupled and the problem setup is ill-conditioned. Hence, the uncertainty estimate on the $A_0(1)$ SRP coefficient is hardly moved from its *a priori* value as shown in Figure 6.4. This results shows that one may not be able perform estimation of both the $A_0(1)$ SRP coefficient and the μ, simultaneously, in the nadir-pointing attitude

www.manaraa.com

or any other attitude profile that ties the spacecraft body to the orbital motion.

On the other hand, the Sun-pointing and the Earth-pointing attitudes do not present the same problem, since for these attitude profiles the central body rotates around the spacecraft as seen from the spacecraft body-fixed frame. Hence, the coupling between the spacecraft body-fixed SRP coefficients and the central body μ is broken. This is clear in the results shown in Figures 6.5(b) and 6.6(b) where there aren't any large correlations between the SRP coefficients and the μ. Figures 6.5(a) and 6.6(a) further present the estimated uncertainty of the SRP coefficients showing that these coefficients are estimated precisely. In general, there does not exist any strong correlation between the spherical harmonics gravity coefficients and any of the SRP coefficients during any of the attitude profiles. The correlation plots, however, reveal the existence of strong correlations among few SRP Fourier coefficients for the nadir-pointing attitude and the components of the aggregated coefficient for the Sun and Earth-pointing attitudes. This may be a potential concern when estimating the individual coefficients. One way to help mitigate this problem may come from combining the estimation results from different attitude profiles to reduce the coupling among some of these coefficients.

6.2.4.2 Results of the 2^{nd} covariance study

Figure 6.7 shows the uncertainty of the SRP Fourier coefficients after 5 days of simulation for the three different attitude profiles. Note that in this simulation we do not estimate the gravitational parameter μ. These plots shows that, with this assumption, one can estimate the SRP Fourier coefficients with a relatively high level of precision. This includes the $A_0(1)$ term for the nadir-pointing attitude that was not estimated in the first simulation scenario. Furthermore, the covariance analysis results given for the nadir-pointing attitude profile show that a majority of the SRP Fourier coefficients that we are able to estimate precisely are the ones that govern the secular dynamics of the spacecraft orbit elements given by Eq. (5.38) – (5.40). These coefficients are shown in red in Figure 6.7(a). This is a very encouraging result as it shows that one is able to precisely estimate the dominant SRP Fourier coefficients, which, if not estimated correctly, could result in

www.manaraa.com

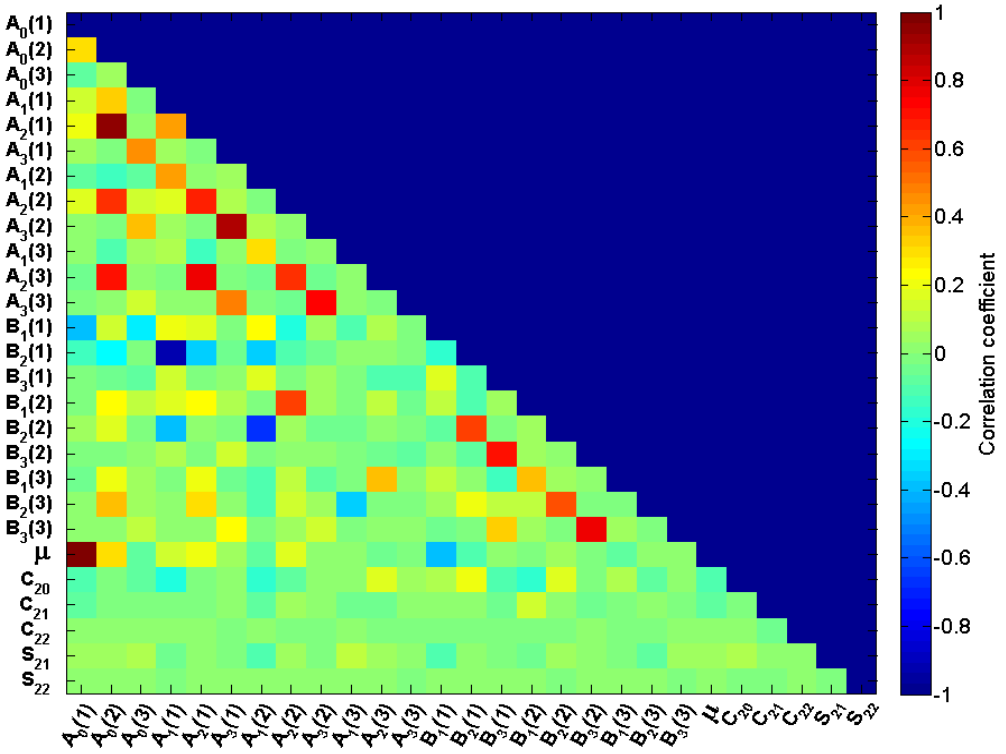

Figure 6.3: Correlation coefficient of the estimated parameters for the nadir-pointing attitude for the 1^{st} covariance study.

large errors in the spacecraft trajectory over time (see Figure 5.4).

Figure 6.7(a) also shows that two other coefficients, namely the $A_0(1)$ and $A_0(3)$ are estimated with a relatively hight precision. These coefficients do not contribute to the secular dynamics of orbit elements. However, as shown in Figures 5.2(a) and 5.2(b), they are prominent coefficients with relatively large values at $\delta_s \approx 90^\circ$, which is the value of the solar latitude at the nadir-pointing attitude profile. Although, these coefficients do not contribute to the secular motion of the orbit elements, their large value suggests that any error in these coefficients could result in large periodic errors in the spacecraft trajectory and navigation solutions. Fortunately, the covariance analysis results show that one can precisely estimate these coefficients. Other higher order coefficient that are shown to be estimated precisely, have far less effect on the trajectory

www.manaraa.com

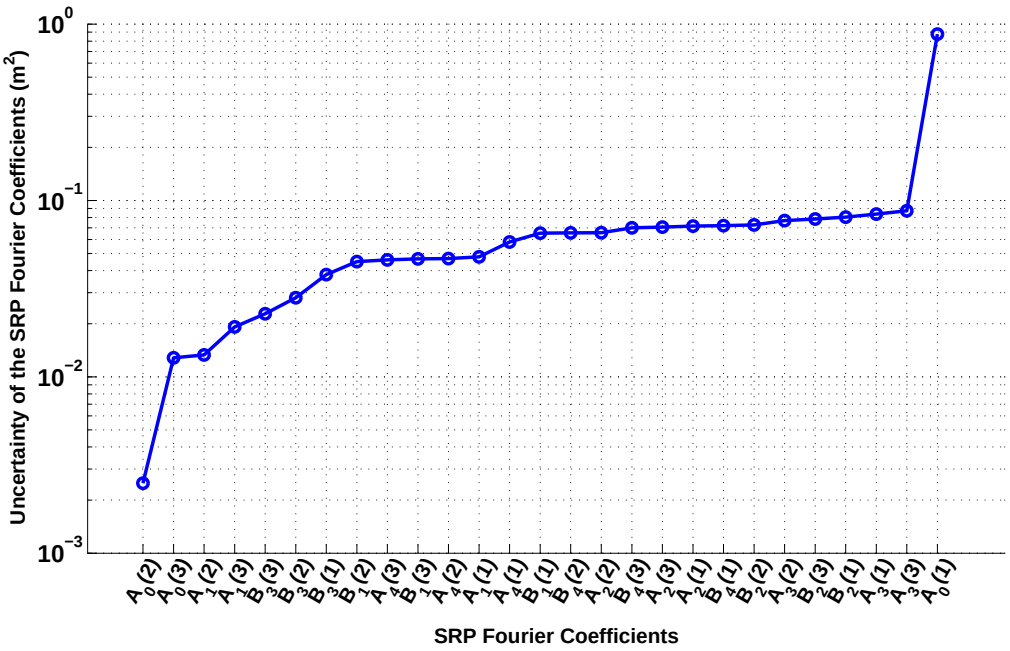

Figure 6.4: Uncertainty of the SRP coefficients the nadir-pointing attitude for the 1st covariance study.

compared to the lower order coefficients. Figures 6.7(b) and 6.7(c) show that the aggregated SRP coefficients are estimated precisely for the Sun-pointing and Earth-pointing attitude profiles, respectively, and the precision level is largely unaffected by the exclusion of the μ parameter from the list of the estimated parameters compared to the results of the first simulation scenario.

Lastly, we look at the results of the covariance study for the rest of the estimated parameters. Table 6.3 shows the results for the TRP coefficients. This table shows the ratio of the CRLB uncertainty after processing the observations to the *a priori* uncertainty of these coefficients, which turns out to be almost equal to unity. The values shown in this table are averaged over all of the surface elements for the nadir-pointing attitude. These values are similar to those given by the other attitude profiles. A ratio close to unity means that the covariance study is not able to collect any information about these coefficients from the dynamics of the spacecraft and/or the observations processed. This is mainly due to a weak TRP signal that is not able to stand out of the measurement noise. Even though one may not be able estimate the TRP Fourier coefficients, including the

www.manaraa.com

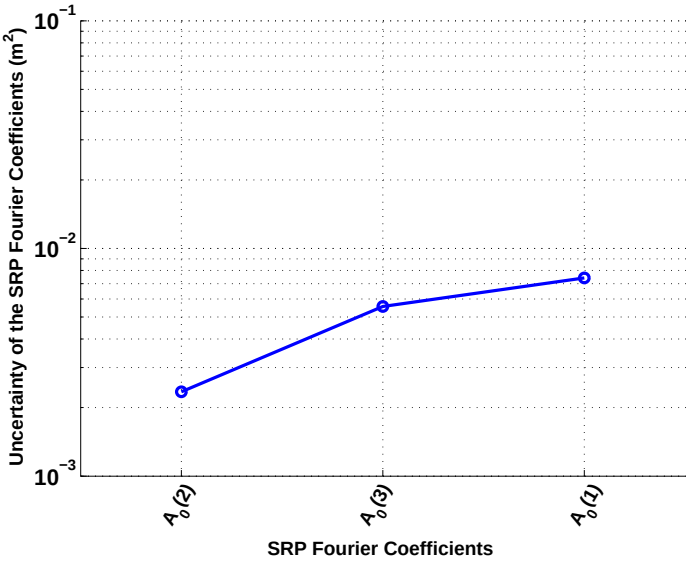

(a) SRP coefficients uncertainty

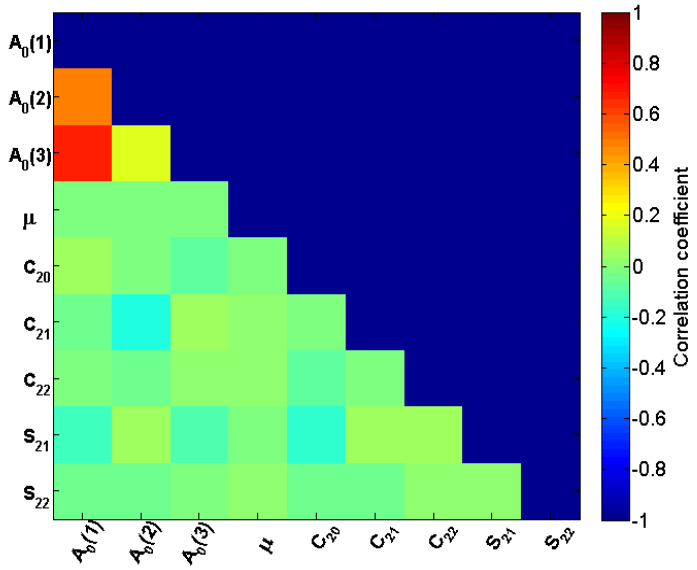

(b) Correlation coefficients

Figure 6.5: Uncertainty and correlation coefficients of the estimated parameters for the Sun-pointing attitude for the 1^{st} covariance study.

TRP effect in the dynamical model could improve the precision of the orbit determination process as we show in Section 6.3. Finally, for the sake of completeness we present the CRLB uncertainty achieved for the gravitational parameter μ and the spherical harmonics coefficients from the co-

www.manaraa.com

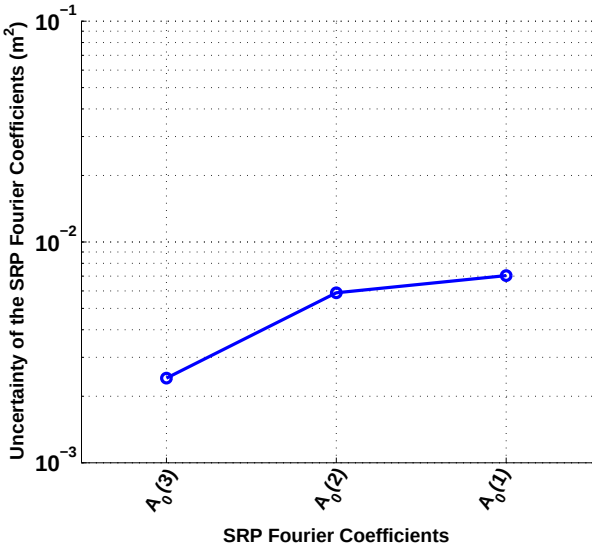

(a) SRP coefficients uncertainty

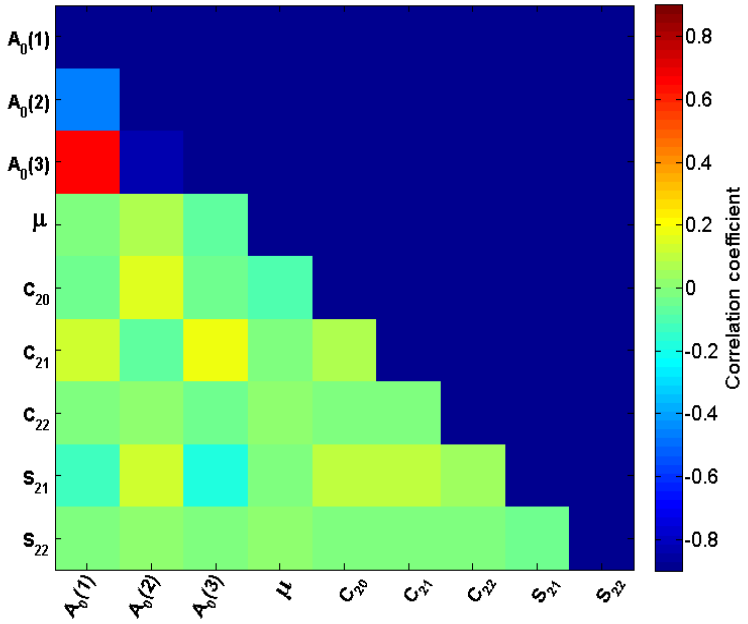

(b) Correlation coefficients

Figure 6.6: Uncertainty and correlation coefficients of the estimated parameters for the Earth-pointing attitude for the 1st covariance study.

variance study. This information is presented in Table 6.4 for the spherical harmonics coefficients up to the degree and order 5.

www.manaraa.com

Table 6.3: Ratio of the TRP coefficient uncertainties.

Coefficient	$A_n(1)$	$A_n(2)$	$A_n(3)$
$\sigma_{\text{CRLB}}/\sigma_{a\ priori}$	0.99	0.99	0.99

Table 6.4: Uncertainty of the spherical harmonics coefficients from the covariance study.

Parameter		Nadir-pointing		Sun-pointing		Earth-pointing	
μ		4.2E-12		1.3E-13		1.4E-13	
Degree	Order	σ_C	σ_S	σ_C	σ_S	σ_C	σ_S
2	0	2.75E-04	–	2.53E-04	–	2.64E-04	–
2	1	2.80E-04	2.85E-04	2.82E-04	2.61E-04	2.56E-04	2.60E-04
2	2	1.29E-03	1.30E-03	1.27E-03	1.27E-03	1.26E-03	1.27E-03
3	0	8.45E-04	–	8.15E-04	–	8.27E-04	–
3	1	3.95E-04	4.02E-04	4.58E-04	4.58E-04	4.31E-04	4.59E-04
3	2	3.32E-03	3.33E-03	2.98E-03	3.05E-03	3.06E-03	3.12E-03
3	3	5.25E-03	5.24E-03	5.31E-03	5.27E-03	5.35E-03	5.36E-03
4	0	3.13E-03	–	1.82E-03	–	1.83E-03	–
4	1	2.87E-04	2.89E-04	4.71E-04	7.56E-04	4.04E-04	3.73E-04
4	2	6.81E-03	6.81E-03	6.36E-03	6.36E-03	6.47E-03	6.55E-03
4	3	8.96E-03	8.94E-03	8.75E-03	8.74E-03	8.88E-03	8.87E-03
4	4	9.36E-03	9.36E-03	9.39E-03	9.37E-03	9.42E-03	9.42E-03
5	0	8.13E-03	–	7.57E-03	–	7.45E-03	–
5	1	1.93E-04	1.90E-04	6.35E-04	4.41E-04	1.83E-04	1.24E-04
5	2	9.22E-03	9.27E-03	9.07E-03	9.04E-03	9.20E-03	9.14E-03
5	3	9.88E-03	9.88E-03	9.83E-03	9.83E-03	9.86E-03	9.86E-03
5	4	9.94E-03	9.94E-03	9.93E-03	9.93E-03	9.94E-03	9.94E-03
5	5	9.96E-03	9.96E-03	9.96E-03	9.96E-03	9.97E-03	9.97E-03

www.manaraa.com

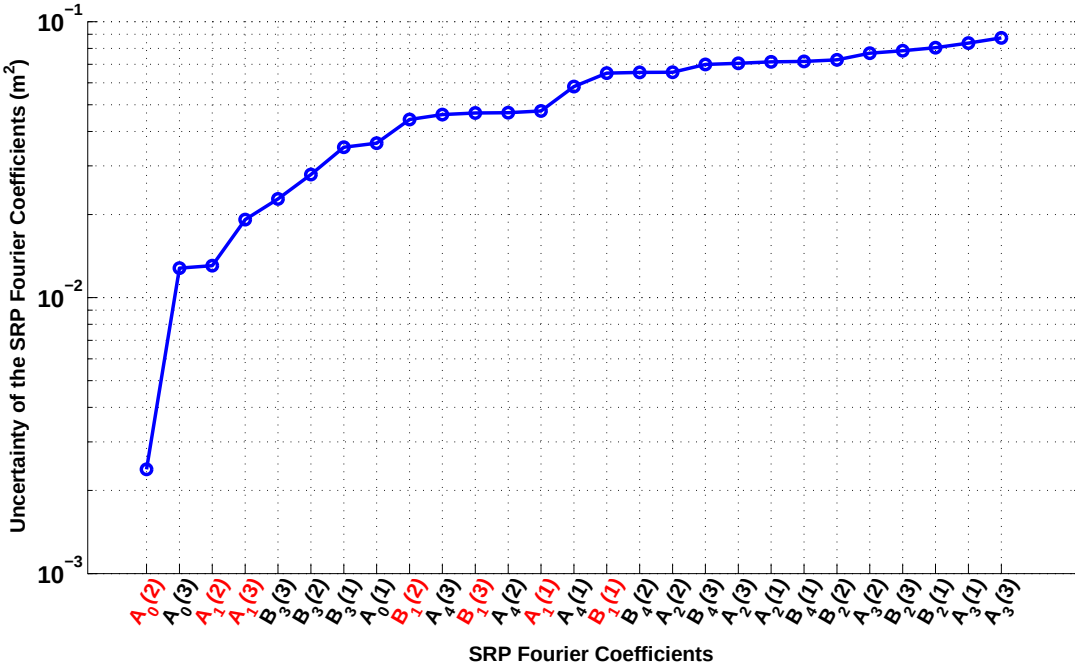

(a) Nadir-pointing attitude

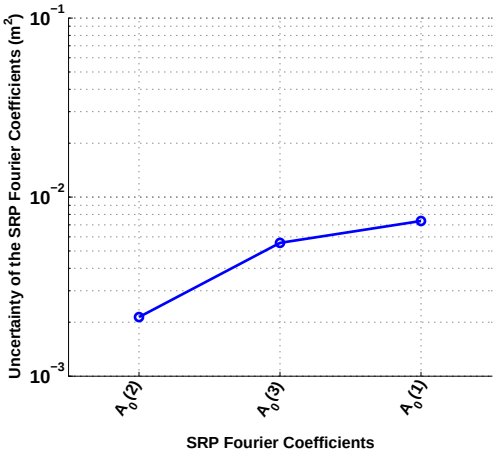

(b) Sun-pointing attitude

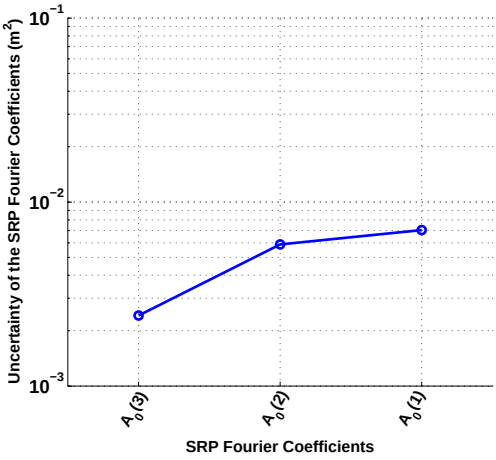

(c) Earth-pointing attitude

Figure 6.7: Uncertainty of the SRP Fourier coefficients after 5 days of simulation for the 2nd simulation.

6.2.5 Translation of Results Between Different Attitude Profiles

The covariance studies presented in the previous section are cases in which the spacecraft is assumed to follow the same attitude profile throughout the observation arc. However, in reality

www.manaraa.com

the spacecraft may switch between different attitude profiles during the estimation arc, as is the case for the OSIRIS-REx spacecraft during the gravity science phase of the mission. During this phase, the OSIRIS-REx spacecraft will switch between a nadir-pointing type attitude profile and a Sun-pointing attitude regime. Although, this issue is a matter of practical details for a specific mission profile, we discuss the possible remedy for the sake of completeness.

For a case like this we need to set the estimated state elements such that the estimation filter could transfer the information between different attitude profiles without a need for stopping and restarting of the estimation arc. To do so, we recall from Section 5.2.2 that for the Sun-pointing and Earth-pointing attitudes we defined a Fourier coefficients as an aggregate of the infinite number of the actual spacecraft body-fixed frame coefficients. For instance the aggregate SRP coefficient for the Sun-pointing attitude was defined by

$$\mathbf{A}_0^{\odot} = \sum_{n=0}^{\infty} \mathbf{A}_n. \tag{6.66}$$

One may decompose this equation into two parts as the following

$$\mathbf{A}_0^{\odot} = \sum_{n=0}^{\ell} \mathbf{A}_n + \delta\mathbf{A}_0^{\odot}, \tag{6.67}$$

where the first part of this equation is the sum of individual Fourier coefficients up to the order ℓ and second part is the sum of the remaining coefficients for orders $\ell + 1$ and higher. For an estimation arc with multiple attitude profiles the filter can be set up such that it estimates the individual coefficients up the order ℓ during the nadir-pointing attitude and only estimates the remainder quantity $\delta\mathbf{A}_0^{\odot}$ during the Sun-pointing attitude, while taking the best estimate values of the lower order individual coefficient as known parameters. Similar approach may be used for translating the information between the nadir-pointing and the Earth-pointing attitude profiles.

6.3 Orbit Determination Simulations

In this section we present the results from several simulation studies that track a simulated spacecraft orbiting about a small body. These studies are designed with the intension to test to

www.manaraa.com

performance of the Fourier series expansion models that are developed for representing SRP and TRP effects on spacecraft. In Section 6.3.1 we test the performance of the SRP Fourier expansion and contrast it with the simplified cannonball model that is often used in the spacecraft navigation. This section also presents a simulation study that estimates the SRP Fourier coefficients via the OD solution in the presence of errors in these coefficients. Section 6.3.2 evaluates the effects of mis-modeled TRP on the spacecraft navigation in the close proximity of a small body and the performance of the TRP Fourier model in generating precise OD solution.

6.3.1 The OD Performance of the SRP Fourier vs. the Cannonball Model

Eq. (4.4) provides the expression for the SRP acceleration based on a cannonball model. As mentioned earlier, a cannonball model assumes that the force imparted on the spacecraft due to SRP is strictly in the direction of the sunlight pointing away from the Sun [46]. For the purpose of the spacecraft navigation it is convenient to rewrite this equation in the following form

$$\mathbf{a}_{SRP} = C_R \frac{P(R)}{B} \hat{\mathbf{r}}_{\odot}, \tag{6.68}$$

where the C_R is known as the reflectivity coefficient that is equivalent to $1+\rho$ in Eq. (4.4). The vector $\hat{\mathbf{r}}_{\odot}$ is a unit vector pointing from the Sun to the spacecraft. Note that this vector is slightly different from the $\hat{\mathbf{d}}$ vector used in Eq. (4.4), which is a vector pointing from the Sun to the small body. This slight distinction is disregarded in the derivation of the averaged dynamics of orbit elements in Chapter 4. During an OD process that uses the cannonball model we include the parameter C_R in the list of the estimated parameters and updates its value to perform a best fit trajectory to the observations. However, this model may not be sufficient for precise OD as the cannonball model is just a rough approximation to the actual effect of SRP on a spacecraft.

To illustrate this we propagate a trajectory and compare the acceleration imparted on the a simulated spacecraft due SRP under different model assumptions. The central body is chosen to be Bennu and we pick a 1 km initially circular terminator orbit to perform the propagation for 5 days. The spacecraft shape is the 10-plate model illustrated by Figure 2.2 and the surface

www.manaraa.com

properties of it given by Table 5.1. Figures 6.8 and 6.9 show the components of the SRP acceleration shown in the spacecraft body-fixed frame under different models. For the plate model we use the actual shape model of the spacecraft to compute the SRP acceleration. The value of the C_R for the cannonball model is picked such that the acceleration in the sun-line direction matches that of the plate model at the epoch. It is easy to see from these figures that a cannonball model does not accurately represent the SRP acceleration. This is specially clear on the $\hat{\mathbf{x}}_b$ direction. Also note that a zero order Fourier series model is not able to account for minor fluctuations in the SRP acceleration and to improve that one needs to include higher order coefficients as well.

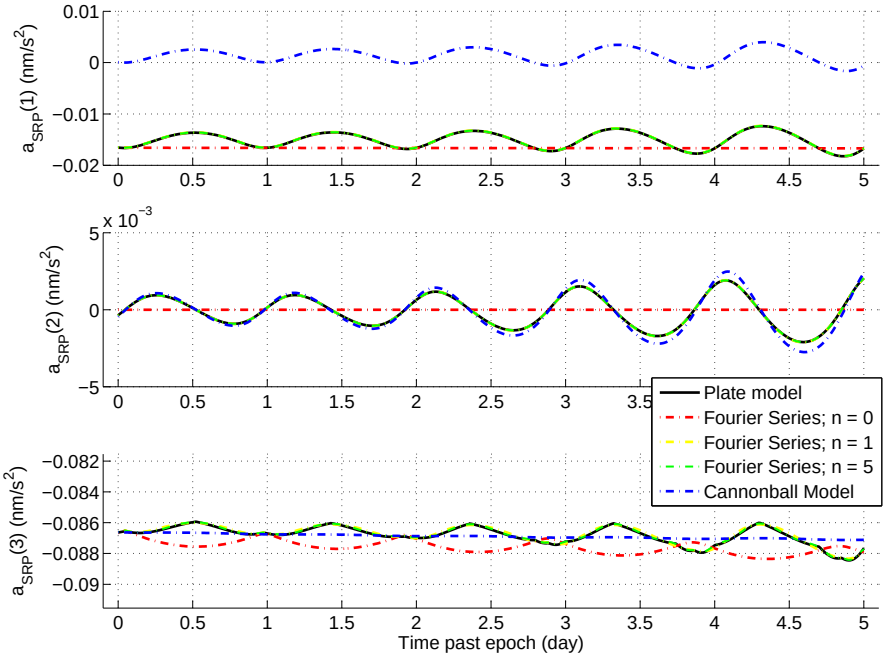

Figure 6.8: Spacecraft body-fixed frame SRP acceleration due to different models in the nadir-pointing attitude.

6.3.1.1 Case I simulation: SRP Fourier vs. the cannonball model

This simulation study is performed to shows the effect of the mis-modeled SRP acceleration under the cannonball model assumption on the orbit determination solution and the advantage of

www.manaraa.com

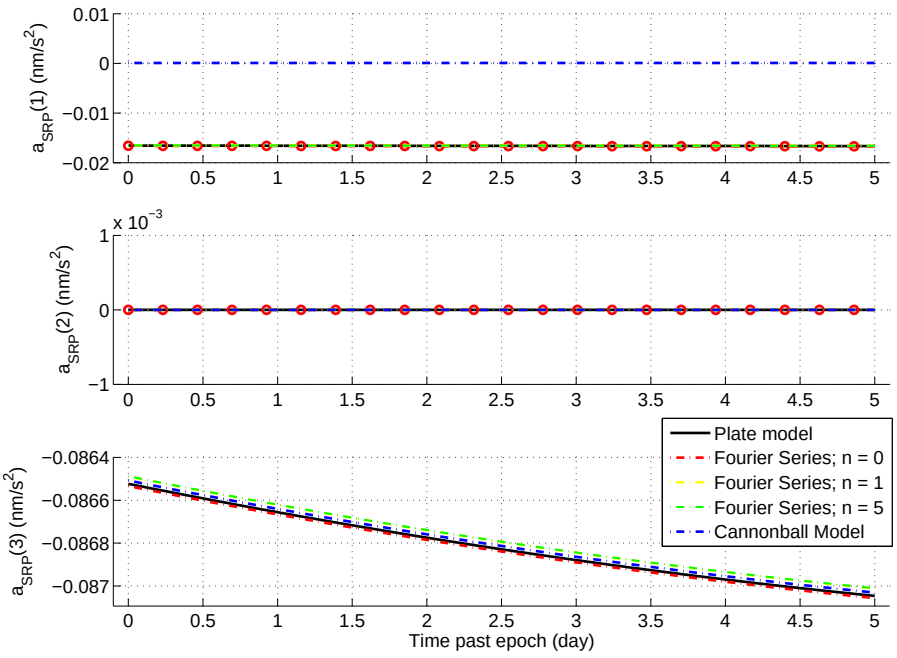

Figure 6.9: Spacecraft body-fixed frame SRP acceleration due to different models in the Sun-pointing attitude.

using a Fourier series expansion instead. The truth trajectory is a 1 km initially circular terminator orbit about Bennu. Table 6.5 summarizes the dynamical model that is used in generating this truth trajectory. The epoch of the simulation is chosen such that the asteroid is in its perihelion that the start of the trajectory. The orbit is propagated for 1 day while the spacecraft is assumed to be in the nadir-pointing attitude profile. The truth trajectory is used to generate simulated landmark and DSN measurements. These measurements are generated in accordance to the same measurement model that was discussed in Section 6.2.3. During the nadir-pointing attitude profile the camera is assume to point towards the center of Bennu.

The estimated parameter set in this simulation is the spacecraft position and velocity vectors with 10 meters of *a priori* uncertainty in the position and 10 cm/sec in the velocity in all three cartesian directions. In the case of the cannonball model, we also estimate the C_R parameter. When using a Fourier series model, we estimate the coefficients up to order 5. The initial state of the

www.manaraa.com

Table 6.5: The truth force models used in the simulation studies

Simulation Epoch:	2019 Jan 10 18:42:10.321 TDB
Force Model	
Central Body:	Bennu ($\mu = 5.2\ m^3/s^2$)
Gravity Model:	16×16 spherical harmonics expansion
SRP:	10-plate model (see Figure 2.2)
TRP:	10-plate model (see Figure 2.2)
Third body:	Sun (point mass)

spacecraft is perturbed from its true state by an error generated from a Gaussian distribution of zero mean and a standard deviation of 10 meters in position and 10 cm/sec in velocity at each direction. Furthermore, we include an initial error in the value of the SRP coefficients that corresponds to 3 degrees of error in the spacecraft attitude. Available landmark measurements are processed once every 5 minutes, while the DSN range and range-rete measurements are processed once every 1 minute during each simulation. Measurement noise is added to the simulated observations for each simulation run according to the noise levels indicated in Table 6.2. Other errors are included in the dynamics of the filter model, which are summarized in Table 6.6. No process noise is added in these simulations.

Figure 6.10 shows the accuracy of the position and velocity estimates of the spacecraft after several filter iterations under the cannonball model assumption for the SRP acceleration. This figure shows that the filter is not able to accurately estimate the truth trajectory of the spacecraft. The clear signal in the range-rate post-fit residuals shown in Figure 6.11 is also an indication of the mis-modeled SRP acceleration. On the other hand, the accuracy and the post-fit residuals of the second filter given by Figures 6.12 and 6.13, respectively, show that the Fourier series model is able to accurately estimate the spacecraft state and generate noise like post-fit residuals. Additionally, Table 6.7 shows the accuracy of the estimated SRP coefficients that are achieved by the second filter. These results show that the filter is able to estimate these coefficients with a high level of

www.manaraa.com

Table 6.6: Filter Models for Case I Simulation

Force Model	**Filter 1 - Cannonball**	**Filter 2 - Fourier Series**
Central Body:	Bennu ($\mu = 5.2\ m^3/s^2$)	Same
Gravity Model:	5×5 field	Same
SRP:	Fourier expansion; n = 10	Cannonball Model
Third body:	Sun (point mass)	Same
Estimated Parameters	1-σ *a priori* Uncertainty	Initial Error
Both Filters		
Spacecraft position		
X, Y, Z	10 m	$\sim N(0, 10^2)\ m$
Spacecraft velocity		
V_x,V_y,V_z	10 cm/s	$\sim N(0, 10^2)\ cm/s$
Filter 1		
Coefficient of reflectivity, C_R	1.0	10% error
Filter 2		
SRP Fourier Coefficients	Derived from the error analysis error limits.	3 deg attitude error

accuracy. Processing longer observation arcs may further improve the estimation accuracy on the SRP coefficients. Similar results between the cannonball model and the SRP Fourier series are achieved for the other two attitude profiles, although they are not presented here.

6.3.2 TRP Effects on Orbit Determination Solutions

Section 5.4 showed that TRP accounts for only a small percentage of the total perturbing forces that are imparted on a spacecraft orbiting a small body. However, its effect may become noticeable when generating a precise OD solution or when propagating the uncertainty of an OD solution for a long time span. In this section we perform two sets of simulation studies to evaluate the effects of not modeling or mis-modeling of TRP on an OD solution.

www.manaraa.com

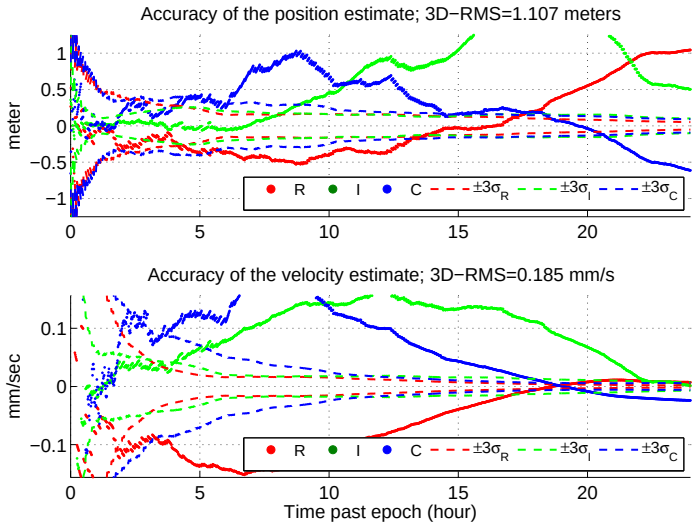

Figure 6.10: Accuracy of the spacecraft position and velocity estimates for filter 1, Case I; Cannonball model for the SRP.

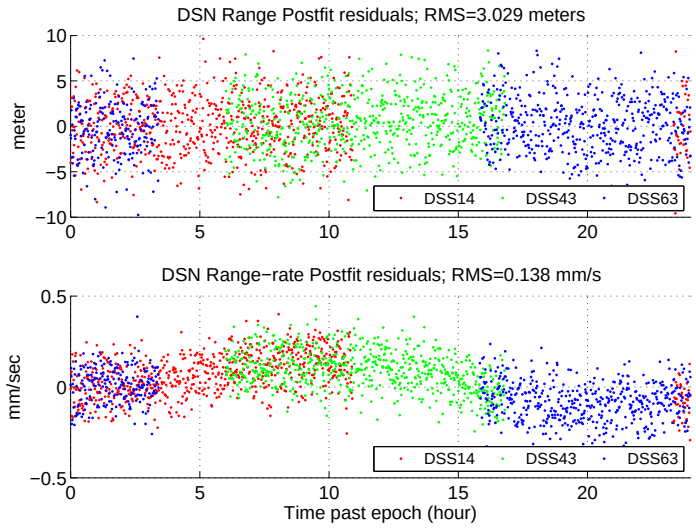

Figure 6.11: Range-rate post-fit residuals for filter 1, Case I; Cannonball model for the SRP.

6.3.2.1 Case II simulation: TAG rehearsal trajectory OD

First, we study navigating a simulated OSIRIS-REx spacecraft during its TAG rehearsal trajectory that is shown in Figure 5.11. As mentioned in Section 5.4 the force imparted on the spacecraft due to TRP may increase up to 20% of the SRP effect. Hence, we are interested in quantifying

www.manaraa.com

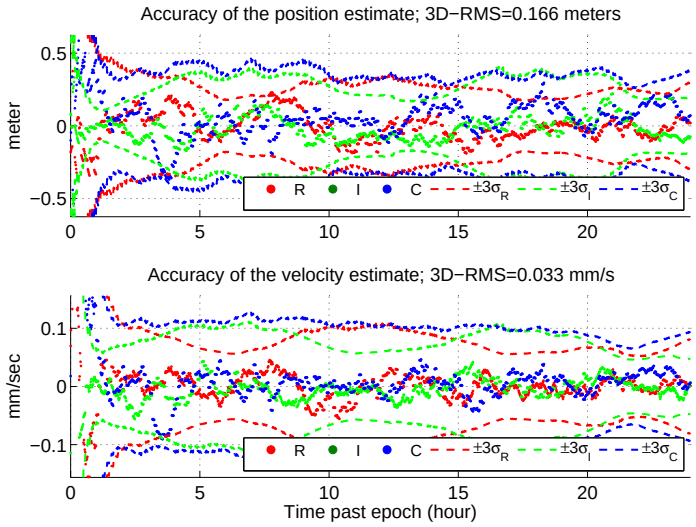

Figure 6.12: Accuracy of the spacecraft position and velocity estimates for filter 2, Case I; Fourier series model for the SRP.

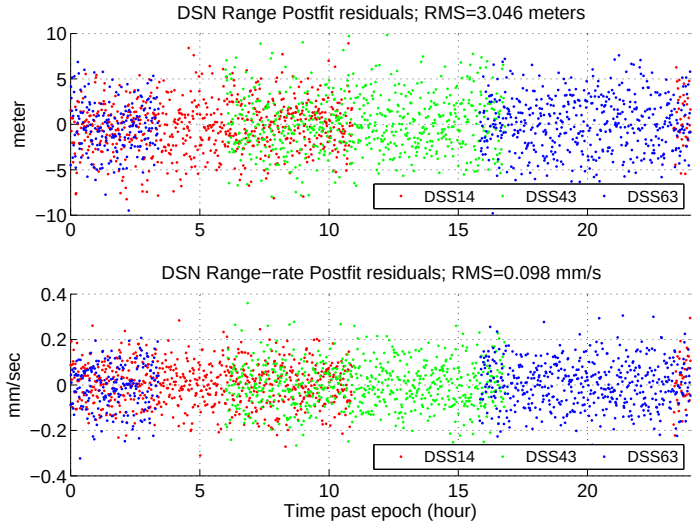

Figure 6.13: Range-rate post-fit residuals for filter 2, Case I; Fourier series model for the SRP.

the effect this force may have in the navigation solution during this trajectory. The truth trajectory of the simulation is very similar to the trajectory shown in Figure 5.11, where the spacecraft starts from a 1 km circular terminator orbit and passes through a check point, which is 125 meters above the TAG point at the -45° latitude after 4 hours and continues for 2 more hours in that trajectory. The force model used for generating this trajectory is the same as what is shown

www.manaraa.com

Table 6.7: Accuracy of the SRP Fourier coefficients from Filter 2, Case I

Coefficient Degree	**1st Component**	**2nd Component** (m^2)	**3rd Component** (m^2)
A			
0	0.0002	0.0051	0.0021
1	0.0953	-0.0709	-0.0458
2	0.1797	-0.1169	-0.0135
3	-0.0923	-0.0019	0.0509
4	0.0107	0.1281	0.0550
5	-0.0444	-0.0559	0.0108
B			
1	-0.0774	-0.3024	0.0250
2	-0.0739	-0.1388	0.0988
3	0.0634	0.2431	0.0326
4	0.0799	-0.2051	-0.1687
5	0.0222	0.0085	-0.0622

in Table 6.5. The spacecraft is assumed to be in the nadir-pointing attitude during this trajectory. The truth trajectory is used to generate simulated optical and DSN measurements according to the same measurement model that was discussed in Section 6.2.3. The navigation camera is assumed to be pointing towards the center of Bennu during the entire arc. Figure 6.14 shows the number of visible simulated landmarks and the spacecraft altitude during the TAG rehearsal trajectory.

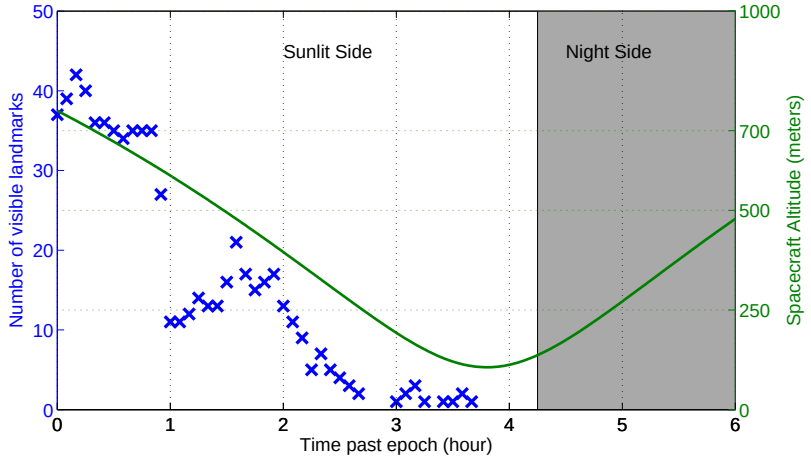

Figure 6.14: Number of visible landmarks and the spacecraft altitude during TAG rehearsal trajectory.

The estimated parameter set in this simulation is the spacecraft state with 10 meters of *a*

www.manaraa.com

priori uncertainties in the position and 10 cm/sec in the velocity in all three cartesian directions. Two sets of Monte-Carlo simulations are performed for this study, one that includes the TRP effect and another one that does not. For each set we run 300 cases. For each case, the initial state of the spacecraft is perturbed from the truth state by an error generated from a Gaussian distribution of zero mean and a standard deviation of 10 meters in the position and 10 cm/sec in the velocity at each direction. Available landmark measurements are processed once every 5 minutes, while the DSN range and range-rete measurements are processed once every 1 minute during each simulation. Measurement noise is added to the simulated observations for each simulation run according to the noise levels indicated in Table 6.2. Other errors are included in the dynamics of the filter model, which are summarized in Table 6.8. No process noise is added for the case where the TRP effect is not included in the filter model. This helps isolate the effect of mis-modeling of TRP on the OD solution. Table 6.9 summarizes the results of the 300 Monte Carlo filter runs for each of

Table 6.8: Filter Model for the Case II Simulations

Simulation Epoch: 2019 Jan 10 18:42:10.321 TDB	
Filter Force Model	
Central Body:	Bennu ($\mu = 5.2\ m^3/s^2$)
Gravity Model:	5×5 field
SRP:	Fourier expansion n = 10
TRP:	Fourier expansion n = 10 (if included)
Third body:	Sun (point mass)

the simulation cases, with and without the TRP effect.

As shown in these results, the weighted RMS of the observations for both cases is close to unity meaning that the filter is able to extract most of the signal from the observations. However, the RMS values show that the filter is performing slightly better for the case that TRP effect is included in the force model. This is more pronounced in the accuracy of the filter, where the 3D-RMS of the position and velocity accuracies are about twice as large for the case that does not

www.manaraa.com

include the TRP effect. The reason that the mis-modeling of the TRP effect is not easily noticeable in the observation RMS values may be due to the short observation arc and the large observation noise compared to the magnitude of the TRP signal. We explored this further in the second set of the simulation studies (see Section 6.3.2.2) by processing longer observation arcs. The 3D-RMS of the accuracy, however, clearly shows that mis-modeling of the TRP has a negative effect on the accuracy of the estimated state. Figures 6.15 and 6.16 show the accuracy plots of a sample simulation run with and without including the TRP in the filter model. The initial errors and the measurement noise components are the same for both cases. These figures show that the accuracy of the state estimate falls out of 3σ uncertainty bounds due to mis-modeling of the TRP effect.

Table 6.9: Summary of the Monte Carlo filter analysis for the TRP effect.

	OpNav weighted RMS		DSN weighted RMS		3D-RMS	
	Sample	Line	Range	Range-rate	Position (m)	Velocity (mm/s)
With TRP	1.027	1.016	1.004	1.009	0.113	0.05
Without TRP	1.119	1.068	1.004	1.058	0.282	0.13

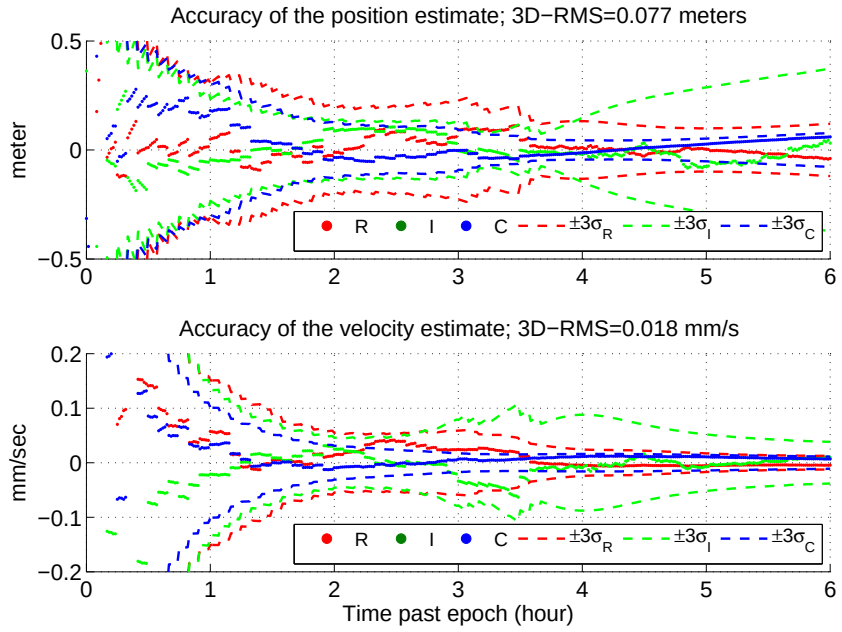

Figure 6.15: Accuracy plots of a sample simulation run for the case II; TRP effect is included in the filter model.

www.manaraa.com

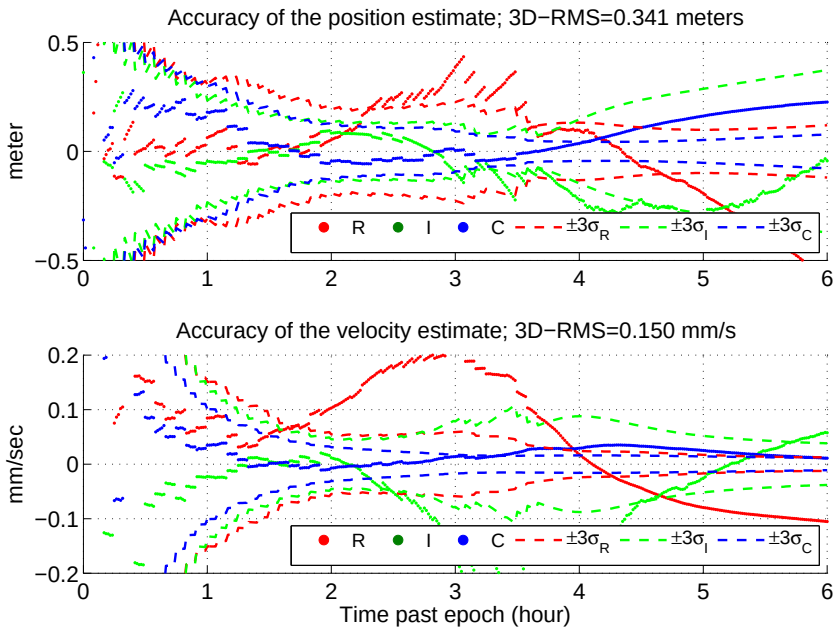

Figure 6.16: Accuracy plots of a sample simulation run for the case II; TRP effect is not included in the filter model.

6.3.2.2 Case III simulation

The Case III simulation considers processing a longer observation arc and assessing the TRP effect on the OD solution. The truth trajectory for this simulation is a 1 km circular terminator orbit about Bennu. The truth and filter models are the same as those used in the previous study (Case II simulation). The truth trajectory is propagated for two days and the OpNav landmark and DSN radiometric observations are generated based this truth trajectory in the same fashion as in the previous section. The estimated parameters are the spacecraft position and velocity vectors. The measurement noise, the state *a priori* uncertainties, and the state initial errors are the same as those given for the simulations in the previous section. Two filters are considered for this simulation, one that includes the TRP effect, and another one that does not. For the filter that dose not include the TRP effect we include a first order Gauss-Markov process noise (see Section 2.5 for details) with a correlation time of 1000 seconds and a noise level of $\sigma = 1E-4\ nm/s^2$ in the radial direction and $\sigma = 5E-5\ nm/s^2$ in the in-track and cross-track directions. The process noise is

www.manaraa.com

used to compensate for the un-modeled TRP effect so that the filter does not diverge during the long arc.

The filtering strategy for this simulation is such that we run the filters for 1 day and compute the best estimated state of the spacecraft. The spacecraft trajectory is then propagated forward in time for 1 more day based on best estimated state from the filter. During the 2nd day of the propagation, the measurement residuals are computed without updating the spacecraft state. This process is sometimes referred to as a "*pass-through*". Pass-through residuals are used to help validate a filter solution. The presence of large signals in the pass-through residual plots is an indication of significant mis-modeling in the dynamics the filter is not able to resolve. Figures 6.17 and 6.18 show the accuracy plots of the estimated states for both filters during the first day. These plots show that both filters are able to contain the estimated error within the 3σ uncertainty bounds. However, note that the uncertainty level in the second filter case is much higher due to the effect of the process noise. The estimated mis-modeled accelerations for the second filter are shown in Figure 6.19. Finally, Figures 6.20 and 6.21 show the pass-through residuals

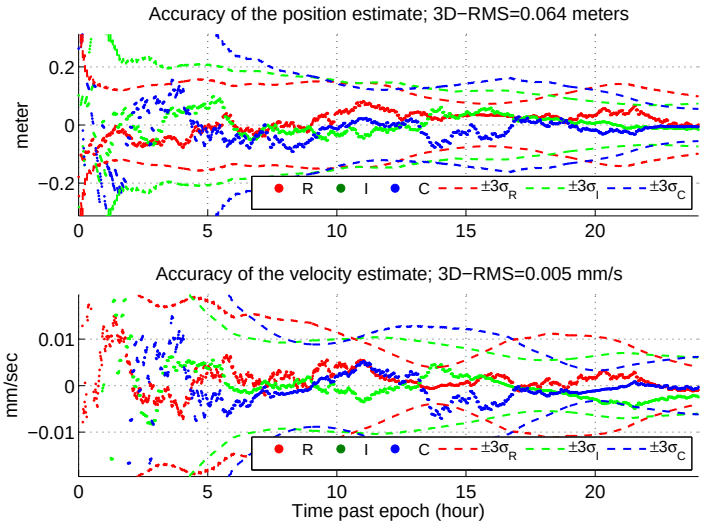

Figure 6.17: Case III: Accuracy plot of the 1st filter for 1 km circular terminator orbit.

for the first filter results. For the second filter these residuals are shown in Figures 6.22, and 6.23. These results show a clear signal in the pass-through residuals due to the mis-modeling of the TRP

www.manaraa.com

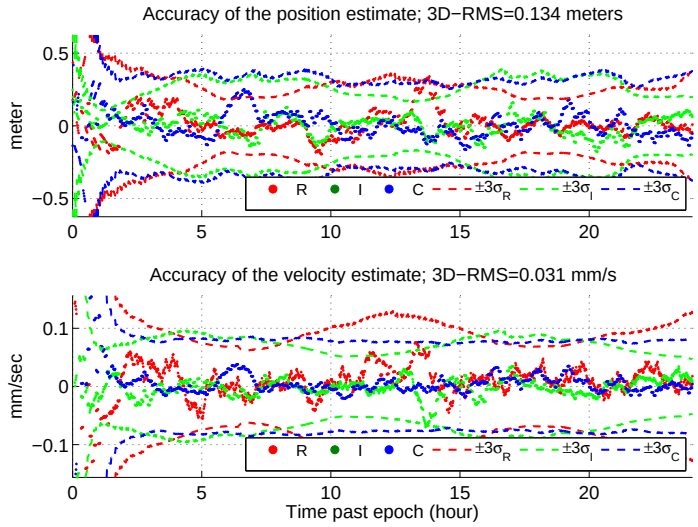

Figure 6.18: Case III: Accuracy plot of the 2nd filter for 1 km circular terminator orbit.

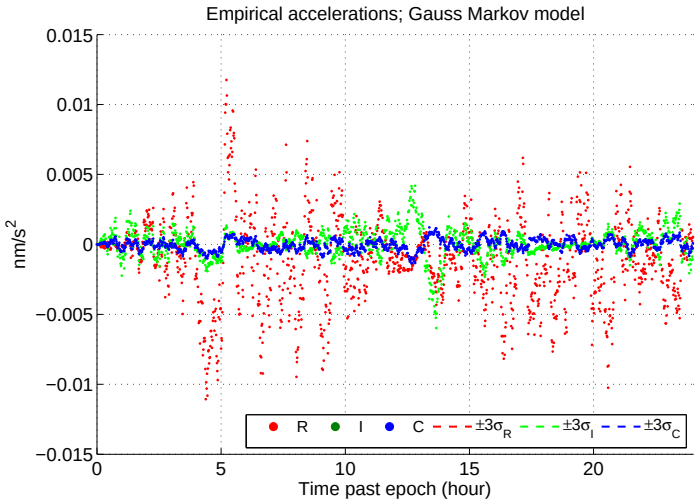

Figure 6.19: Case III: Empirical accelerations due to the mis-modeled TRP.

effect in the second filter, which does not exists in the first filter results.

6.4 Chapter Summary

This chapter utilizes the Fourier series representation of the SRP and the TRP in generating precise orbit determination solutions for a simulated spacecraft orbiting around a small body.

www.manaraa.com

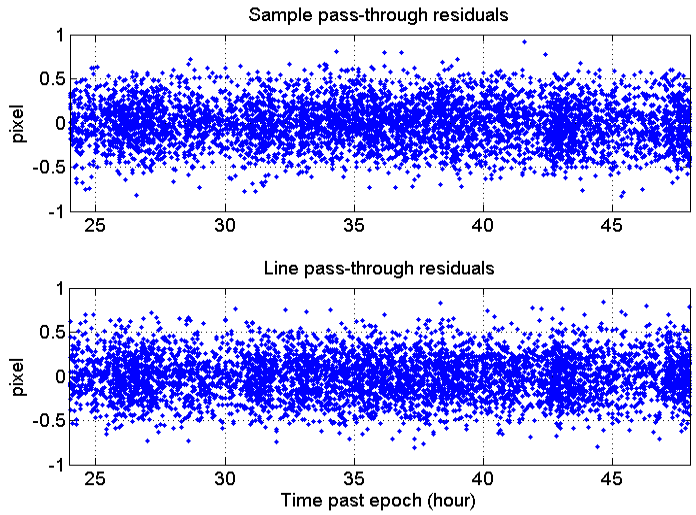

Figure 6.20: Case III: Pass-through residuals of the OpNav measurements for the 1st filter results.

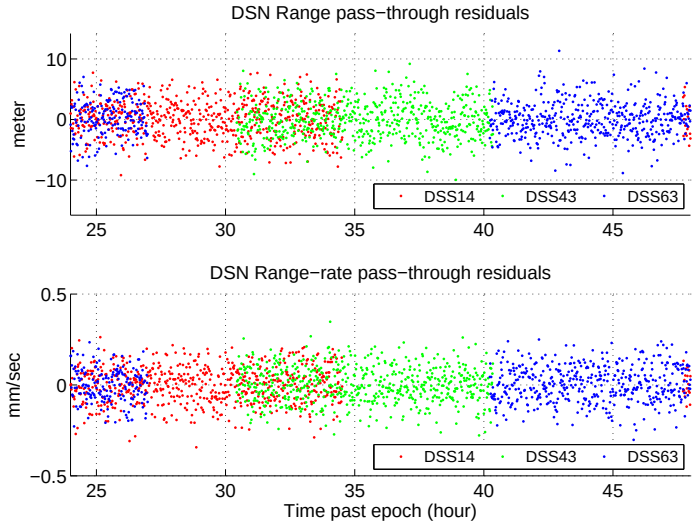

Figure 6.21: Case III: Pass-through residuals of the DSN measurements for the 1st filter results.

A complete set of equations are presented for the computation of the partial derivatives of the Fourier series model with respect to various estimation parameters. These partial derivatives are necessary for the computation of the variational equations used in the estimation process. We then use the laid out estimation framework in a comprehensive covariance analysis. The covariance study provides the level of estimation precision that is possible for each SRP fourier coefficient.

www.manaraa.com

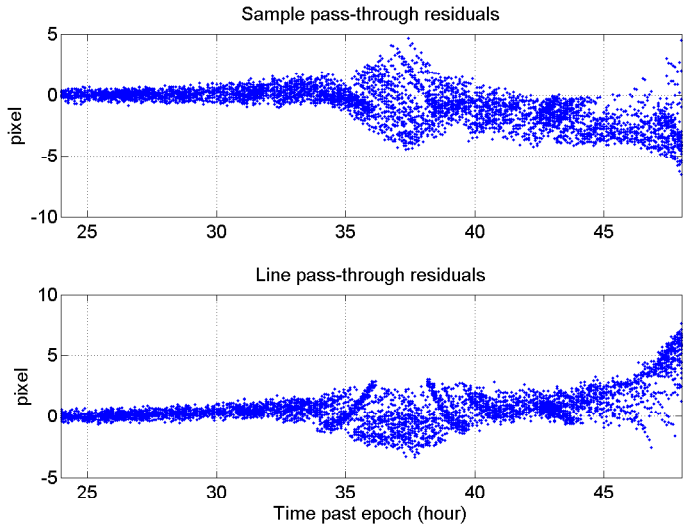

Figure 6.22: Case III: Pass-through residuals of the OpNav measurements for the 2nd filter results.

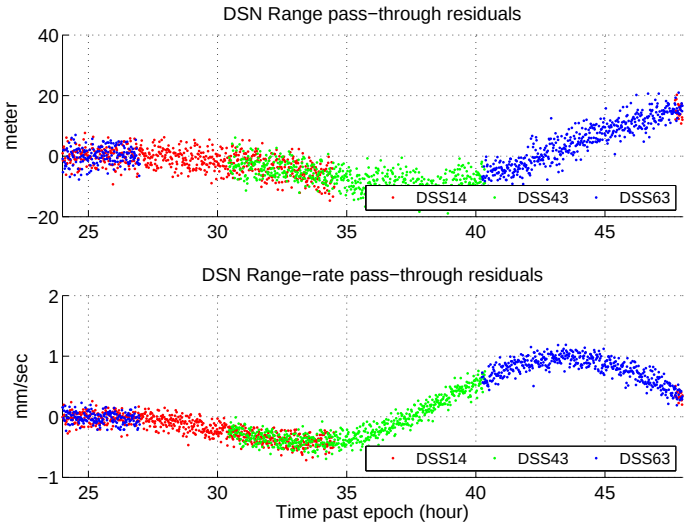

Figure 6.23: Case III: Pass-through residuals of the DSN measurements for the 2nd filter results.

The results from this study show that, in general, one can estimate the Fourier coefficients with a high level of precision. The results also show potentially strong correlations that may exist between the Fourier coefficients and the gravitational parameter of the central body during the nadir-pointing attitude. This coupling is removed for the other two attitude profiles, namely the Sun-pointing and the Earth-pointing attitudes.

www.manaraa.com

Furthermore, it is shown that there is a good agreement between the analytical expressions and the covariance analysis results. According to the covariance analysis, one can precisely estimate the coefficients that have prominent contribution to the secular dynamics of an orbit. Other coefficients with large periodic effects are also among those that are estimated with a high level of precision.

A set of full simulation studies conclude the work presented in this chapter. In these simulation studies we test the performance of the proposed estimation framework in generating precise orbit determination solutions in the presence of dynamical and modeling errors. While the simplified cannonball model is not sufficient to accurately represent the perturbing effect of the SRP on a spacecraft with a complex shape, the Fourier series expansion is shown to be able to accurately represent the SRP effect on a spacecraft and produce precise OD solutions. The study further shows that the mis-modeled TRP may have a notable effect on an OD solution especially for a trajectory that is close to the surface of the central body over the sunlit side of the object. Using the Fourier series representation of the TRP removes such mis-modeling and produces precise OD solutions that are valid for long propagation times.

www.manaraa.com

Chapter 7

Gravitational Potential and the Derivation of Spherical Harmonics

Spacecraft are perturbed significantly by the irregular and complex gravitational field that exists around small bodies. This is particularly important for spacecraft that plan to descend down to the surface of these objects in a landing or a TAG trajectory. Therefore, it is crucial to accurately model the surface proximity gravitational field of a small body in order to ensure a safe and successful landing or TAG operation. In Section 3.1 we briefly talked about the gravitational potential of an arbitrary body of mass and the gravitational acceleration derived from it. In this chapter, we revisit this formulation in further depth. After reviewing the formulation of the gravitational potential we consider the derivation of two gravitational field expansions, namely the exterior and the interior. The well known spherical harmonics expansions [39] may be derived from these gravitational field expansions. The relatively simple and efficient form of the spherical harmonics expansion allows for its ubiquitous use in spacecraft navigation and precise orbit determination. However, the derivation of the gravitational field expansions reveals their fundamental limitations due to the existence of their strict convergent regions. In fact, the inherent limitation of the exterior field expansion in accurately modeling the surface proximity gravitational field of small bodies is the motivation behind the derivation of alternative methods, such as the interior field expansion [92]. Later in the this chapter we review the derivation of the interior gravitational field expansion as well as a discussion on the potential benefits of such expansion over the conventional form of the gravitational expansion.

www.manaraa.com

7.1 Formulation of the Gravitational Potential

Let us rewrite the definition of the gravitational potential for an arbitrary body mass $\mathscr{B}$ that is given by Eq. 3.2. That is

$$U = G \int_{\mathscr{B}} \frac{\mathrm{d}m'}{\zeta}, \tag{7.1}$$

where ζ is the distance between the differential mass element $\mathrm{d}m'$ and the point p in the gravitational field where the potential is evaluated, a.k.a. the *field point*. Figure 7.1 shows the field point p in the gravitational field of an arbitrary body of mass. This field point is located by the latitude ϕ, the longitude λ, and the radial distance of r from an arbitrary center of the coordinate system. According to the law of cosines, the distance of the field point from the differential mass element $\mathrm{d}m'$ is given by

$$\begin{aligned} \zeta^2 &= r^2 + (r')^2 - 2rr' \cos\alpha, \\ \cos\alpha &= \sin\phi \sin\phi' + \cos\phi \cos\phi' \cos(\lambda - \lambda') \end{aligned} \tag{7.2}$$

where the prime subscript denotes the spherical coordinates of the differential mass element and α is the angle between the position vectors $\mathbf{r}$ and $\mathbf{r}'$.

In general, there are two approaches for solving the gravitational potential of an object. One method that is widely used is by recalling the fact that the gravitational potential function satisfies the Laplace's equation, i.e. $\nabla^2 U = 0$. References [31, 32, 39] and [47] discuss this approach in detail by expressing Laplace's differential equation in an spherical coordinate and using the separation of variables to solve that equation. The resulting solution is an infinite series of orthogonal spherical harmonic basis functions that integrate over the surface of an sphere. In this work, however, we follow a second approach that utilizes the expansion of the integral definition of the gravitational potential given by Eq. (7.1). This approach is favored for our work since it clearly shows the boundary within which the series expansion is guaranteed to converge. This method is discussed in further detail in References [92] and we present some of the derivation steps in the following section.

www.manaraa.com

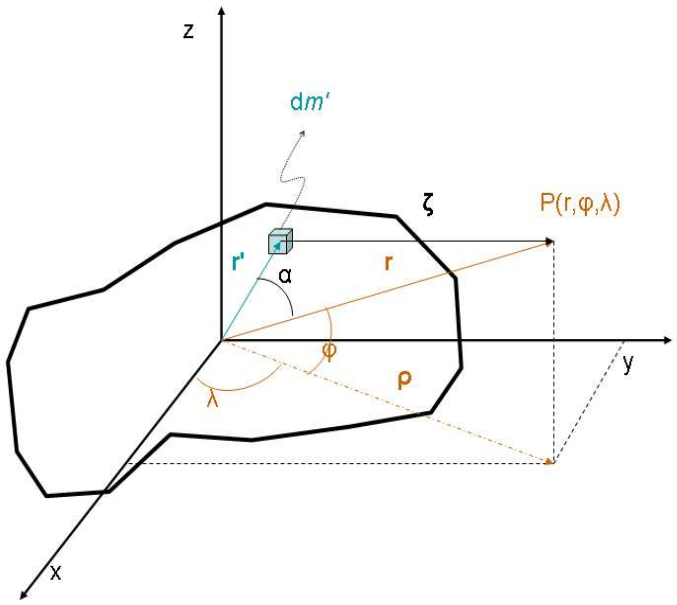

Figure 7.1: A schematic view of a field point in the gravitational field of an arbitrary body of mass.

7.2 The Exterior Gravitational Potential Expansion

In this section we present the derivation of the exterior gravitational field expansion. Substituting the expression for ζ from Eq. (7.2) inside Eq. (7.1) gives

$$U = G \int_{\mathscr{B}} \frac{\mathrm{d}m'}{\sqrt{r^2 + (r')^2 - 2rr' \cos\alpha}}. \tag{7.3}$$

Factoring out r in the denominator results in

$$U = G \int_{\mathscr{B}} \frac{\mathrm{d}m'}{r\sqrt{1 + t^2 - 2\mu t}}, \tag{7.4}$$

where $t = r'/r$ and $\mu = \cos\alpha$. The expression $(1 + t^2 - 2\mu t)^{-1/2}$ inside the integrand is the generating function for the well known Legendre polynomials, $P_n(\mu)$ [31](§ 9) and [65](§ 16.1). The generating function is related to the Legendre polynomials via the following expression

$$\frac{1}{\sqrt{1 + t^2 - 2\mu t}} = \sum_{n=0}^{\infty} t^n P_n(\mu). \tag{7.5}$$

www.manaraa.com

This series is guaranteed to converge for $|t| < 1$ [31, 92]. In other words, the series expansion of the gravitational potential described by Eq. (7.5) is convergent anywhere in the space around the body of mass that is farther from the origin than all of the mass elements $\mathrm{d}m'$. This limitation brings up the idea of the "exterior" gravity field expansion. Exterior gravity field is valid in the space outside of a circumscribing sphere (a.k.a. exterior Brillouin sphere) that encompasses the entire body of mass. Substituting Eq. (7.5) inside Eq. (7.4), one may write the exterior gravity field expansion of an arbitrary body of mass in the following form

$$U^e = G \int_{\mathscr{B}} \sum_{n=0}^{\infty} \frac{(r')^n}{r^{n+1}} P_n(\mu) \mathrm{d}m'. \tag{7.6}$$

The superscript e denotes the exterior gravity field expansion distinguishing it from an interior gravity field expansion that is discussed later. Figure 7.2 shows a schematic view of the outline of an exterior gravity field Brillouin sphere.

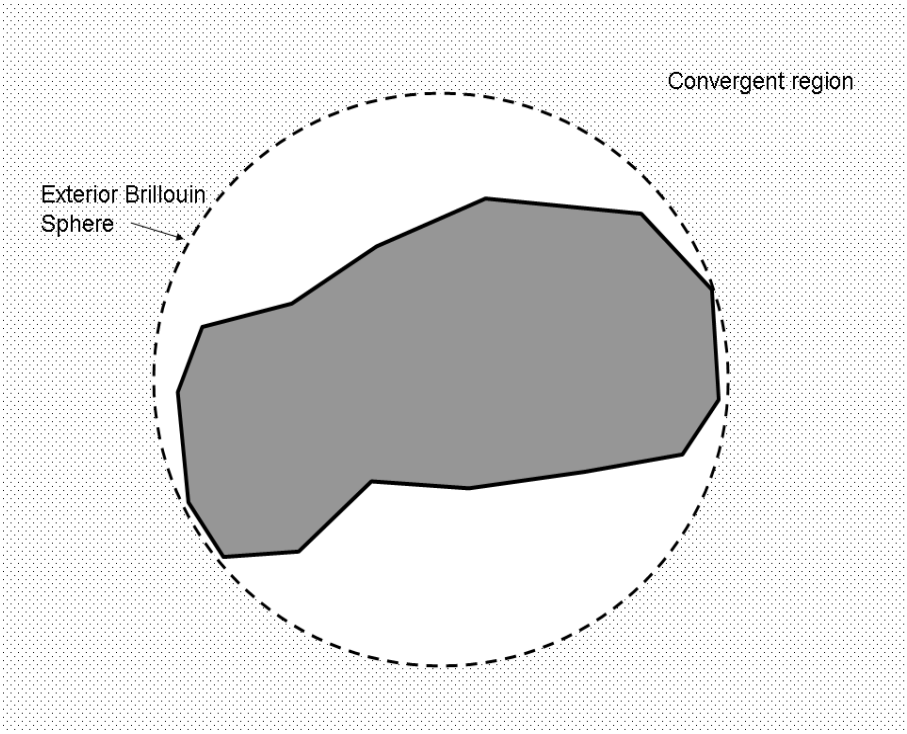

Figure 7.2: A schematic view of an exterior Brillouin sphere for an arbitrary body.

www.manaraa.com

7.2.1 Spherical Harmonics Expansion of an Exterior Field

We now use the so-called *addition theorem* [31](§ 91) to separate Eq. (7.6) into arguments that depend only on the field point coordinates and those that depend only on the coordinates of the differential mass elements. The addition theorem is given by [31](§ 91)

$$P_n(\cos\alpha) = \sum_{m=0}^{n} \frac{(2-\delta_{0,m})(n-m)!}{(n+m)!} \left\{ \begin{array}{l} P_{nm}(\sin\phi)\cos(m\lambda) \times P_{nm}(\sin\phi')\cos(m\lambda') \\ +P_{nm}(\sin\phi)\sin(m\lambda) \times P_{nm}(\sin\phi')\sin(m\lambda') \end{array} \right\}, \tag{7.7}$$

which expresses a degree n Legendre polynomial as a function of the *associated* Legendre polynomials, P_{nm}, with degree n and order m. One may substitute Eq. (7.7) into Eq. (7.6) and change the order of the integration with the summations to get

$$\begin{aligned} U^e = G \sum_{n=0}^{\infty} \frac{1}{r^{n+1}} \sum_{m=0}^{n} P_{nm}(\sin\phi)\cos(m\lambda) \left\{ \frac{(2-\delta_{0,m})(n-m)!}{(n+m)!} \int_{\mathscr{B}} (r')^n P_{nm}(\sin\phi')\cos(m\lambda')\mathrm{d}m' \right\} \\ +G \sum_{n=0}^{\infty} \frac{1}{r^{n+1}} \sum_{m=1}^{n} P_{nm}(\sin\phi)\sin(m\lambda) \left\{ \frac{2(n-m)!}{(n+m)!} \int_{\mathscr{B}} (r')^n P_{nm}(\sin\phi')\sin(m\lambda')\mathrm{d}m' \right\}. \end{aligned} \tag{7.8}$$

In the equation above, the expressions inside the curly brackets do not depend on the coordinates of the field point and are only a function of the mass distribution of the body. In fact, for a given body of mass, the value of these expressions are constant and are only a function the degree n and the order m. These expressions result in what is called the *dimensional* spherical harmonics coefficients [32](§ 2.5) and are given by

$$\begin{aligned} A^e_{nm} &= \frac{(2-\delta_{0,m})(n-m)!}{(n+m)!} \int_{\mathscr{B}} (r')^n P_{nm}(\sin\phi')\cos(m\lambda')\mathrm{d}m', \\ B^e_{nm} &= \frac{2(n-m)!}{(n+m)!} \int_{\mathscr{B}} (r')^n P_{nm}(\sin\phi')\sin(m\lambda')\mathrm{d}m', \qquad m>0. \end{aligned} \tag{7.9}$$

The non-dimensional coefficients are defined by [32](§ 2.5)

$$\begin{aligned} C^e_{nm} &= \frac{1}{M^*(R^*_e)^n} A^e_{nm}, \text{ and} \\ S^e_{nm} &= \frac{1}{M^*(R^*_e)^n} B^e_{nm}, \end{aligned} \tag{7.10}$$

www.manaraa.com

where M^* and R_e^* are the reference mass and the reference radius of the expansion, respectively. The value of these parameters are arbitrary, however it is conventional to set the reference mass equal to the total mass of the body and the reference radius to the radius of the exterior Brillouin sphere. Therefore, the non-dimensional exterior spherical harmonics coefficients are given by

$$C_{nm}^e = \frac{(2-\delta_{0,m})(n-m)!}{M^*(n+m)!}\int\limits_{\mathscr{B}}\left(\frac{r'}{R_e^*}\right)^n P_{nm}(\sin\phi')\cos(m\lambda')\mathrm{d}m',$$
$$S_{nm}^e = \frac{2(n-m)!}{M^*(n+m)!}\int\limits_{\mathscr{B}}\left(\frac{r'}{R_e^*}\right)^n P_{nm}(\sin\phi')\sin(m\lambda')\mathrm{d}m', \qquad m>0. \tag{7.11}$$

Substituting the expressions from Eq. (7.11) into Eq. (7.8) results in the final form of the spherical harmonics expansion of an exterior gravitational field, which is given by

$$U^e = \frac{GM^*}{R_e^*}\sum_{n=0}^{\infty}\sum_{m=0}^{n}\left(\frac{R_e^*}{r}\right)^{n+1} P_{nm}(\sin\phi)\Big\{C_{nm}^e\cos(m\lambda)+S_{nm}^e\sin(m\lambda)\Big\}. \tag{7.12}$$

In general, one further step is performed to defined the *fully normalized* spherical harmonics expansion and its corresponding coefficients. This is done due to the fact the associated Legendre polynomial increases rapidly in its value, while the non-dimensional coefficients (C_{nm}^e & S_{nm}^e) decrease rapidly in their value with the increased degree and order of the expansion. Numerical issues might occur when computing these parameters, separately. To resolve this issue, the fully normalized parameters are defined by

$$\begin{aligned}\bar{P}_{nm} &= \Pi_{nm}P_{nm},\\ \bar{C}_{nm}^e &= \frac{1}{\Pi_{nm}}C_{nm}^e, \text{ and}\\ \bar{S}_{nm}^e &= \frac{1}{\Pi_{nm}}S_{nm}^e,\end{aligned} \tag{7.13}$$

where Π_{nm} is called the normalization factor and is given by [39] (§ 1.2)

$$\Pi_{n,m} = \sqrt{\frac{(2-\delta_{0,m})(2n+1)(n-m)!}{(n+m)!}}. \tag{7.14}$$

The expression for the normalization factor is derived from the orthogonality condition of the surface spherical harmonics [39] (§ 1.2). The computation of the normalized Legendre polynomials and the spherical harmonics coefficients is numerically more stable than that for the unnormalized versions of these parameters. Also, note that the definitions given by Eq.(7.13) do

www.manaraa.com

not change the value of the product of a degree n and order m associated Legendre polynomial with its corresponding spherical harmonics coefficients. Hence, the fully normalized version of the spherical harmonics expansion of an exterior gravitational field may be written by

$$U^e = \frac{GM^*}{R_e^*} \sum_{n=0}^{\infty} \sum_{m=0}^{n} \left(\frac{R_e^*}{r} \right)^{n+1} \bar{P}_{nm}(\sin\phi) \Big\{ \bar{C}_{nm}^e \cos(m\lambda) + \bar{S}_{nm}^e \sin(m\lambda) \Big\}. \tag{7.15}$$

7.2.2 Limitations of the Exterior Gravity Field Expansion

The exterior spherical harmonics expansion of the gravitational field is a widely used method to compute and represent the gravitational attraction about a non-spherical object [31, 32, 39, 47]. This is a powerful method that has been used in numerous fields of research such as satellite geodesy, precise orbit determination, planetary sciences, and also small body exploration. However, as mentioned in the previous section, this method is limited to the space outside of the smallest circumscribing sphere around the body of mass. This limitation is not a major issue for objects that are fairly spherical, such as the planetary bodies. Many of the asteroids and comets, on the other hand, are usually very irregularly shaped. As a result the divergence issue of the exterior gravity field expansion may result in large amounts of errors in representing the surface proximity gravitational field of small bodies. To put this in context we show two example cases. Figure 7.3 shows the contour plots of a 4×4 exterior gravity field acceleration errors about Bennu. The plots show the space around the asteroid on three XY, XZ, and YZ planes. The colors on these contour plots correspond to the percent acceleration error that is given by

$$a_{err} = \frac{|\mathbf{a}_{poly} - \mathbf{a}_{ext}|}{|\mathbf{a}_{poly}|} \times 100, \tag{7.16}$$

where $\mathbf{a}_{poly}$ is the gravitational accelerations computed by a constant density polyhedron model of Bennu (see Eq. (3.4)) and $\mathbf{a}_{ext}$ is the same computed by the exterior gravity field spherical harmonics expansion. The error values are presented in the $\log_{10}$ scale, hence a 0 on the plots means a 1% error, a 1 on the plots means a 10% error, and so on. The outline of the exterior Brillouin sphere and the asteroid are also sown on these plots. Figure 7.4 shows the same information for a

www.manaraa.com

10×10 exterior gravity field acceleration error about Asteroid (433) Eros, which is a much more elongated body compared to Bennu that has a fairly spherical shape.

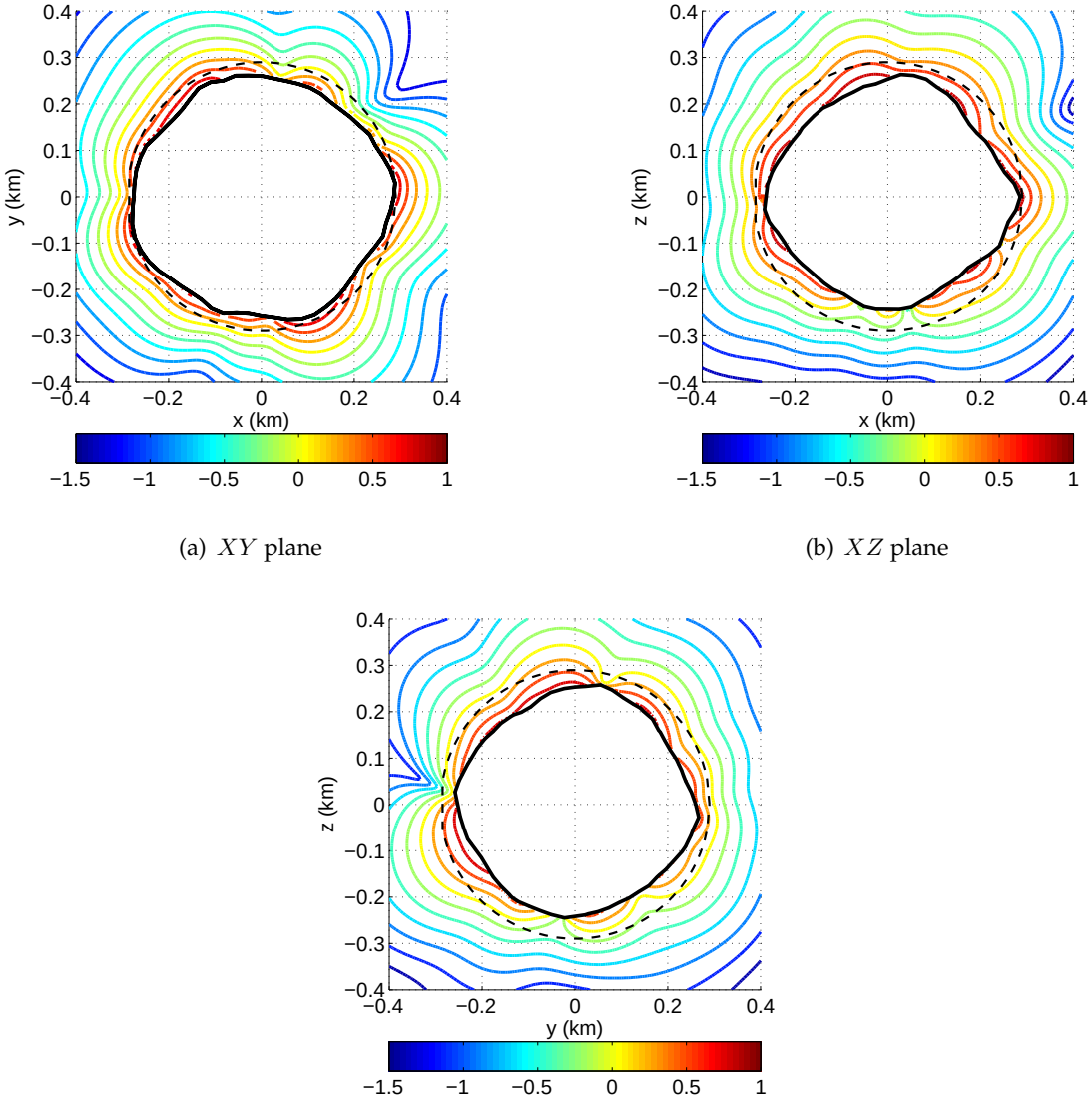

(a) XY plane

(b) XZ plane

(c) YZ plane

Figure 7.3: Percent error in the gravitational acceleration of a 4×4 exterior gravity field compared to a constant density polyhedron model about Bennu.

The contour plots show that errors in the exterior gravity field increase quickly for the field points that are closer to the surface of the object, particularly for those that are within the Brillouin sphere. For Bennu, which is a fairly spherical object, the error rises to up to 10%. This shows

www.manaraa.com

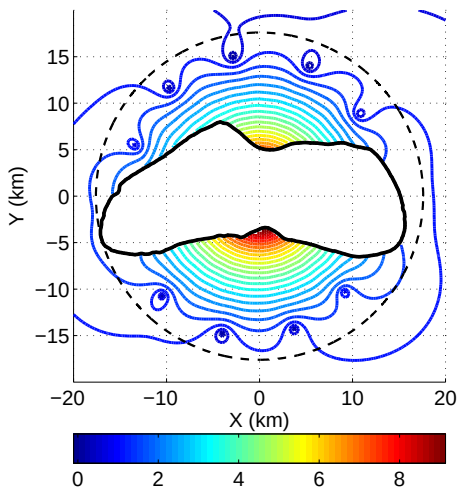

(a) XY plane

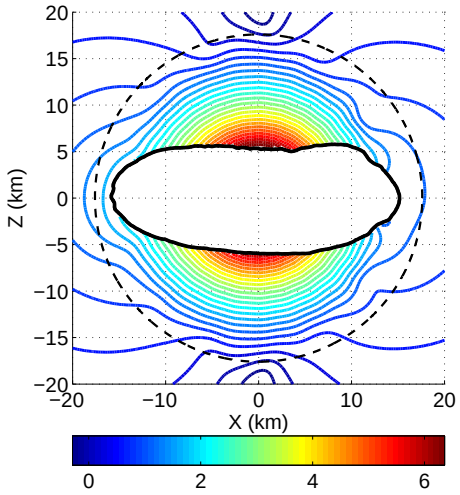

(b) XZ plane

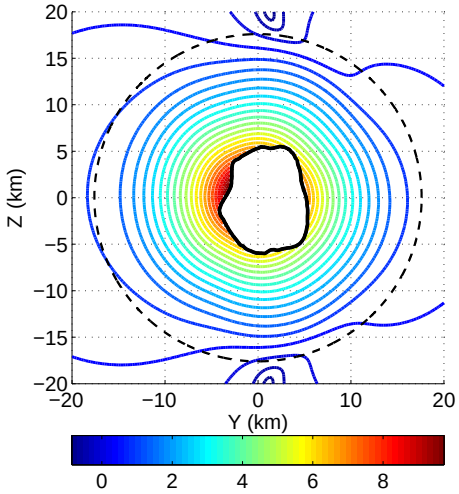

(c) YZ plane

Figure 7.4: Percent error in the gravitational acceleration of a 10×10 exterior gravity field compared to a constant density polyhedron model about Eros.

that for small bodies, whose shapes are close to a sphere the exterior gravity field expansion may be used to model the surface proximity gravitational field of the object. Although the exterior field expansion diverges from the true value of the gravitational field, this divergence is not very significant. However, for Eros the divergence of the exterior field expansion is quite significant. Figure 7.4 shows that the exterior gravity field error reaches up to $10^9\%$ around the neck area

www.manaraa.com

of the asteroid that is farthest from the Brillouin sphere boundary. This example illustrates that an exterior gravity field is not a sufficient method to provide an accurate representation of the surface proximity gravity field for highly irregularly shaped objects. This is an important issue for spacecraft that plan to land on the surface of such objects. As illustrated in Figure 7.5, a significant portion of a landing or TAG trajectory of a spacecraft may lie inside the circumscribing sphere of a small body, which may pose a serious limitation on preforming precise landing operations.

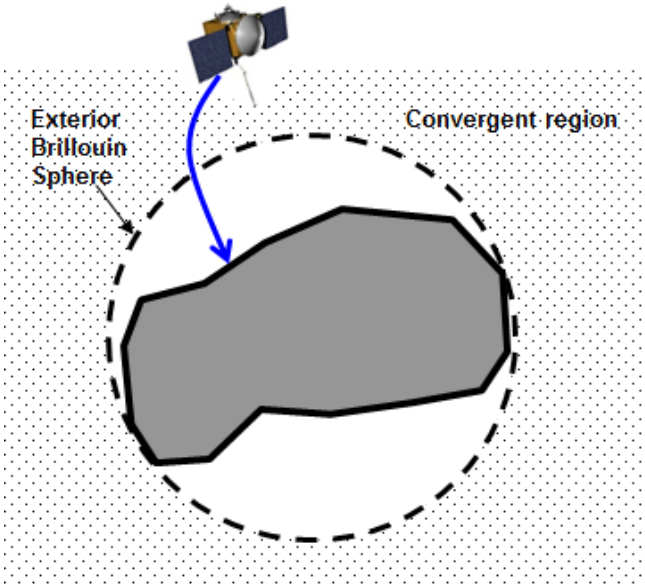

Figure 7.5: A schematic view of a landing trajectory on an irregularly shaped object.

Other methods are developed for computing the gravitation potential of a non-spherical object via, for instance, a constant density polyhedron shape model [90, 91, 93] or an ellipsoidal harmonics expansion [21], [31](Ch. XI). One may use a constant density shape model to compute an exact solution to the gravitation potential anywhere on or outside of that shape mode. However, the high computational cost of this method makes it unattractive for spacecraft navigation work or its implementation aboard a spacecraft. Besides, this model assumes a constant density for the object, which is not true in reality. The ellipsoidal harmonics expansion may also be used to mitigate the divergence issue of the exterior spherical harmonics expansion [21]. The convergent

www.manaraa.com

region of an ellipsoidal harmonics expansion is anywhere outside of a circumscribing ellipsoid. A circumscribing ellipsoid lies closer to the surface of an elongated body of mass compared to a circumscribing sphere. This model, however, suffers from the same divergence issues for a field point that is outside of its convergent region.

Recent studies [85, 92] have developed an *interior* gravity field spherical harmonics expansion that extents down to the surface of an object without divergence issues. This is due to the fact that the convergent region of an interior spherical harmonics expansion is defined inside a spherical region that is outside of the body of mass and may be tangent to the surface of the object. Reference [85] showed that an interior gravity field can accurately describe the surface proximity gravitational potential of an arbitrary object. We review the derivation of this form of gravitational field expansion in the next section and study its possible application for spacecraft navigation in Chapter 8.

7.3 The Interior Gravitational Potential Expansion

An interior gravity field expansion is derived by following the same steps that are presented for the derivation of an exterior gravity field expansion. However there is a slight, but crucial, difference between the derivation of the two models that is presented here. We start by restating Eq. (7.6) that is given by

$$U = G \int_{\mathscr{B}} \frac{\mathrm{d}m'}{\sqrt{r^2 + (r')^2 - 2rr' \cos\alpha}}. \tag{7.17}$$

This time we factor out r' in the denominator to get

$$U = G \int_{\mathscr{B}} \frac{\mathrm{d}m'}{r'\sqrt{t^2 + 1 - 2\mu t}}. \tag{7.18}$$

We now have $t = r/r'$. Once again we recognize the expression $(1 + t^2 - 2\mu t)^{-1/2}$ inside the integrand may be expressed by a series expansion shown in Eq. (7.5). Recall that this series is guaranteed to converge for $|t| < 1$ [65] (§ 16.1). In other words, the series converges to the true value of the gravitational potential at any field point that is closer to the origin than every differential mass element $\mathrm{d}m'$. There are couple of ways to envision a Brillouin sphere that will satisfy

www.manaraa.com

this criterion [85]. One way that is most practical is to place the origin of the gravity field outside of the body of mass and construct a large enough sphere that is tangent to the surface of the body at the closest point. This is called the interior Brillouin sphere [92]. The interior gravity field is convergent anywhere inside this sphere. Figure 7.6 shows the outline of an interior Brillouin sphere placed outside an arbitrary body of mass.

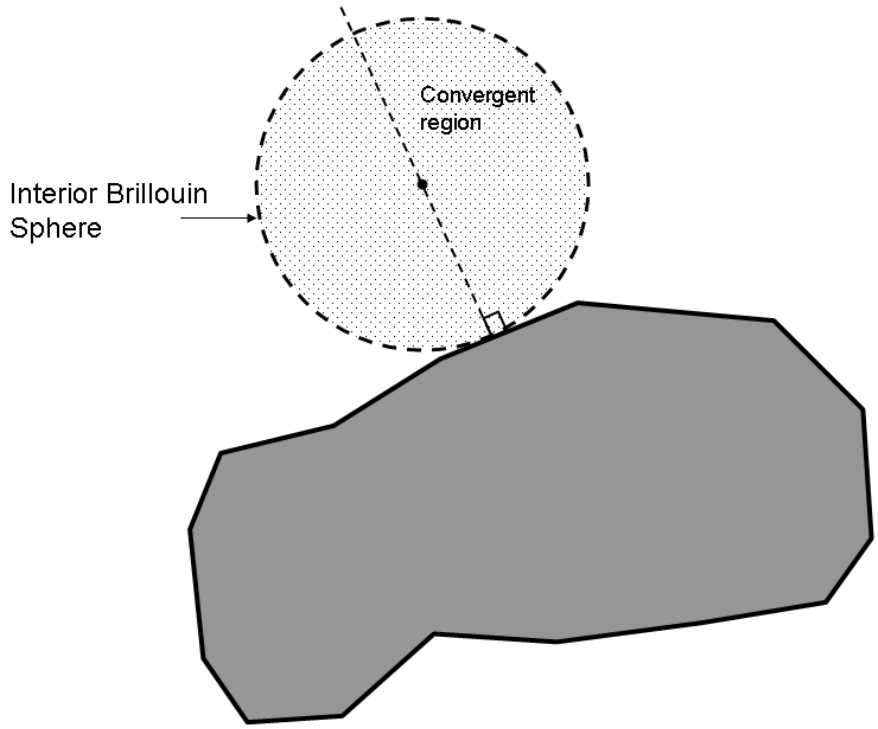

Figure 7.6: A schematic view of an interior Brillouin sphere for an arbitrary body.

At this point we are able to define the interior gravity field expansion by substituting Eq. (7.5) into Eq. (7.18) and noting that $t = r/r'$. Doing so we get

$$U^i = G \int_{\mathscr{B}} \sum_{n=0}^{\infty} \frac{r^n}{(r')^{n+1}} P_n(\mu) \mathrm{d}m'. \tag{7.19}$$

The superscript i denotes the interior gravity field expansion.

www.manaraa.com

7.3.1 Spherical Harmonics Expansion of an Interior Gravity Field

Once again one may take advantage of the *addition theorem* to separate Eq. (7.19) into arguments that only depend on the field point coordinates and those that only depend on the coordinates of the differential mass elements. Doing so and following the same steps explained for the exterior gravity field (see Section 7.2.1) we arrive at the following equation that defines the interior gravity field in the form of a spherical harmonics expansion:

$$U^i = \frac{GM^*}{R_i^*} \sum_{n=0}^{\infty} \sum_{m=0}^{n} \left(\frac{r}{R_i^*} \right)^n P_{nm}(\sin\phi) \Big\{ C_{nm}^i \cos(m\lambda) + S_{nm}^i \sin(m\lambda) \Big\}, \tag{7.20}$$

where the interior spherical harmonics coefficients are given by

$$\begin{aligned} C_{nm}^i &= \frac{(2-\delta_{0,m})(n-m)!}{M^*(n+m)!} \int_{\mathscr{B}} \left(\frac{R_i^*}{r'} \right)^{(n+1)} P_{nm}(\sin\phi') \cos(m\lambda') \mathrm{d}m', \\ S_{nm}^i &= \frac{2(n-m)!}{M^*(n+m)!} \int_{\mathscr{B}} \left(\frac{R_i^*}{r'} \right)^{(n+1)} P_{nm}(\sin\phi') \sin(m\lambda') \mathrm{d}m', \qquad m > 0. \end{aligned} \tag{7.21}$$

Variable R_i^* is the reference radius of the interior gravity field. Much like the exterior field, the value of the reference radius is arbitrary and is used along with the reference mass M^* to non-dimensionalize the coefficients. We set this value equal to the radius of the interior Brillouin sphere. Note that this derivation skips through explicitly defining the dimensional interior gravity field coefficients as they are derived in a similar way to their exterior counterparts. Also, the fully normalized interior gravity field coefficients are defined in the same fashion as before via

$$\begin{aligned} \bar{C}_{nm}^i &= \frac{1}{\Pi_{nm}} C_{nm}^i, \text{ and} \\ \bar{S}_{nm}^i &= \frac{1}{\Pi_{nm}} S_{nm}^i. \end{aligned} \tag{7.22}$$

Substituting these coefficients and the normalized associated Legendre polynomials in Eq. (7.20) results in the fully normalized version of the spherical harmonics expansion for the interior gravity field. This expansion is given by

www.manaraa.com

$$U^i = \frac{GM^*}{R_i^*} \sum_{n=0}^{\infty} \sum_{m=0}^{n} \left(\frac{r}{R_i^*} \right)^n \bar{P}_{nm}(\sin\phi) \Big\{ \bar{C}_{nm}^i \cos(m\lambda) + \bar{S}_{nm}^i \sin(m\lambda) \Big\}. \tag{7.23}$$

It is clear that the spherical harmonics expansion of an interior gravity field takes a form that is very similar to that of an exterior gravity field. However, there are certain subtleties that are worth noting. It is well know that the zeroth degree and order coefficient of the exterior gravity field, i.e. C_{00}^e, is equal to unity if we set the reference mass equal to the total mass of the body. Moreover, the first degree and order coefficients of the exterior field are identically equal to zero if the body-fixed coordinate frame is assumed to be centered at the center of mass of the object. The second degree and order coefficients of the exterior field also have physical meanings as they are closely related to the moments of the inertia of the body of mass [77] (Ch. 2). Unlike the exterior field coefficients, the interior field coefficients do not have clear physical interpretations. Also we note that the first term in the series expansion of an interior field, namely $G \int_{\mathscr{B}} (r')^{-1} \mathrm{d}m'$, is merely a constant bias term that corresponds to the zeroth degree and order coefficient, i.e. C_{00}^i. Since this term does not contribute to the field point acceleration, it may be disregarded altogether.

7.4 Chapter Summary

This chapter reviews the formulation of the gravitational potential field and the derivation of the gravitational field expansions both for an exterior and an interior field. The fully normalized spherical harmonics expansions are presented for both types of the expansions. The exterior spherical harmonics expansion is a powerful method for modeling the gravitational perturbations of non-spherical objects. This method has been used to accurately represent the gravitational field of objects that are close to an sphere in shape, such as the planetary bodies and many of their moons. However, it turns out that due to a fundamental limitation of this type of expansion, this method is not suitable for representing the surface proximity gravitational field of highly irregularly shaped objects, such as asteroids and comets. Spacecraft bound to a landing or TAG trajectory close to a highly irregularly shaped object may experience large errors in the gravitational

www.manaraa.com

field representation that could divert them from their course.

The interior gravity field and its spherical harmonics expansion form is one way to address this issue. This field exists and is valid inside a spherical region called the interior Brillouin sphere that extends all the way down to the surface of an arbitrary body of mass. Using this formulation one may be able to accurately represent the surface gravitational field of a small body and successfully navigate spacecraft during their landing or TAG operations. In the next chapter, we present numerical analyses of an interior gravity field and compare its performance to that of an exterior gravity field expansion. We further use this field to perform simulated navigation of a spacecraft during a landing trajectory bound to the surface of a small body.

www.manaraa.com

Chapter 8

Surface Proximity Gravitational Field Modeling and Estimation

Chapter 7 presented a formulation for the interior gravitational field expansion that is valid in the surface proximity of irregularly shaped objects. This formulation may provide an alternate way of representing the surface proximity gravitational field over the conventional exterior spherical harmonics model. However, in order to utilize an interior gravity model one has to be able to perform a reliable measurement and estimation of its coefficients. As it turns out, estimating the coefficients of an interior field is very challenging. Previous research [86] developed a method to compute the interior gravity field coefficients using a constant density polyhedron model. While a powerful method for generating *a priori* values for these coefficients, this method does not provide direct means to measure the uncertainty of the computed coefficients. One may also estimate the interior field coefficients using an existing exterior gravitational field and a set of sample field points that lie in a region of space that overlaps the convergent region of both of the models [85, 86]. This method is able to provide an *a priori* measure of the values and uncertainties for the interior gravity field coefficients. However, it requires an existing exterior gravity field of an object and a sufficiently large area that overlaps the convergent regions of both models. Depending on the shape of an object and the size of the intended interior gravity field, a sufficiently large overlapping region between an interior and an exterior field may not always exist.

A direct estimation of an interior field coefficients via orbit determination solution has not been studied before. In this chapter, we examine the feasibility of directly estimating the coefficients of an interior gravity field via an orbit determination solution. First, via a covariance study,

www.manaraa.com

we evaluate the precision level that may be achieved for the interior gravity field coefficients. For this work we analyze the surface proximity gravitational field of Eros. In particular, the study focuses on analyzing the gravitation field of the space immediately above the estimated landing site of the NEAR spacecraft [1] . Following the covariance analysis, we present a simulation study of tracking a spacecraft during a landing trajectory and utilizing an interior gravity field to perform its navigation.

8.1 Estimating the Interior Gravity Field Coefficients - Covariance Studies

At the end of its mission, through a set of end mission maneuvers (EMM's) [2] , the NEAR spacecraft descended to the surface of Asteroid (433) Eros. The landing site is estimated to be at about -36° latitude and $+81^\circ$ longitude. This point is inside a large depression in the eastern hemisphere of the asteroid, called the Himeros [3] . The radius at this point is about 6.4 kilometers, which is much smaller than the circumscribing radius of the object at about 17.6 kilometers [96]. In other words the landing site is well within the circumscribing sphere of the asteroid where the exterior spherical harmonics expansion is not able to accurately represent the true gravity field. It took the NEAR spacecraft about 4.5 hours to descend to the surface from the orbit it originated from. In this section we implement a set of covariance analyses to measure the expected level of estimation precision possible for the interior gravity field coefficients during a similar amount of time when a spacecraft passes through the convergent region of an interior gravity field.

8.1.1 Simulation Setup

The truth trajectories used in this study are a set of simulated flyby trajectories that are designed to fly over the NEAR landing site at a closest approach distance of 8 kilometers. The flyby trajectory planes are designed to be close to the asteroid's equatorial plane and their directions are simulated to be in the same direction as the asteroid's rotation. This way, the spacecraft is able to

[1] http://near.jhuapl.edu/news/sci_updates/01feb20.html
[2] http://sbn.psi.edu/pds/resource/near/catalog/raderosds.cat
[3] http://sbn.psi.edu/pds/resource/near/documents/msi/observation_overview.txt

www.manaraa.com

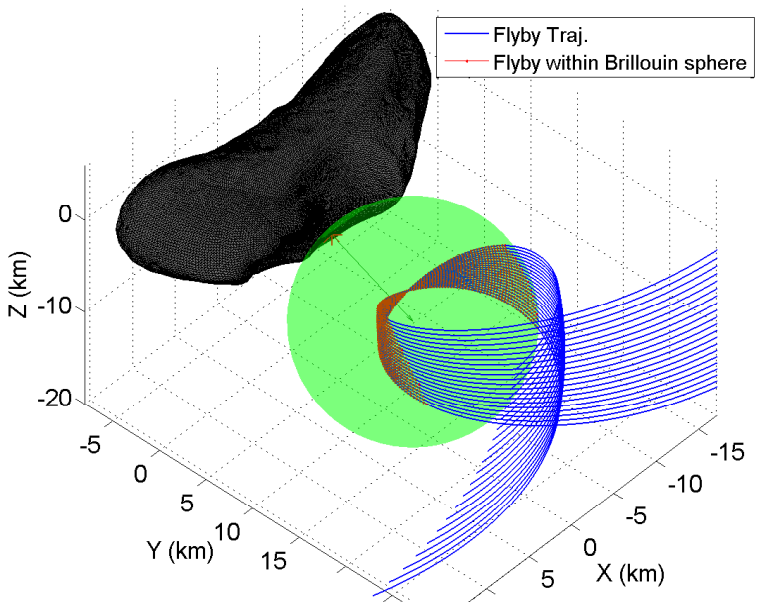

Figure 8.1: Sample flyby trajectory through a 10 km Brillouin sphere of an interior gravity field.

spend more time flying within the Brillouin sphere of an interior gravity field that is also rotating with the asteroid. Figure 8.1 shows a sample set of flyby trajectories as they pass through an interior gravity field Brillouin sphere with a radius of 10 kilometers. These trajectories are shown in the asteroid body-fixed frame. The estimated state used in the covariance analysis is given by

$$\mathbf{X} = \left[\mathbf{r}^{\mathrm{T}} \;\; \mathbf{v}^{\mathrm{T}} \;\; \mathbf{CS}_{\ell}^{i}\right]^{\mathrm{T}} \tag{8.1}$$

where vectors $\mathbf{r}$ and $\mathbf{v}$ are the position and velocity vectors of the spacecraft. The vector $\mathbf{CS}_{\ell}^{i}$ contains a set of estimated interior gravity field coefficients up the degree and order ℓ. This is given by

$$\mathbf{CS}_{\ell}^{i} = [\bar{C}_{10}^{i} \;\; \bar{C}_{11}^{i} \;\; \bar{S}_{11}^{i} \;\; \ldots \;\; \bar{C}_{\ell\ell}^{i} \;\; \bar{S}_{\ell\ell}^{i}]^{\mathrm{T}}. \tag{8.2}$$

where the $\bar{C}^{i}$ and $\bar{S}^{i}$ are fully normalized versions of the interior gravity field coefficients. Equation 7.22 defines these coefficients. The *a priori* uncertainties of the spacecraft position and velocity are assumed to be 100 meters and 1 m/sec at each direction, respectively. The *a priori* uncertainties for the interior gravity field coefficients are derived using an existing exterior gravity field. This method is described in the next section. The time evolution of the estimated state elements are

www.manaraa.com

given by

$$\begin{aligned} \dot{\mathbf{r}} &= \mathbf{v}, \\ \dot{\mathbf{v}} &= \mathbf{a}_{\oplus} + \mathbf{a}_{SRP} + \mathbf{a}_{3^{\text{rd}}}, \text{ and} \\ \dot{\mathbf{C}}\mathbf{S}_{\ell}^{i} &= 0, \end{aligned} \tag{8.3}$$

where $\mathbf{a}_{\oplus}$ is the acceleration due to the gravitation of the central body, which in this case is the asteroid. The gravitational acceleration of the asteroid is computed using a constant density polyhedron model [93] of Eros for the generation of the truth trajectory. The accelerations due to SRP and Sun's third-body perturbation are given by $\mathbf{a}_{SRP}$ and $\mathbf{a}_{3^{\text{rd}}}$, respectively. The SRP acceleration is computed using a cannonball model for this study. Table 8.1 summarizes the dynamical model that is used in generating the truth trajectories.

Table 8.1: Truth Model Parameters

Simulation Epoch:	2020 Feb 1 00:00:00.000 TDB
Force Model	
Central Body:	(433) Eros ($\mu = 4.4621E-4 km^3/s^2$) [59]
Gravitational Perturbations:	Constant density polyhedron
Solar Radiation Pressure:	Cannonball Model
Third body:	Sun (point mass)

8.1.2 Derivation of the *a priori* Uncertainties for the Interior Gravity Coefficients

The *a priori* uncertainties of the interior gravity field coefficients are computed from an existing exterior gravity field and the derivation of a best fit solution between the acceleration values given by the two gravity models in a region of space that overlaps the convergent region of the both models. This method was used previously [86] to compute a best estimate coefficient values for an interior gravity field. In this study we use this method to map the uncertainty of an existing exterior gravity field onto an interior field. The idea behind this method is that in an overlapping area inside the convergent regions of both of the exterior and interior gravity expansions, both

www.manaraa.com

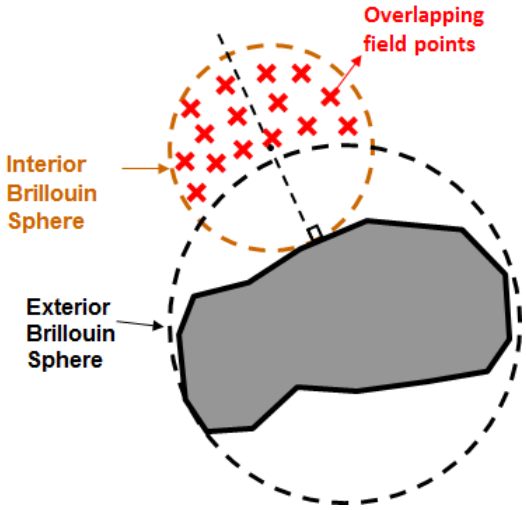

Figure 8.2: An illustration of the overlapping area between an exterior and an interior gravity field.

models have to converge to the same value of the field potential and gravitational acceleration. Hence, one may derive a best fit solution that minimizes the difference between the field point potential or gravitational accelerations computed by both models for a set of sample points. In this study we use the gravitational acceleration for the derivation of such a solution. Figure 8.2 illustrates an overlapping region between an exterior and an interior gravity field and the sample points that are used to generate the best fit solution.

The problem is formulated to minimize the cost function J given by

$$\min J = \frac{1}{2}\left(\frac{\partial U^e}{\partial \mathbf{r}} - Q^i \mathbf{CS}^i\right)^{\mathrm{T}} W \left(\frac{\partial U^e}{\partial \mathbf{r}} - Q^i \mathbf{CS}^i\right), \tag{8.4}$$

where $\partial U^e/\partial \mathbf{r}$ is the gravitational acceleration due to an exterior gravity field, Q^i is the partial derivative of the gravitational acceleration with respect to the interior gravity coefficients (References [85] and [92] present the derivation of these partials), and W is the sample point weighting function given by

$$W = (Q^e P^e [Q^e]^{\mathrm{T}})^{-1}. \tag{8.5}$$

Parameter Q^e is the partial derivative of the gravitational acceleration with respect to the exterior

www.manaraa.com

gravity coefficients (see Appendix A for details) and P^e is the covariance matrix for these coefficients. Based on the cost function defined by Eq. (8.4), the best estimate (least squares solution) of the interior gravity coefficients $\hat{\mathbf{CS}}^i$ and their uncertainties (in the form a covariance matrix $\overline{P}^i$) are given by

$$\hat{\mathbf{CS}}^i_k = (\overline{P}^i_k)^{-1}\left([Q^i]^{\mathrm{T}}(Q^eP^e[Q^e]^{\mathrm{T}})^{-1}\frac{\partial U^e}{\partial \mathbf{r}} + (\overline{P}^i_{k-1})^{-1}\mathbf{CS}^i_{k-1}\right),$$
$$\overline{P}^i_k = \left((\overline{P}^i_{k-1})^{-1} + [Q^i]^{\mathrm{T}}(Q^eP^e[Q^e]^{\mathrm{T}})^{-1}Q^i\right)^{-1}. \tag{8.6}$$

The subscript k indicates that the solution is given after processing the information from k sample points. The bar "$\bar{}$" symbol over the covariance matrix signifies that what we get out of this process is going to be an *a priori* uncertainty that is used by the subsequent covariance analysis. At the step $k = 0$ the covariance matrix is set to an identity matrix of the correct size, i.e. $\overline{P}^0_i = I$.

For the covariance study presented here we sample a total of $2,000$ field points equally spaced inside the overlapping region between the interior Brillouin sphere that is being estimated and an exterior Brillouin sphere. The exterior gravity field covariance matrix P^e is formed as a diagonal matrix, whose diagonal elements are populated by the squared values of the coefficients uncertainties given by the NEAR15A model. This is a 15×15 spherical harmonics gravity field representation of Eros provided by References [14] and [59]. After processing all of the sample points, the square root of the values on the diagonal of the final $\overline{P}_i$ are used as the *a priori* values of the interior gravity coefficients in the covariance study.

In the absence of an exterior gravity field for an object, one may use a numerical method that performs small variations to the polyhedron shape model and the density distribution of the object and computes the interior gravity field coefficients for each instance in order to get a measure of the uncertainty for these coefficients. Reference [57] performs a similar approach to measure the uncertainties of the exterior gravity field coefficients for Bennu.

www.manaraa.com

8.1.3 Measurement Model

Similar to the other covariance studies presented thus far, the observations used in this covariance study are a combination of sample and line measurements from a set of simulated surface landmarks as well as simulated radiometric measurements between three DSN antennas and a spacecraft. Optical landmark observations are generated from a total of 100 landmarks that are selected randomly on the surface of the asteroid in the close proximity of the landing site. A fairly wide-angle camera is assumed to be mounted on the spacecraft with a focal length of about 12 mm and a 30° field of view (FOV) with a 512×512 pixels array. A 2° limit above the horizon determines when a landmark is in view of the camera, given that it falls within the FOV limit of the camera and is illuminated by the sunlight. The camera is assumed to point towards the landing site during the flybys. For the radiometric measurements we simulate range and range-rate observations between DSN antennas and a spacecraft. Three DSN antennas are chosen for this simulation, namely DSS14 in Goldstone, CA, DSS43 in Canberra, Australia, and DSS63 in Madrid, Spain. A local antenna mask of 10° is applied to the DSN antennas when generating these measurements. The observations are generated when the line-of-sight between a DSN antenna and the spacecraft is not occulted.

All of the measurements are generated once every 1 minute during the time that the spacecraft is flying within the Brillouin sphere of an interior gravity field, as depicted by Figure 8.1. Table 8.2 summarizes the *a priori* uncertainties and measurement errors that are used in the covariance study.

8.1.4 Covariance Analysis Results

Figure 8.3 shows the results from the covariance study for a 10 km interior gravity field fixed above the landing site. This figure shows the uncertainty achieved from processing different amounts of observations versus the degree of the gravity coefficients. The figure also shows the actual values of the gravity coefficients and their *a priori* uncertainties that are derived from an

www.manaraa.com

Table 8.2: Summary of the estimated state *a priori* uncertainties and measurement errors

Parameter	1-σ *a priori* Uncertainty
Spacecraft position	
X, Y, Z	100 m
Spacecraft velocity	
V_x,V_y,V_z	1 m/sec
Interior gravity coefficients	Derived from a 15×15 exterior gravity field, (see Eq. (8.6)).
Measurements weighting	
Pixel and Line	0.2 pixels
DSN Observations	
Range	10 cm
Range-rate	0.5 mm/sec

exterior gravity field. These results show that for an interior gravity field with a radius of 10

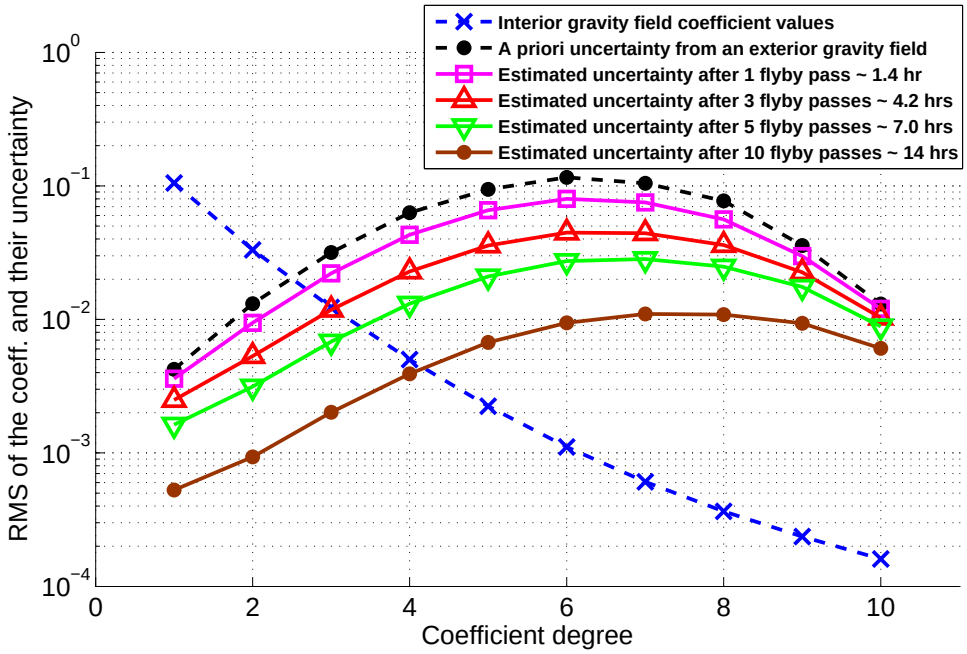

Figure 8.3: Estimated level of uncertainties achieved from processing different amounts of observations for an interior gravity field with a radius of 10 kilometers.

kilometers, one may be able to estimate up to degree and order 3 after processing 7 hours worth of observations. After 4.2 hours, the estimation barely reaches to the degree and order of 3.

Based on these results, we analyze the performance of a 3×3 interior gravity field in com-

www.manaraa.com

parison to an exterior gravity field representation. For the exterior gravity field, we use a 12×12 spherical harmonics expansion generated from a constant density polyhedron model [91]. Figure 8.4 shows the results of this comparison. This figure shows two slices of a contour plot that represent the percent error between the gravitational acceleration computed either by an exterior or an interior gravity field and that computed by a constant density polyhedron model. Density information of the asteroid is given by Reference [59]. Colors of the contour plots represent the percent error in the gravitational acceleration in the $\log_{10}$ scale. The acceleration errors are computed inside the Brillouin sphere of an interior gravity field with a radius of 10 kilometers. The center of the sphere is along the surface normal above the NEAR landing site. Figure 8.4(a) shows that using an exterior spherical harmonics expansion to compute the gravitational field results in errors of up to $10^5\%$ in the area that is close to the surface of the asteroid. However, using an interior spherical harmonics expansion (see Figure 8.4(b)) results in errors on the order of about $10\% - 20\%$ (RMS of the error is about 17%) in the area close to the surface of the asteroid, while yielding even smaller errors in the area closer to the center of the Brillouin sphere. These results show that even a 3×3 interior gravity field results in a significant improvement in representing a surface proximity gravitations field.

Another important parameter that has a significant effect on the accuracy of an interior gravity field is the size of the field radius. The larger the field radius is, the higher degree and order coefficients are needed in order to accurately represent the gravitational field of the object in the close proximity of its surface [85]. This is clear from Figure 8.6(a), where it shows the RMS of the error in the gravitational acceleration computed by a 3×3 interior gravity field with different radii compared to that computed by a constant density polyhedron model. On the other hand, the larger the field radius is, the easier it is for spacecraft to fly through the field and sample the gravity field for a longer period. We study this effect by repeating the covariance analysis for interior gravity fields with the field radii of 8, 12, and 15 kilometers. For radii larger than 15 kilometers above the landing site, the surrounding mountain ridge penetrates significantly inside the Brillouin sphere of the interior gravity field resulting in modeling errors. Figure 8.5 shows

www.manaraa.com

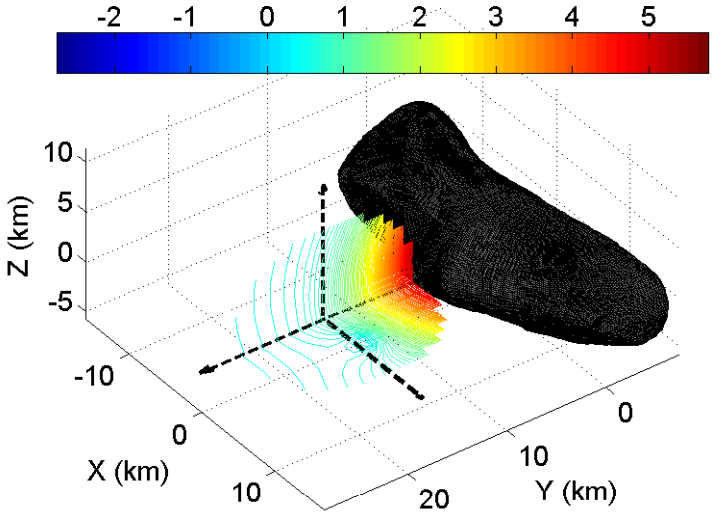

(a) A 12×12 exterior field acceleration error

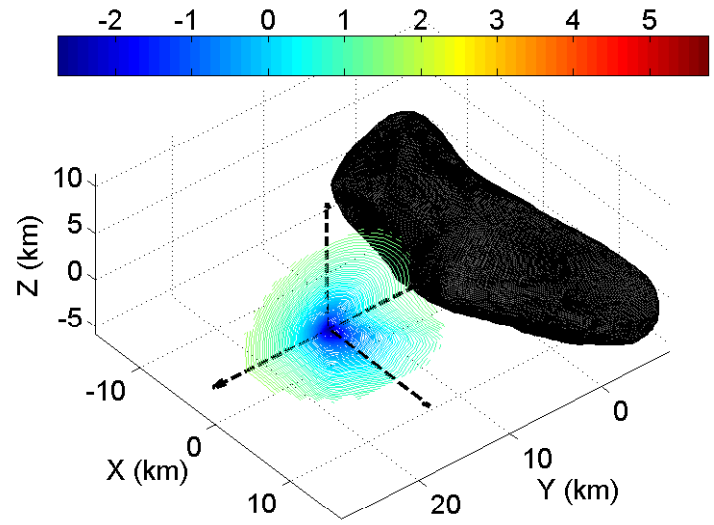

(b) A 3×3 interior field acceleration error

Figure 8.4: Contour plots of the percent error in the gravitational acceleration of an exterior and an interior spherical harmonics as compared to a constant density polyhedron model in an area right above the $-36°$ latitude and $+81°$ longitude. Errors are shown in $\log_{10}$ scale.

the results from a similar covariance analysis for an interior gravity field with a field radius of 15 kilometers. Comparing these results with those presented in Figure 8.3 shows that the estimation

www.manaraa.com

precision is improved significantly for the same number of flyby passes for a larger gravity field. Table 8.3 summarizes the size of the gravity field that one is able to resolve after 5 flyby passes for different sizes of the gravity field radius. This table shows that after the same number of flyby passes, the size of the gravity field that one is able to resolve increases with the increased field radius. However, there is a caveat for these results, which is presented in Figure 8.6(b).

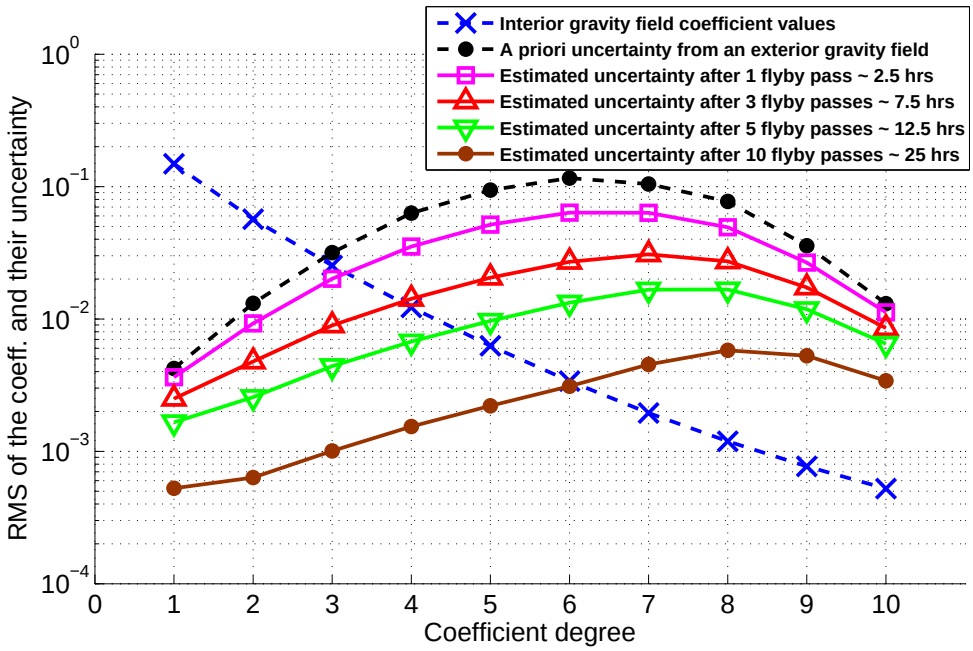

Figure 8.5: Estimated level of uncertainties achieved from processing different amounts of observations for an interior gravity field with a radius of 15 kilometers.

Table 8.3: Estimated interior gravity field size after 5 passes per field radius

Field radius (km)	Gravity field size
8	2×2
10	3×3
12	3×3
15	4×4

This figure shows the RMS of the gravity field error due to the coefficient uncertainties after the 5^{th} flyby pass of the estimation process versus different field radii. These results are generated by adding a random Gaussian error of zero mean and a standard deviation equal to the level

www.manaraa.com

of uncertainty achieved by the estimation process after the 5^{th} flyby pass to the actual value of the interior gravity field coefficients. We repeat this process 100 times and compute the RMS of the acceleration error computed from an interior gravity field. A constant density polyhedron model is assumed to be the truth model for this comparison. These results show that when we

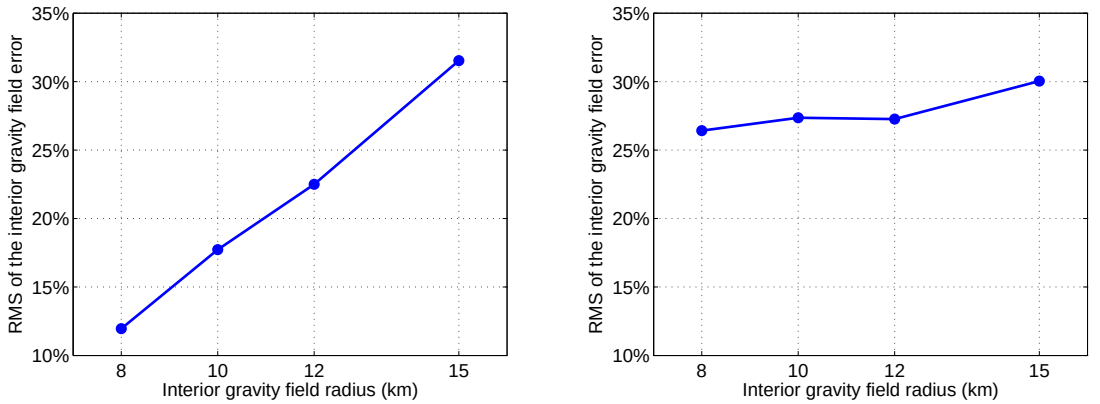

(a) Acceleration error for a 3×3 interior field

(b) Acceleration error after the 5^{th} flyby pass

Figure 8.6: RMS of the gravitational acceleration errors of an interior gravity field with different field radii compared to a constant density polyhedron model.

consider the errors in the gravity field representation due to the uncertainties in the gravity field coefficients, the accuracies of the interior gravity fields are degraded. After 5 flyby passes of the estimation process, different field sizes show similar performances in terms of the accuracy of the gravity field representation. However, an 8 km interior gravity field results in a relatively smaller error despite the shorter amount of time spent by the spacecraft flying through this field compared to the larger fields.

8.1.5 Interior Gravity Field Divergence Outside of its Brillouin Sphere

The interior gravity field Brillouin sphere is designed such that it is tangent to the surface of the body of mass at one point, call it a *contact point*. As a result, points on the surface of the object that are close to the contact point are not contained inside the Brillouin sphere of that field. The interior gravity field expansion is not defined for those points and it will start to diverge from the

www.manaraa.com

true gravitational field value. This might potentially be an issue for using the interior gravity field to track a spacecraft during its landing or TAG trajectory since such a trajectory may not end at the nominally planned contact point and a portion of the trajectory may fall outside of the interior Brillouin sphere. Therefore, it is important to characterize the divergence behavior of an interior gravity field outside its Brillouin sphere.

Figure 8.7 shows the divergence characteristic of different interior gravity fields as a function of the ratio of the distance of the field point from its origin over the field radius. These fields are computed above the estimated NEAR landing site. The vertical axis of the plot shows the RMS of the acceleration error of the interior gravity field compared to the acceleration computed by a constant density polyhedron model. For this figure we use a 3×3 interior gravity field, whose coefficients are derived from a constant density polyhedron model. Each marked point on the curves shows the RMS of the field error for all the points that fall between that marker and the one before it. This plot shows that the percent error increases exponentially as the field point moves closer to the boundary of the convergent region and continues to increase in the same fashion outside of this region. Also note that for a 3×3 gravity field error increases much faster for a field with a larger radius compared to a field with a smaller radius. For a field radius of 8 km the error is on the order of 25% around a distance of 1.1 times the field radius. This error is on the order of 70% for a 15 km field. Figure 8.8 shows the similar results for different sizes of the gravity fields that can be recovered after 5 flyby passes according to the covariance study in the previous section. The error values shown on this plot are averaged from 100 sample fields whose coefficient values are perturbed according to their estimated coefficient uncertainties after the 5^{th} flyby pass. These errors represent a more realistic picture of the field divergence compared to Figure 8.7. Nonetheless, they show a similar divergence behavior for different fields.

8.2 Landing Trajectory Navigation

For the final analysis, we look at a simulation study that utilizes the interior gravity field to navigate a simulated spacecraft during a landing trajectory. We choose the NEAR mission

www.manaraa.com

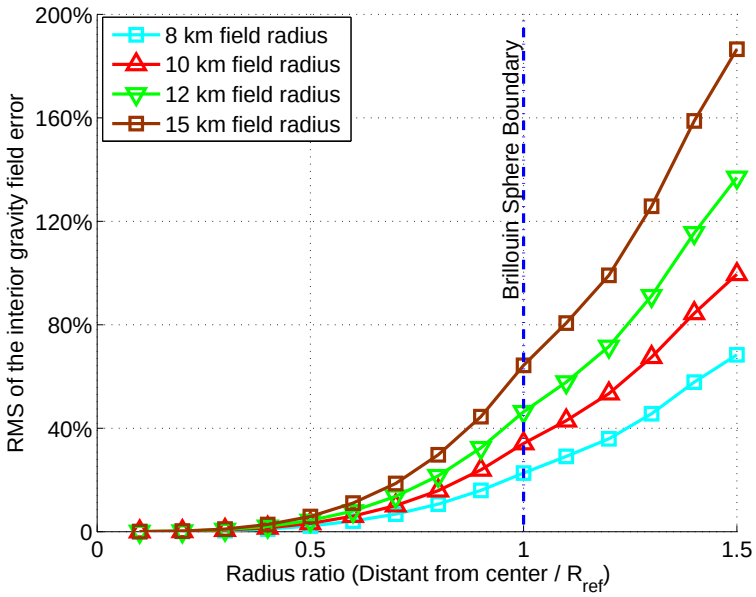

Figure 8.7: Divergence behavior of a 3×3 interior field derived from a constant density polyhedron model.

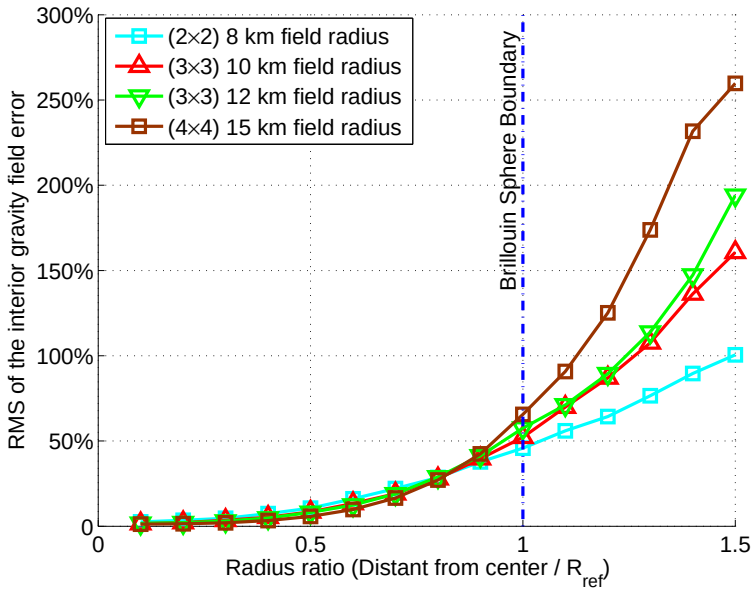

Figure 8.8: Divergence behavior of an estimated interior gravity field after the 5^{th} flyby passes.

estimated landing spot as the target point for the lander. At the end of its mission, the NEAR spacecraft descended down to the surface of Eros to touch down at a spot with estimated coordi-

www.manaraa.com

nates of -36° latitude and $+81^\circ$ longitude. The spacecraft performed 5 end of mission maneuvers (EMM) to complete this trajectory. In this study, we simulate a similar trajectory for the lander.

8.2.1 Simulating the Landing Trajectory

The truth trajectory is generated starting from this target point and propagating the trajectory backward in time after an initial liftoff velocity of 5.5 m/s that is in the normal direction to the surface at the landing spot. Five other maneuvers in the form of impulsive ΔV's are designed to carry the simulated spacecraft to an altitude of about 10 km above the surface at the landing spot. Table 8.4 summarizes the list of the ΔV's are given in an asteroid centered inertial frame and their execution times t_m with respect to the touch down epoch, t_0. The trajectory is designed to be contained inside a 10 km interior Brillouin sphere that is tangent to the surface of the asteroid at the landing spot. It takes the spacecraft about 4 hours to move across the 10 km Brillouin sphere. In this simulation, we assume that the asteroid does not rotate about it's rotation axis to simplify the generation of the DSN measurements between the simulated spacecraft and the Earth. Figure 8.9 shows the designed landing trajectory as well as the interior Brillouin sphere that contains it.

Table 8.4: Summary of the maneuvers for the simulated landing trajectory

$t_m - t_0$ (min)	ΔV_X (m/s)	ΔV_Y (m/s)	ΔV_Z (m/s)	$\lvert\Delta \mathbf{V}\rvert$ (m/s)
-30	-2.185	4.002	-1.907	4.942
-60	-1.203	2.797	-1.168	3.261
-100	-1.025	3.382	-1.246	3.747
-160	-1.174	3.621	-1.375	4.048
-220	-0.485	1.044	-0.457	1.239

The force model that is used to generate the truth trajectory as well as the one used by the estimation filter are summarized in table 8.5. For the gravity field attraction we use a 10×10 interior gravity field that is generated from a constant density polyhedron model. Other forces are the SRP effect with a cannonball model assumption and the third body perturbation of the Sun. The gravity field coefficients used in the filter are perturbed from their nominal values by a 5% Gaussian error. The uncertainty on the coefficients is based on the $1-\sigma$ uncertainty level given by

www.manaraa.com

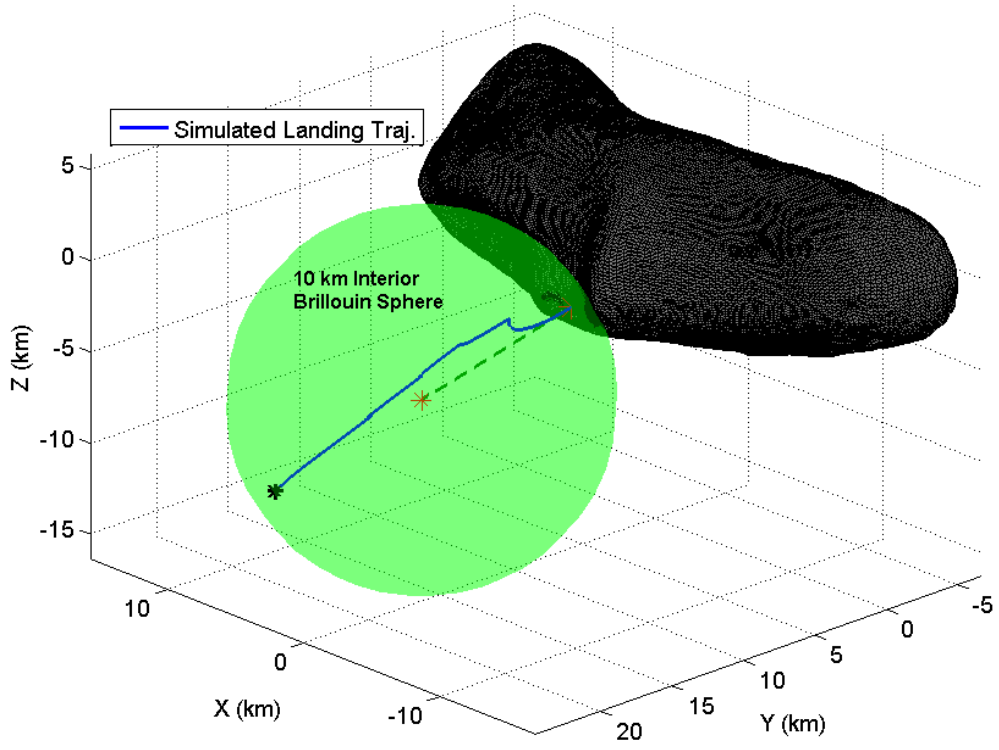

Figure 8.9: A view of the simulated landing trajectory with a 10 km interior field.

the 5^{th} flyby pass through the 10 km radius field. This is shown in Figure 8.3 by the green curve with the upsidedown triangle markers. We also include a 5% Gaussian error on the maneuver components used in the filter force model.

8.2.2 Filtering Strategy

The estimated parameters are same as those shown in Eq. (8.7) with an addition of a list of estimated maneuvers along the trajectory. Hence, the estimate parameters are given by

$$\mathbf{X} = \left[\mathbf{r}^{\mathrm{T}} \;\; \mathbf{v}^{\mathrm{T}} \;\; \mathbf{CS}_{\ell}^{i} \;\; \Delta\mathbf{V}\right]^{\mathrm{T}}, \tag{8.7}$$

where $\Delta\mathbf{V} = [\Delta\mathbf{V}_1^{\mathrm{T}} \;\; \Delta\mathbf{V}_2^{\mathrm{T}} \;\; \ldots \Delta\mathbf{V}_5^{\mathrm{T}}]$ is the list of the impulsive changes in the velocity used in the generation of the landing trajectory. The vector $\Delta\mathbf{V}_i$ represents the i^{th} impulsive maneuver. The maneuver epochs are assumed to be known and are not estimated. The dynamics of the lander is

www.manaraa.com

Table 8.5: Truth and filter models

	Truth Model	Filter Model
Force Model		
Central Body:	Eros ($\mu = 4.4621E-4 km^3/s^2$) [59]	Same
Gravitational Perturbations:	10×10, 10 km interior field	5×5 field plus a 5% error
Solar Radiation Pressure:	Cannonball Model	Same
Third body:	Sun (point mass)	Same
Maneuvers:	see Table 8.4	Same plus a 5% error
Filter Parameter Errors:	1-σ *a priori* Uncertainty	Initial Error
Spacecraft position X, Y, Z	10 m	$\sim N(0, 10^2)\ m$
Spacecraft velocity V_x,V_y,V_z	10 cm/s	$\sim N(0, 10^2)\ cm/s$
Interior gravity coefficients	Given by the 5^{th} flyby through a 10 km field (see Figure 8.3).	5%
Maneuver components	5% of the maneuver magnitudes	5%

www.manaraa.com

given by

$$\begin{aligned}
&\dot{\mathbf{r}} = \mathbf{v}, \\
&\dot{\mathbf{v}} = \mathbf{a}_{\oplus} + \mathbf{a}_{SRP} + \mathbf{a}_{3^{\text{rd}}} + \textstyle\sum_{i=1}^{5} \Delta\mathbf{V}_i \delta(t - \tau_i), \\
&\dot{\mathbf{CS}}_{\ell}^{i} = 0, \text{ and} \\
&\Delta\dot{\mathbf{V}}_i = 0, \quad i = 1,\ 2,\ \ldots,\ 5.
\end{aligned} \tag{8.8}$$

where $\delta(t)$ is the Dirac delta function with the following properties

$$\begin{aligned}
&\int_{-\infty}^{\infty} \delta(t)dt = 1, \text{ and} \\
&\delta(t) = 0, \text{ for } t \neq 0.
\end{aligned} \tag{8.9}$$

Using the Dirac delta function allows for the implementation of the impulsive $\Delta\mathbf{V}$ in the dynamical system defined above. In this simulation, we use the method laid out in Reference [80] to derive the variational equations and to estimate the impulsive maneuvers. The observations are generated based on the truth trajectory and in accordance to the measurement model described in Section 8.1.3. The OpNav observations are generated from 10 simulated landmarks that are randomly scattered around the landing spot in a range of $\pm 30°$. The camera is assumed to point towards the landing site during the trajectory. The OpNav observations are generated once every 2 minutes, while the DSN observations are generated once every 1 minute. The *a priori* uncertainties of the estimated state elements are given in Table 8.5. Measurement weighting is the same as that given in Table 8.2. The *a priori* uncertainties for the impulsive maneuvers are assumed to be equivalent to the error magnitude on the maneuvers. We use a SRIF to sequentially process the observations. Once a maneuver event is reached a batch filter is used to solve for the maneuver. Throughout the estimation process a first-order Gauss-Markov process noise (see Eq.(2.29)) is included to offset the inherent error in the dynamical model due to the truncated gravity field. We use an empirical acceleration uncertainty of $2E-9\ km/s^2$ in the velocity direction and $3E-10\ km/s^2$ in the other two directions perpendicular to the velocity vector.

www.manaraa.com

8.2.3 Estimation Results

We perform a Monte Carlo simulation using 500 cases whose dynamical model, observations, and state element errors are drawn randomly form the error distributions given in Tables 8.2 and 8.9. The performance statistics are computed for each filter run and their averaged values from the 500 cases are summarized in Table 8.6. All of the metrics are computed after letting the filter settle which is after about 1 hour from the start of the filter. These results show that the filter is able to perform an accurate estimation of the truth trajectory and the landing site using an interior gravity field model.

Table 8.6: Monte Carlo filter run statistics for the landing trajectory

Metric	Parameter	Value	
3D-RMS	Traj. position	4.125	m
	Traj. velocity	46.78	mm/sec
	landing spot position	73.5	cm
	landing spot velocity	9.5	mm/sec
Weighted RMS	sample	0.987	
	line	0.989	
	range	0.978	
	range-rate	0.862	

Figure 8.10 shows an scatter plot of the estimated landing spots given by different filter solutions. This figure also shows a $3-\sigma$ uncertainty ellipse centered at the mean value of the 500 solution cases as well as the target landing spot shown by a red asterisk. This plot shows that the filter is capable of estimating the targeted landing spot with a $3-\sigma$ precision on the order of 0.03° in latitude and 0.025° in longitude. This corresponds to a precision on the order of 3.5 meters $(3-\sigma)$ on the surface. Also, note that the minor axis of the uncertainty ellipse is oriented towards the direction of the maximum information which is given by the direction of the Earth-based observations shown on the plot.

Finally, Figure 8.11 shows the accuracy plot of the position and the velocity estimates along the trajectory for one of the filter runs. It is shown that the estimated elements are contained within the 3σ uncertainty envelopes, however the accuracy is corrupted at the maneuver epochs

www.manaraa.com

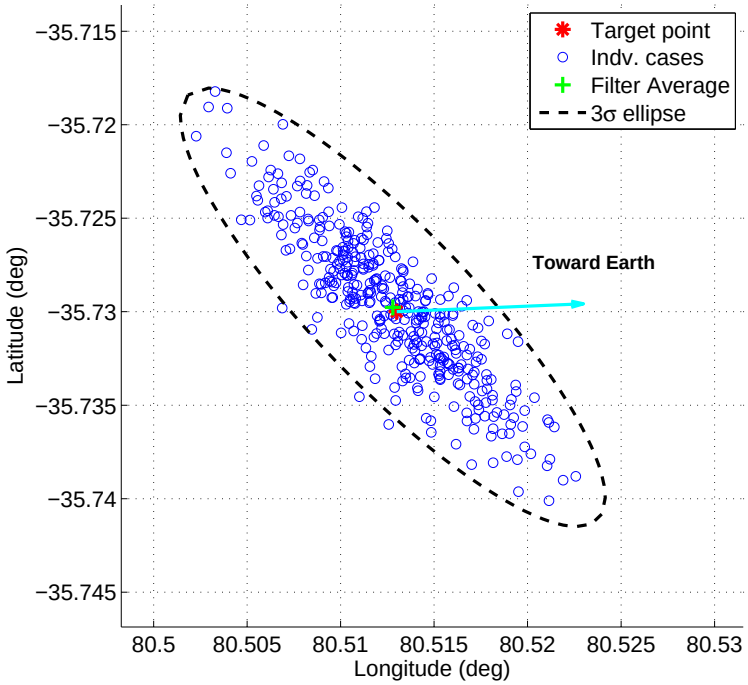

Figure 8.10: Scatter plot of the landing spot solutions.

which are clear by the increased uncertainty level for the velocity components.

8.3 Chapter Summary

In this chapter, we evaluate and characterize the performance of several interior spherical harmonics expansions in modeling the gravitational field of Eros. In particular, we focus on the surface proximity gravitational field above the estimated landing site of the NEAR spacecraft. The regular exterior spherical harmonics expansion is very limited in accurately modeling the surface proximity gravitational field of an irregularly shaped object. We find errors on the order of $10^5\%$ when using an exterior spherical harmonics to model the gravitational field of the asteroid in the close proximity to the NEAR landing site. On the other hand, the interior spherical harmonics expansion shows a significant improvement in modeling the gravitational field in this region. A 3×3 interior gravity field shows an error on the order of $10\%--20\%$ compared to a field generated

www.manaraa.com

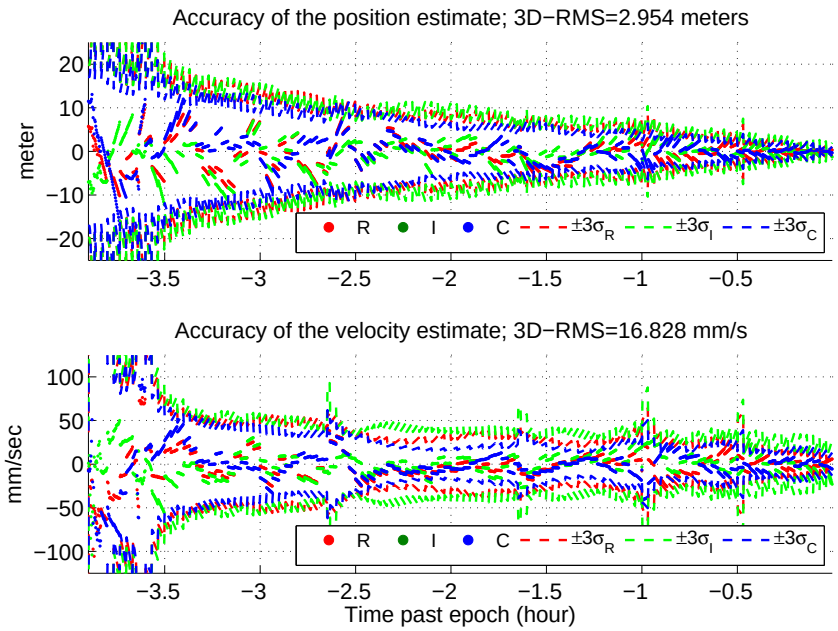

Figure 8.11: Accuracy plot of the position and velocity estimates.

by a constant density polyhedron model.

Furthermore, we implement a covariance analysis to measure the expected level of estimation precision for the interior gravity field coefficients. Estimating the interior gravity field coefficients are challenging. Previous research provided methods of estimating the field coefficients, indirectly, from an exterior gravity field. This covariance analysis aims to evaluate the feasibility of directly estimating the coefficients of an interior gravity field via OD solutions. We simulate a spacecraft flying through the convergent region of an interior gravity field and process simulated optical surface landmark measurements and radiometric measurements. The results of the covariance analysis show that, for a 10 kilometer radius interior gravity field, one may resolve a 3×3 field after 3 to 5 flyby passes of a spacecraft through the Brillouin sphere of the field. For an interior gravity field with 15 kilometer in radius, resolving a 4×4 gravity field is feasible with the same number of flyby passes. This is due to the fact that the spacecraft is able to spend more time flying through a larger gravity field. However, the error analysis shows that a gravity field with a smaller radius results in a slightly higher accuracy compared to a field with a larger radius. The

www.manaraa.com

larger the radius of an interior gravity field is, the higher degree and order coefficients are needed to be able to accurately represent the gravitational field. As a result, when considering the errors due to the uncertainties in the gravity field coefficients, a gravity field with a small radius tends to result in better accuracy levels compared to a field with a larger radius.

Finally, the navigation of a simulated landing trajectory is performed. This simulation presents the feasibility of utilizing an interior gravity field model to track a lander at the surface proximity of an irregularly shaped object. The estimated NEAR spacecraft lading location on the surface of Eros is chosen as the target for the simulated trajectory. This location is far inside the exterior field Brillouin sphere, where the exterior field is not capable of accurately modeling the gravitational field around this location. However, the simulation study shows that a filter that uses an interior gravity model is capable of accurately estimating the truth trajectory of the lander. The filter is also able to recover the target location with a $3-\sigma$ precision on the order of 0.03° in latitude and 0.025° in longitude, despite the existence of several maneuvers along the simulated trajectory.

www.manaraa.com

Chapter 9

Conclusion and Future Work

In this thesis, we investigated new techniques to perform precise orbit determination (OD) of spacecraft orbiting in close proximity of small bodies. Orbital and surface proximity environment of small bodies present significant challenges to mission planners and navigation analysts due to the existence of numerous strong perturbing forces, such as the non-spherical gravitational perturbations, strong solar radiation pressure, small body surface thermal radiation pressure, etc. The complex dynamical environment requires development of new techniques for the propagation of errors and uncertainties in the spacecraft orbital elements as well as the precise treatment of the perturbing forces for the purpose of the spacecraft navigation.

Following some background material presented in Chapters 2 and 3, Chapter 4 presents a comprehensive sensitivity analysis of the sun-terminator orbits around small bodies to maneuver execution error and uncertainty. Understanding the complex dynamical environment around a small body under a strong SRP perturbation is key to accurate modeling of spacecraft orbit and the precise propagation of the orbit uncertainties over time. We derive a set of closed form solutions that describe the secular evolution of the errors in the orbital elements of spacecraft in orbit around small bodies. These equations are then utilized to perform a sensitivity analysis of the sun-terminator orbits to small perturbations such as small maneuver errors. The results from this study shows that in general a frozen type terminator orbit is less sensitive to small perturbations and error compared to an initially circular terminator orbit of the same size. Large oscillations in the orbital elements of an initially circular terminator orbit may present a challenge to the plan-

www.manaraa.com

ning and execution of mission events such as surface imaging campaigns or TAG maneuvers. Asteroid's heliocentric true anomaly is also found to have a significant effect on the progression of the maneuver uncertainties with an important implication on the timing of orbit insertion and targeting maneuver designs.

In Chapter 5, we present a model based on a Fourier series expansion for the precise representation of SRP effects on spacecraft orbiting around small bodies with an example application for the OSIRIS-REx spacecraft. We first derive analytical solutions that govern the secular dynamics of an orbit of a spacecraft that follows a specific attitude profile. The derived analytical solutions show that there is a small set of prominent Fourier coefficients that contribute to the secular motion of the orbit elements. Following the analytical derivations, we implement a sensitivity analysis that evaluates the effects of errors in the Fourier coefficients on errors in the spacecraft trajectory. Results from the error analysis shows that a handful of the lower degree coefficients, mainly those that result in the secular dynamics, result in the largest amount of the error in the trajectory and the error magnitude diminishes rapidly for the higher degree coefficients. Finally, in this chapter we expand the utilization of the Fourier series expansion to model TRP effects and show that it is able to accurately represent TRP effects on spacecraft in close proximity of a small body.

Chapter 6 utilizes the Fourier series representation of the SRP and TRP in generating precise orbit determination solutions for simulated spacecraft orbiting around a small body. First it presents a complete set of equations for the computation of the partial derivatives necessary for the use of this model in an estimation process. Then the laid out estimation formulation is used in a covariance analysis to measure the expected level of estimation precision that is possible for each SRP fourier coefficient via an orbit determination solution. The results show that while one may be able to estimate the SRP Fourier coefficients with a high level of precision, there are certain precautions to consider when estimating SRP coefficients and the gravitational parameter of the central body, simultaneously. Strong correlations between the $A_0(1)$ coefficient and the gravitational parameter during the nadir-pointing attitude generates an ill-conditioned systems for

www.manaraa.com

the estimation of this particular coefficient in the nadir-pointing attitude. However, this coupling is removed for the other two attitude profiles, namely the Sun-pointing and the Earth-pointing attitudes.

The simulation studies presented in Chapter 6 show that the proposed Fourier series expansion is able to produce precise OD solutions. Even though its effect is relatively small, the mis-modeled TRP is shown to have a notable effect on the orbit determination solution especially for a trajectory that is close to the surface of the central body. The Fourier series representation of the TRP removes such mis-modeling and produces precise OD solutions that are valid for long propagation times. This chapter concludes the discussion on the SRP and TRP modeling.

Chapters 7 and 8 focus on improved modeling of the surface proximity gravitational field of an irregularly shaped object. Chapters 7 presents a discussion on the derivation of two types of gravitational field expansions, namely the exterior and the interior fields. The derivation establishes a convergent region for both of the expansions called the Brillouin sphere. Since the exterior field expansion is valid anywhere outside of its Brillouin sphere, it is limited in accurately representing the gravitational field on the surface proximity of irregularly shaped objects. For instance, very large errors on the order of $10^5\%$ are observed when using the exterior field in modeling the gravitational field in the neck area of Asteroid (433) Eros. An interior gravity field expansion, however, is valid inside its Brillouin sphere that extends all the way down to the surface of an arbitrary body of mass. Using this formulation one may be able to accurately represent the surface gravitational field of an irregularly shaped object and successfully navigate spacecraft during their landing or TAG operations.

Finally, in Chapter 8 we utilize the interior gravity field expansion in a set of covariance and simulation studies. We characterize the surface proximity gravitational field of Eros immediately above the estimated landing site of the NEAR spacecraft. Via a covariance analysis we show that it is feasible to directly measure and estimate the interior gravity field coefficients via an orbit determination solution. This method is advantageous over other indirect methods for the estimation of these coefficients. Finally, a simulation study is performed to utilize the interior

www.manaraa.com

gravity field to track a simulated lander on the surface of Eros. The simulation study shows that a filter that uses an interior gravity model is capable of accurately estimating the truth trajectory of the lander and recover the target location of the lander with a high level of precision.

There are several avenues of future research on the topics covered in this thesis. On the concept of the secular dynamics of the orbit elements under the strong SRP effect, we presented three special solutions, namely the frozen-nodes orbits, the frozen-terminator orbits, and the initially circular terminator orbits. Other special solutions are shown to exist for this system [77]. Due to the simple periodic nature of this system, we suspect the existence of several other special solutions each leading to a family of orbits that may be of interest to future missions to small bodies.

On the topic of the estimation of the SRP Fourier coefficients via OD solutions we made the assumption that the SRP coefficients are single valued parameters during our observation arcs. This is a valid assumption for the particular attitude profiles that are studies in this work. However, recall that these coefficients are a function of the solar latitude in the spacecraft body-fixed frame. For attitude profiles for which the solar latitude changes significantly over time, the single valued assumption of for the coefficients may not be valid anymore as their functional form is not constant along different solar latitude values. For such attitude profiles, one may estimate the actual functional form of a Fourier coefficient rather than a single point along that function. Further studies may implement such mechanism.

Lastly, on the topic of the surface proximity gravitational field, one avenue of further research may be to utilize the localized interior gravity field to infer improved information on the localized density distribution and the internal structure of an object. The interior gravity field is suspected to have more sensitivity to small density inhomogeneities close to the surface of an object compared to the conventional exterior gravity field. Another avenue of further research is to utilize the interior gravity field to process the actual observations from the landing of the NEAR spacecraft to gain improved understanding of the surface gravitational field of the neck region of Eros that may provide an improved constraint on its density distribution around that region.

www.manaraa.com

Bibliography

[1] A. Albuja and D.J. Scheeres. Defunct satellites, rotation rates and the YORP effect. Proceedings of the Advanced Maui Optical and Space Surveillance Technologies Conference [CD], Wailea, Hawaii, pages 156 – 163, 2013.

[2] A. Albuja and D.J. Scheeres. Effects of optical and geometrical properties on YORP effect for inactive satellites. In Advanced Maui Optical and Space Surveillance Technologies Conference, volume 1, page 34, 2014.

[3] Antonella Albuja, Daniel J. Scheeres, and Jay W. McMahon. Evolution of angular velocity for defunct satellites as a result of YORP: An initial study. Advances in Space Research, 2015.

[4] Y. Bar-Sever and D. Kuang. New empirically derived solar radiation pressure model for global positioning system satellites. Technical Report IPN Progress Report 42 – 159, Jet Propulsion Laboratory, Pasadena, California, November 2004.

[5] Richard H. Battin. An introduction to the mathematics and methods of astrodynamics. American Institute of Aeronautics and Astronautics, Reston, VA, 1999.

[6] K. Berry, B. Sutter, A. May, K. Williams, B. W. Barbee, M. Beckman, and B. Williams. OSIRIS-REx Touch-And-Go (TAG) Mission Design and Analysis. In Proceedings of the 36th Annual AAS Guidance and Control Conference, No. AAS 13–095, Breckenridge, CO, Feb. 1–6, 2015. AAS/AIAA.

[7] Srinivas V. Bettadpur. Hotine's geopotential formulation: revisited. Bulletin géodésique, 69(3):135–142.

[8] S. Bhaskaran. Autonomous Navigation for Deep Space Missions. In Proceedings of the 12th International Conference on Space Operations, Stockholm, Sweden, 2012. SpaceOps 2012.

[9] S. Bhaskaran, S. Nandi, S. Broschart, M. Wallace, L. Alberto Cangahuala, and C. Olson. Small Body Landings Using Autonomous Onboard Optical Navigation. The Journal of the Astronautical Sciences, 58(3), 2011.

[10] G.J. Bierman. Factorization Methods for Discrete Sequential Estimation. Academic Press, New York, NY 10003, USA, 1977.

[11] W. F. Bottke, Jr., D. Vokrouhlický, D. P. Rubincam, and M. Broz. The Effect of Yarkovsky Thermal Forces on the Dynamical Evolution of Asteroids and Meteoroids, pages 395–408. March 2002.

المنارة للاستشارات

www.manaraa.com

[12] Sharyl M. Byram. The Effects of Outgassing Jets On the Rotation of a Comet Nucleus and on the Trajectory of an Orbiting Spacecraft. PhD thesis, The University of Michigan, Ann Arbor, MI, 2009.

[13] E.H. Cardiff. Volatile Extraction and *In Situ* Resource Utilization for the Moon applied to Near Earth Objects. In Annual Meeting of the Lunar Exploration Analysis Group, Greenbelt, Maryland, 2012.

[14] A. F. Cheng, A. G. Santo, K. J. Heeres, J. A. Landshof, R. W. Farquhar, R. E. Gold, and S. C. Lee. Near-Earth Asteroid Rendezvous: Mission overview. Journal of Geophysical Research, 102, 1997.

[15] Steven R. Chesley, Davide Farnocchia, Michael C. Nolan, David Vokrouhlický, Paul W. Chodas, Andrea Milani, Federica Spoto, Benjamin Rozitis, Lance A.M. Benner, William F. Bottke, Michael W. Busch, Joshua P. Emery, Ellen S. Howell, Dante S. Lauretta, Jean-Luc Margot, and Patrick A. Taylor. Orbit and bulk density of the OSIRIS-REx target Asteroid (101955) Bennu. Icarus, 235:5 – 22, 2014.

[16] J. F. Crifo, A. L. Itkin, and A. V. Rodionov. The Near-Nucleus Coma Formed by Interacting Dusty Gas Jets Effusing from a Cometary Nucleus: I. Icarus, 116:77–112, July 1995.

[17] Leland E. Cunningham. On the computation of the spherical harmonic terms needed during the numerical integration of the orbital motion of an artificial satellite. Celestial mechanics, 2(2):207–216.

[18] E. Fantino and S. Casotto. Methods of harmonic synthesis for global geopotential models and their first-, second- and third-order gradients. Journal of Geodesy, 83(7):595–619, 2008.

[19] William M. Folkner, James G. Williams, Dale H. Boggs, Ryan S. Park, and Petr Kuchynka. The planetary and lunar ephemerides DE430 and DE431. Technical Report IPN Progress Report 42 – 196, Jet Propulsion Laboratory, Pasadena, California, February 2014.

[20] J. Gal-Edd and A. Cheuvront. The OSIRIS-REx Asteroid Sample Return Mission operations design. In Aerospace Conference, 2015 IEEE, pages 1 – 9, March 2015.

[21] R. Garmier, J. Barriot, A. S. Konopliv, and D. K. Yeomans. Modeling of the Eros gravity field as an ellipsoidal harmonic expansion from the NEAR Doppler tracking data. Geophysical Research Letters, 29(8):72–1–72–3, 2002.

[22] R.W. Gaskell. Digital identification of cartographic control points. Photogrammetric Engineering and Remote Sensing, 54:723–727, 1988.

[23] R.W. Gaskell. Automated landmark identification for spacecraft navigation. In Proceedings of the AIAA/AAS Astrodynamics Specialists Conference, Quebec, 2001. AAS 01–422.

[24] R.W. Gaskell. Determination of landmark topography from imaging data. In Advances in the Astronautical Sciences, Guidance and Control, Breckenridge, Colorado, 2002. AAS 02-021.

[25] R.W. Gaskell, O.S. Barnouin-Jha, D.J. Scheeres, A.S. Konopliv, T. Mukai, S. Abe, J. Saito, M. Ishiguro, T. Kubota, T. Hashimoto, J. Kawaguchi, M. Yoshikawa, K. Shirakawa, T. Kominato, N. Hirata, and H. Demura. Characterizing and navigating small bodies with imaging data. Meteoritics & Planetary Science, 43(6):1049–1061, 2008.

www.manaraa.com

[26] J.W. Gibbs. Elements of Vector Analysis: Arranged for the Use of Students in Physics. Elements of Vector Analysis. Tuttle, Morehouse & Taylor, 1884.

[27] S. D. Gillam, W. M. Owen, A. T. Vaughanand, T. C. M. Wang, J. D. Costello, R. A. Jacobson, D. Bluhm, J. L. Pojman, and R. Ionasescu. Optical Navigation for the Cassini/Huygens Mission. In Proceedings of the AIAA/AAS Astrodynamics Specialist Conference, Mackinac Island, MI, 2007. AAS/AIAA.

[28] Karl-Heinz Glassmeier, Hermann Boehnhardt, Detlef Koschny, Ekkehard Kührt, and Ingo Richter. The rosetta mission: Flying towards the origin of the solar system. Space Science Reviews, 128(1):1–21, 2007.

[29] R. G. Gottlieb. Fast Gravity, Gravity Partials, Normalized Gravity, Gravity Gradient Torque and Magnetic Field: Derivation, Code and Data. Technical report, NASA Lyndon B. Johnson Space Center, 1993.

[30] Alan W. Harris. A thermal model for near-earth asteroids. Icarus, 131(2):291 – 301, 1998.

[31] W. E. Hobson. The Theory of Spherical and Ellipsoidal Harmonics. Chelsea Pub. Co., New York, 1965.

[32] B. Hofmann-Wellenhof and H. Moritz. Physical Geodesy. Springer Vienna, 2006.

[33] Jennifer S. Hudson and Daniel J. Scheeres. Reduction of low-thrust continuous controls for trajectory dynamics. Journal of Guidance, Control, and Dynamics, 32(3):780–787, 2009.

[34] C. Jackman and P. Dumont. Optical Navigation Capabilities for Deep Space Missions. In Proceedings of the 23rd AAS/AIAA Space Flight Mechanics Conference, Kauai, Hawaii, 2013. AAS/AIAA.

[35] Coralie D. Jackman, Derek S. Nelson, Jr. William M. Owen, Marc W. Buie, S. Alan Stern, Harold A. Weaver, Leslie A. Young, Kimberly Ennico, and Catherine B. Olkin. New Horizons optical navigation on approach to Pluto. In Proceedings of the 39th Annual AAS Guidance, Navigation and Control Conference. AAS 16–083, February 5–10, 2016.

[36] Andrew H. Jazwinski. In Stochastic Processes and Filtering Theory, volume 64 of Mathematics in Science and Engineering. Academic Press, Inc., New York, NY 10003, USA, 1970.

[37] T. J. Jones and D. Morrison. Recalibration of the photometric/radiometric method of determining asteroid sizes. Astronomical Journal, 79:892 – 895, 1974.

[38] R.E. Kalman. A new approach to linear filtering and prediction problems. Transactions of the ASME–Journal of Basic Engineering, 82(Series D):35–45, 1960.

[39] W. M. Kaula. Theory of Satellite Geodesy, Applications of Satellites to Geodesy. Blaisdell Publishing Company, Waltham, MA, 1966.

[40] P.C. Knocke, J.C. Ries, and B.D. Tapley. Earth radiation pressure effects on satellites. In Proceedings of the AIAA/AAS Astrodynamics Conference, pages 577–587, Minneapolis, MN, August 15–17, 1988. AIAA 88–4292.

www.manaraa.com

[41] Gerhard L. Kruizinga, Eric D. Gustafson, Paul F. Thompson, David C. Jefferson, Tomas J. Martin-Mur, Neil A. Mottinger, Frederic J. Pelletier, and Mark S. Ryne. Mars Science Laboratory orbit determination. In 23rd International Symposium on Space Flight Dynamics, Pasadena, California, October 29 – November 2 2012.

[42] D. A. Lautman. Perturbations of a close-Earth satellite due to sunlight diffusely reflected from the Earth. Celestial mechanics, 15(4):387–420, 1977.

[43] L. A. Lebofsky and J. R. Spencer. Asteroids II, chapter Radiometry and thermal modeling of asteroids., pages 128–147. University of Arizona Press, Tucson, AZ, 1989.

[44] Larry A. Lebofsky, Mark V. Sykes, Edward F. Tedesco, Glenn J. Veeder, Dennis L. Matson, Robert H. Brown, Jonathan C. Gradie, Michael A. Feierberg, and Richard J. Rudy. A refined "standard"thermal model for asteroids based on observations of 1 Ceres and 2 Pallas. Icarus, 68(2):239 – 251, 1986.

[45] J.M. Leonard, F.G. Nievinski, and G.H. Born. Gravity error compensation using second-order Gauss-Markov processes. Journal of Spacecraft and Rockets, 50(1):217–229, 2012.

[46] David M. Lucchesi. Reassessment of the error modelling of non-gravitational perturbations on LAGEOS II and their impact in the Lense–Thirring determination. Part I. Planetary and Space Science, 49(5):447 – 463, 2001.

[47] W. D. MacMillan. The theory of the potential. Number 2 in Theoretical mechanics. McGraw-Hill Book Company, inc., 1930.

[48] Amy Mainzer, Fumihiko Usui, and David E. Trilling. Asteroids IV, chapter Space-Based Thermal Infrared Studies of Asteroids, pages 89–106. University of Arizona Press, Tucson, AZ, 2015.

[49] J. A. Marshall and Scott B. Luthcke. Modeling radiation forces acting on Topex/Poseidon for precision orbit determination. Journal of Spacecraft and Rockets, 31(1):99 – 105, 1994.

[50] Tomas J. Martin-Mur, Gerhard L. Kruizinga, P. Daniel Burkhart, Mau C. Wong, and Fernando Abilleira. Mars Science Laboratory navigation results. In 23rd International Symposium on Space Flight Dynamics, Pasadena, California, October 29 – November 2 2012.

[51] N. Mastrodemos, B. Rush, D. Vaughan, and W. Owen Jr. Optical navigation for the Dawn mission at Vesta. In 23rd International Symposium on Space Flight Dynamics, Pasadena, CA, 29 Oct. – 2 Nov. 2012.

[52] Erwan Mazarico, Maria T. Zuber, Frank G. Lemoine, and David E. Smith. Effects of self-shadowing on nonconservative force modeling for Mars-orbiting spacecraft. Journal of Spacecraft and Rockets, 46(3):662–669, 2009.

[53] C.R. McInnes. Solar Sailing: Technology, Dynamics and Mission Applications. Springer Praxis Books. Springer London, 2013.

[54] Jay McMahon and Daniel Scheeres. Secular orbit variation due to solar radiation effects: a detailed model for BYORP. Celestial Mechanics and Dynamical Astronomy, 106(3):261–300, 2010.

www.manaraa.com

[55] Jay W. McMahon and Daniel J. Scheeres. New solar radiation pressure force model for navigation. Journal of Guidance, Control, and Dynamics, 33(5):1418 – 1428, 2010.

[56] Jay W. McMahon and Daniel J. Scheeres. Improving orbit determination with low-order Fourier solar radiation pressure models. In AAS/AIAA Astrodynamics Specialist Conference, Hilton Head, South Carolina, August 2013.

[57] J.W. McMahon, D.J. Scheeres, D. Farnocchia, and S.R. Chesley. Optimizing Small Body Gravity Field Estimation over Short Arcs. In Proceedings of the 2015 AAS/AIAA Astrodynamics Specialist Conference, No. AAS 15–669, Vail, CO, Aug. 9–13 , 2015. AAS/AIAA.

[58] F. Mignard and M. Henon. About an Unsuspected Integrable Problem. Celestial mechanics, 33(3):239–250, July 1984.

[59] J. K. Miller, A. S. Konopliv, P. G. Antreasian, J. J. Bordi, S. Chesley, C. E. Helfrich, W. M. Owen, T. C. Wang, B. G. Williams, D. K. Yeomans, and D. J. Scheeres. Determination of shape, gravity, and rotational state of Asteroid 433 Eros. Icarus, 155(doi:10.1006/icar.2001.6753), 2002.

[60] Peter J. Mohr, David B. Newell, and Barry N. Taylor. CODATA recommended values of the fundamental physical constants: 2014. arXiv:1507.07956.

[61] O. Montenbruck and E. Gill. Satellite Orbits: Models, Methods, and Applications. Physics and astronomy online library. Springer Berlin Heidelberg, 2000.

[62] Michael Müller. Surface Properties of Asteroids from Mid-Infrared Observations and Thermophysical Modeling. PhD thesis, Freien Universität, Department of Earth Sciences, Berlin, 2007.

[63] F.G. Nievinski, B. Yonko, and G.H. Born. Improved orbit determination using second-order Gauss-Markov processes. Advances in the Astronautical Sciences, 140(AAS 11–119).

[64] Michael C. Nolan, Christopher Magri, Ellen S. Howell, Lance A.M. Benner, Jon D. Giorgini, Carl W. Hergenrother, R. Scott Hudson, Dante S. Lauretta, Jean-Luc Margot, Steven J. Ostro, and Daniel J. Scheeres. Shape model and surface properties of the OSIRIS-REx target Asteroid (101955) Bennu from radar and lightcurve observations. Icarus, 226(1):629 – 640, 2013.

[65] P. V. O'Neil. Advanced Engineering Mathematics. Wadsworth Publishing Company, Belmont, California, 1987.

[66] W. M. Owen, P. J. Dumont, and C. D. Jackman. Optical Navigation Preparations for New Horizons Pluto Flyby. In Proceedings of the 23rd International Symposium on Space Flight Dynamics, Pasadena, California, 2012. Jet Propulsion Laboratory, National Aeronautics and Space Administration.

[67] Stephen J. Paddack. Rotational bursting of small celestial bodies: Effects of radiation pressure. Journal of Geophysical Research, 74(17):4379 – 4381, 1969.

[68] J. E. Riedel, W. M. Owen, J. A. Stuve, A. P. Synnott, and R. M. Vaughan. Optical navigation during the Voyager Neptune encounter. In Proceedings of the Astrodynamics Conference, Portland, OR, 1990. AAS/AIAA.

www.manaraa.com

[69] B. Rievers, C. Lämmerzahl, M. List, , S. Bremer, and H. Dittus. New powerful thermal modelling for high-precision gravity missions with application to Pioneer 10/11. New Journal of Physics, 11(11), 2009.

[70] Benny Rievers, Stefanie Bremer, Meike List, Claus Lmmerzahl, and Hansjrg Dittus. Thermal dissipation force modeling with preliminary results for Pioneer 10/11. Acta Astronautica, 66(34):467 – 476, 2010.

[71] Benny Rievers and Claus Lammerzahl. High precision thermal modeling of complex systems with application to the flyby and Pioneer anomaly. Annalen Phys., 523:439–449, 2011.

[72] H. Rim, C. Webb, S. Yoon, and B. Schutz. Radiation pressure modeling for ICESat precision orbit determination. In paper presented at the AIAA/AAS Astrodynamics Specialist Conference and Exhibit, number AIAA 2006-6666, Keystone, Colorado, 21 – 24 August 2006. AIAA.

[73] A. J. Rosengren. Long–term Dynamical Behavior of Highly Perturbed Natural and Artificial Celestial Bodies. PhD thesis, University of Colorado, Boulder, Boulder, CO 80309, 2014.

[74] A. J. Rosengren and D. J. Scheeres. On the Milankovitch Orbital Elements for Perturbed Keplerian Motion. Celest Mech Dyn Astr, 118(3):197–220, 2014.

[75] A. E. Roy and P. E. Moran. Studies in the Application of Recurrence Relations to Special Perturbation Methods. III. Non-Singular Differential Equations for Special Perturbations. Celestial Mechanics, 7:236–255, Feb 1973.

[76] D. J. Scheeres. Orbit Mechanics About Asteroids and Comets. Journal of Guidance, Control, and Dynamics, 35(3), May-June 2012.

[77] D. J. Scheeres. Orbital Motion in Strongly Perturbed Environments. Springer–Verlag Berlin Heidelberg, 1 edition, 2012.

[78] D. J. Scheeres, B. M. Sutter, and A. J. Rosengren. Design, Dynamics and Stability of the OSIRIS-REx Sun-Terminator Orbits. In paper presented at the 23rd AAS/AIAA Space Flight Mechanics Meeting, Kauai, Hawaii, February 2013. AIAA.

[79] D.J. Scheeres. The dynamical evolution of uniformly rotating asteroids subject to YORP. Icarus, 188(2):430 – 450, 2007.

[80] D.J. Scheeres, R. Gaskell, S. Abe, O. Barnouin-Jha, T. Hashimoto, J. Kawaguchi, T. Kubota, J. Saito, M. Yoshikawa, N. Hirata, T. Mukai, M. Ishiguro, T. Kominato, K. Shirakawa, and M. Uo. The *Actual* Dynamical Environment about Itokawa. In AIAA/AAS Astrodynamics Specialist Conference and Exhibit, number AIAA 2006–6661, Keystone, Colorado, 2006.

[81] Zdenek Sekanina, Donald E. Brownlee, Thanasis E. Economou, Anthony J. Tuzzolino, and Simon F. Green. Modeling the nucleus and jets of Comet 81P/Wild 2 based on the stardust encounter data. Science, 304(5678):1769–1774, 2004.

[82] John R Spencer, Larry A Lebofsky, and Mark V Sykes. Systematic biases in radiometric diameter determinations. Icarus, 78(2):337 – 354, 1989.

www.manaraa.com

[83] T. A. Springer, G. Beutler, and M. Rothacher. A new solar radiation pressure model for GPS satellites. GPS Solutions, 2(3):50 – 62, 1999.

[84] G. L. Stephens, G. G. Campbell, , and T. H. Yonder Haar. Earth radiation budgets. Journal of Geophysical Research, 86(C10):9739–9760, 1981.

[85] Y. Takahashi. Gravity Field Characterization around Small Bodies. PhD thesis, University of Colorado at Boulder, Boulder, CO, 2013.

[86] Y. Takahashi, D. J. Scheeres, and R. A. Werner. Surface Gravity Fields for Asteroids and Comets. Journal of Guidance, Control, and Dynamics, 36(2):362–374, 2013.

[87] B. D. Tapley, B. E. Schutz, and G. H. Born. Statistical Orbit Determination. Elsevier Academic Press, Burlington, MA, USA, 2004.

[88] J. H. Taylor. The Cramer-Rao Estimation Error Lower Bound Computation for Deterministic Nonlinear Systems. IEEE Transactions On Automatic Control, AC-24(2), 1979.

[89] D. A. Vallado. Fundamentals of Astrodynamics and Applications. Springer, New York, NY 10013, USA, 2007.

[90] R. A. Werner. The gravitational potential of a homogeneous polyhedron or don't cut corners. Celestial Mechanics and Dynamical Astronomy, 59(3):253–278, 1994.

[91] R. A. Werner. Spherical harmonic coefficients for the potential of a constant-density polyhedron. Computers & Geosciences, 23(10):1071 – 1077, 1997.

[92] R. A. Werner. Evaluating Descent and Ascent Trajectories Near Non-Spherical Bodies. Technical Report NPO-46697, Jet Propulsion Laboratory, Pasadena, CA, November 2010.

[93] R. A. Werner and D. J. Scheeres. Exterior gravitation of a polyhedron derived and compared with harmonic and mascon gravitation representations of asteroid 4769 Castalia. Celestial Mechanics and Dynamical Astronomy, 65(3):313–344, 1996.

[94] Jr. William M. Owen. Methods of optical navigation. In Proceedings of the 21st AAS/AIAA Space Flight Mechanics Meeting. AAS 11–215, 2011.

[95] Stanley P. Wyatt. Dynamics of Satellites / Dynamique des Satellites: Symposium Paris, May 28–30, 1962 / Symposium Paris, 28–30 Mai 1962, chapter The effect of terrestrial radiation pressure on satellite orbits, pages 180–196. Springer Berlin Heidelberg, Berlin, Heidelberg, 1963.

[96] Maria T. Zuber, David E. Smith, Andrew F. Cheng, James B. Garvin, Oded Aharonson, Timothy D. Cole, Peter J. Dunn, Yanping Guo, Frank G. Lemoine, Gregory A. Neumann, David D. Rowlands, and Mark H. Torrence. The Shape of 433 Eros from the NEAR-Shoemaker Laser Rangefinder. Science, 289(5487):2097–2101, 2000.

www.manaraa.com

Appendix A

The Fully Normalized Partial Derivatives of an Exterior Gravity Field Expansion

This section summarizes the first and second partial derivatives of the exterior gravity field represented by a spherical harmonics expansion. The derivation follows Cunningham's method [17] with the difference that here we derive the fully normalized version of this method. We can rewrite Eq. (3.7) as the following

$$U^e = \mu \, \Re \left\{ \sum_{n=0}^{\infty} \sum_{m=0}^{n} R_{\oplus}^{n} \bar{V}_{n,m} [\bar{C}_{nm}^{e} - i \bar{S}_{nm}^{e}] \right\}, \tag{A.1}$$

where $R_{\oplus}$ is the reference radius of the expansion, $\Re\{\cdot\}$ refers to the real part of the enclosed complex function and the fully normalized basis function $\bar{V}_{n,m}$ is given by

$$\bar{V}_{n,m} = \Pi_{nm} \frac{1}{\mathbf{r}_b^{n+1}} P_{n,m}(\sin\phi) \exp(im\lambda). \tag{A.2}$$

The vector $\mathbf{r}_b = [x \;\; y \;\; z]^{\mathrm{T}}$ is the field point position vector expressed in the body-fixed frame of the central attracting body, while ϕ and λ are the latitude and longitude of the field point position in this frame. Function P_{nm} is the well known associated Legendre polynomial of degree n and order m. With this definition we have

$$\begin{aligned} x &= r_b \cos(\phi) \cos(\lambda), \\ y &= r_b \cos(\phi) \sin(\lambda), \text{ and} \\ z &= r_b \sin(\phi). \end{aligned} \tag{A.3}$$

The variable $\Pi_{n,m}$ is the normalization factor that is given by

$$\Pi_{n,m} = \sqrt{\frac{(2 - \delta_{0,m})(2n+1)(n-m)!}{(n+m)!}}, \tag{A.4}$$

www.manaraa.com

where $\delta_{i,j}$ is the Kronecker delta and is equal to 1 if $i = j$ and 0 otherwise. There exists a set of recursive relationships for computing the basis function of difference degrees and orders. These are given by

$$\bar{V}_{n,n} = \sqrt{\frac{(1+\delta_{1,n})(2n+1)}{2n}}\,\frac{(x+iy)}{r_b^2}\bar{V}_{n-1,n-1}\ ,$$

$$\bar{V}_{n,m} = \sqrt{\frac{4n^2-1}{n^2-m^2}}\,\frac{z}{r_b^2}\,\bar{V}_{n-1,m}\ , \qquad \text{for } n = 1, \tag{A.5}$$

$$\bar{V}_{n,m} = \sqrt{\frac{4n^2-1}{n^2-m^2}}\,\frac{z}{r_b^2}\,\bar{V}_{n-1,m} - \sqrt{\frac{(2n+1)((n-1)^2-m^2)}{(2n-3)(n^2-m^2)}}\,\frac{1}{r_b^2}\bar{V}_{n-2,m}\ , \quad \text{for } n \geq 2.$$

The recursion starts with $\bar{V}_{0,0} = 1/r_b$. From Eq. (A.1) we have

$$\frac{\partial^\ell U^e}{\partial^\ell} = \mu\,\Re\left\{\sum_{n=0}^{\infty}\sum_{m=0}^{n} R_\oplus^n \frac{\partial^\ell \bar{V}_{nm}}{\partial^\ell}[\bar{C}_{nm}^e - i\bar{S}_{nm}^e]\right\}. \tag{A.6}$$

The idea behind this formulation is that one can that advantage of the fact that the partial derivatives of the basis function $\bar{V}_{n,m}$ is given by a simple linear combination of the basis functions of different degrees and orders, much like the recursive formula stated earlier. Using such recursive expressions, one can simply compute the first and second partial derivatives of the gravitational potential function directly in cartesian coordinates. The recursive formula for the first and the second partial derivatives are given below.

A.1 The Fully Normalized First Partial Derivatives

The recursive formula for the first partial derivatives are given by

$$\begin{aligned}
\frac{\partial \bar{V}_{nm}}{\partial x} &= -\mathcal{K}_1 \bar{V}_{n+1,1} && m = 0,\\
&= -\frac{1}{2}\mathcal{K}_2 \bar{V}_{n+1,m+1} + \frac{1}{2}\mathcal{K}_3 \bar{V}_{n+1,m-1} && m \geq 1,\\
\frac{\partial \bar{V}_{nm}}{\partial y} &= \mathcal{K}_1\, i\, \bar{V}_{n+1,1} && m = 0,\\
&= \frac{1}{2}\mathcal{K}_2\, i\, \bar{V}_{n+1,m+1} + \frac{1}{2}\mathcal{K}_3\, i\, \bar{V}_{n+1,m-1} && m \geq 1, \text{ and}\\
\frac{\partial \bar{V}_{nm}}{\partial z} &= -\mathcal{K}_4 \bar{V}_{n+1,m}, && m \geq 0,
\end{aligned} \tag{A.7}$$

www.manaraa.com

where

$$\mathcal{K}_1 = \sqrt{\frac{(n+2)(n+1)(2n+1)}{2(2n+3)}},$$

$$\mathcal{K}_2 = \sqrt{\frac{(n+m+2)(n+m+1)(2n+1)}{2n+3}},$$

$$\mathcal{K}_3 = \sqrt{\frac{2(n-m+2)(n-m+1)(2n+1)}{(2-\delta_{1,m})(2n+3)}}, \text{ and} \tag{A.8}$$

$$\mathcal{K}_4 = \sqrt{\frac{(n-m+1)(n+m+1)(2n+1)}{(2n+3)}}.$$

www.manaraa.com

A.2 The Fully Normalized Second Partial Derivatives

The recursive formula for the second partial derivatives are given by

$$\begin{aligned}
\frac{\partial^2 \bar{V}_{nm}}{\partial x^2} &= \frac{1}{2}\mathcal{K}'_1 \bar{V}_{n+2,2} - \frac{1}{2}\mathcal{K}'_2 \bar{V}_{n+2,0} && m = 0, \\
&= \frac{1}{4}\mathcal{K}'_3 \bar{V}_{n+2,3} - \frac{1}{4}\mathcal{K}'_4 (3\Re\{\bar{V}_{n+2,1}\} + \Im\{\bar{V}_{n+2,1}\}) && m = 1, \\
&= \frac{1}{4}\mathcal{K}'_5 \bar{V}_{n+2,m+2} - \frac{1}{2}\mathcal{K}'_6 \bar{V}_{n+2,m} + \frac{1}{4}\mathcal{K}'_7 \bar{V}_{n+2,m-2} && m \geq 2, \\
\\
\frac{\partial^2 \bar{V}_{nm}}{\partial x \partial y} &= -\frac{1}{2}\mathcal{K}'_1 \, i \, \bar{V}_{n+2,2} && m = 0, \\
&= -\frac{1}{4}\mathcal{K}'_3 \, i \, \bar{V}_{n+2,3} - \frac{1}{4}\mathcal{K}'_4 \, i \, \bar{V}^*_{n+2,1} && m = 1, \\
&= -\frac{1}{4}\mathcal{K}'_5 \, i \, \bar{V}_{n+2,m+2} - \frac{1}{4}\mathcal{K}'_7 \, i \, \bar{V}_{n+2,m-2} && m \geq 2, \\
\\
\frac{\partial^2 \bar{V}_{nm}}{\partial y^2} &= -\frac{1}{2}\mathcal{K}'_1 \bar{V}_{n+2,2} + \frac{1}{2}\mathcal{K}'_2 \bar{V}_{n+2,0} && m = 0, \\
&= -\frac{1}{4}\mathcal{K}'_3 \bar{V}_{n+2,3} - \frac{1}{4}\mathcal{K}'_4 (\Re\{\bar{V}_{n+2,1}\} + 3\Im\{\bar{V}_{n+2,1}\}) && m = 1, \\
&= -\frac{1}{4}\mathcal{K}'_5 \bar{V}_{n+2,m+2} - \frac{1}{2}\mathcal{K}'_6 \bar{V}_{n+2,m} - \frac{1}{4}\mathcal{K}'_7 \bar{V}_{n+2,m-2} && m \geq 2, \\
\\
\frac{\partial^2 \bar{V}_{nm}}{\partial x \partial z} &= \mathcal{K}'_8 \bar{V}_{n+2,1} && m = 0, \\
&= \frac{1}{2}\mathcal{K}'_9 \bar{V}_{n+2,m+1} - \frac{1}{2}\mathcal{K}'_{10} \bar{V}_{n+2,m-1} && m \geq 1, \\
\\
\frac{\partial^2 \bar{V}_{nm}}{\partial y \partial z} &= -\mathcal{K}'_8 \, i \, \bar{V}_{n+2,1} && m = 0, \\
&= -\frac{1}{2}\mathcal{K}'_9 \, i \, \bar{V}_{n+2,m+1} - \frac{1}{2}\mathcal{K}'_{10} \, i \, \bar{V}_{n+2,m-1} && m \geq 1, \\
\\
\frac{\partial^2 \bar{V}_{nm}}{\partial z^2} &= \mathcal{K}'_6 \bar{V}_{n+2,m} && m \geq 0,
\end{aligned} \tag{A.9}$$

where the asterisk "$*$" indicates the complex conjugate of a complex function and $\Im\{\cdot\}$ returns the imaginary part of the enclosed complex function. The basis functions used in the second partial

www.manaraa.com

derivatives are given by

$$\mathcal{K}'_1 = \sqrt{\frac{(n+4)!(2n+1)}{2n!(2n+5)}},$$

$$\mathcal{K}'_2 = \frac{(n+2)!}{n!}\sqrt{\frac{2n+1}{2n+5}},$$

$$\mathcal{K}'_3 = \sqrt{\frac{(n+5)!(2n+1)}{(n+1)!(2n+5)}},$$

$$\mathcal{K}'_4 = \sqrt{\frac{(n+3)!(2n+1)}{(n-1)!(2n+5)}},$$

$$\mathcal{K}'_5 = \sqrt{\frac{(n+m+4)!(2n+1)}{(n+m)!(2n+5)}},$$

$$\mathcal{K}'_6 = \sqrt{\frac{(n-m+2)!(n+m+2)!(2n+1)}{(n-m)!(n+m)!(2n+5)}},$$

$$\mathcal{K}'_7 = \sqrt{\frac{2(n-m+4)!(2n+1)}{(n-m)!(2-\delta_{2,m})(2n+5)}},$$

$$\mathcal{K}'_8 = \sqrt{\frac{(n+3)!(n+1)(2n+1)}{2n!(2n+5)}},$$

$$\mathcal{K}'_9 = \sqrt{\frac{(n+m+3)!(n-m+1)(2n+1)}{(n+m)(2n+5)}}, \text{ and}$$

$$\mathcal{K}'_{10} = \sqrt{\frac{2(n-m+3)!(n+m+1)(2n+1)}{(n-m)!(2-\delta_{1,m})(2n+5)}}. \tag{A.10}$$

To perform estimation of the spherical harmonics coefficients themselves or for using them in a covariance study, one also needs to compute the partial derivative of the gravitational acceleration with respect to those coefficients. The derivation of these equations is straightforward as

www.manaraa.com

the gravitational acceleration is a linear combination of the spherical harmonics coefficients. Let $\mathbf{a}_g = \dfrac{\partial U^e}{\partial \mathbf{r}_b}$ be the gravitational acceleration derived from the spherical harmonic expansion using Eq. (A.6). Therefore, the partial derivative of this acceleration with respect to the spherical harmonics coefficients are simply given by

$$\begin{cases} \dfrac{\partial \mathbf{a}_g}{\partial \bar{C}^e_{nm}} = \mu R^n_\oplus \, \Re \left\{ \dfrac{\partial \bar{V}_{nm}}{\partial \mathbf{r}_b} \right\}, \text{ and} \\ \\ \dfrac{\partial \mathbf{a}_g}{\partial \bar{S}^e_{nm}} = \mu R^n_\oplus \, \Im \left\{ \dfrac{\partial \bar{V}_{nm}}{\partial \mathbf{r}_b} \right\}. \end{cases} \tag{A.11}$$

www.manaraa.com

Appendix B

Orbital Elements for Asteroid (101955) Bennu

Table B.1 summarizes the relevant orbital and physical parameters for Bennu [15] as well as the other related astronomical constants [19].

Table B.1: Summary of the orbit parameters for Bennu

Gravitational parameter (μ):	$5.2 \pm 0.6\ m^3/s^2$
Semi-major axis (A):	$\approx 1.126\ AU$
Orbit eccentricity (E):	≈ 0.2037
Rotation period:	4.29746±0.002 hr.
Thermal inertia (Γ):	$310 \pm 70\ J\ m^{-1}s^{-0.5}K^{-1}$
Surface emissivity:	0.90 ± 0.05
Bond albedo:	0.017 ± 0.002
Geometric albedo:	0.04 ± 0.002
Astronomical Constants	
Sun's gravitational parameter (μ_S):	$132,712,440,041.939\ km^3/s^2$
Astronomical unit (AU):	$149597870.700\ km$

www.manaraa.com

Appendix C

Derivation of Perturbed Trajectories about Targeted Circular Terminator Orbit

Here we present the derivation of the dynamical equation of perturbed trajectories about a targeted circular terminator orbit. For a trajectory that naturally evolves into a circular terminator orbit, the position and velocity vectors of the spacecraft at the time of the targeting maneuver are given by

$$\begin{aligned}
\mathbf{r}_{t_m} &= r_{t_m}\left(-\frac{1}{e_{\perp_{t_m}}}\cos\Lambda\sin\psi_{t_m}\sin f_{t_m}\hat{\mathbf{d}} + \frac{1}{e_{\perp_{t_m}}}\big(1-\cos^2\Lambda(1-\cos\psi_{t_m})\big)\sin f_{t_m}\hat{\mathbf{y}} \mp \cos f_{t_m}\hat{\mathbf{z}}\right),\\
\mathbf{v}_{t_m} &= \sqrt{\frac{\mu}{a^-(1-e_{t_m}^2)}}\left(-\frac{1}{e_{\perp_{t_m}}}\cos\Lambda\sin\psi_{t_m}(e_{t_m}+\cos f_{t_m})\hat{\mathbf{d}}\right.\\
&\qquad\left.+\frac{1}{e_{\perp_{t_m}}}(e_{t_m}+\cos f_{t_m})\big(1-\cos^2\Lambda(1-\cos\psi_{t_m})\big)\hat{\mathbf{y}} \pm \sin f_{t_m}\hat{\mathbf{z}}\right),
\end{aligned} \tag{C.1}$$

where $e_{t_m} = (1-\cos\psi_{tm})\sin\Lambda\cos\Lambda$, $r_{t_m} = a^-(1-e_{t_m}^2)/(1+e_{t_m}\cos f_{t_m})$, and $e_{\perp_{t_m}} = \sqrt{\cos^2\Lambda\sin^2\psi_{t_m} + \big(1-\cos^2\Lambda(1-\cos\psi_{t_m})\big)^2}$. We may now substitute the position and velocity vectors inside Eq. (4.33) to arrive at the following expression for the partial derivative of the state elements with respect to maneuver error $\delta\mathbf{v}_{t_m}$:

www.manaraa.com

$$\left.\frac{\partial \mathbf{e}}{\partial \mathbf{v}}\right|_{t_m} = \sqrt{\frac{a^-(1-e_{t_m}^2)}{\mu}}\frac{1}{e_{\perp_{t_m}}^2(1+e_{t_m}\cos f_{t_m})}\Bigg\{ \big(\cos^2\Lambda \sin f_{t_m}\sin^2\psi_{t_m}(e_{t_m}+\cos f_{t_m})\big)\hat{\mathbf{d}}\hat{\mathbf{d}}$$
$$-\big(\cos\Lambda\sin f_{t_m}\sin\psi_{t_m}((\cos\psi_{t_m}-1)\cos^2\Lambda+1)(e_{t_m}+\cos f_{t_m})\big)\hat{\mathbf{d}}\hat{\mathbf{y}}$$
$$-e_{\perp_{t_m}}(\pm\cos\Lambda\sin\psi_{t_m}(e_{t_m}\cos f_{t_m}-\cos^2 f_{t_m}+2))\hat{\mathbf{d}}\hat{\mathbf{z}}$$
$$-(\cos\Lambda\sin f_{t_m}\sin\psi_{t_m}((\cos\psi_{t_m}-1)\cos^2\Lambda+1)(e_{t_m}+\cos f_{t_m}))\hat{\mathbf{y}}\hat{\mathbf{d}}$$
$$(\sin f_{t_m}((\cos\psi_{t_m}-1)\cos^2\Lambda+1)^2(e_{t_m}+\cos f_{t_m}))\hat{\mathbf{y}}\hat{\mathbf{y}}$$
$$e_{\perp_{t_m}}(\pm(\cos^2\Lambda\cos\psi_{t_m}-\cos^2\Lambda+1)(e_{t_m}\cos f_{t_m}-\cos^2 f_{t_m}+2))\hat{\mathbf{y}}\hat{\mathbf{z}}$$
$$e_{\perp_{t_m}}(\pm\cos\Lambda\sin\psi_{t_m}(\cos^2 f_{t_m}+2e_{t_m}\cos f_{t_m}+1))\hat{\mathbf{z}}\hat{\mathbf{d}}$$
$$-e_{\perp_{t_m}}(\pm(\cos^2\Lambda\cos\psi_{t_m}-\cos^2\Lambda+1)(\cos^2 f_{t_m}+2e_{t_m}\cos f_{t_m}+1))\hat{\mathbf{z}}\hat{\mathbf{y}}-\frac{e_{\perp_{t_m}}^2\sin 2f_{t_m}}{2}\hat{\mathbf{z}}\hat{\mathbf{z}}\Bigg\}, \tag{C.2}$$

$$\left.\frac{\partial \mathbf{h}}{\partial \mathbf{v}}\right|_{t_m} = \sqrt{\frac{a^-(1-e_{t_m}^2)}{\mu}}\frac{1}{e_{\perp_{t_m}}^2(1+e_{t_m}\cos f_{t_m})}\Bigg\{ \pm e_{\perp_{t_m}}\cos f_{t_m}\sqrt{1-e_{t_m}^2}\;\hat{\mathbf{d}}\hat{\mathbf{y}}$$
$$+(\sin f_{t_m}((\cos\psi_{t_m}-1)\cos^2\Lambda+1)\sqrt{1-e_{t_m}^2}\,)\hat{\mathbf{d}}\hat{\mathbf{z}}\mp e_{\perp_{t_m}}\cos f_{t_m}\sqrt{1-e_{t_m}^2}\;\hat{\mathbf{y}}\hat{\mathbf{d}}$$
$$(\cos\Lambda\sin f_{t_m}\sin\psi_{t_m}\sqrt{1-e_{t_m}^2}\,)\hat{\mathbf{y}}\hat{\mathbf{z}}-(\sin f_{t_m}((\cos\psi_{t_m}-1)\cos^2\Lambda+1)\sqrt{1-e_{t_m}^2}\,)\hat{\mathbf{z}}\hat{\mathbf{d}}$$
$$-(\cos\Lambda\sin f_{t_m}\sin\psi_{t_m}\sqrt{1-e_{t_m}^2}\,)\hat{\mathbf{z}}\hat{\mathbf{y}}\Bigg\}. \tag{C.3}$$

www.manaraa.com

Appendix D

Fourier Series Expansion of a Radius Function

In taking the average of the orbit elements in the eccentric orbit case, we encounter quadratures of a radius function of the form

$$K(\cos(\theta)) = \frac{1}{(1 + e\cos(\theta))^p}. \tag{D.1}$$

A general Fourier series expansion for a function of this form is given in Reference [77] as the following

$$\frac{1}{(1 + e\cos(\theta))^p} = \sum_{m=0}^{\infty} b_m^p \cos(m\theta), \tag{D.2}$$

where

$$\begin{aligned} b_0^p &= \frac{\sqrt{1-e^2}}{(1-e^2)^p} f_0^p, \text{ and} \\ b_k^p &= (-1)^k 2 \left(\frac{e}{2}\right)^k \frac{\sqrt{1-e^2}}{(1-e^2)^p} f_k^p. \end{aligned} \tag{D.3}$$

The coefficients f_k^p are given by

$$\begin{aligned} f_k^1 &= \left(\frac{2}{1+\sqrt{1-e^2}}\right)^k, \\ f_k^{p+1} &= \begin{cases} \frac{(p-k)!(p+k)!}{p!^2} \sum_{l=0}^{\lfloor (p-k)/2 \rfloor} \frac{p!}{l!(l+k)!(p-k-2l)!} \left(\frac{e}{2}\right)^{2l} & p+1 > k \\ \frac{p-k}{p}(1-e^2) f_k^p + 2 f_{k-1}^{p+1} & p+1 \leq k \end{cases} \end{aligned} \tag{D.4}$$

where "$\lfloor\ \rfloor$" denotes the floor of the enclosed quantity. It turns out that the value of the coefficients drop very rapidly as the order of the expansion increases. This is especially true for the small

www.manaraa.com

values of e. For $p = 2$ and $p = 3$ the first couple of the terms of the expansion are given by

$$\frac{1}{(1 + e\cos(\theta))^2} = \frac{1}{(1 - e^2)^{3/2}} - \frac{2e}{(1 - e^2)^{3/2}}\cos(\theta) + \text{HOT}, \tag{D.5}$$

$$\frac{1}{(1 + e\cos(\theta))^3} = \frac{2 + e^2}{2(1 - e^2)^{5/2}} - \frac{3e}{(1 - e^2)^{5/2}}\cos(\theta) + \text{HOT}. \tag{D.6}$$

www.manaraa.com

Appendix E

Basis Functions for the Secular Equations

This section summarizes a set of basis functions that are used in the derivation of the secular dynamics of the orbit elements for an eccentric orbit.

E.1 Double Primed Secular Equations Basis Functions

The basis functions used in the secular equations for the eccentricity vector shown in Eq. (5.35) are given by

$$
\begin{aligned}
\mathcal{F}_0^1 &= \quad 6b_0^3 + 4eb_1^3 + b_2^3 \\
\mathcal{F}_1^1 &= \quad 8eb_0^3 + 7b_1^3 + 4eb_2^3 + b_3^3 \\
\mathcal{F}_1^2 &= -4eb_0^3 - 5b_1^3 - 2eb_2^3 + b_3^3 \\
\mathcal{F}_2^1 &= \quad 2b_0^3 + 4eb_1^3 + 6b_2^3 + 4eb_3^3 + b_4^3 \\
\mathcal{F}_2^2 &= \quad 2b_0^3 - 2eb_1^3 - 6b_2^3 - 2eb_3^3 + b_4^3 \\
\mathcal{G}_n^1 &= \quad b_{n-2}^3 + 4eb_{n-1}^3 + 6b_n^3 + 4eb_{n+1}^3 + b_{n+2}^3 \qquad n \geq 3 \\
\mathcal{G}_n^2 &= \quad b_{n-2}^3 - 2eb_{n-1}^3 - 6b_n^3 - 2eb_{n+1}^3 + b_{n+2}^3 \qquad n \geq 3,
\end{aligned}
\tag{E.1}
$$

www.manaraa.com

$$
\begin{aligned}
\mathcal{Z}_1^1 &= b_3^3 - b_1^3 \\
\mathcal{Z}_1^2 &= 4eb_0^3 + b_1^3 - 2eb_2^3 - b_3^3 \\
\mathcal{Z}_1^3 &= \mathcal{Z}_1^1 + \mathcal{Z}_1^2 \\
\mathcal{Z}_2^1 &= -2b_0^3 + b_4^3 \\
\mathcal{Z}_2^2 &= 2b_0^3 + 2eb_1^3 - 2eb_3^3 - b_4^3 \\
\mathcal{Z}_2^3 &= \mathcal{Z}_2^1 + \mathcal{Z}_2^2 \\
\mathcal{Y}_n^1 &= b_{n+2}^3 - b_{n-2}^3 && n \geq 3 \\
\mathcal{Y}_n^2 &= b_{n-2}^3 + 2eb_{n-1}^3 - 2eb_{n+1}^3 - b_{n+2}^3 && n \geq 3 \\
\mathcal{Y}_n^3 &= \mathcal{Y}_n^1 + \mathcal{Y}_n^2 && n \geq 3,
\end{aligned}
\tag{E.2}
$$

where the quantity b_k^p is defined by Eq. (D.3). For the angular momentum equation shown in Eq. (5.36), the basis functions are

$$
\begin{aligned}
c_n &= (b_{n-1}^3 + b_{n+1}^3), \text{ and} \\
d_n &= (b_{n-1}^3 - b_{n+1}^3), \text{ for } n \geq 2.
\end{aligned}
\tag{E.3}
$$

Finally, the following basis functions are used for the energy expression shown in Eq. (5.37) are given by

$$
\begin{aligned}
\epsilon_1 &= 2b_0^2 + 2eb_1^2 + b_2^2, \\
\epsilon_n &= b_{n-1}^2 + 2eb_n^2 + b_{n+1}^2, \quad n \geq 2 \\
\zeta_1 &= 2b_0^2 - b_2^2, \\
\zeta_n &= b_{n-1}^2 - b_{n+1}^2, \qquad n \geq 2.
\end{aligned}
\tag{E.4}
$$

www.manaraa.com

E.2 Single Primed Secular Equations Basis Functions

The basis functions for the secular equations of the eccentricity vector shown in Eq. (5.38) are given by

$$\begin{aligned}
\mathcal{F}_0'^1 &= \quad 4b_0^3 e + 8b_1^3 + 6b_2^3 e, \\
\mathcal{F}_0'^2 &= \quad 4b_0^3 e - 4b_1^3 - 6b_2^3 e, \\
\mathcal{F}_1'^1 &= \quad 8b_0^3 + 5b_1^3 e + 4b_2^3 + 3b_3^3 e, \\
\mathcal{F}_1'^2 &= -4b_0^3 - 3b_1^3 e - 4b_2^3 - 3b_3^3 e, \\
\mathcal{F}_2'^1 &= \quad 6b_0^3 e + 4b_1^3 + 2b_2^3 e + 4b_3^3 + 3b_4^3 e, \\
\mathcal{F}_2'^2 &= -6b_0^3 e - 2b_1^3 + 2b_2^3 e - 2b_3^3 - 3b_4^3 e, \\
\mathcal{G}_n'^1 &= \quad 3b_{n-2}^3 e + 4b_{n-1}^3 + 2b_n^3 e + 4b_{n+1}^3 + 3b_{n+2}^3 e \quad n \geq 3, \\
\mathcal{G}_n'^2 &= -3b_{n-2}^3 e - 2b_{n-1}^3 + 2b_n^3 e - 2b_{n+1}^3 - 3b_{n+2}^3 e \quad n \geq 3.
\end{aligned} \tag{E.5}$$

$$\begin{aligned}
\mathcal{Z}_1'^1 &= \quad 4b_0^3 + 3b_1^3 e - 2b_2^3 - 3b_3^3 e, \\
\mathcal{Z}_1'^2 &= \quad 8b_0^3 + 5b_1^3 e - 2b_2^3 - 3b_3^3 e, \\
\mathcal{Z}_1'^3 &= \quad \mathcal{Z}_1^3, \\
\mathcal{Z}_2'^1 &= \quad 6b_0^3 e + 2b_1^3 - 2b_3^3 - 3b_4^3 e, \\
\mathcal{Z}_2'^2 &= \quad 6b_0^3 e + 4b_1^3 - 4b_3^3 - 3b_4^3 e, \\
\mathcal{Z}_2'^3 &= \quad \mathcal{Z}_2^3, \\
\mathcal{Y}_n'^1 &= \quad 3b_{n-2}^3 e + 2b_{n-1}^3 - 2b_{n+1}^3 - 3b_{n+2}^3 e \quad n \geq 3, \\
\mathcal{Y}_n'^2 &= \quad 3b_{n-2}^3 e + 4b_{n-1}^3 - 4b_{n+1}^3 - 3b_{n+2}^3 e \quad n \geq 3, \\
\mathcal{Y}_n'^3 &= \quad \mathcal{Y}_n^3 \qquad\qquad\qquad\qquad\qquad\qquad\quad n \geq 3.
\end{aligned} \tag{E.6}$$

For the energy expression given by Eq.(5.40), the basis functions are

www.manaraa.com

$$
\begin{aligned}
\epsilon'_0 &= 2eb_1^2 + 2b_2^2, \\
\epsilon'_1 &= 2eb_0^2 + b_1^2 + eb_2^2 + b_3^2, \\
\epsilon'_2 &= 2b_0^2 + eb_1^2 + eb_3^2 + b_4^2, \\
\epsilon'_n &= b_{n-2}^2 + eb_{n-1}^2 + eb_{n+1}^2 + b_{n+2}^2, \\
\zeta'_1 &= 2eb_0^2 + b_1^2 - 2b_2^2 - b_3^2, \\
\zeta'_2 &= 2b_0^2 + eb_1^2 - eb_3^2 - b_4^2, \\
\zeta'_n &= b_{n-2}^2 + eb_{n-1}^2 - eb_{n+1}^2 - b_{n+2}^2 \qquad n \geq 2.
\end{aligned}
\tag{E.7}
$$

www.manaraa.com

Appendix F

Partial Derivatives of the Geometric Range and Range-rate Measurements

The partial derivatives of the range and the range-rate measurements (see Eq. (6.50)) with respect to the spacecraft position and velocity vector are given by

$$\frac{\partial \rho_i}{\partial \mathbf{r}} = -\frac{(\mathbf{r}_i - \mathbf{r})^{\mathrm{T}}}{|\mathbf{r}_i - \mathbf{r}|},$$
$$\frac{\partial \rho_i}{\partial \mathbf{v}} = [0]_{1\times 3} \qquad \forall\, i. \tag{F.1}$$

$$\frac{\partial \dot{\rho}_i}{\partial \mathbf{r}} = -\frac{(\mathbf{v}_i - \mathbf{v})^{\mathrm{T}}}{|\mathbf{r}_i - \mathbf{r}|} + (\mathbf{r}_i - \mathbf{r}) \cdot (\mathbf{v}_i - \mathbf{v}) \frac{(\mathbf{r}_i - \mathbf{r})^{\mathrm{T}}}{|\mathbf{r}_i - \mathbf{r}|^3}, \text{ and}$$
$$\frac{\partial \dot{\rho}_i}{\partial \mathbf{v}} = -\frac{(\mathbf{r}_i - \mathbf{r})^{\mathrm{T}}}{|\mathbf{r}_i - \mathbf{r}|}, \tag{F.2}$$

where $\mathbf{r}_i$ and $\mathbf{v}_i$ are the position and velocity vectors of the i^{th} antenna expressed in an inertial coordinate frame and $\mathbf{r}$ and $\mathbf{v}$ are the position and velocity vectors of a spacecraft expressed in the same coordinate frame.

www.manaraa.com